Czech Technical University in Prague
Faculty of Electrical Engineering
Department of Physics

Contribution to three problems of nonlinear acoustics

Habilitation Thesis

Milan Červenka

January 2021

Acknowledgements

I would like to thank Michal Bednařík for his collaboration with me, and his long-lasting support of my work. I am especially grateful to my wife for her endless patience with me, for her running our family, giving me enough space to think about acoustics. I am grateful to all my former or present colleagues, who showed their interest in my work and helped me pursue my goals.

Contents

Chapter 1

Introduction

Nonlinear acoustics is the branch of acoustics, where, contrary to linear acoustics, the amplitudes of the individual acoustic variables cannot be considered infinitesimally small anymore. The finite-amplitudes of the acoustic-field quantities result in interesting phenomena, such as harmonic distortion, generation of shocks or steady fluid flows, and many others. These phenomena may be of interest in various applications, or they may be undesirable. In both cases, it is important to understand them.

When the nonlinear effects connected with the finite-amplitude acoustic fields are studied theoretically, the well-established linear theory cannot be employed anymore. That is why nonlinear model equations, derived in the various degrees of simplification, are searched for. The most simple models allow for their analytical solutions, either exact or approximate ones. However, in many cases, these analytical solutions are not known, or they are so complicated that their practical utilization is hardly possible. In these cases, various computational methods find their application.

In the following chapters, three topical problems of nonlinear acoustics are presented and discussed, to which the author contributed during the last ten years, mainly employing various numerical computational techniques.

First, it is an efficient generation of high-amplitude waves in acoustic resonators. We show that it is possible to maximize the acoustic pressure amplitude of the standing wave by choosing a suitable resonator shape. The appropriate shape depends on the driving method, and we propose a computational procedure for its determination. We demonstrate the functionality of the proposed approach in the case of a loudspeaker-driven resonator. We also present the design and mathematical model of a compact resonant system for the generation of a low-frequency acoustic wave with a large amplitude of the acoustic particle displacement.

Second, it is the understanding of the complex behavior of Rayleigh streaming in high-amplitude acoustic fields. Even if acoustic streaming was first theoretically studied almost 140 years ago, there have been unexplained discrepancies between the theoretical predictions and experimental data since today. Employing numerical simulations, we have revealed a strong sensitivity of the acoustic streaming structure on the transverse temperature distribution in the streaming fluid. With this knowledge, we have identified a physical mechanism that explains the experimental observations.

Third, it is an easy-to-use computational approach for modeling highly-directional low-frequency sound beams radiated from small transducers–the parametric acoustic array. Contrary to the previously published works, our approach is not limited by the paraxial approximation so that the off-axis field, as well as the near-field, can be predicted.

Chapter 2

Resonators for the generation of high-amplitude acoustic fields

2.1 Introduction

It has been known for about fifty years, see [1, 2], that it is difficult to mechanically drive standing acoustic wave in a closed fluid-filled tube (an acoustic resonator) into high amplitudes, because nonlinear effects cause the transport of acoustic energy into higher harmonics, which results in the generation of a shock wave and thereby to increased acoustic energy dissipation.

On the other hand, many following studies have shown that if the resonators are suitably shaped, it is possible to generate effectively standing acoustic waves even with overpressure exceeding the ambient pressure several times, which enables their utilization in a variety of practical applications. Pumping of fluids, stabilization of electric discharges [3, 4] for plasma-chemical reactors or thermoacoustics [5] can be given as examples.

D. F. Gaitan and A. A. Atchley [6] showed that introduction of the cross-section variability in a piston-driven resonator can significantly reduce energy transfer from the fundamental to the higher modes, prevent shock-formation and increase an amplitude of the standing wave.

Ch. C. Lawrenson *et al.* [7] presented in their experimental paper concept of Resonant Macrosonic Synthesis (RMS) whereby they obtained acoustic pressure amplitude more than an order larger than it had been possible before. The concept is based on so-called dissonant resonators, whose varying-cross-section cavities don't have the higher eigenfrequencies coincident with the harmonics of the nonlinearly distorted waveform, which results in the suppression of a shock-wave formation. The authors demonstrated a strong dependence of obtained maximum amplitude on the resonator shape (cylindrical, conical, horn-cone hybrid and bulb).

Yu. A. Ilinskii *et al.* [8] presented in their seminal theoretical paper a quasi-one-dimensional model equation expressed in terms of the velocity potential for description of high-amplitude standing waves in axi-symmetric, but otherwise arbitrarily shaped acoustic resonators. The model comprises nonlinearity, viscous bulk attenuation and, entire-resonator driving by an inertial force (shaker-driving). A numerical algorithm was proposed for integration of the model equation in the frequency domain, the numerical simulations were conducted in case of a cylindrical, conical and bulb-shaped resonator. The numerical results were in a good agreement with the experimental ones. The model was subsequently supplemented [9] to account for energy losses in the boundary layer and the losses due to acoustically generated turbulence.

M. F. Hamilton *et al.* [10] and M. P. Mortell and B. R. Seymour [11] investigated theoretically the dependence of the resonance frequencies of the varying-cross-sectioned resonators on their shapes and their nonlinear shifts.

Y.-D. Chun and Y.-H. Kim [12] investigated numerically the influence of an entirely-driven resonant cavity shape on the compression ratio (ratio of the maximum and minimum pressure attained at chosen point in the resonator cavity during one period) using a quasi-one-dimensional model equation based on the conservation laws integrated in the time-domain using a high-order finite-difference scheme. From the several simple studied shapes (cylindrical, conical, 1/2-cosine and 3/4-cosine), the 1/2-cosine offered the best performance.

R. R. Erickson and B. T. Zinn [13] developed a Galerkin-method-based algorithm for time-domain integration of the model equation proposed in paper [8]. They also showed that the exponentially shaped resonator's compression ratio strongly and non-trivially depends on its geometrical parameters.

C. Luo *et al.* [14] studied theoretically the effect of the resonator shape and dimension on its compression ratio in the case of axi-symmetric and low-aspect-ratio exponential geometry, observing its decrease with shortening the resonator length and smaller radius-to-length ratio. X. Li *et al.* [15] optimized the parameters of simple-shaped resonator cavities in order to maximize the compression ratio by means of numerical simulations based on a nonlinear wave equation with volume acoustic energy attenuation model [8]. Within the numerical experiments, they achieved the value of 48 in the case of an optimized horn-cone shape. C. Luo *et al.* [16] conducted numerical experiments in order to compare piston- or shaker-driving of exponentially shaped cavity finding similar results. Q. Min *et al.* [17] demonstrated experimentally the possibility of generating strongly nonlinear acoustic fields in loudspeaker-driven dissonant tubes.

In all the above-mentioned papers, the same approach was employed, i.e. the resonator shapes were described using smooth elementary functions with fixed or adjustable (Refs. [13], [15]) parameters, e.g., all the resonator cavities were non-symmetrical, wide at one end and narrow at the other one, where the maximum pressure (or compression ratio) were obtained.

In this chapter, a more general approach is presented. We employ parametrizing acoustic resonator shapes using control points interconnected with cubic-splines. Employing a linear theory, suitable shapes of resonators maximizing acoustic pressure in the resonators are searched for. As the optimization is based on a linear theory, the model cannot predict the amplitudes and phases of the higher harmonics, which is the cornerstone of the RMS technique. However, cross-section variability makes the optimized resonator shapes dissonant and therefore shock-wave formation is suppressed. As a result, the optimized resonator shapes provide higher amplitudes of acoustic pressure than the ones proposed previously provided that the higher harmonics are not excited too much.

Within this chapter, a closely related topic–generation of a low-frequency standing wave with high amplitude of acoustic particle displacement, is also discussed.

This chapter is based on author's works [18, 19, 20, 21, 4], see also the Appendices A.1, A.2, A.3, A.4, and A.5.

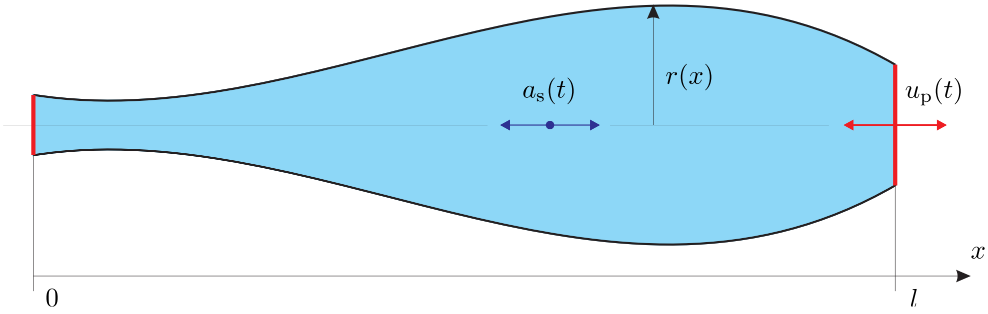

Figure 2.1: Resonator with a variable cross-section, driven by an inertial force, or a vibrating piston.

2.2 Optimized resonators: A simplified approach

2.2.1 Mathematical model

For the description of the acoustic field in a fluid-filled variable-cross-section resonator, see Fig. 2.1, driven by an external (inertial) force or a vibrating piston, we can issue from the quasi-one-dimensional model equation derived in [8], which, after linearisation, has the form

$$\frac{c_0^2}{r^2}\frac{\partial}{\partial x}\left(r^2\frac{\partial\varphi}{\partial x}\right)-\frac{\partial^2\varphi}{\partial t^2}=-\frac{\delta_{\rm v}}{r^2}\frac{\partial^2}{\partial t\partial x}\left(r^2\frac{\partial\varphi}{\partial x}\right)+\frac{{\rm d}a_{\rm s}}{{\rm d}t}x, \tag{2.1}$$

where φ is the velocity potential, x is the spatial coordinate along the resonator cavity, t is the time, $r = r(x)$ is the varying resonator radius, c_0 is the small-signal speed of sound, $a_{\rm s} = a_{\rm s}(t)$ is the driving acceleration, $\delta_{\rm v} = (\zeta + 4\eta/3)/\rho_0$ is the attenuation coefficient, where ζ and η are the bulk and shear viscosities. Left side of Eq. (2.1) represents the Webster's horn equation, see, e.g., [22, 23, 24], the first term on the right side accounts for the acoustic energy dissipation, the last term represents the driving by an inertial force.

In the first approximation, acoustic velocity v and acoustic pressure p' can be calculated from the velocity potential as

$$v=\frac{\partial\varphi}{\partial x},\qquad p'=-\rho_0\frac{\partial\varphi}{\partial t}-\rho_0a_{\rm s}x, \tag{2.2}$$

where ρ_0 is the fluid ambient density.

If the resonator is driven by an inertial force, Eq. (2.1) is solved with the boundary conditions $\partial\varphi/\partial x = 0$ for $x = 0$ and $x = l$, where l is the resonator length. If the resonator is driven by a piston at $x = l$ vibrating with velocity $u_{\rm p}(t)$, Eq. (2.1) is solved with the boundary conditions $\partial\varphi/\partial x = 0$ for $x = 0$, and $\partial\varphi/\partial x = u_{\rm p}(t)$ for $x = l$.

For some shape functions $r(x)$, analytical solutions to Eq. (2.1) are known, but, in general, the solution must be searched numerically. Within this work, the solution was sought employing the method of eigenfunction expansions, see, e.g., [25], as follows.

For a given shape function $r(x)$, eigenfunctions F_k and corresponding eigenfrequencies Ω_k were found by a numerical solution of the equation

$$\frac{1}{\pi^2R^2}\frac{{\rm d}}{{\rm d}X}\left(R^2\frac{{\rm d}F}{{\rm d}X}\right)+\Omega^2F=0 \tag{2.3}$$

with homogeneous Neumann boundary conditions at $X = 0$ and $X = 1$. Here, $X = x/l$, $R = r/l$, and $\Omega = \omega/\omega_0$ is the dimensionless frequency, where $\omega_0 = \pi c_0/l$ is the first angular resonant frequency of a constant-cross-sectioned resonator with length l. The individual values Ω_k thus represent the individual resonant frequencies of the shaped resonator.

Employing this information, see [18] (Appendix A.1), acoustic pressure amplitude p_0 at a given point in the resonator (here, $x = 0$), for a given resonance frequency Ω_k and driving acceleration amplitude a_0 can be calculated as

$$p_{0\text{s}} = \beta K_\text{s} a_{0\text{s}}, \qquad p_{0\text{p}} = \beta K_\text{p} a_{0\text{p}}.$$

Here indices s,p stand for s=shaker (inertial force) driving, and p=piston driving; the coefficient $\beta = \rho_0 c_0 l^2/\pi^2 \delta_\text{v}$ depends on the fluid material properties and the resonator length, and, finally,

$$K_\text{s} = \frac{\pi}{\Omega_k} \left| \frac{\langle X|F_k\rangle}{\langle F_k|F_k\rangle} F_k(0) \right|, \tag{2.4a}$$

$$K_\text{p} = \frac{1}{\pi \Omega_k^3} \left| \frac{\langle 1 + 2X(\mathrm{d}R/\mathrm{d}X)/R + \pi^2\Omega_k^2 X^2/2|F_k\rangle}{\langle F_k|F_k\rangle} F_k(0) \right|, \tag{2.4b}$$

where

$$\langle F|G\rangle = \int_0^1 F(X)\, R^2(X)\, G(X)\, \mathrm{d}X.$$

The factors K_s, K_p are dimensionless factors which depend on nothing but the resonator shape. From here, it follows that if a resonator shape maximizing the acoustic pressure amplitude is to be determined, the shape factors (2.4) are the quantities to be maximized. The different forms of the factors K_s and K_p indicate that the optimum resonator shape depends on the method of driving.

2.2.2 Resonator shape function and its optimization

So as not to restrict the resonator's shape to a specific pre-defined elementary function with only a few adjustable parameters, it is defined using N control points distributed regularly at positions

$$X_i = \frac{i}{N-1}, \qquad i = 0, 1, \ldots, N-1,$$

whose corresponding values $R(X_i) = R_i$ are found in a pre-defined interval $R_i \in \langle R_\text{min}, R_\text{max}\rangle$.

The function $R(X)$ is obtained using the cubic-spline-interpolation of the control points (the function and its first and second derivatives are continuous) with zero derivatives at the ends of the interval. The values R_i are chosen in order that $R_\text{min} \le R(X) \le R_\text{max}$ for any $X \in \langle 0, 1\rangle$. With the resonator shape defined, an eigenfrequency Ω_k is looked for numerically in an interval $\langle \Omega_\text{min}, \Omega_\text{max}\rangle$.

As an objective function to be maximized, the shape factors (2.4) are used.

As the parameter search space for the objective function is many- (N-) dimensional ($\mathbb{R}^N$), and moreover, it is not continuous (some control-points sets lead to $R(X)$ that does not lie in the pre-defined interval $\langle R_\text{min}, R_\text{max}\rangle$, possibly there is no eigenfrequency $\Omega_k \in \langle \Omega_\text{min}, \Omega_\text{max}\rangle$), a heuristic optimization methods seem to have reasonable use for this type of problem [26]. In this concrete case, a variant of Evolution Strategies $(\mu + \lambda)$-ES was utilized. For more details, see [18] (Appendix A.1).

Cylindrical, $R(X) = const.$ $K_\mathrm{s} = 1.27, \quad K_\mathrm{p} = K_\mathrm{s}/2$ $\Omega_k = 1, 2, 3, 4, 5, \dots$	Conical, $R_\mathrm{min}/R_\mathrm{max} = 1/9$ $K_\mathrm{s} = 1.77, \quad K_\mathrm{p} = 1.14$ $\Omega_k = 1.28, 2.23, 3.19, 4.15, 5.13, \dots$
Opt. for shaker, $R_\mathrm{min}/R_\mathrm{max} = 2/5$ $K_\mathrm{s} = 2.98$ $\Omega_k = 0.61, 1.90, 3.14, 3.90, 5.05, \dots$	Opt. for piston, $R_\mathrm{min}/R_\mathrm{max} = 2/5$ $K_\mathrm{p} = 6.08$ $\Omega_k = 0.64, 1.61, 2.75, 3.93, 5.07, \dots$
Opt. for shaker, $R_\mathrm{min}/R_\mathrm{max} = 1/5$ $K_\mathrm{s} = 5.46$ $\Omega_k = 0.36, 1.95, 3.43, 3.96, 5.41, \dots$	Opt. for piston, $R_\mathrm{min}/R_\mathrm{max} = 1/5$ $K_\mathrm{p} = 38.38$ $\Omega_k = 0.38, 1.48, 2.78, 4.08, 5.33, \dots$

Table 2.1: Parameters of individual resonant cavities.

2.2.3 Numerical results

Within the numerical experiments, the resonator shapes were parametrized employing $N = 10$ control points. As it is reasonable to assume that the resonator's performance depends on the ratio of the minimum and maximum radius, the numerical experiments were conducted for $R_\mathrm{min}/R_\mathrm{max} = 1/5$ and $2/5$, both, for the shaker and piston driving.

The numerical results are summarized in Tab. 2.1, where, for the sake of comparison, there also are shown the results for a constant-cross-sectioned (cylindrical), and a conical resonator with $R_\mathrm{min}/R_\mathrm{max} = 1/9$ (similar to the one studied in [8]). As it turns out that the resonators are most effectively driven at the fundamental resonance Ω_1, the shape factors K_s, K_p are always presented for Ω_1.

For the cylindrical resonator, the shape factor for the shaker-driven resonator attains the value of $K_\mathrm{s} = 1.27$, the one for the piston driving $K_\mathrm{p} = K_\mathrm{s}/2$, which means, that with the same acceleration amplitude, the piston-driving provides half an acoustic pressure amplitude than in the case of the shaker-driving. Major disadvantage of this simple shape is the fact, that the higher eigenfrequencies are the integer multiples of the fundamental eigenfrequency which results in substantial nonlinear distortion in the high-amplitude fields and evolution of the shock-wave.

In the case of the conical resonator, see Tab. 2.1, the factors K_s and K_p attain higher values than in the previous case and again, the shaker-driving is more effective. What is also important is the fact that the higher eigenfrequencies are not the integer multiples of the first one, so that the nonlinearly generated higher harmonics are not coincident with the eigenfrequencies and thus they are suppressed.

The shapes of the optimized resonators are depicted in Fig. 2.2 and their parameters are summarized in the bottom two rows of Tab. 2.1. It can be seen that the optimum shapes are rather simple, the ones for the piston driving are symmetric, whereas the ones for the shaker driving are non-symmetric.

Generally, the shape factors for the optimized resonators exceed the ones for the simple-shaped ones (cylindrical, conical), the smaller the ratio $R_\mathrm{min}/R_\mathrm{max}$, the higher the values of the shape factors. Surprisingly enough, for a given value of $R_\mathrm{min}/R_\mathrm{max}$, the shape factor for the piston driving optimization exceeds the one for the shaker driving one.

A common feature of the optimized resonators is the fact that they are low-frequency ones, for example, for the piston driving optimization, for $R_\mathrm{min}/R_\mathrm{max} = 2/5$, $\Omega_1 = 0.64$, and for $R_\mathrm{min}/R_\mathrm{max} = 1/5$, $\Omega_1 = 0.38$. The optimized resonators, as it can be expected, are dissonant – the higher eigenfrequencies are not the integer multiples of the first one, which helps to

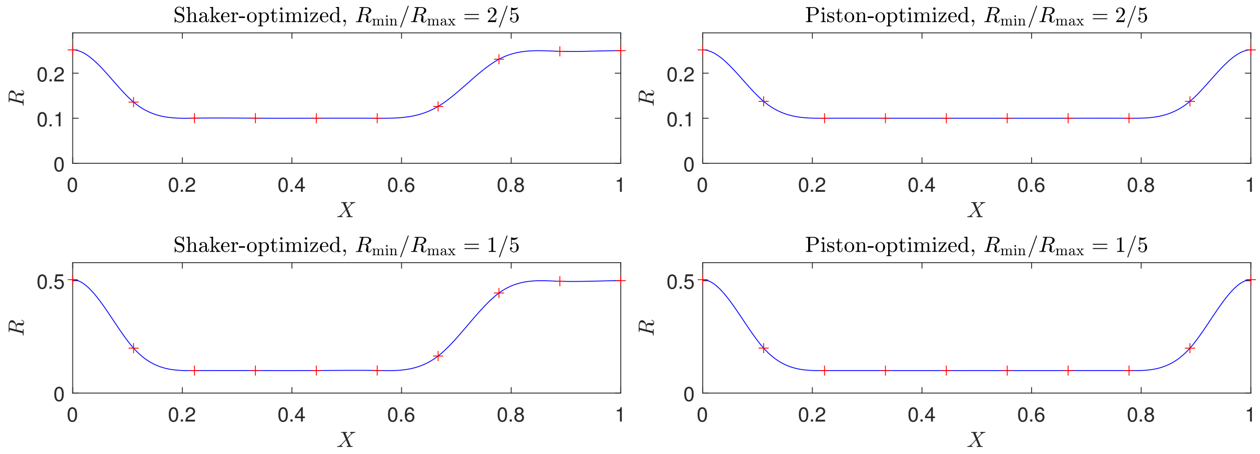

Figure 2.2: Optimized resonator shapes for shaker and piston driving, $R_{\min}/R_{\max} = 2/5$, and $R_{\min}/R_{\max} = 1/5$.

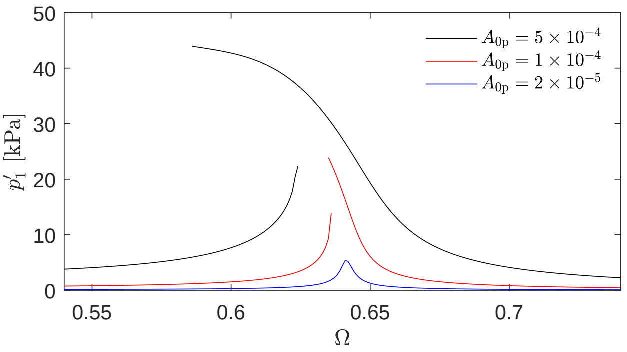

Figure 2.3: Frequency characteristics of the piston-optimised piston-driven resonator with $R_{\min}/R_{\max} = 2/5$ for different normalized driving acceleration amplitudes $A_{0\mathrm{p}}$.

prevent the shock formation at large acoustic pressure amplitudes. For more details, see [18] (Appendix A.1).

It is important to bear in mind that the optimization was based on the linear theory, but, in the high-amplitude acoustic fields, nonlinear phenomena take place and influence the overall performance. For this reason, nonlinear theory introduced in [8] was used to study the optimized resonators' properties at large amplitudes. As the working medium, air at normal conditions was used, see [18] (Appendix A.1) for the details.

Figure 2.3 shows the frequency characteristics (amplitude of the fundamental harmonics at $X = 0$) of the piston-optimized piston-driven acoustic resonator with $R_{\min}/R_{\max} = 2/5$ for different normalized piston acceleration amplitudes. The frequency characteristics exhibits softening behavior with hysteresis for higher driving accelerations.

Left panel of Fig. 2.4 shows the distribution of amplitudes of the first three harmonics of acoustic pressure along the same resonator as in the previous case for $A_{\mathrm{p}0} = 5 \times 10^{-4}$ and $\Omega = 0.586$. This frequency is reached using slow downwards frequency-sweep, at this point, maximum amplitude of the acoustic pressure is attained (see Fig. 2.3). The small-amplitude resonance frequency for this resonator (see Tab. 2.1) is $\Omega_{\mathrm{lin}} = 0.642$. It can be seen that the acoustic field is strongly nonlinearly distorted and that the 2nd harmonics attains similar amplitudes as the fundamental one. The right panel of Fig. 2.4 shows the same for the conical

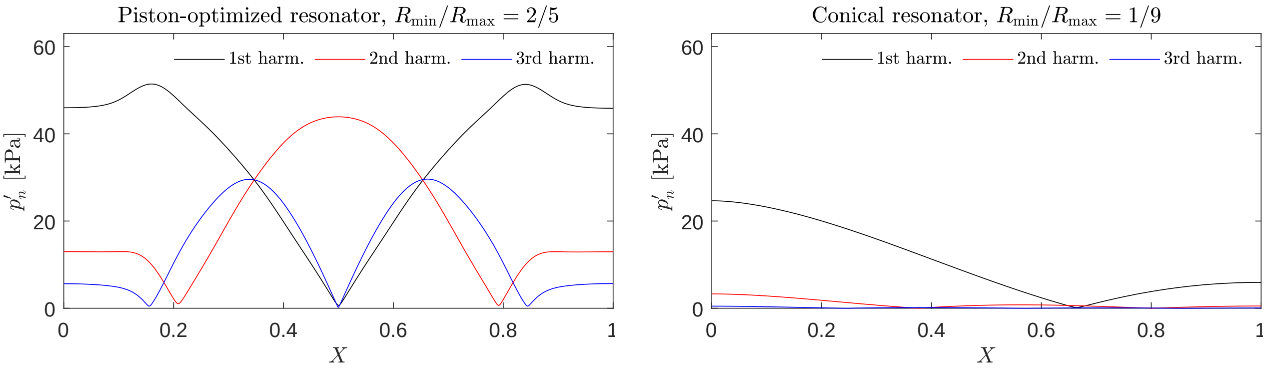

Figure 2.4: Distribution of acoustic pressure amplitude spectrum along the resonator axis; left panel: piston-optimized resonator, $R_{\text{min}}/R_{\text{max}} = 2/5$; right panel: conical resonator, $R_{\text{min}}/R_{\text{max}} = 1/9$. In both the cases, the resonators are driven with a vibrating piston with the same normalized acceleration amplitude $A_{0\text{p}} = 5 \times 10^{-4}$.

resonator (Tab. 2.1). It can be observed that the 1^{st} harmonics attains approximately only half an amplitude at $X = 0$ compared with the optimized resonator.

It has been shown that the piston driving gives rise to higher acoustic pressure amplitudes than the shaker driving when the optimized resonators are used with the same driving acceleration amplitudes. Even if the shaker-driven cavity is technically much simpler in the concrete applications (there is no need of tightening of the moving piston), it requires more powerful (and thus more expensive) driving system. Replacement of the moving piston with e.g., a horn-driver thus seems to show a direction to low-cost applications utilizing high-amplitude acoustic fields. The presented approach can also be easily modified to design, e.g., resonators with pre-defined frequency characteristics.

It is important to emphasize that the used model is rather simplified. However, this approach allows to formulate simple results which have, on the other hand, limited validity. In the following section, more realistic physical model including the dissipation effect of the boundary layer as well as the non-acoustic dissipation mechanisms is adopted. The interest is especially focused on the optimization of a complex system consisting of a resonant cavity attached to a horn-driver used as a driving element.

2.3 Optimized resonators: A loudspeaker-driven resonator

2.3.1 Mathematical model

For the description of finite-amplitude standing waves in axisymmetric variable-cross-section resonators, the following quasi-one-dimensional model equation derived in the second approximation was used (see [19] – Appendix A.2):

$$\frac{\partial^2\varphi}{\partial t^2} - \frac{c_0^2}{r^2}\frac{\partial}{\partial x}\left(r^2\frac{\partial\varphi}{\partial x}\right) = -\frac{\partial}{\partial t}\left(\frac{\partial\varphi}{\partial x}\right)^2 - \frac{\gamma-1}{2c_0^2}\frac{\partial}{\partial t}\left(\frac{\partial\varphi}{\partial t}\right)^2 - \\ - x\frac{\mathrm{d}a_\mathrm{s}}{\mathrm{d}t} + \frac{\delta}{c_0^2}\frac{\partial^3\varphi}{\partial t^3} - \frac{2c_0^2\varepsilon}{\sqrt{\pi}r^2}\int_{-\infty}^{t}\frac{1}{\sqrt{t-\tau}}\frac{\partial}{\partial x}\left[r\frac{\partial\varphi(x,\tau)}{\partial x}\right]\mathrm{d}\tau, \quad (2.5)$$

where the meaning of the individual symbols is the same as in Sec. 2.2.1. Moreover, γ is the adiabatic exponent, $\delta = [\zeta + 4\eta/3 + \kappa(1/c_V - 1/c_p)]/\rho_0$ is the diffusivity of sound, where η, ζ are the coefficients of shear and bulk viscosity, respectively, κ is the coefficient of thermal conduction, c_p, c_V are the specific heats at constant pressure and volume, respectively. Coefficient ε is defined as $\varepsilon = \sqrt{\nu_0}[1+(\gamma-1)/\sqrt{\mathrm{Pr}}]$, where $\nu_0 = \eta/\rho_0$ is the kinematic viscosity, and $\mathrm{Pr} = \eta c_\mathrm{p}/\kappa$ is the Prandtl number.

The substantial difference between the model represented by Eq. (2.5), and the one represented by Eq. (2.1), is the accounting for the energy losses in the viscothermal boundary layer (represented by the last term on the right side of Eq. (2.5)). Additional losses due to acoustically generated turbulence [9] can be incorporated into this term in a straightforward way.

In the case of the piston- or shaker-driving, Eq. (2.5) can be solved with the same boundary conditions as it has bee mentioned in Sec. 2.2.1. If a loudspeaker at $x = l$ is used as a driving element the boundary conditions can be given as

$$\left.\frac{\mathrm{d}\varphi}{\mathrm{d}x}\right|_{x=0} = 0, \qquad \mathcal{L}\left[p'(x=l), v(x=l), u\right] = 0, \quad (2.6)$$

where $\mathcal{L}$ is a linear operator describing the relationship between the acoustic pressure p', acoustic velocity v, and the driving voltage u in the loudspeaker model, see the details in [19] (Appendix A.2).

2.3.2 Optimization procedure

The optimization procedure developed in this case is similar to the one described in Sec. 2.2.1 as it is detailed in [19] (Appendix A.2). Again, the resonator shape is parametrized by a set of N control points, which are interconnected by cubic splines. Equation (2.5) is linearised and solved numerically in the frequency domain; in the case of the loudspeaker driving, the boundary conditions are represented by Eq. (2.6). As before, the quantity to be maximized is the acoustic pressure at one end of the resonator ($x = 0$), namely, the objective function was introduced as

$$k_{pu} = \frac{|\hat{p}'(x=0, \Omega=\Omega_\mathrm{resonance})|}{|\hat{u}|}, \quad (2.7)$$

where $\hat{p}'$, $\hat{u}$ represent the complex amplitudes of the acoustic pressure and the loudspeaker driving voltage. The dimensionless frequency Ω is introduced the same way as in Sec. 2.2.1; the resonance is determined by searching for the maximum in a pre-defined interval $\Omega_\mathrm{resonance} \in \langle\Omega_\mathrm{min}, \Omega_\mathrm{max}\rangle$ employing the Brent's method [27].

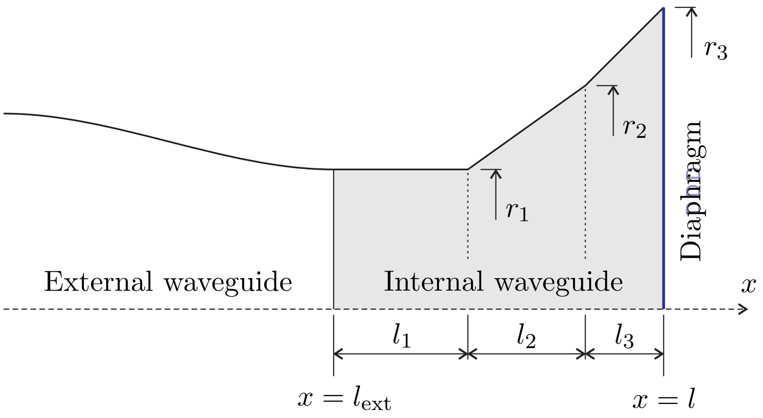

Figure 2.5: Model geometry of the internal waveguide of loudspeaker driver Selenium D405Ti; $l_1 = 24\,\text{mm}$, $l_2 = 21\,\text{mm}$, $l_3 = 14\,\text{mm}$, $r_1 = 25\,\text{mm}$, $r_2 = 39.5\,\text{mm}$, $r_3 = 53.5\,\text{mm}$. The total resonator length $l = l_{\text{ext}} + l_1 + l_2 + l_3$.

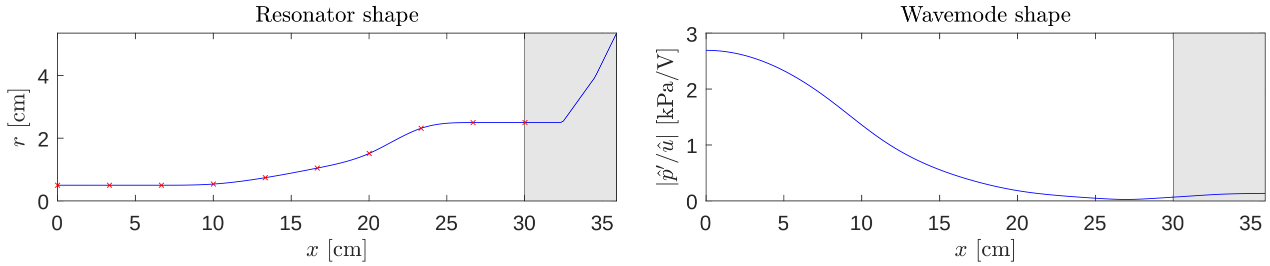

Figure 2.6: Left panel: shape of the optimized resonator; right panel: distribution of normalized acoustic pressure amplitude along the resonator axis. The grey area delimits the driver's internal waveguide.

2.3.3 Results

Physical and numerical experiments were conducted with air as a working medium at room conditions. The resonator shape was parametrized employing $N = 10$ control points, the loudspeaker used for the driving was the compression driver Selenium D405Ti. The driver has an output radius $r_1 = 25\,\text{mm}$ and an internal waveguide, see Fig. 2.5 which becomes a part of the resonant system. The length of the optimized (external) part of the resonator was set to $l_{\text{ext}} = 30\,\text{cm}$, its radius at $x = l_{\text{ext}}$ (where it is attached to the driver) $r(l_{\text{ext}}) = r_1$, see Fig. 2.5, and the minimum allowed radius $r_{\text{min}} = r_1/5$.

The electromechanical model parameters of the driver were determined by measurement, see [19] (Appendix A.2) for the details.

Shape of the optimized resonator can be seen in the left panel of Fig. 2.6. Its profile is very simple and smooth, the radius decreases towards the position $x = 0$, where the acoustic pressure amplitude is maximized. The right panel of Fig. 2.6 shows the distribution of the acoustic pressure amplitude (divided by the driving voltage) along the resonator axis.

In order to assess the performance of the optimized solution, the results were compared with the case of a cylindrical resonator ($r(x) = r_1$), and a conical resonator (with radius decreasing from r_1 to $r_1/5$ at $x = 0$); all the resonators have the same length $l_{\text{ext}} = 30\,\text{cm}$. The parameters are summarized in Tab. 2.2. It can be seen that the optimized resonator provides ca. 6× higher pressure then the cylindrical resonator, and ca. 2.4× higher pressure

Resonator	k_{pu} [Pa/V]	$\Omega_{\text{resonance}}$
Cylindrical	451	$0.828, 1.783, 2.869, 3.883, 4.909, \ldots$
Conical	1133	$1.089, 2.012, 3.012, 3.983, 4.982, \ldots$
Optimized	2693	$1.188, 1.789, 2.916, 4.064, 4.921, \ldots$

Table 2.2: Parameters of simple-shaped resonators and the optimized one; driving by the loudspeaker driver.

than the conical one. All the resonators are dissonant, which is, besides the variability of the cross-section, caused by the properties of the loudspeaker's electromechanical system, and by the thermoviscous boundary layer accounted for in the model.

2.3.4 Experimental validation

The numerical results have also been validated experimentally. The above-mentioned resonant cavities were milled in two pieces of a duralumin block and attached to the pressure driver Selenium D405Ti. The experimental results were compared with the numerical ones obtained using Eq. (2.5) which was solved numerically in the frequency domain. The model of additional losses due to acoustically generated turbulence in boundary layer [9] provided good agreement of theoretical and experimental data in the case of the strongest driving of the optimized resonator.

Figure 2.7 shows frequency characteristics of amplitude of the first harmonics of acoustic pressure measured and calculated in the case of individual resonators for different driving voltage amplitudes. The agreement of the experimental and numerical data is quite good in the case of the cylindrical (top-left) and conical resonator (top-right) even for higher driving voltages. In the case of the optimized resonator, the agreement is a little worse. For driving voltage amplitude of 1 V, the resonance frequency calculated $f_{\text{r calc}} = 571$ Hz differs from the resonance frequency measured $f_{\text{r meas}} = 551$ Hz by 3.6%. This discrepancy can possibly be attributed to the differences between the mathematical description of the resonator shape and the actual shape of the manufactured resonator. Considering this fact, the frequencies in the bottom panel of Fig. 2.7 were normalized to individual resonance frequencies $\Omega' = f/f_{\text{r},i}$.

For driving voltage amplitude of 15 V the first harmonics in the optimized resonator attains an amplitude of $|\hat{p}'_1| = 36\,000\,\text{Pa}$ at resonance, which is 2× more than in case of the conical resonator and 5.4× more than in case of the cylindrical resonator. It can be seen in Fig. 2.8 that the time-course of the acoustic pressure is distorted, but a shock-wave is not present due to the resonator dissonance.

The presented results show that even if the optimization procedure is based on a linear theory (and thus it cannot predict behavior of strongly nonlinear acoustic fields), it provides a systematic means of design of resonant cavities for high-amplitude acoustic applications such as, e.g., thermoacoustic devices. Utilizing the appropriately optimized resonant cavities together with commercially available loudspeakers could increase economic attractiveness of potential applications.

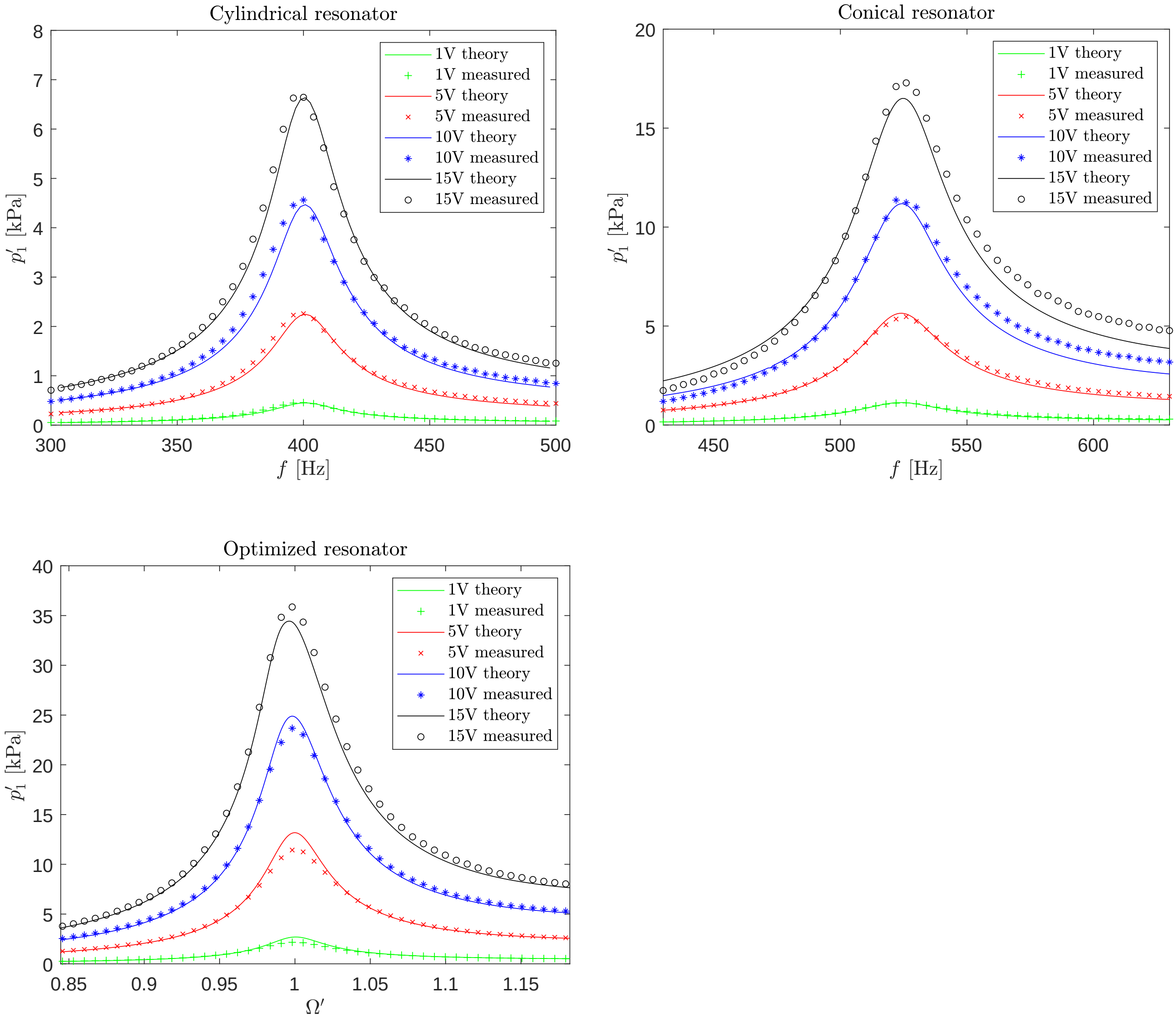

Figure 2.7: Frequency characteristics of amplitude of the first harmonics of acoustic pressure in loudspeaker-driven cylindrical, conical, and optimized resonator–comparison of theoretical and experimental data.

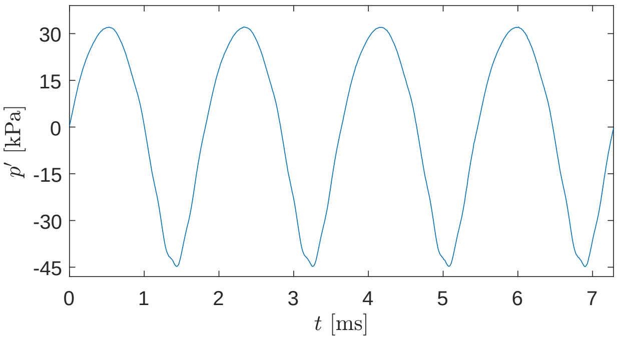

Figure 2.8: Time course of acoustic pressure measured in the optimized resonator at $f = 549\,\mathrm{Hz}$ (resonance), driving voltage amplitude $u_0 = 15\,\mathrm{V}$.

2.4 Acoustic particle displacement resonator

One way to enhance destruction of toxic pollutants, decomposition of volatile organic compounds or combustion, is using a non-thermal plasma. Therefore, the creation of a space- and time-homogeneous non-equilibrium low-temperature plasma in the entire discharge reactor volume is an important pre-requisite for triggering these processes and for increasing their efficiency. We have demonstrated, see [4] (Appendix A.5), that the application of an acoustic field on the discharge in the filamentary streamer regime substantially extends the range of currents for which the discharge voltage remains more or less constant, i.e., it allows a substantial increase in the power delivered to the discharge. The application of an acoustic field on the discharge causes the discharge to spread within the discharge chamber, see Fig. 2.9, and consequently, a highly reactive non-equilibrium plasma is created throughout the inter-electrode space.

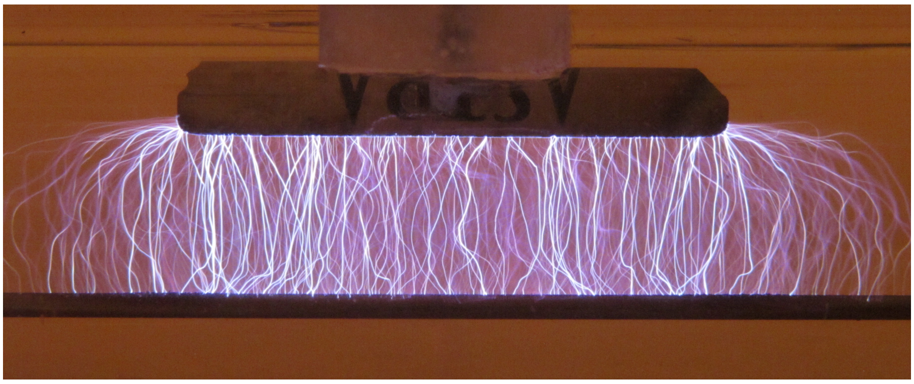

Figure 2.9: Negative corona discharge in air at atmospheric conditions in acoustic field. RMS value of the discharge voltage: 8.4 kV, RMS value of the discharge current: 33.5 mA, frequency of the acoustic wave: 50 Hz, amplitude of acoustic velocity: 25 $\mathrm{ms^{-1}}$, amplitude of acoustic particle displacement: 8 cm.

For these applications, a compact resonator driven with two loudspeakers, allowing for the generation of low-frequency (tens of hertz) acoustic field with high amplitude of acoustic velocity and particle displacement, has been developed. In order to be able to predict its performance and optimize its parameters, corresponding mathematical model has been proposed, see [21] (Appendix A.4).

2.4.1 Arrangement

The proposed device, see [21] (Appendix A.4) for the details, is schematically depicted in Fig. 2.10. It consists of two electrodynamic transducers (loudspeakers) B&C 6MD38-8, enclosed in small loudspeaker-boxes, connected in antiphase in series, which drive acoustic field in a waveguide (plexiglass tube with inner radius $r_1 = 12$ mm, length $2 \times l_1 = 300$ mm and thickness 2 mm) through conical segments (made from plastic funnels, small inner radius $r_1 = 12$ mm, large inner radius $r_2 = 75$ mm, length $l_2 = 60$ mm) and short segments with inner radius r_2 and length $l_3 = 40$ mm. Due to the antiphase driving of the loudspeakers, the primary acoustic field (the first harmonics) has node of the acoustic pressure and anti-node of the acoustic velocity and the particle displacement at the centre of the waveguide.

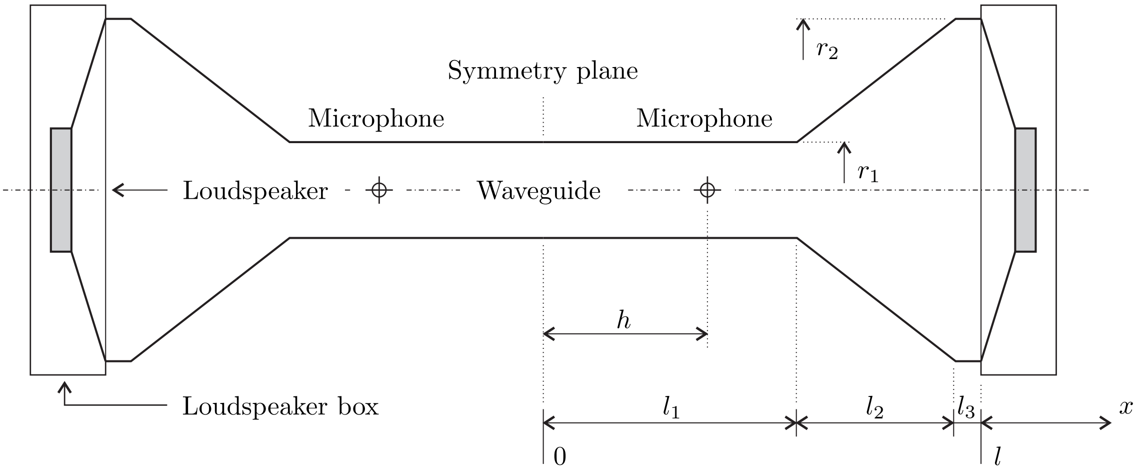

Figure 2.10: Arrangement of the device.

2.4.2 Mathematical model

High-amplitude acoustic field inside a variable-cross-section waveguide can be described using a set of two quasi-one-dimensional equations, see [21] (Appendix A.4) for the derivation:

$$\frac{\partial p'}{\partial x} = -\rho_0 \frac{\partial v}{\partial t} - \frac{p'}{c_0^2}\frac{\partial v}{\partial t} + \frac{v}{c_0^2}\frac{\partial p'}{\partial t} + \frac{2}{r}\frac{\mathrm{d}r}{\mathrm{d}x}\rho_0 v^2 + \frac{\rho_0 \delta_\mathrm{v}}{c_0^2}\frac{\partial^2 v}{\partial t^2}, \tag{2.8a}$$

$$\frac{\partial v}{\partial x} = -\frac{1}{\rho_0 c_0^2}\frac{\partial p'}{\partial t} - \frac{2}{r}\frac{\mathrm{d}r}{\mathrm{d}x}v + \frac{\gamma}{2\rho_0^2 c_0^4}\frac{\partial p'^2}{\partial t} + \frac{1}{2c_0^2}\frac{\partial v^2}{\partial t} + \frac{\delta_\mathrm{t}}{\rho_0 c_0^4}\frac{\partial^2 p'}{\partial t^2} + \frac{2\varepsilon}{r^2}\frac{\partial^{1/2}(rv)}{\partial t^{-1/2}\partial x}. \tag{2.8b}$$

Meaning of the individual symbols is the same as used in Secs. 2.2.1, 2.3.1, moreover, $\delta_\mathrm{t} = \kappa(1/c_V - 1/c_p)/\rho_0$ is the diffusivity of sound due to the thermal conduction.

Set of equations (2.8) is equivalent to Eq. (2.5), however, instead of velocity potential being used as the variable, acoustic pressure and velocity are used instead, which is more suitable in this case. Similarly as in Eq. (2.5), additional losses due to the acoustically generated turbulence, which appear to play an important role in this case, are incorporated into the coefficient ε in a straightforward way, see [9].

Similarly as in Sec. 2.3.1, the loudspeakers are modelled employing a linear lumped-element model, which represents the boundary conditions for Eq. (2.8); the corresponding model parameters are determined by measurement, see [21] (Appendix A.4) for the details.

It is well-known from hydraulics that pressure drops appear in high-Reynolds-number flows through channels with cross-section changes (junctions). These effects are called the minor losses, they result from flow separation, vorticity generation, turbulence and other effects. For a steady flow, the pressure drop resulting from the minor losses is characterized by the dimensionless parameter K as

$$\Delta p = \frac{1}{2}K\rho v^2, \tag{2.9}$$

where ρ is the fluid density and v is the flow velocity. The values of K for variety of geometries are tabulated, see, e.g., [28].

Relation (2.9) can according to Iguchi's hypothesis, see, e.g., [29], be used even in case of unsteady flows represented by acoustic waves, if the acoustic particle displacement amplitude is larger than all other dimensions in the vicinity. According to [29, 30], Eq. (2.9) can be in

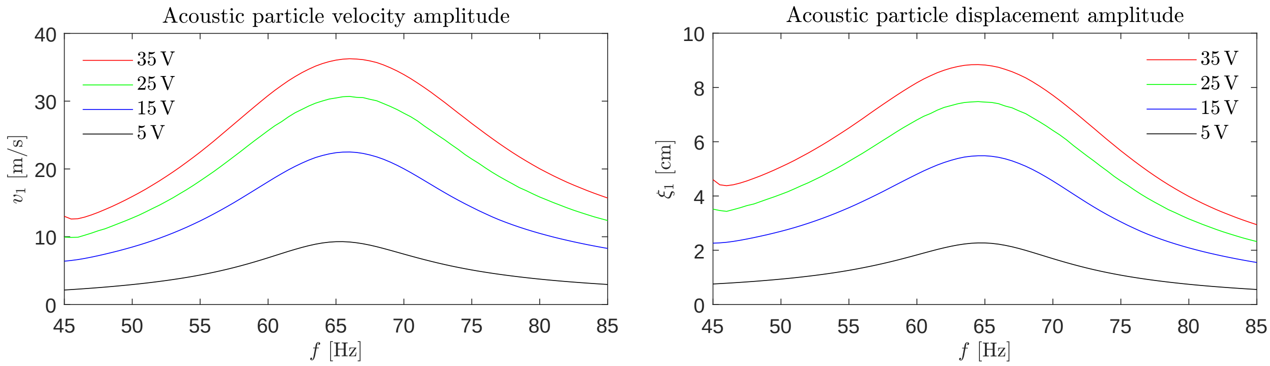

Figure 2.11: Frequency characteristics of amplitude of the first harmonics of acoustic velocity (left) and particle displacement (right) measured at the centre of the waveguide for various driving voltage amplitudes u_0.

case of oscillatory flows rewritten as

$$\Delta p'(t) = -\frac{1}{2}K\rho_0|v(t)|v(t), \tag{2.10}$$

where $v(t)$ now stands for the acoustic velocity. The minus sign in Eq. (2.10) provides the correct sign of the pressure drop with respect to the flow orientation. In this case, minor losses are modelled at the junctions of the constant-cross-section part of the waveguide (with radius r_1) and the conical segments, see Fig. 2.10.

Equation (2.8), together with the relationship modelling the minor losses was solved numerically in the frequency domain, see [21] (Appendix A.4) for the details.

2.4.3 Results

All experiments were conducted in air at room conditions. Corresponding parameters were used in the numerical model.

Two 1/8" microphones were placed symmetrically along the centre in the waveguide wall, see Fig. 2.10, separated by the distance of $2 \times h = 160\,\mathrm{mm}$, measuring acoustic pressures ${p'}_{\mathrm{A}}(t)$ and ${p'}_{\mathrm{B}}(t)$. Acoustic velocity and particle displacement at the centre of the resonator were determined by two-microphone method, see, e.g., [31].

Left panel of Fig. 2.11 shows frequency characteristics of amplitude of the first harmonics of acoustic velocity measured using the two-microphone technique at the centre of the waveguide for several driving voltages u_0. It can be observed that for $u_0 = 35\,\mathrm{V}$, the velocity amplitude reaches the value of 36.3 m/s at resonance frequency of 66 Hz. In this case, the power input of the device is 29 W. It is apparent that due to nonlinear losses, the maximum velocity amplitude is not proportional to the driving amplitude and that there is small resonance-frequency shift–the resonance frequency increases with the driving voltage amplitude.

Right panel of Fig. 2.11 shows frequency characteristics of amplitude of the first harmonics of acoustic particle displacement at the centre of the waveguide for several driving voltages. The maximum displacement amplitude reaches value of 8.8 cm for $u_0 = 35\,\mathrm{V}$ and $f = 64.5\,\mathrm{Hz}$.

Acoustic velocity in the waveguide is almost distortion-free even if the acoustic pressure in the narrow tube is distorted by the second harmonics, see Fig. 2.12. The reason is that the second harmonics distribution is symmetric, i.e. $\hat{p}'_2(x) \approx \hat{p}'_2(-x)$, and almost constant along

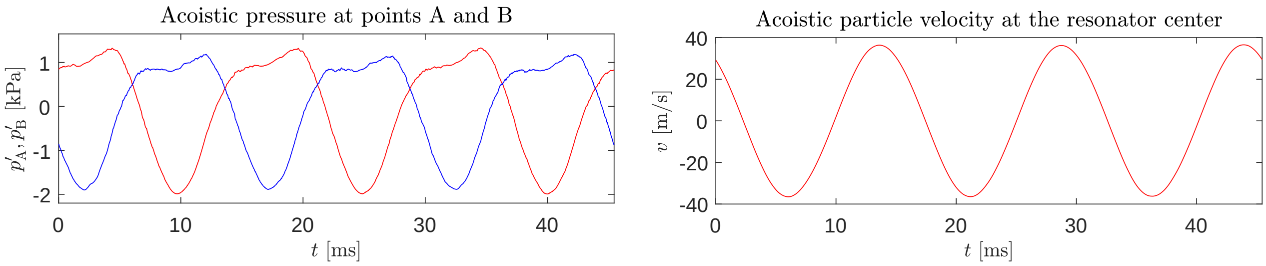

Figure 2.12: Left: acoustic pressures p'_A, p'_B measured for $u_0 = 35\,\mathrm{V}$ and $f = 66\,\mathrm{Hz}$, right: corresponding acoustic velocity.

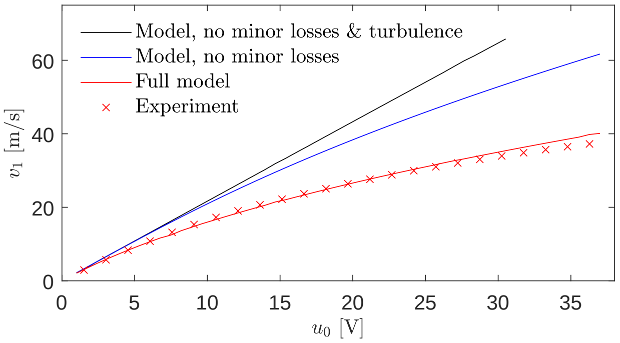

Figure 2.13: Comparison of experimental and theoretical results.

the narrow tube which results in a negligible acoustic pressure gradient and acoustic velocity (see below).

Figure 2.13 shows dependence of the acoustic velocity amplitude at the centre of the waveguide on driving voltage amplitude for $f = 65\,\mathrm{Hz}$; measured and calculated using the proposed model with individual loss mechanisms taken into account.

It can be seen that if the minor losses and the losses due to the turbulence in the boundary layer [9] are not taken into account (black line), the model predicts almost linear dependence of the acoustic velocity amplitude on the driving amplitude as the energy dissipation in higher harmonics is negligible. This is because of the fact that the higher harmonics are not resonantly amplified (the resonator is strongly dissonant) and thus the acoustic energy transfer into them is ineffective. The blue line corresponds to the situation when turbulent losses are taken into account and minor losses are not. Again, the model overestimates the velocity amplitude. When all the nonlinear loss mechanisms are taken into account, the model (red line) fits the experimental data well.

Figure 2.14 shows distribution of amplitudes of the first three harmonics of acoustic pressure and velocity calculated for $u_0 = 35\,\mathrm{V}$ and $f = 65\,\mathrm{Hz}$. The vertical lines delimit the central narrow part of the waveguide. It can be observed that in correspondence with the adopted assumptions, the pressure gradient of the first harmonics is almost constant along the narrow part of the waveguide, whereas the second harmonics amplitude is almost constant (its gradient has almost zero value). In the central part, the amplitude of the second harmonics exceeds the first one. The jumps at the junctions of the central waveguide with the conical segments follow from the adopted "local" model of the minor losses.

The proposed arrangement allows for an efficient generation and resonant amplification of low-frequency sound fields, where its physical dimensions are much smaller than the wave-

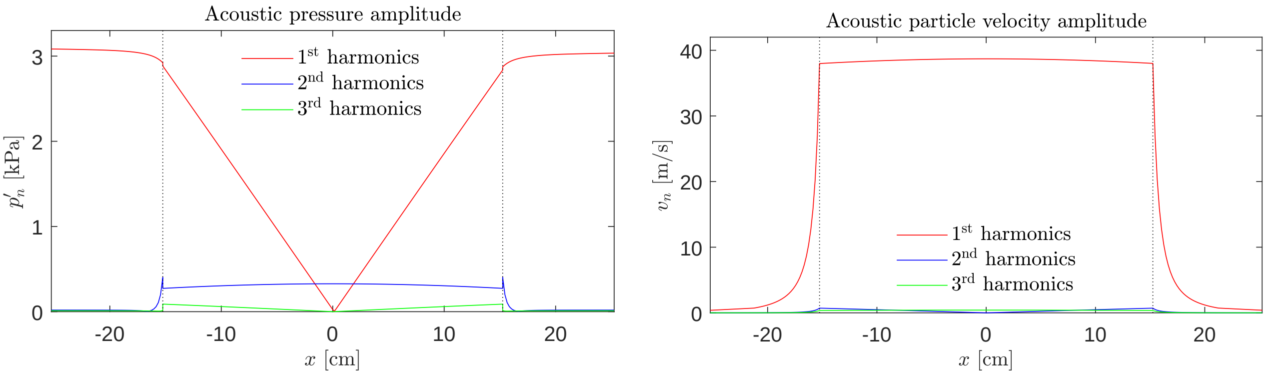

Figure 2.14: Distribution of the acoustic pressure (left) and the particle velocity (right) harmonics amplitudes along the waveguide, $u_0 = 35\,\mathrm{V}$, $f = 65\,\mathrm{Hz}$.

length, in the current case $\lambda/l_{\mathrm{tot}} \approx 7.5$. The primary motivation for its design was the stabilization of electric discharges in plasma-chemical reactors, but, there are many other potential applications. We have demonstrated that in order to predict its performance accurately, non-classical means of the acoustic energy dissipation, such as the turbulence in the viscous boundary layer and minor losses, must be taken into account.

Chapter 3

Thermal effects on Rayleigh acoustic streaming

3.1 Introduction

Acoustic streaming [32, 33, 34, 35] is another physical phenomenon which can be encountered in acoustic resonators. It refers to a second-order net mean fluid flow generated by and superimposed on the first-order acoustic field. Apart from the fact that the acoustic streaming is an interesting physical phenomenon, it plays an important role in many applications where it can be both useful or undesirable. For example, in thermoacoustics [29], the streaming is usually an unwanted mechanism of convective heat transport which reduces the efficiency of high-amplitude thermoacoustic devices; on the other hand, the heat transport supported by acoustic streaming [36] could find its application in cooling hot objects like electronic components. In acoustofluidics [37], the acoustic streaming prevents manipulation of small particles by acoustic radiation force in microfluidic devices; on the other hand, it can be actively utilized in these devices for mixing and pumping fluids.

Based on different mechanisms by which acoustic streaming is generated, it can be sorted [35] into several categories. Boundary-layer-driven streaming, or Rayleigh streaming, appears in a standing wave resonator because of shear viscous forces near the fluid-solid boundary. Eckart streaming (or "quartz wind") is generated as a result of attenuation of high-intensity travelling acoustic waves within the fluid volume. Jet-driven streaming is associated with the periodic suction and ejection of a viscous fluid through a change of cross-section area in a resonator. Finally, there is a travelling-wave (Gedeon) streaming associated with acoustic wave propagating in a waveguide with a looped topology. This text is further focussed on the boundary-layer-driven (Rayleigh) streaming.

The first observational evidences of the acoustic streaming date back to the mid-nineteenth century, when M. Faraday observed steady air currents established adjacent to vibrating elastic surfaces [38]. A similar phenomenon had been noticed by Savart a few years earlier. In another experiment, V. Dvořák observed mean air flows in high-amplitude standing wave in a Kundt's tube [39]. The flow was from the acoustic velocity anti-node towards the acoustic velocity node close to the tube wall. In the tube interior, there was a return flow in the opposite direction–from the acoustic velocity node to the acoustic velocity anti-node.

Acoustic streaming is a nonlinear effect, so that it cannot be analysed employing the methods of linear acoustics. Lord Rayleigh [40] was the first one who provided the theoretical

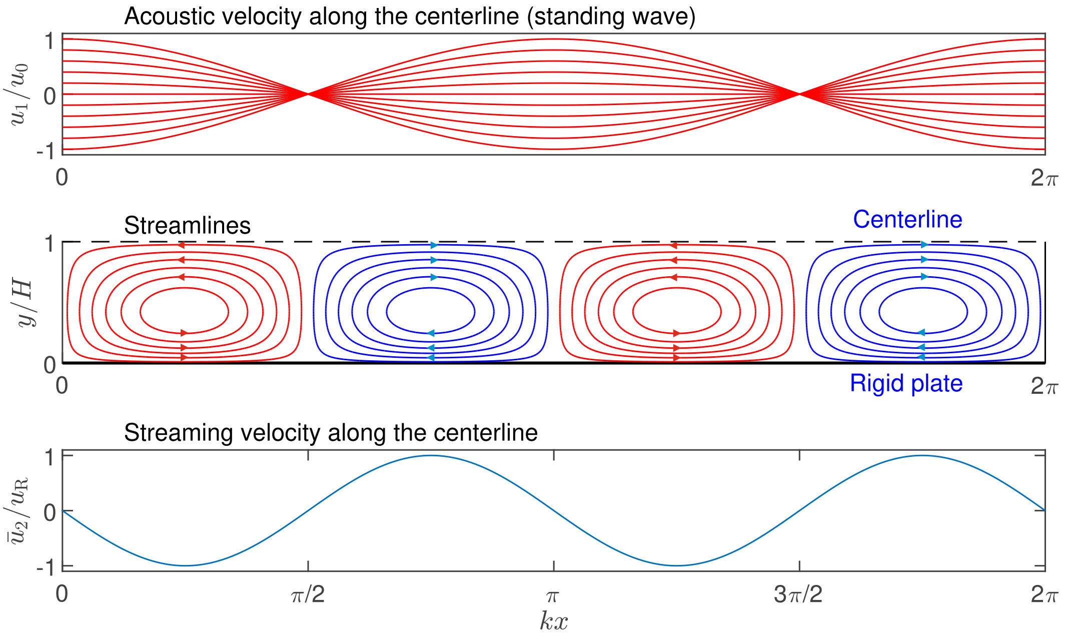

Figure 3.1: Rayleigh streaming calculated employing Eqs. (3.1): top–acoustic velocity along the centerline, middle–streamlines, bottom–streaming velocity profile along the centerline. Here, $u_\mathrm{R} = 3u_0^2/16c_0$ is so-called Rayleigh velocity.

explanation for both the above-mentioned phenomena. To solve the nonlinear fluid-dynamics equations, he used the method of successive approximations, in which the first-order solution (acoustic field) is used to calculate the driving functions for the second-order solution (streaming field), where both the solutions are calculated by linearised equations. This approach has become a predominate analytical tool since then for the study of the acoustic streaming.

Regarding the Dvořák's observation, Rayleigh considered a standing acoustic wave between two parallel plates separated by the distance $2H$. He assumed that the plates' separation distance was much larger than the viscous boundary layer thickness, and much smaller than the wavelength.

If the acoustic particle velocity along the centerline is

$$u_1 = u_0 \cos(kx)\cos(\omega t),$$

where u_0 is the acoustic velocity amplitude at the antinodes, k is the wavenumber, x is the spatial coordinate along the centerline, ω is the angular frequency, and t is the time, the Rayleigh solution far from the boundary layer can be approximated, see, e.g., [35, 40], as

$$\overline{u}_2 = -\frac{3u_0^2}{16c_0}\sin(2kx)\left[1 - 3\left(1 - \frac{y}{H}\right)^2\right], \tag{3.1a}$$

$$\overline{v}_2 = -\frac{3u_0^2}{16c_0}2kH\cos(2kx)\left[1 - \frac{y}{H} - \left(1 - \frac{y}{H}\right)^3\right] \tag{3.1b}$$

where $\overline{u}_2, \overline{v}_2$ are the streaming velocities along and perpendicular to the plates, respectively, c_0 is the small-signal sound speed, and y is the spatial coordinate parallel to the plates.

Equations (3.1) describe the outer (= outside the boundary-layer) streaming cells associated with the Rayleigh streaming. Each of the streaming cells, see Fig. 3.1, spans quarter a wavelength in the axial direction and half the channel width in the transverse direction. Along the centerline, the axial streaming velocity profile $\overline{u}_2$ is sinusoidal with the period of half the wavelength.

H. Schlichting theoretically studied the acoustic streaming inside the boundary layer in a standing wave along a flat plate [41]. He predicted the existence of “inner” streaming vortices with quarter a wavelength size in the axial direction, and the width comparable to the boundary layer thickness. V. K. Schuster and W. Matz, see [42], reproduced the Rayleigh’s calculation for the problem of a standing acoustic wave in a cylindrical tube with radius R.

More recently, acoustic streaming in a thermoviscous fluid confined between two arbitrarily separated plates having non-zero mean axial temperature gradient was studied by R. Waxler [43]. When the analysis was applied for the case of plates spacing large compared to the visco-thermal boundary layer thickness, outer as well as inner streaming profiles were obtained. H. Bailliet *et al.* [44] incorporated temperature dependence of viscosity and heat conduction and extended the analysis also for cylindrical geometry.

M. F. Hamilton *et al.* [45] presented a fully analytical solution for acoustic streaming generated by a standing wave in a rectangular channel (resonator) of arbitrary width, driven with an inertial force and filled with a viscous fluid. They have shown that apart from the driving frequency, the acoustic streaming structure, see Fig. 3.2, depends only on the ratio of the channel half-width H, and the viscous boundary layer thickness. They have determined the critical value of this ratio necessary for the development of the outer streaming cells. In related work [46], the authors further generalized the solution to take into account thermal conductivity and temperature-dependence of viscosity of the fluid and extended the analysis for the case of cylindrical tubes.

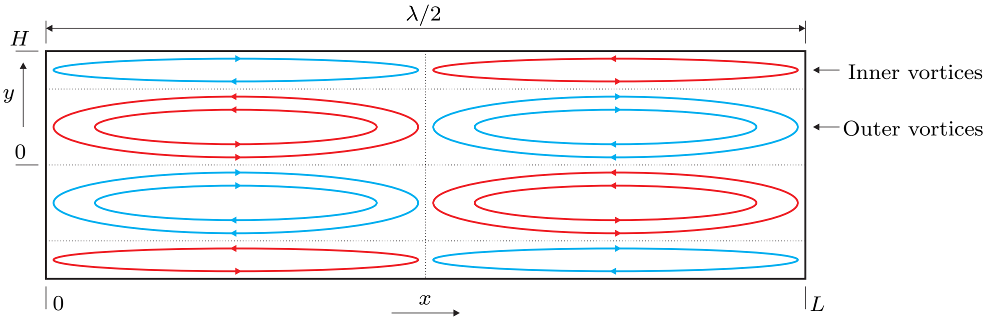

Figure 3.2: Structure of the inner and outer streaming cells in a resonant channel.

The above-mentioned theoretical works [41, 42, 43, 44, 45, 46] employ the original Rayleigh’s approach [40] in treating the second-order momentum equation for the averaged streaming velocity. Namely, the equation is linearised, which substantially simplifies the analysis, however, this way, the inertial effects on the streaming flow are not captured. In the case of “slow” streaming these effects are negligible compared to the viscous effect on the streaming flow and the employed approach provides correct results.

Employing a perturbation analysis with asymptotic expansions, L. Menguy and J. Gilbert [47] calculated “nonlinear,” or “fast” acoustic streaming generated by a standing wave in a cylindrical waveguide, demonstrating the distortion of the streamlines as a consequence of inertial effects on the streaming fluid motion.

They have identified a parameter–the nonlinear Reynolds number

$$\mathrm{Re}_{\mathrm{nl}} = \left(\frac{u_0}{c_0} \times \frac{R}{\delta_{\mathrm{v}}} \right)^2 , \tag{3.2}$$

where u_0 is the standing wave amplitude, R is the waveguide radius, and δ_{v} is the viscous boundary layer thickness. This parameter determines whether the fluid inertia effects on the streaming motion can be neglected ($\mathrm{Re}_{\mathrm{nl}} \ll 1$ – streaming can be considered as "slow") or not. Their analysis, due to the convergence issues, covers the region $\mathrm{Re}_{\mathrm{nl}} \lessapprox 6$.

Acoustic streaming in high-amplitude acoustic fields–fast streaming–is today most often theoretically studied by methods of computational fluid dynamics (CFD), i.e., by the direct numerical solution (DNS) of the compressible Navier-Stokes equations in the time domain.

M. K. Aktas and B. Farouk [48], and V. Daru *et al.* [49] studied acoustic streaming generated by strongly nonlinear acoustic fields in two-dimensional rectangular channels employing this approach. They observed complex streaming patterns strongly deviating from the slow streaming ones, [45, 46], including the development of additional outer vortices. I. Reyt *et al.* [50] conducted the numerical simulations as well as measurements for the case of a cylindrical tube. Even if the methods of CFD are rather straightforward, allowing for the study of acoustic streaming in complex geometries, they are computationally very costly, because the need to capture the structure of boundary layers requires a very fine time-step of integration and the transients can be even hundreds or thousands of cycles long. For this reason, see, e.g., the argumentation in [49], the numerical simulations are conducted for very small resonators operating at the ultrasonic frequencies, which complicates the comparison of the numerical results with experimental data, as for these small geometries, the experimental measurements would be hardly possible.

Experimental methods for the study of the fast Rayleigh streaming (conducted at the audio frequencies) utilize Laser Doppler Velocimetry (LDV), see, e.g., [50, 51, 52, 53, 54] or Particle Image Velocimetry, see, e.g., [53, 55, 56, 57].

Of these works, M. W. Thompson *et al.* [51] used LDV for the measurement of the acoustic streaming in a cylindrical tube at high values of $\mathrm{Re}_{\mathrm{nl}}$. They found out that for higher values of $\mathrm{Re}_{\mathrm{nl}}$, the streaming profile deviates considerably from the prediction by N. Rott [58] or L. Menguy and J. Gilbert [47]. They have shown in an experimental way that this streaming profile distortion is connected with temperature gradient developed along the resonator walls due to thermoacoustically driven heat flux. At the time, there has not been any theory at hand explaining this behaviour, nevertheless, the authors have speculated that this effect may be connected with the heat carried by the streaming flow.

I. Reyt *et al.* [50] compared their measurements of acoustic streaming in a cylindrical resonator using LDV with the numerical data obtained by a DNS. They obtained similar experimental results (distorted streaming profiles) as M. W. Tnompson *et al.* [51] with a small temperature gradient along the resonator. The numerical calculations were performed at the condition of isothermal resonator walls; qualitative and overall quantitative agreement between the experimental and numerical results has been achieved so that the authors identified the inertial effects as the primary reason for the distortion of the streaming profile for high values of $\mathrm{Re}_{\mathrm{nl}}$.

In their recent work, V. Daru *et al.* [59] argue, based on the results of numerical experiments, that the inertial effects cannot be the leading mechanism of the streaming structure distortion observed in experiments and DNS; they consider the role of the nonlinear interactions between the streaming flow and the acoustic field.

We show in the following sections, by means of numerical simulations, that the acoustic streaming structure is extremely sensitive to the fluid temperature distribution transverse to the resonator axis, and that even for moderate values of $\mathrm{Re}_{\mathrm{nl}}$, the streaming profile can be considerably distorted from the sinusoidal one, predicted by the Rayleigh's theory, if there is even weak temperature gradient along the resonator walls. This acoustic-field-amplitude-dependent distortion is not caused by the effect of the fluid inertia, but, it is connected with the streaming-driven convective heat transport in a fluid with a mean temperature gradient. The streaming profile distortion described within this work is of the same type as it has been found in experiments [50, 51, 53, 54].

The results described within this work cannot be obtained using the previous theoretical models dealing with acoustic streaming in temperature-inhomogeneous fluids [58, 43, 44], as these models do not take into account the transverse temperature distribution and they do not capture the effect of the acoustic-streaming-driven convective heat transport.

The rest of this chapter is based on the author's works [60, 61, 62], see also the Appendices A.6, A.7, and A.8.

3.2 Mathematical model

Being an inherently nonlinear effect, acoustic streaming must be studied employing nonlinear equations. Namely, the Navier-Stokes equations of the fluid dynamics, see, e.g., [63], are most often used as the starting point in the context of acoustic streaming. In order to avoid computationally very demanding direct numerical integration of the Navier-Stokes equations, which has been employed previously [48, 49, 50], especially on large geometries (compared to viscous boundary layer thickness), the variant of the method of successive approximations, used in a similar context by A. Boufermel *et al.* [64], was adopted. Within this approach, the fluid-dynamics variables are decomposed as

$$\varphi = \varphi_0 + \varphi_{\mathrm{a}} + \varphi_{\mathrm{n}}, \qquad \varphi_{\mathrm{n}} \ll \varphi_{\mathrm{a}},$$

where φ_0 represents the steady state mean value of a quantity φ without acoustic perturbation, φ_{a} represents the first-order acoustic perturbation (primary field), harmonic in time with an angular frequency ω, and φ_{n} represents the products of nonlinear interactions including higher harmonics as well as time-independent (or slowly varying) components (secondary field). Next, a time-average of this relation is calculated over one period of the acoustic component, resulting in $\langle \varphi \rangle = \varphi_{\mathrm{m}}(\boldsymbol{r}, t_{\mathrm{s}}) = \varphi_0 + \langle \varphi_{\mathrm{n}} \rangle$, where φ_{m} represents an averaged quantity, variable in space ($\boldsymbol{r}$ is the position vector), and slowly varying in the time (t_{s} is the "slow" time related to the large-time-scale phenomena).

Applying this scheme, see [62] (Appendix A.8) for the details, we get the equations for the first-order acoustic quantities (denoted with the index "a")

$$\frac{\partial \rho_\mathrm{a}}{\partial t} + \boldsymbol{\nabla}\cdot(\rho_\mathrm{m}\boldsymbol{u}_\mathrm{a}) = 0, \tag{3.3a}$$

$$\rho_\mathrm{m}\frac{\partial \boldsymbol{u}_\mathrm{a}}{\partial t} + \boldsymbol{\nabla}\cdot\left\{p_\mathrm{a}\boldsymbol{I} - \mu_\mathrm{m}\left[\boldsymbol{\nabla}\boldsymbol{u}_\mathrm{a} + (\boldsymbol{\nabla}\boldsymbol{u}_\mathrm{a})^\mathrm{T}\right] + \frac{2}{3}\mu_\mathrm{m}(\boldsymbol{\nabla}\cdot\boldsymbol{u}_\mathrm{a})\boldsymbol{I}\right\} = -\rho_\mathrm{m}\boldsymbol{a}, \tag{3.3b}$$

$$\rho_\mathrm{m}c_\mathrm{pm}\left(\frac{\partial T_\mathrm{a}}{\partial t} + \boldsymbol{u}_\mathrm{a}\cdot\boldsymbol{\nabla}T_\mathrm{m}\right) - \frac{\partial p_\mathrm{a}}{\partial t} - \boldsymbol{\nabla}\cdot(\kappa_\mathrm{m}\boldsymbol{\nabla}T_\mathrm{a}) = 0, \tag{3.3c}$$

$$\frac{p_\mathrm{a}}{p_\mathrm{m}} = \frac{T_\mathrm{a}}{T_\mathrm{m}} + \frac{\rho_\mathrm{a}}{\rho_\mathrm{m}}, \tag{3.3d}$$

where ρ is the fluid density, p is the pressure, $\boldsymbol{u}$ is the fluid particle velocity, T is the temperature, $\boldsymbol{a}$ is the inertial acceleration (driving the acoustic field), $c_\mathrm{pm} = c_\mathrm{p}(T_\mathrm{m})$, $\mu_\mathrm{m} = \mu(T_\mathrm{m})$, and $\kappa_\mathrm{m} = \kappa(T_\mathrm{m})$, where c_p is the specific heat capacity at constant pressure, μ is the shear viscosity, and κ is the coefficient of thermal conduction. Further, $\boldsymbol{I}$ is the identity matrix, and the upper index T stands for the matrix transpose.

Similarly, the equations for the time-averaged quantities can be obtained in the form

$$\frac{\partial \rho_\mathrm{m}}{\partial t_\mathrm{s}} + \boldsymbol{\nabla}\cdot(\rho_\mathrm{m}\boldsymbol{u}_\mathrm{m}) = M, \tag{3.4a}$$

$$\rho_\mathrm{m}\frac{\mathrm{d}\boldsymbol{u}_\mathrm{m}}{\mathrm{d}t_\mathrm{s}} + \boldsymbol{\nabla}\cdot\left\{p_\mathrm{m}\boldsymbol{I} - \mu_\mathrm{m}\left[\boldsymbol{\nabla}\boldsymbol{u}_\mathrm{m} + (\boldsymbol{\nabla}\boldsymbol{u}_\mathrm{m})^\mathrm{T}\right] + \frac{2}{3}\mu_\mathrm{m}(\boldsymbol{\nabla}\cdot\boldsymbol{u}_\mathrm{m})\boldsymbol{I}\right\} = \boldsymbol{F}, \tag{3.4b}$$

$$\rho_\mathrm{m}c_\mathrm{pm}\frac{\mathrm{d}T_\mathrm{m}}{\mathrm{d}t_\mathrm{s}} - \frac{\mathrm{d}p_\mathrm{m}}{\mathrm{d}t_\mathrm{s}} - \boldsymbol{\nabla}\cdot(\kappa_\mathrm{m}\boldsymbol{\nabla}T_\mathrm{m}) = Q, \tag{3.4c}$$

$$p_\mathrm{m} = \rho_\mathrm{m}R_\mathrm{s}T_\mathrm{m}, \tag{3.4d}$$

where R_s is the specific gas constant, and the operator $\mathrm{d}()/\mathrm{d}t$ stands for the material derivative. The source terms $M, \boldsymbol{F}$, and Q emerge in Eqs. (3.4) as a consequence of employing the method of successive approximations; they comprise nonlinear combinations of the first-order acoustic field quantities, calculated from Eqs. (3.3), see [62] (Appendix A.8) for the details. Namely, M is the mass source, $\boldsymbol{F}$ represents the excitation force (Reynolds stress, the force caused by the dependence of viscosity on acoustic temperature), and Q represents the heat source.

In context of the acoustic streaming, averaged mass transport velocity (the ratio of the total mass flux to the average density–further referred to as the streaming velocity) is of interest, see, e.g., [45, 64], which is introduced as

$$\boldsymbol{U}_\mathrm{m} = \boldsymbol{u}_\mathrm{m} + \langle\rho_\mathrm{a}\boldsymbol{u}_\mathrm{a}\rangle/\rho_\mathrm{m}.$$

The sets of equations (3.3) and (3.4) are mutually coupled. The mean temperature distribution calculated from Eqs. (3.4) needs to be known for the calculation of the acoustic-field quantities from Eqs. (3.3), and the acoustic-field quantities need to be known for the calculation of the source terms $M, \boldsymbol{F}$, and Q for Eqs. (3.4)–not shown here, see [62] (Appendix A.8).

However, in the case of "weak acoustic field" (and very slow streaming), the situation gets simplified substantially. In these conditions, if the acoustic streaming-driven heat convection can be neglected compared to the heat conduction, the energy equation (3.4c) decouples from the set of equations (3.4) and (3.3), and in the steady-state, it gets the form

$$\boldsymbol{\nabla}\cdot(\kappa_\mathrm{m}\boldsymbol{\nabla}T_\mathrm{m}) = 0. \tag{3.5}$$

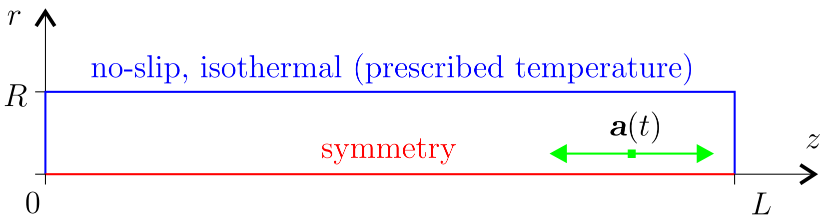

Figure 3.3: Geometry of the problem.

This means that the equations can be solved step by step, see [61] (Appendix A.7):

1. The fluid mean temperature is calculated using Eq. (3.5) supplemented with appropriate boundary conditions.
2. The first-order acoustic field in the fluid with the mean temperature distribution $T_\mathrm{m}(\boldsymbol{r})$ is calculated using Eqs. (3.3).
3. The second-order time-averaged field is calculated using the set of Eqs. (3.4a), (3.4b), and (3.4d).

All the equations, for both the decoupled as well as the coupled problem, were solved numerically employing the finite-element software COMSOL Multiphysics [65], see also [61, 62] (Appendices A.7, A.8) for the details of the implementation.

3.3 Numerical results

3.3.1 Configuration and parameters of the simulations

The numerical simulations were conducted for the case of a rigid-walled cylindrical tube (resonator) with the length L and the inner radius R. The tube was assumed to be closed with rigid caps at the ends, and filled with air (considered as an ideal gas) at normal pressure. Acoustic field was assumed to be driven by a time-harmonic inertial acceleration at the frequency of $\lambda/2-$resonance, oriented along the tube symmetry axis, see Fig. 3.3. Due to the symmetry, the problem was solved in 2D axi-symmetric r, z-cylindrical coordinate system.

The boundary conditions (BCs) on the resonator walls for the acoustic-field equations (3.3) were set as follows. The acoustic temperature $T_\mathrm{a} = 0$ (isothermal BCs), the acoustic velocity vector $\boldsymbol{u}_\mathrm{a} = \boldsymbol{0}$ (no-slip BCs). The BCs for the second-order averaged field were set as $T_\mathrm{m} = T_\mathrm{w}$, where T_w is a prescribed wall temperature, and $\boldsymbol{u}_\mathrm{m} = \boldsymbol{0}$ (no-slip BCs).

3.3.2 Slow streaming with the convective heat transport neglected

First, the simpler problem of the slow streaming, in which the acoustic-streaming-driven convective heat transport can be neglected, was studied. As it has been mentioned in Sec. 3.2, in this case, the model equations decouple and the steady-state mean fluid temperature can be calculated using Eq. (3.5).

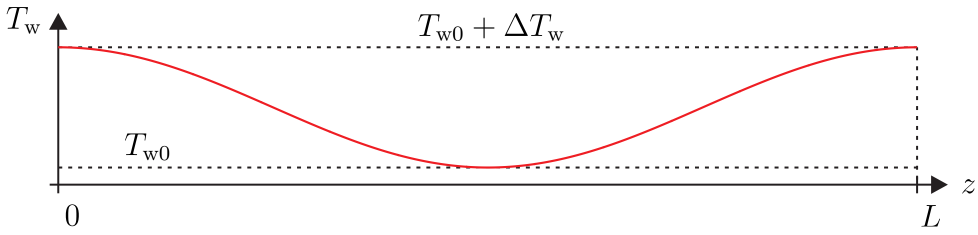

Figure 3.4: Wall temperature distribution–Eq. (3.7).

Based on a parametric study, it has been shown in [61] (Appendix A.7) that the acoustic streaming structure is particularly influenced by the mean temperature gradient in the direction perpendicular to the resonator axis[1].

If $\Delta_r T_\mathrm{m}(z) = T_\mathrm{m}(0,z) - T_\mathrm{m}(R,z) < 0$, acoustic streaming near the resonator axis is locally supported, if $\Delta_r T_\mathrm{m}(z) > 0$, it is locally opposed which may even result in the streaming velocity reversal near the resonator axis, which is connected with the development of additional outer vortices.

It is interesting to note that even if there were previous works taking into the account temperature gradients in the resonant channels ([58, 43, 44]), the authors did not consider the transverse temperature gradient, and they only considered the temperature gradient in the axial direction – to which the acoustic streaming is not very sensitive.

However, the transverse temperature gradient in the resonator fluid is directly connected with the temperature distribution along the resonator walls. It can be shown, see, e.g., [66], that if $L \gg R$, it approximately holds

$$T_\mathrm{m}(r,z) \approx \frac{1}{4}\frac{\mathrm{d}^2 T_\mathrm{w}}{\mathrm{d}z^2}\left(R^2 - r^2\right) \qquad \Rightarrow \qquad \Delta_r T_\mathrm{m}(z) \approx \frac{R^2}{4}\frac{\mathrm{d}^2 T_\mathrm{w}}{\mathrm{d}z^2}. \tag{3.6}$$

The influence of the fluid temperature variation is demonstrated in the following example. Let's assume a tube (resonator) with the radius $R = 1.5\,\mathrm{cm}$ and the length $L = 30\,\mathrm{cm}$. The wall temperature distribution is set as

$$T_\mathrm{w}(z) = \frac{\Delta T_\mathrm{w}}{2}\left[1 + \cos\left(\frac{2\pi z}{L}\right)\right] + T_\mathrm{w0}, \tag{3.7}$$

where $T_\mathrm{w0} = 20\,^\circ\mathrm{C}$, and ΔT_w differs in individual cases. The temperature distribution (3.7) is depicted in Fig. 3.4.

The numerical results are always presented for the case of $\lambda/2$-resonance. As the resonance frequency depends on the fluid temperature distribution, its value is searched for by frequency sweep maximizing the acoustic pressure at point $(r,z) = (0,0)$ in the resonator.

Figure 3.5 shows the streamlines for various values of ΔT_w. The red lines correspond to counter-clockwise rotating streaming cells, the blue lines correspond to clockwise rotating ones. The top-left panel shows the case of $\Delta T_\mathrm{w} = 0\,^\circ\mathrm{C}$ (no temperature inhomogeneity), where two outer vortices of the Rayleigh streaming can be observed. The inner boundary-layer Schlichting vortices are also present, but, they cannot be seen as in this case the ratio of the resonator radius and the viscous boundary layer thickness is ca. 164. It can be observed

---

[1] In the work [61], the resonant channel was assumed to be a rectangular one, in this case, the geometry is cylindrical one. Nevertheless, the qualitative behaviour of the acoustic streaming is the same in both the geometries.

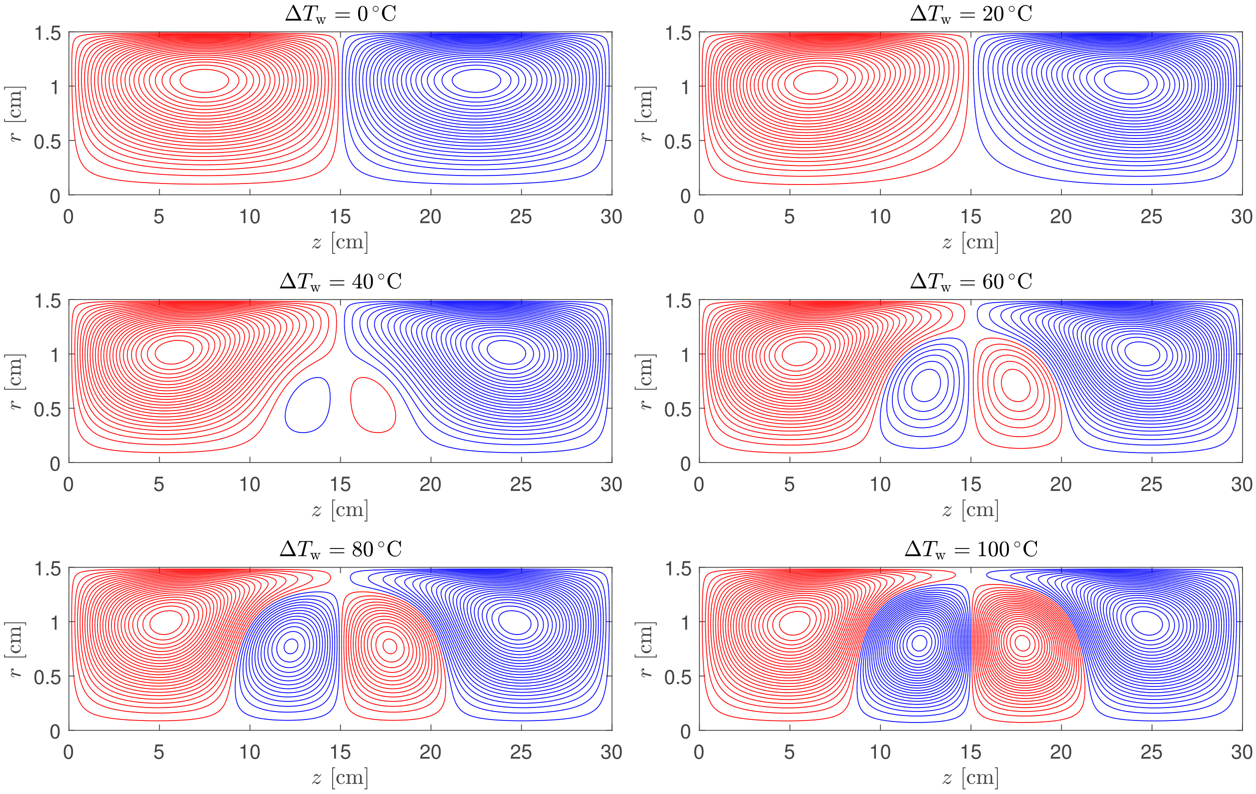

Figure 3.5: Acoustic streaming structure for the wall temperature distribution given by Eq. (3.7) for various values ΔT_w.

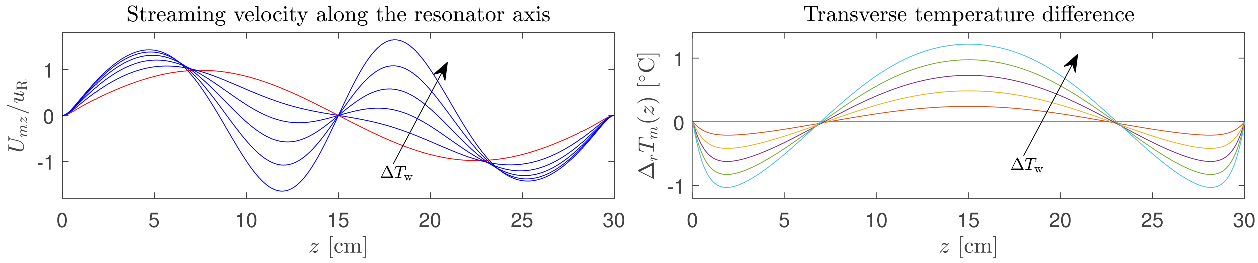

Figure 3.6: Left: Normalized streaming velocity along the resonator axis for $\Delta T_\mathrm{w} = (0, 20, 40, 60, 800, 100)\,^\circ\mathrm{C}$. Right: transverse temperature differences for the same values of ΔT_w.

in the rest of the panels in Fig. 3.5 that as the wall temperature difference ΔT_w increases, two additional outer cells emerge, pushing the original outer cells towards the ends of the resonator.

The development of the additional outer streaming cells is connected with the streaming velocity reversal in the vicinity of the resonator axis, as it was explained earlier. For various values of ΔT_w, the left panel of Fig. 3.6 shows the z-component of the streaming velocity along the resonator axis, normalized to the Rayleigh velocity[2]

$$u_\mathrm{R} = \frac{3}{8}\frac{u_{a0}^2}{c_0}, \tag{3.8}$$

where u_{a0} is the amplitude of the longitudinal acoustic velocity component on the resonator axis. The red line corresponds to $\Delta T_\mathrm{w} = 0\,^\circ\mathrm{C}$; the distribution is sinusoidal, as it is predicted by previous works, see, e.g., [42, 46]. With the increasing value of ΔT_w, the distribution deviates more and more from the sinusoidal one, and for $\Delta T_\mathrm{w} \gtrapprox 40\,^\circ\mathrm{C}$, the streaming velocity reversion occurs. The right panel of Fig. 3.6 shows the reason for the local streaming velocity deviation–the transverse temperature difference $\Delta_r T_\mathrm{m}$. As it was explained earlier, if $\Delta_r T_\mathrm{m} < 0$, the streaming velocity is supported (increased), and if $\Delta_r T_\mathrm{m} > 0$, the streaming velocity is opposed (in a force-like manner), and it is ultimately reversed. Note that very small values of $\Delta_r T_\mathrm{m}$ are enough to completely change the acoustic streaming structure. More numerical examples can be found in [61], see Appendix A.7.

3.3.3 The effect of convective heat transport on the acoustic streaming structure

Within this section, it is shown that even for moderate values of Re_nl, the streaming profile can be considerably distorted from the sinusoidal one predicted by the Rayleigh's theory, if there is even a weak temperature gradient along the resonator walls. This acoustic-field-amplitude-dependent distortion is not caused by the effect of the fluid inertia, but, it is connected with the streaming-driven convective heat transport in a fluid with a mean temperature gradient.

In order to capture the streaming-driven convective heat transport, Eqs. (3.3) and (3.4) must be solved simultaneously as one set of equations, see the details in [62] (Appendix A.8). All the numerical results presented here are calculated in the conditions of $\lambda/2$-resonance, which is searched for by a frequency sweep.

The parameters used for the numerical simulations presented here are the same as the ones used in Sec. 3.3.2. Also, Eq. (3.7) is used to prescribe the resonator wall temperature distribution. Using the formula (3.7)–cf. the previous section, in this context has a particular importance.

Formula (3.7) models, see [51], the steady-state wall temperature distribution due to the thermoacoustic heat transport. In the standing wave, there exists a time-averaged heat flux between the walls and the inner fluid which transports the heat from the acoustic-velocity antinodes towards the acoustic-velocity nodes [67, 5]. This flux, which is proportional to the square of the acoustic velocity amplitude [67], is balanced by the heat conduction within the walls and the heat flux to the outer environment; the resulting wall-temperature gradient thus depends on particular external factors, and that is why it is *prescribed* by Eq. (3.7) here.

---

[2] The definition of u_R is different for rectangular and cylindrical resonators (cf. Fig. 3.1), see, e.g., [46].

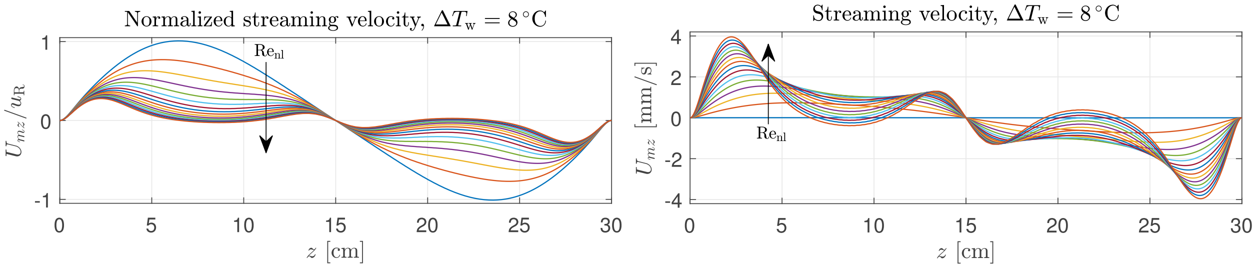

Figure 3.7: Normalized (left panel) and non-normalized (right panel) streaming velocity along the resonator axis, $\Delta T_{\mathrm{w}} = 8\,^{\circ}\mathrm{C}$, $\mathrm{Re}_{\mathrm{nl}} = 0.001, 0.2, 0.4, \ldots, 2.8, 3.0$; steady state.

Figure 3.7 shows the distribution of steady-state averaged mass transport velocity along the resonator axis for individual values of $\mathrm{Re}_{\mathrm{nl}}$ both normalized to the Rayleigh velocity (left panel) and non-normalized (right panel).

Here, $\mathrm{Re}_{\mathrm{nl}}$ is not exclusively understood as a measure of the flow-inertia effect on the streaming field, it is employed as an established parameter related to the streaming velocity (according to the Rayleigh's theory, streaming velocity should be proportional to $\mathrm{Re}_{\mathrm{nl}}$).

In the case of $\mathrm{Re}_{\mathrm{nl}} = 0.001$, the streaming velocity has such a small value that the convective heat transport is negligible. The normalized streaming velocity along the axis reaches the maximum value of $U_{\mathrm{m}z}/u_{\mathrm{R}} \approx 1$; the distribution slightly differs from the sinusoidal one [42]. If the streaming velocity increases, its distribution quickly gets distorted, and the value of the normalized streaming velocity in maxima decreases. With further increasing $\mathrm{Re}_{\mathrm{nl}}$, the normalised streaming velocity between the velocity nodes and antinodes further decreases; it reaches zero value for $\mathrm{Re}_{\mathrm{nl}} \approx 2.4$ and its direction reverses for higher values of $\mathrm{Re}_{\mathrm{nl}}$. Considering the non-normalised streaming velocity, the situation looks somewhat more complex; while its value increases with $\mathrm{Re}_{\mathrm{nl}}$ monotonically near the acoustic velocity nodes and antinode, between them, it first increases, then reaches maximum, decreases and then changes its sign. It can be seen in both the versions of the figure that the incremental change of the streaming velocity is bigger for lower values of $\mathrm{Re}_{\mathrm{nl}}$ then for higher ones.

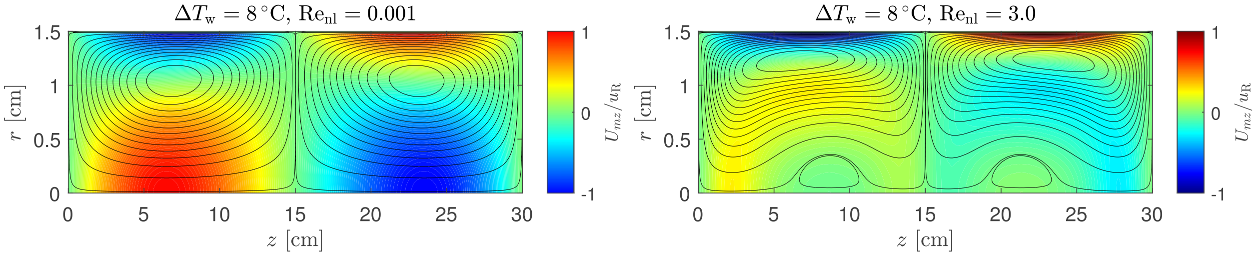

Figure 3.8: Streaming velocity (z-component) and streamlines for $\Delta T_{\mathrm{w}} = 8\,^{\circ}\mathrm{C}$ and different values of $\mathrm{Re}_{\mathrm{nl}}$; steady state.

Figure 3.8 shows the streamlines for the case of $\mathrm{Re}_{\mathrm{nl}} = 0.001$ and $\mathrm{Re}_{\mathrm{nl}} = 3.0$. If the streaming velocity is small (left panel), two outer vortices can be observed as expected [46]. The inner vortices are not appreciable because of the high value of the ratio of the resonator radius and the viscous boundary layer thickness. For higher streaming velocity (right panel) the streamlines are distorted, and two weak additional outer vortices appear near the resonator axis, which is connected with the reversal of the streaming velocity at the resonator axis seen in Fig. 3.7. More numerical examples are given in [62] (Appendix A.8).

This behaviour can be explained employing the observations outlined in Sec. 3.3.2 and thoroughly examined in [61] (Appendix A.7). If the resonator driving is increased, $\mathrm{Re}_{\mathrm{nl}}$ increases, acoustic streaming becomes a more effective means of the heat transport which results in the re-distribution of the mean fluid temperature. Acoustic streaming convects the heat along the resonator axis from the warmer areas near the end-walls towards the resonator centre, see Fig. 3.9.

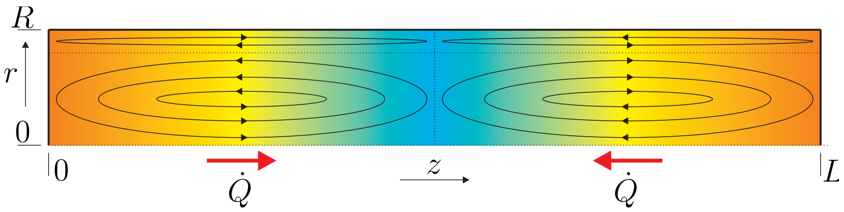

Figure 3.9: Heat transport in a resonator due to acoustic streaming.

However, this heat transport also increases the value of $\Delta_r T_{\mathrm{m}}(z)$ in the resonator central part, see the example in Fig. 3.10, leading to the opposition to the acoustic streaming and reducing its effectiveness in convecting the heat. This effect manifests itself by decreasing incremental temperature change with increasing $\mathrm{Re}_{\mathrm{nl}}$ seen in Fig. 3.10. This feedback behaviour explains the distortion of the streaming structure in temperature-inhomogeneous fluids and its dependence on $\mathrm{Re}_{\mathrm{nl}}$ through the convective term $\boldsymbol{u}_{\mathrm{m}} \cdot \boldsymbol{\nabla} T_{\mathrm{m}}$ in the energy equation (3.4c).

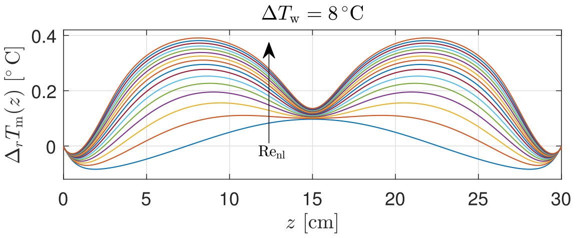

Figure 3.10: Distribution of temperature difference $\Delta_r T_{\mathrm{m}}(z)$ along the resonator for $\Delta T_{\mathrm{w}} = 8\,^{\circ}\mathrm{C}$ and $\mathrm{Re}_{\mathrm{nl}} = 0.001, 0.2, 0.4, \ldots, 2.9, 3.0$.

The departure of the streaming velocity distribution from the sinusoidal one presented in Fig. 3.7 is of the same type as it has been found experimentally [50, 51, 53]. In the above-mentioned experiments, the reason for the departure is two-fold: (a) because of the thermoacoustically induced temperature distribution along the resonator walls, and (b) because of the inertial effects of the streaming flow. In the experiments, these two effects come hand in hand as the streaming velocity, as well as the heat flux between the resonator wall and the inner fluid, are proportional to the square of the acoustic velocity. The numerical results presented here were obtained for $\mathrm{Re}_{\mathrm{nl}} \leq 3$, which means that the inertial effects on the streaming fluid flow are small [47] and the streaming field distortion is caused purely by the fluid temperature inhomogeneity.

3.4 Discussion

We have shown that the acoustic streaming structure is extremely sensitive to the fluid transverse temperature distribution, which is an important fact for thermoacoustic applications where an intricate interactions between acoustic, thermal, and streaming fields play a crucial role.

We have also demonstrated, that even in the case of relatively weak temperature gradients, the acoustic-streaming-driven convective heat transport is responsible for a considerable distortion of the streaming profile, this effect is much stronger than the effect of the fluid inertia on the streaming flow. The streaming profiles observed within this work are consistent with the available experimental data. Based on the results obtained within this work, this conclusion can be drawn. For a good quantitative agreement between experimental and theoretical data, the thermal effects must be comprised within the model describing acoustic streaming, and even slight wall-temperature gradients cannot be ignored any more.

Chapter 4

Non-paraxial model of parametric acoustic array

4.1 Introduction

The concept of parametric acoustic array (PAA) has been introduced in 1963 by P. J. Westervelt [68]. This technique allows to generate low-frequency highly directional side-lobes-free sound beams from sources (radiators) with relatively small aperture. The principle is as follows, see Fig. 4.1, and, e.g., [68, 34, 69].

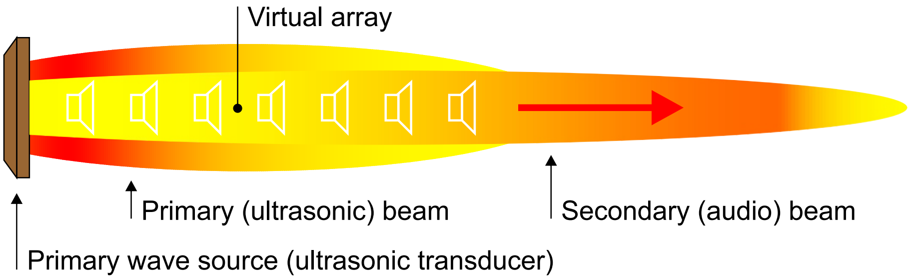

Figure 4.1: Generation of audible sound beam through PAA.

Two collimated ultrasonic beams of similar frequencies are radiated in the same direction, where at least one of them has a finite amplitude. As these (primary) waves propagate in the medium, nonlinear effects give rise to the generation of a secondary field, one component of which is the (low-frequency) difference-frequency one, by forming a phased array of virtual sources that resonantly pump acoustic energy into this component. The directivity of this low-frequency wave is much higher than if it were radiated directly by the primary-field radiator. It is obvious that a small percentage change of one of the primary frequencies results in a large percentage change in the difference-frequency, which means that wideband radiation (in the difference-frequency) can be accomplished using a narrowband high-frequency transducer. Since its discovery the PAA has found its application in sonar, parametric loudspeakers, etc., see e.g., [70, 71, 72, 73, 74, 75].

The process of the generation of a difference-frequency wave in a field of highly-directional finite-amplitude primary waves is a rather complex one, and its mathematical description requires some degree of approximation and simplification. This problem has been addressed by many authors in different ways.

In his pioneering work, P. J. Westervelt [68] described the far-field properties of the difference-frequency waves based on the assumption that the nonlinear interactions are limited only to the near-field of the primary waves which were modelled as collimated plane waves. T. G. Muir and J. G. Willette [76] calculated the sum- and difference-frequency field under the assumption that the nonlinear interactions take place only in the far-field of the primary waves, which were modelled analytically using the formula for the far-field of a uniformly vibrating piston. G. S. Garrett *et. al.* [77] proposed a model for the parametric radiation from an axisymmetric source in the quasilinear and paraxial approximation based on the numerical calculation of a triple integral. T. Kamakura *et. al.* [78] studied the propagation of high-amplitude waves generated by a piston vibrating at two similar frequencies by numerical integration of parabolic KZK equation. In works [79, 80], method of multi-Gaussian beam expansion has been employed for the fast calculation of difference-frequency fields in the quasi-linear and paraxial approximation. H. Nomura *et. al.* [81] simulated the parametric sound generation by means of direct numerical integration of the Navier-Stokes equations in the time domain. This approach in principle allows to study more complex configurations, however, the numerical integration in the time domain over a large spatial domain (if the far-field behaviour is studied) results in an enormous computational time and a big amount of stored data which need to be post-processed in order to obtain the spectral content of the sound field.

The common characteristic of most of the above-mentioned papers and many others is that the difference-frequency field is calculated in the paraxial approximation, which means, that the corresponding models provide reliable results up to ca. 20° from the transducer axis and they fail to provide any prediction in the nearfield. Within the following text, we introduce a computationally efficient approach that does not rely on the paraxial approximation and that can be used for the study of more complex problems than what has been studied in the previous works. The rest of this chapter is related to the author's works [82, 83, 84], see the Appendices A.9, A.10, and A.11.

4.2 Model equations

As the acoustic fields employed in PAA are usually only weakly nonlinear, wave equations derived under the second-order approximation are accurate enough to capture the important physical effects (nonlinearity, diffraction, thermoviscous dissipation).

Such a wave equation, derived by S. I. Aanonsen *et al.*, see, e.g., [85, 34], reads

$$\boldsymbol{\nabla}^2 p' - \frac{1}{c_0^2}\frac{\partial^2 p'}{\partial t^2} + \frac{\delta}{c_0^2}\boldsymbol{\nabla}^2\frac{\partial p'}{\partial t} = -\frac{\beta}{\rho_0 c_0^4}\frac{\partial^2 p'^2}{\partial t^2} - \boldsymbol{\nabla}^2\mathcal{L} - \frac{1}{c_0^2}\frac{\partial^2\mathcal{L}}{\partial t^2}, \tag{4.1}$$

where p' is the acoustic pressure, t is the time, c_0 is the small-signal adiabatic sound speed, ρ_0 is the ambient fluid density, β is the parameter of nonlinearity of the fluid, for an ideal gas $\beta = (\gamma+1)/2$, where γ is the adiabatic exponent, $\delta = \left[4\mu/3 + \mu_\mathrm{B} + \kappa\left(1/c_V - 1/c_p\right)\right]/\rho_0$ is the diffusivity of sound, where μ, μ_B are the coefficients of shear and bulk viscosity, respectively, κ is the coefficient of thermal conduction, and c_p, c_V are the specific heats at constant pressure and volume, respectively. The symbol $\mathcal{L}$ stands for the Lagrangian density which reads

$$\mathcal{L} = \rho_0\frac{v^2}{2} - \frac{p'^2}{2\rho_0 c_0^2}, \tag{4.2}$$

where $v^2 = \boldsymbol{v} \cdot \boldsymbol{v}$ is the square of the acoustic particle velocity vector.

In the second approximation, $\mathcal{L} = 0$ in the case of progressive plane waves. Then, the general model equation Eq. (4.1) reduces into the well-known Westervelt equation[1] [85, 34, 68] which reads

$$\boldsymbol{\nabla}^2 p' - \frac{1}{c_0^2}\frac{\partial^2 p'}{\partial t^2} + \frac{\delta}{c_0^2}\boldsymbol{\nabla}^2 \frac{\partial p'}{\partial t} = -\frac{\beta}{\rho_0 c_0^4}\frac{\partial^2 p'^2}{\partial t^2}. \tag{4.3}$$

As it is discussed in Refs. [85, 34] the Westervelt equation describes correctly (in the second-order approximation) plane progressive waves, however, even with the omission of the Lagrangian density, the cumulative nonlinear effects are still captured correctly even in the case of non-plane wave propagation, the Lagrangian density is associated only with local (non-cumulative) nonlinear effects. Due to its relative simplicity [compared to Eq. (4.1)] the Westervelt equation is widely used in the modelling of PAA.

If we introduce the velocity potential φ such that $\boldsymbol{v} = \boldsymbol{\nabla}\varphi$ and employ the second-order relationship between the acoustic pressure and the velocity potential, see, e.g., [20] (Appendix A.3),

$$p' = -\rho_0 \frac{\partial \varphi}{\partial t} - \frac{\rho_0}{2}(\boldsymbol{\nabla}\varphi)^2 + \frac{\rho_0}{2c_0^2}\left(\frac{\partial \varphi}{\partial t}\right)^2, \tag{4.4}$$

in the second approximation, the wave equation Eq. (4.1) can be recast [85] into

$$\boldsymbol{\nabla}^2 \varphi - \frac{1}{c_0^2}\frac{\partial^2 \varphi}{\partial t^2} + \frac{\delta}{c_0^2}\boldsymbol{\nabla}^2 \frac{\partial \varphi}{\partial t} = \frac{1}{c_0^2}\frac{\partial}{\partial t}\left[(\boldsymbol{\nabla}\varphi)^2 + \frac{\beta - 1}{c_0^2}\left(\frac{\partial \varphi}{\partial t}\right)^2\right], \tag{4.5}$$

which is the well-known Kuznetsov equation [86]. Equations (4.1) and (4.5) are derived under the same degree of approximation and they are equivalent. Note, that Eq. (4.5) is related to Eq. (2.5).

4.3 Successive approximations

Solution of the wave equations presented in Sec. 4.2 can be substantially simplified under the assumption of weakly nonlinear field, employing the method of the successive approximations, see, e.g., [34]. Similarly as it has been used in Sec. 3.2, the quasi-linear solutions of the governing equations are assumed to have the form

$$\psi(\boldsymbol{r}, t) = \psi_1(\boldsymbol{r}, t) + \psi_2(\boldsymbol{r}, t), \tag{4.6}$$

where ψ represents the given acoustic variable (acoustic pressure, velocity potential), ψ_1 is the linear solution (approximation) of Eqs. (4.1), (4.3), or (4.5), representing the primary field, and ψ_2 is a small correction to ψ_1, representing the secondary field due to the nonlinear interactions. Obviously, $|\psi_2| \ll |\psi_1|$.

The primary (ultrasonic) acoustic field is assumed to be composed of two time-harmonic fields at similar frequencies f_c (carrier), and f_s (side-band), where $f_\mathrm{c} > f_\mathrm{s}$. Within this work, the difference-frequency component f_d of the secondary field is of the interest, where $f_\mathrm{d} = f_\mathrm{c} - f_\mathrm{s}$. Being time-harmonic, all the components of the acoustic variables are further represented by their complex amplitudes $\psi_j(\boldsymbol{r}, t) = \Re[\tilde{\psi}_j(\boldsymbol{r})\mathrm{e}^{\mathrm{i}\omega_j t}]$, where $j = \mathrm{c}, \mathrm{s}, \mathrm{d}$, and $\mathrm{i} = \sqrt{-1}$.

---

[1] This equation was employed by P. J. Westervelt in his pioneering work on PAA [68].

For the primary-field components, the linearised Eqs. (4.1), (4.3), or (4.5) reduce to homogeneous Helmholtz equation

$$\boldsymbol{\nabla}^2\tilde{\psi}_j + k_j^2\tilde{\psi}_j = 0, \tag{4.7}$$

where $j = \mathrm{c}, \mathrm{s}$, and $k_j \approx \omega_j/c_0 - \mathrm{i}\omega_j^2\delta/2c_0^3$ is the complex wavenumber the imaginary part of which describes the thermoviscous attenuation.

For the difference-frequency secondary field, Eqs. (4.1), (4.3) reduce to inhomogeneous Helmholtz equation

$$\boldsymbol{\nabla}^2\tilde{p}_\mathrm{d} + k_\mathrm{d}^2\tilde{p}_\mathrm{d} = \tilde{q}_{p\mathrm{d}}, \tag{4.8}$$

where the source term

$$\tilde{q}_{p\mathrm{d}} = \frac{\beta\omega_\mathrm{d}^2}{\rho_0 c_0^4}\tilde{p}_\mathrm{c}\tilde{p}_\mathrm{s}^* - \left(\boldsymbol{\nabla}^2 - k_\mathrm{d}^2\right)\tilde{\mathcal{L}}_\mathrm{d}, \tag{4.9}$$

where

$$\tilde{\mathcal{L}}_\mathrm{d} = \frac{\rho_0}{2}\tilde{\boldsymbol{v}}_\mathrm{c}\cdot\tilde{\boldsymbol{v}}_\mathrm{s}^* - \frac{\tilde{p}_\mathrm{c}\tilde{p}_\mathrm{s}^*}{2\rho_0 c_0^2} \tag{4.10}$$

for Eq. (4.1). The asterisk stands for the complex conjugate, and $\tilde{\mathcal{L}}_\mathrm{d} = 0$ for the Westervelt equation [Eq. (4.3)].

For the difference-frequency secondary field, Eq. (4.5) reduces to

$$\boldsymbol{\nabla}^2\tilde{\varphi}_\mathrm{d} + k_\mathrm{d}^2\tilde{\varphi}_\mathrm{d} = \tilde{q}_{\varphi\mathrm{d}}, \tag{4.11}$$

where

$$\tilde{q}_{\varphi\mathrm{d}} = \frac{\mathrm{i}\omega_\mathrm{d}}{c_0^2}\left[\tilde{\boldsymbol{v}}_\mathrm{c}\cdot\tilde{\boldsymbol{v}}_\mathrm{s}^* + (\beta-1)\frac{\omega_\mathrm{c}\omega_\mathrm{s}}{c_0^2}\tilde{\varphi}_\mathrm{c}\tilde{\varphi}_\mathrm{s}^*\right]. \tag{4.12}$$

Using the difference-frequency, and primary-field velocity potentials, the difference-frequency acoustic pressure can be calculated, employing Eq. (4.4), as

$$\tilde{p}_\mathrm{d} = -\mathrm{i}\omega_\mathrm{d}\rho_0\tilde{\varphi}_\mathrm{d} - \frac{\rho_0}{2}\tilde{\boldsymbol{v}}_\mathrm{c}\cdot\tilde{\boldsymbol{v}}_\mathrm{s}^* + \frac{\rho_0\omega_\mathrm{c}\omega_\mathrm{s}}{2c_0^2}\tilde{\varphi}_\mathrm{c}\tilde{\varphi}_\mathrm{s}^*. \tag{4.13}$$

4.4 Numerical strategies

There are several numerical strategies for the solution of the above-mentioned equations, some of them are discussed in the following text. These strategies can be demonstrated on a simple model problem–the parametric radiation of a baffled circular piston, see Fig. 4.2.

The piston is assumed to have the radius a, its complex vibration amplitude $\tilde{u}_j$ being an axi-symmetric one, i.e., $\tilde{u}_j = \tilde{u}_j(r)$, where $r = \sqrt{x^2 + y^2}$.

4.4.1 Direct numerical integration

Complex amplitude of the acoustic pressure of the primary field at a point P, for the calculation of the source terms (4.9), (4.12), can be calculated employing the Rayleigh integral, see, e.g., [23], as

$$\tilde{p}_j(\boldsymbol{r}) = \frac{\mathrm{i}k_j\rho_0 c_0}{2\pi}\int_{-\infty}^{\infty}\int_{-\infty}^{\infty}\tilde{u}_j(x',y')\frac{\mathrm{e}^{-\mathrm{i}k_j R}}{R}\,\mathrm{d}x'\mathrm{d}y', \quad j = \mathrm{c}, \mathrm{s}, \tag{4.14}$$

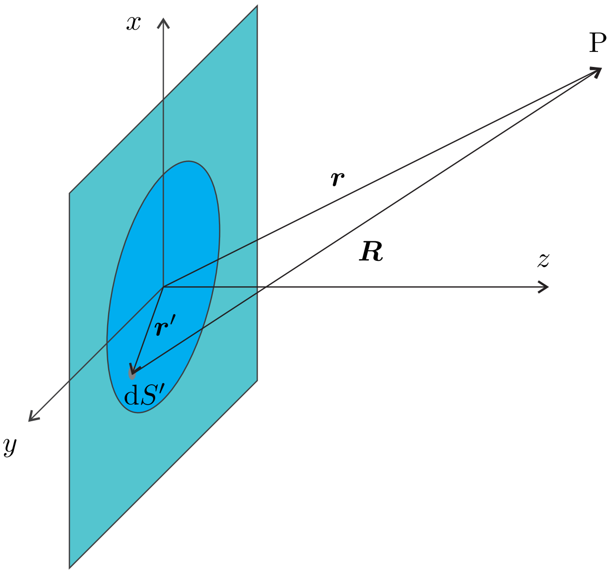

Figure 4.2: Geometrical arrangement; P is the point, where acoustic field is determined.

where $R = \sqrt{(x-x')^2 + (y-y')^2 + z^2}$. The other acoustic-field variables, such as the velocity potential and the particle velocity vector can be calculated from Eq. (4.14) employing linear theory, see [84] (Appendix A.11).

Once the source term for the inhomogeneous Helmholtz equation (4.8) or (4.11) has been (formally) determined, the difference-frequency field can be calculated employing the Green's theory, see, e.g., [87]. For example, in the case of Eq. (4.8), the solution reads

$$\tilde{p}_{\mathrm{d}}(\boldsymbol{r}) = \frac{1}{4\pi} \int_{z'=0}^{\infty} \int_{y'=-\infty}^{\infty} \int_{x'=-\infty}^{\infty} \tilde{q}_{\mathrm{pd}}(\boldsymbol{r}') \left(\frac{\mathrm{e}^{-\mathrm{i}k_{\mathrm{d}}R^{+}}}{R^{+}} + \frac{\mathrm{e}^{-\mathrm{i}k_{\mathrm{d}}R^{-}}}{R^{-}} \right) \mathrm{d}x'\mathrm{d}y'\mathrm{d}z', \tag{4.15}$$

where

$$R^{-} = \sqrt{(x-x')^2 + (y-y')^2 + (z-z')^2}, \qquad R^{+} = \sqrt{(x-x')^2 + (y-y')^2 + (z+z')^2},$$

see [82] (Appendix A.9). Solution to Eq. (4.11) would be formulated analogously.

Equation (4.15) represents the exact solution to the inhomogeneous Helmholtz equation, however, as it is based on the fifth-fold integral, its numerical evaluation is extremely difficult, which is also complicated by the oscillatory character of the argument of the integral (4.14).

4.4.2 Multi-Gaussian beam expansion

In the cases of $|k_{\mathrm{c}}a| \sim |k_{\mathrm{s}}a| \gg 1$, i.e., the primary wave is radiated in the form of highly directional beams, multi-Gaussian beam expansion can be applied.

Here, the Green's function in Eq. (4.14) can be simplified into the Fresnel approximation, see, e.g., [88], as

$$\frac{\mathrm{e}^{-\mathrm{i}k_j R}}{R} \approx \frac{1}{z} \exp\left\{ -\mathrm{i}k_j \left[z + \frac{(x-x')^2 + (y-y')^2}{2z} \right] \right\}. \tag{4.16}$$

If, subsequently, the distribution of the piston velocity is expanded into a series of the Gaussian functions $g(\xi)$, see [89],

$$\tilde{u}_j(r = \sqrt{x^2+y^2} = a\xi) = \tilde{u}_{0j} f(a\xi) \approx \tilde{u}_{0j} g(a\xi), \qquad \text{where} \qquad g(\xi) = \sum_{n=1}^{N} A_n \mathrm{e}^{-B_n \xi^2},$$

where $\tilde{u}_{0j}$ represents complex amplitude, and A_n, B_n are complex coefficients, Eq. (4.14) can be integrated analytically, resulting in

$$\tilde{p}_j(\boldsymbol{r}) = \mathrm{i}\rho_0 c_0 \tilde{u}_{0j} k_j a^2 \mathrm{e}^{-\mathrm{i}k_j z} \sum_{n=1}^{N} \frac{A_n \exp\left[-\frac{k_j B_n (x^2+y^2)}{k_j a^2 - 2\mathrm{i}B_n z}\right]}{k_j a^2 - 2\mathrm{i}B_n z}. \tag{4.17}$$

Again, the other acoustic variables can be calculated from the solution (4.17) employing linear theory and substituted into the source terms of the inhomogeneous Helmholtz equation (4.8) or (4.11). For example, the solution to the Westervelt equation can be obtained using the formulas (4.17), (4.9), and (4.15) in the form of a three-fold integral. Numerical examples demonstrating this approach can be found in [82] (Appendix A.9).

Determination of the multi-Gaussian beam expansion coefficients

As the Gaussian functions are non-orthogonal, we have used a heuristic method for calculation of these coefficients. Unlike Wen and Breazeale [89] and others, we proposed to search for them by minimization of the function

$$Q(A_1, B_1, \ldots, A_N, B_N) = \int_0^\infty \left| f(\xi) - \sum_{n=1}^{N} A_n \mathrm{e}^{-B_n \xi^2} \right|^2 \xi \, \mathrm{d}\xi. \tag{4.18}$$

The differential $\xi \mathrm{d}\xi$ stems from the fact that the integration takes place in the polar coordinates (Wen and Breazeale [89] and others omitted the multiplicative weighting factor ξ in the differential). Apart from the geometrical meaning of the coefficient ξ, its presence in formula (4.18) greatly simplifies evaluation of the function in some important cases as it is demonstrated in [83] (Appendix A.10).

4.4.3 Finite element method

Another approach for avoiding the direct numerical evaluation of the fifth-fold integral introduced in Sec. 4.4.1 employs the finite element method (FEM) for the calculation of the secondary field [Eqs. (4.8) or (4.11)], see [84] (Appendix A.11). The primary field [Rayleigh integral (4.14)] can be either calculated (a) numerically as a two-fold integral, (b) employing the boundary element method (BEM), or (c) the finite element method, see the discussion in [84] (Appendix A.11). The approaches (a,b) are less heavy on the computational resources, as the primary field is only evaluated at the mesh points for the secondary-field equation. Moreover, the approaches (a,b) do not require the introduction of non-reflecting boundary conditions preventing the spurious reflections of the primary waves. The approaches (a,b) have been implemented in the finite-element software COMSOL Multiphysics [65], see [84] (Appendix A.11) for the details.

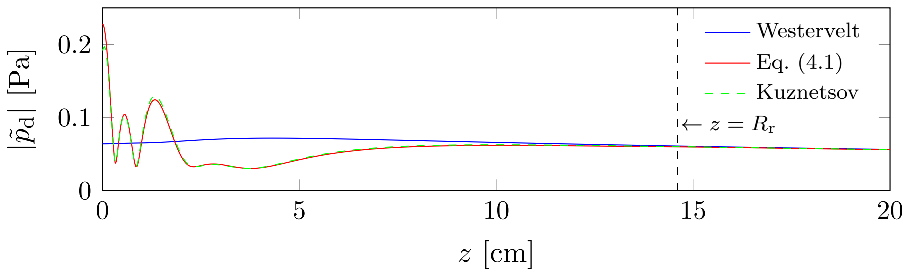

Figure 4.3: Comparison of the numerical results: difference-frequency wave, $f_\mathrm{d} = 1\,\mathrm{kHz}$, piston with parabolic velocity distribution; the vertical dashed line marks the Rayleigh distance.

4.5 Numerical results and discussion

Here, we present some results obtained employing the approach described in Sec. 4.4.3. Within all the examples shown here, acoustic field is calculated in air at normal conditions, and classical thermoviscous attenuation is taken into account. In all the following cases, the carrier frequency $f_\mathrm{c} = 40\,\mathrm{kHz}$, and the primary-field source (radiator) has the radius $a = 2\,\mathrm{cm}$. As the problem possesses the axial symmetry, the acoustic field is calculated in $(r,\, z)$ axi-symmetric cylindrical coordinates.

The complex amplitude of the piston vibration velocity at frequencies f_c, f_s is assumed to have the form

$$\begin{aligned} \tilde{u}_j(r) &= u_0 && \text{(uniform distribution)},\\ \tilde{u}_j(r) &= u_0(1 - r^2/a^2) && \text{(parabolic distribution)},\\ \tilde{u}_j(r) &= u_0(1 - r^2/a^2)^2 && \text{(quartic distribution)}, \end{aligned} \tag{4.19}$$

where $j = \mathrm{c,s}$. In all the numerical results presented here, for the simplicity, $u_0 = 1\,\mathrm{m\,s^{-1}}$.

Figure 4.3 shows the distribution of the amplitude of the acoustic pressure of the difference-frequency wave ($f_\mathrm{d} = 1\,\mathrm{kHz}$) along the z-axis in the near-field of the carrier wave (for $f_\mathrm{c} = 40\,\mathrm{kHz}$, the Rayleigh distance $R_\mathrm{r} = \Re[k_\mathrm{c}]a^2/2 = 14.6\,\mathrm{cm}$). The velocity-distribution of the piston is the parabolic one, see Eq. (4.19).

The difference-frequency field is calculated employing Eq. (4.1), (red line), the Westervelt equation [Eq. (4.3), blue line], and the Kuznetsov equation [Eq. (4.5), green line]. As Eq. (4.1) and the Kuznetsov equation are derived under the same approximation, the numerical results correspond to each other very well. As in the Westervelt equation the Lagrangian density [Eq. (4.2)] is assumed to be zero, which is not fulfilled in the near-field of the primary wave, the prediction by the Westervelt equation differs from Eq. (4.1) and the Kuznetsov equation. However, in the far-field, beyond the Rayleigh distance, the predictions of all the three equations match to each other as it is expected.

As the numerical evaluation of the source term [Eq. (4.9)] for Eq. (4.1) is much more expensive than the source term [Eq. (4.12)] for the Kuznetsov equation, as it is necessary to calculate the second-order spatial derivatives of the primary-field quantities, the Kuznetsov equation [Eq. (4.5)] is employed for the calculation of the near field further on.

Figure 4.4 shows the acoustic pressure amplitude of the difference-frequency wave along the z-axis for $f_\mathrm{d} = 1\,\mathrm{kHz}$ and individual piston velocity distributions [see Eq. (4.19)]. The solid lines correspond to the predictions by the Kuznetsov equation, the dashed lines are related to the Westervelt equation. It can be observed that the structure of the near-field (resolved by the

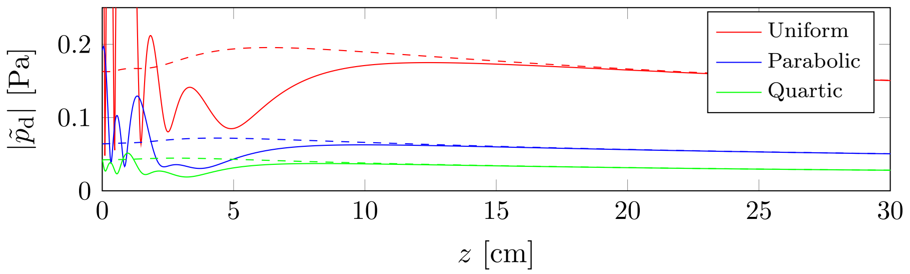

Figure 4.4: Difference-frequency wave along the z-axis for $f_\mathrm{d} = 1\,\mathrm{kHz}$, and individual piston velocity distributions. Predictions by the Kuznetsov equation (solid lines), and the Westervelt equation (dashed lines).

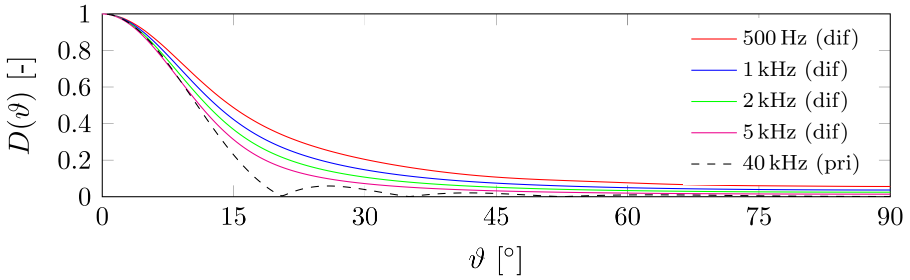

Figure 4.5: Directivity function of the piston with the parabolic velocity distribution calculated at the distance $r_0 = 2\,\mathrm{m}$ from the piston centre; dashed line – the primary wave (40 kHz), solid lines – individual difference frequencies.

Kuznetsov equation) depends on the piston velocity distribution[2] and again, the predictions of both the equations correspond to each other in the far-field. The difference in the amplitudes (at a given point in the far-field) for the individual piston velocity distributions are caused by the fact that the amount of the radiated acoustic energy for the individual cases differs.

Figure 4.5 shows the directivity function $D(\vartheta) = |\tilde{p}(r_0, \vartheta)/\tilde{p}(r_0, 0)|$ calculated at the distance $r_0 = 2\,\mathrm{m}$ from the centre of the piston with the parabolic velocity distribution. It can be observed that the low-frequency difference-frequency field (solid lines) has a similar directivity as the high-frequency carrier wave (dashed line), and that the directivity of the difference-frequency wave increases with its frequency. Radiation from this piston directly at the frequencies shown in the figure (500 Hz – 5 kHz) would be essentially omnidirectional.

More numerical results and examples, including the parametric radiation from the horned piston are given in [84] (Appendix A.11).

The presented computational approach represents an efficient tool for the study of parametric radiation of low-frequency highly directional sound beams. As the method is not based on the paraxial approximation, both the near-field as well as the of-axis field is properly resolved. Employing the BEM-FEM methods also enables to study more complex configurations, utilizing, e.g., horns, acoustic lenses, phononic crystals, etc.

---

[2] It is also shown in [84] (Appendix A.11) that the structure of the near-field (resolved by the Kuznetsov equation) is strongly frequency-dependent.

Chapter 5

Conclusions and future outlooks

Within this thesis, I have summarized part of the work on which I have collaborated with my colleagues during the last ten years and which contributed to solving existing problems and furthered understanding of fundamental phenomena in the field of nonlinear acoustics. These are the main results that we have achieved:

- We have proposed a systematic approach for determining the shapes of acoustic resonators maximizing the acoustic pressure amplitude. We have shown that these shapes differ for the individual methods of driving. The proposed approach has been validated experimentally. With these optimized resonators, high-amplitude acoustic fields can be generated efficiently, which is important for the potential applications.
- Employing numerical experiments, we have revealed the high sensitivity of the Rayleigh acoustic streaming structure on the transverse temperature gradients in fluid-filled acoustic resonators. With this knowledge, we have identified a feedback mechanism that explains the distortion of the streaming profile observed in experiments. By this work, we have contributed to the solution of one of the contemporary problems of nonlinear acoustics.
- We have proposed a versatile computational approach for the study of parametrically radiated sound. The proposed method does not employ the paraxial approximation and allows for the studying of complex configurations. The proposed approach represents an easy-to-use tool that can be utilized for the design and optimization of small, highly-directional audio-frequency radiators.

In my future work, I would like to capitalize on the methods and results described within this thesis, together with those I have not included, see, e.g., [90, 91, 92, 93, 94, 95]. These are the possible directions of my future research:

- Acoustic black holes, which are theoretically predicted structures minimizing the acoustic wave reflection. The basic principle here is the slow-down of the sound speed to zero in the “singularity.” Apart from the fact that these non-conventional structures are very interesting from the theoretical point of view, they may represent an attractive alternative to conventional treatments employing a bulk of porous absorbing materials.
- Broadband perfect absorbers, which are finely-tuned resonant structures allowing for almost 100 % acoustic energy absorption. In these structures, only their inherent losses

are usually employed, which leads to relatively simple designs with compact dimensions, again, avoiding a bulk of porous absorbing materials.

- Phononic structures for the sound insulation, combining the effect of Bragg scattering with local resonances. These structures represent light-weight alternatives to conventional sound barriers. Incorporation of the local resonators and structural optimization can dramatically increase the sound insulation performance, especially in the low-frequency range, preserving compact dimensions.
- And whatever interesting the future brings…

Bibliography

[1] A. B. Coppens and J. V. Sanders, "Finite-amplitude standing waves in rigid-walled tube," *J. Acoust. Soc. Am.*, vol. 43, pp. 516–529, 1968.

[2] J. D. B. Cruikshank, "Experimental investigation of finite-amplitude acoustic oscillations in a closed tube," *J. Acoust. Soc. Am.*, vol. 52, pp. 1024–1036, 1972.

[3] T. Nakane, "Discharge phenomenon in high-intensity acoustic standing wave field," *IEEE Trans. Plasma Sci.*, vol. 33, no. 2, pp. 356–357, 2005.

[4] R. Bálek, M. Červenka, and S. Pekárek, "Acoustic field effects on a negative corona discharge," *Plasma Sources Sci. T.*, vol. 23, pp. 1–9, 2014.

[5] G. W. Swift, "Thermoacoustic engines," *J. Acoust. Soc. Am.*, vol. 84, no. 1, pp. 1145–1180, 1988.

[6] D. F. Gaitan and A. A. Atchley, "Finite amplitude standing waves in harmonic and anharmonic tubes," *J. Acoust. Soc. Am.*, vol. 93, pp. 2489–2495, 1993.

[7] C. C. Lawrenson, B. Lipkens, T. S. Lucas, D. K. Perkins, and T. W. V. Doren, "Measurements of macrosonic standing waves in oscillating closed cavities," *J. Acoust. Soc. Am.*, vol. 104, pp. 623–636, 1998.

[8] Y. A. Ilinskii, B. Lipkens, T. S. Lucas, T. W. V. Doren, and E. A. Zabolotskaya, "Nonlinear standing waves in an acoustical resonator," *J. Acoust. Soc. Am.*, vol. 104, pp. 2664–2674, 1998.

[9] Y. A. Ilinskii, B. Lipkens, and E. A. Zabolotskaya, "Energy losses in an acoustical resonator," *J. Acoust. Soc. Am.*, vol. 109, pp. 1859–1870, 2001.

[10] M. F. Hamilton, Y. A. Ilinskii, and E. A. Zabolotskaya, "Linear and nonlinear frequency shifts in acoustical resonators with varying cross sections," *J. Acoust. Soc. Am.*, vol. 110, pp. 109–119, 2001.

[11] M. P. Mortell and B. R. Seymour, "Nonlinear resonant oscillations in closed tubes of variable cross-section," *J. Fluid Mech.*, vol. 519, pp. 183–199, 2004.

[12] Y.-D. Chun and Y.-H. Kim, "Numerical analysis for nonlinear resonant oscillations of gas in axisymmetric closed tubes," *J. Acoust. Soc. Am.*, vol. 108, pp. 2765–2774, 2000.

[13] R. R. Erickson and B. T. Zinn, "Modeling of finite amplitude acoustic waves in closed cavities using the Galerkin method," *J. Acoust. Soc. Am.*, vol. 113, pp. 1863–1870, 2003.

[14] C. Luo, X. Y. Huang, and N. T. Nguyen, “Effect of resonator dimensions on nonlinear standing waves,” *J. Acoust. Soc. Am.*, vol. 117, pp. 96–103, 2005.

[15] X. Li, J. Finkbeiner, G. Raman, C. Danielsb, and B. M. Steinetz, “Optimized shapes of oscillating resonators for generating high-amplitude pressure waves,” *J. Acoust. Soc. Am.*, vol. 116, pp. 2814–2821, 2004.

[16] C. Luo, X. Y. Huang, and N. T. Nguyen, “Generation of shock-free pressure waves in shaped resonators by boundary driving,” *J. Acoust. Soc. Am.*, vol. 121, pp. 2515–2521, 2007.

[17] Q. Min, Q.-Y. Zhang, J.-J. Tian, Q.-B. Wang, and W.-Q. He, “A study on the dissonant standing-wave tube with variable section and its extremely nonlinear standing-wave field,” *Phys. Lett. A*, vol. 377, pp. 99–106, 2012.

[18] M. Červenka and M. Bednařík, “On the optimization of an acoustic resonator shape with respect to acoustic pressure amplitude,” *Acust. Acta Acust.*, vol. 99, pp. 183–191, 2013.

[19] M. Červenka, M. Šoltés, and M. Bednařík, “Optimal shaping of acoustic resonators for the generation of high-amplitude standing waves,” *J. Acoust. Soc. Am.*, vol. 136, pp. 1003–1012, 2014.

[20] M. Bednařík and M. Červenka, “Equations for description of nonlinear standing waves in constant-cross-sectioned resonators,” *J. Acoust. Soc. Am.*, vol. 135, pp. EL134–EL139, 2014.

[21] M. Červenka and M. Bednařík, “Acoustic particle displacement resonator,” *Appl. Acoust.*, vol. 99, pp. 155–160, 2015.

[22] A. D. Pierce, *Acoustics: An Introduction to its Physical Principles and Applications.* Melville: Acoustical Society of America, 1994.

[23] D. T. Blackstock, *Fundamentals of Physical Acoustics.* New York: Wiley-Interscience, 2000.

[24] L. L. Beranek and T. J. Mellow, *Acoustics: Sound Fields and Transducers.* Oxford: Academic Press, 2012.

[25] D. Zwillinger, *Handbook of Differential Equations.* San Diego: Academic Press, 1997.

[26] A. E. Eiben and J. E. Smith, *Introduction to Evolutionary Computing.* Berlin: Springer, 2010.

[27] W. H. Press, S. A. Teukolsky, W. T. Vetterling, and B. P. Flannery, *Numerical Recipes 3rd Edition: The Art of Scientific Computing.* Cambridge: Cambridge University Press, 2007.

[28] I. E. Idelchik, *Handbook of Hydraulic Resistance.* Jaico Publishing House, 2005.

[29] G. W. Swift, *Thermoacoustics: A unifying perspective for some engines and refrigerators.* Melville, New York: Acoustical Society of America, 2002.

[30] S. Backhaus and G. W. Swift, "A thermoacoustic-Stirling heat engine: Detailed study," *J. Acoust. Soc. Am.*, vol. 107, no. 6, pp. 3148–3166, 2000.

[31] F. J. Fahy, *Sound Intensity.* London: Elsevier Applied Science, 1989.

[32] W. L. Nyborg, "Acoustic streaming," in *Physical Acoustics, Vo1. lI, Part B* (W. P. Mason, ed.), pp. 265–331, New York: Academic Press, 1965.

[33] O. V. Rudenko and S. I. Soluyan, *Theoretical Foundations of Nonlinear Acoustics.* New York: Consultants Bureau, 1977.

[34] W. L. Nyborg, "Acoustic streaming," in *Nonlinear Acoustics* (M. F. Hamilton and D. T. Blackstock, eds.), pp. 207–231, San Diego: Academic Press, 1998.

[35] S. Boluriaan and P. J. Morris, "Acoustic streaming: from Rayleigh to today," *Int. J. Aeroacoust.*, vol. 2, no. 3+4, pp. 255–292, 2003.

[36] G. Mozurkewich, "Heat transport by acoustic streaming within a cylindrical resonator," *Appl. Acoust.*, vol. 63, pp. 713–735, 2002.

[37] R. Green, M. Ohlin, and M. Wiklund, "Applications of acoustic streaming," in *Microscale Acoustofluidics* (T. Laurell and A. Lenshof, eds.), pp. 312–336, Cambridge: The Royal Society of Chemistry, 2015.

[38] M. Faraday, "On a peculiar class of acoustical figures; and on certain forms assumed by groups of particles upon vibrating elastic surfaces," *Philos. Trans. R. Soc. Lond.*, vol. 121, pp. 299—340, 1831.

[39] V. Dvořák, "Ueber die Entstehungsweise der Kundt'schen Staubfiguren," *Ann. Physik*, vol. 227, no. 4, pp. 634–639, 1874.

[40] L. Rayleigh, "On the circulation of air observed in Kundt's tubes, and on some allied acoustical problems," *Philos. Trans. R. Soc. Lond.*, vol. 175, pp. 1–21, 1884.

[41] H. Schlichting, "Berechnung ebener periodischer Grenzschichtströmungen," *Physikalische Zeitschrift*, vol. 33, no. 8, pp. 327–335, 1932.

[42] V. K. Schuster and W. Matz, "Über stationare Strömungen im Kundtschen Rohr," *Akust. Zeitschrift*, vol. 5, pp. 349–352, 1940.

[43] R. Waxler, "Stationary velocity and pressure gradients in a thermoacoustic stack," *J. Acoust. Soc. Am.*, vol. 109, pp. 2739–2750, 2001.

[44] H. Bailliet, V. Gusev, R. Raspet, and R. A. Hiller, "Acoustic streaming in closed thermoacoustic devices," *J. Acoust. Soc. Am.*, vol. 110, pp. 1808–1821, 2001.

[45] M. F. Hamilton, Y. A. Ilinskii, and E. A. Zabolotskaya, "Acoustic streaming generated by standing waves in two-dimensional channels of arbitrary width," *J. Acoust. Soc. Am.*, vol. 113, pp. 153–160, 2003.

[46] M. F. Hamilton, Y. A. Ilinskii, and E. A. Zabolotskaya, "Thermal effects on acoustic streaming in standing waves," *J. Acoust. Soc. Am.*, vol. 114, pp. 3092–3101, 2003.

[47] L. Menguy and J. Gilbert, “Non-linear acoustic streaming accompanying a plane stationary wave in a guide,” *Acust. Acta Acust.*, vol. 86, pp. 249–259, 2000.

[48] M. K. Aktas and B. Farouk, “Numerical simulation of acoustic streaming generated by finite-amplitude resonant oscillations in an enclosure,” *J. Acoust. Soc. Am.*, vol. 116, pp. 2822–2831, 2004.

[49] V. Daru, D. Baltean-Carlès, C. Weisman, P. Debesse, and G. Gandikota, “Two-dimensional numerical simulations of nonlinear acoustic streaming in standing waves,” *Wave Motion*, vol. 50, pp. 955–963, 2013.

[50] I. Reyt, V. Daru, H. Bailliet, S. Moreau, J.-C. Valière, D. Baltean-Carlès, and C. Weisman, “Fast acoustic streaming in standing waves: Generation of an additional outer streaming cell,” *J. Acoust. Soc. Am.*, vol. 134, pp. 1791–1801, 2013.

[51] M. W. Thompson, A. A. Atchley, and M. J. Maccarone, “Influences of a temperature gradient and fluid inertia on acoustic streaming in a standing wave,” *J. Acoust. Soc. Am.*, vol. 117, pp. 1839–1849, 2005.

[52] S. Moreau, H. Bailliet, and J.-C. Valièere, “Measurements of inner and outer streaming vortices in a standing waveguide using Laser Doppler Velocimetry,” *J. Acoust. Soc. Am.*, vol. 123, pp. 640–647, 2008.

[53] I. Reyt, H. Bailliet, and J.-C. Valière, “Experimental investigation of acoustic streaming in a cylindrical wave guide up to high streaming Reynolds numbers,” *J. Acoust. Soc. Am.*, vol. 135, pp. 27–37, 2014.

[54] V. Daru, I. Reyt, H. Bailliet, C. Weisman, and D. Baltean-Carlès, “Acoustic and streaming velocity components in a resonant waveguide at high acoustic levels,” *J. Acoust. Soc. Am.*, vol. 141, pp. 563–574, 2017.

[55] M. Nabavi, K. Siddiqui, and J. Dargahi, “Analysis of regular and irregular acoustic streaming patterns in a rectangular enclosure,” *Wave Motion*, vol. 46, pp. 312–322, 2009.

[56] P. Debesse, D. Baltean-Carlès, F. Lusseyran, and M.-X.François, “Oscillating and streaming flow identification in a thermoacoustic resonator, from undersampled PIV measurements,” *Meas. Sci. Technol.*, vol. 25, p. 025005, 2014.

[57] E. S. Ellier, W. Kdous, Y. Bailly, L. Girardot, D. Ramel, and P. Nika, “Acoustic streaming measurements in standing wave resonator using Particle Image Velocimetry,” *Wave Motion*, vol. 51, pp. 1288–1297, 2014.

[58] N. Rott, “The influence of heat conduction on acoustic streaming,” *Z. Angew. Math. Phys.*, vol. 25, pp. 417–421, 1974.

[59] V. Daru, C. Weisman, D. Baltean-Carlès, I. Reyt, and H. Bailliet, “Inertial effects on acoustic Rayleigh streaming flow: Transient and established regimes,” *Wave Motion*, vol. 74, pp. 1–17, 2017.

[60] M. Červenka and M. Bednařík, “Variety of acoustic streaming in 2D resonant channels,” *Wave Motion*, vol. 66, pp. 21–30, 2016.

[61] M. Červenka and M. Bednařík, "Effect of inhomogeneous temperature fields on acoustic streaming structures in resonators," *J. Acoust. Soc. Am.*, vol. 141, no. 6, pp. 4418–4426, 2017.

[62] M. Červenka and M. Bednařík, "Numerical study of the influence of the convective heat transport on acoustic streaming in a standing wave," *J. Acoust. Soc. Am.*, vol. 143, no. 2, pp. 727–734, 2018.

[63] B. Lautrup, *Physics of Continuous Matter, Second Edition: Exotic and Everyday Phenomena in the Macroscopic World.* Boca Raton: CRC Pres, 2011.

[64] A. Boufermel, N. Joly, P. Lotton, M. Amari, and V. Gusev, "Velocity of mass transport to model acoustic streaming: Numerical application to annular resonators," *Acust. Acta Acust.*, vol. 97, pp. 219–227, 2011.

[65] *Acoustics Module User's Guide, COMSOL Multiphysics® v. 5.3a.* Stockholm, Sweden: COMSOL AB, 2017.

[66] N. Sugimoto and K. Tsujimoto, "Amplification of energy flux of nonlinear acoustic waves in a gas-filled tube under an axial temperature gradient," *J.Fluid Mech.*, vol. 456, pp. 377–409, 2002.

[67] P. Merkli and H. Thomann, "Thermoacoustic effects in a resonance tube," *J.Fluid Mech.*, vol. 70, pp. 161–177, 1975.

[68] P. J. Westervelt, "Parametric acoustic array," *J. Acoust. Soc. Am.*, vol. 35, pp. 535–537, 1963.

[69] W.-S. Gan, J. Yang, and T. Kamakura, "A review of parametric acoustic array in air," *Appl. Acoust.*, vol. 73, pp. 1211–1219, 2012.

[70] M. Yoneyama and J. Fujimoto, "The audio spotlight: An application of nonlinear interaction of sound waves to a new type of loudspeaker design," *J. Acoust. Soc. Am.*, vol. 73, pp. 1532–1536, 1983.

[71] F. J. Pompei, "The use of airborne ultrasonics for generating audible sound beams," *J. Audio Eng. Soc.*, vol. 47, pp. 726–731, 1999.

[72] U. Sayin, P. Artís, and O. Guascha, "Realization of an omnidirectional source of sound using parametric loudspeakers," *J. Acoust. Soc. Am.*, vol. 134, pp. 1899–1907, 2013.

[73] N. Tanaka and M. Tanaka, "Active noise control using a steerable parametric array loudspeaker," *J. Acoust. Soc. Am.*, vol. 127, pp. 3526–3537, 2010.

[74] K. Tanaka, C. Shi, and Y. Kajikawa, "Binaural active noise control using parametric array loudspeakers," *Appl. Acoust.*, vol. 116, pp. 170–176, 2017.

[75] M. Arnela, O. Guasch, P. Sánchez-Martín, J. Camps, R. M. Alsina-Pages, and C. Martínez-Suquía, "Construction of an omnidirectional parametric loudspeaker consisting in a spherical distribution of ultrasound transducers," *Sensors*, vol. 18, p. 4317, 2018.

[76] T. G. Muir and J. G. Willette, “Parametric acoustic transmitting arrays,” *J. Acoust. Soc. Am.*, vol. 52, pp. 1481–1486, 1972.

[77] G. S. Garrett, J. N. Tjøta, and S. Tjøta, “Nearfield of a large acoustic transducer, Part II: Parametric radiation,” *J. Acoust. Soc. Am.*, vol. 74, pp. 1013–1020, 1983.

[78] T. Kamakura, N. Hamada, K. Aoki, and Y. Kumamoto, “Nonlinearly generated spectral components in the nearfield of a directive sound source,” *J. Acoust. Soc. Am.*, vol. 85, pp. 2331–2337, 1989.

[79] D. Ding, “A simplified algorithm for the second-order sound fields,” *J. Acoust. Soc. Am.*, vol. 108, pp. 2759–2764, 2000.

[80] J. Yang, K. Sha, W. S. Gan, and J. Tian, “Nonlinear wave propagation for a parametric loudspeaker,” *EICE Trans Fundamentals*, vol. E87A, pp. 2395–2400, 204.

[81] H. Nomura, C. M. Hedberg, and T. Kamakura, “Numerical simulation of parametric sound generation and its application to length-limited sound beam,” *Appl. Acoust.*, vol. 73, pp. 1231–1238, 2012.

[82] M. Červenka and M. Bednařík, “Non-paraxial model for a parametric acoustic array,” *J. Acoust. Soc. Am.*, vol. 134, pp. 933–938, 2013.

[83] M. Červenka and M. Bednařík, “On the structure of multi-Gaussian beam expansion coefficients,” *Acust. Acta Acust.*, vol. 101, pp. 15–23, 2015.

[84] M. Červenka and M. Bednařík, “A versatile computational approach for the numerical modelling of parametric acoustic array,” *J. Acoust. Soc. Am.*, vol. 146, pp. 2163–2169, 2019.

[85] S. I. Aanonsen, T. Barkve, J. N. Tjøtta, and S. Tjøtta, “Distortion and harmonic generation in the nearfield of a finite amplitude sound beam,” *J. Acoust. Soc. Am.*, vol. 75, pp. 749–768, 1984.

[86] V. P. Kuznetsov, “Equation of nonlinear acoustics,” *Sov. Phys. Acoust.*, vol. 16, pp. 467–468, 1970.

[87] P. M. Morse and K. U. Ingard, *Theoretical Acoustics*. New York: McGraw-Hill, 1968.

[88] J. W. Goodman, *Introduction to Fourier Optics*. New York: McGraw-Hill, 1996.

[89] J. J. Wen and M. A. Breazeale, “A diffraction beam field expressed as the superposition of Gaussian beams,” *J. Acoust. Soc. Am.*, vol. 83, pp. 1752–1756, 1988.

[90] M. Červenka and M. Bednařík, “Calculation of an axial temperature distribution using the reflection coefficient of an acoustic wave,” *J. Acoust. Soc. Am.*, vol. 138, pp. EL359–EL364, 2015.

[91] M. Červenka and M. Bednařík, “Acoustic bandpass filters employing shaped resonators,” *J. Sound Vib.*, vol. 383, pp. 76–88, 2016.

[92] M. Červenka and M. Bednařík, “Optimized reactive silencers with narrow side-branch tubes,” *J. Acoust. Soc. Am.*, vol. 144, pp. 2015–2021, 2018.

[93] M. Červenka, M. Bednařík, and J.-P. Groby, “Optimized reactive silencers composed of closely-spaced elongated side-branch resonators,” *J. Acoust. Soc. Am.*, vol. 145, pp. 2210–2220, 2019.

[94] M. Červenka and M. Bednařík, “Optimized compact wideband reactive silencers with annular resonators,” *J. Sound Vib.*, vol. 484, p. 115497, 2020.

[95] T. G. Zielinski, R. Venegas, C. Perrot, M. Červenka, F. Chevillotte, and K. Attenborough, “Benchmarks for microstructure-based modelling of sound absorbing rigid-frame porous media,” *J. Sound Vib.*, vol. 483, p. 115441, 2020.

Appendix A

Included author's publications

Below is the list of selected author's publications related to the thesis.

[1] Červenka, M., Bednařík, M., On the optimization of an acoustic resonator shape with respect to acoustic pressure amplitude, Acust. Acta Acust. 99(2), 183-191, (2013) – Appendix A.1.

[2] Červenka, M., Šoltés, M., Bednařík, M., Optimal shaping of acoustic resonators for the generation of high-amplitude standing waves, J. Acoust. Soc. Am. 136(3), 1003-1012, (2014) – Appendix A.2.

[3] Bednařík, M., Červenka, M., Equations for description of nonlinear standing waves in constant-cross-sectioned resonators, J. Acoust. Soc. Am. 135(3), EL134-EL139, (2014) – Appendix A.3.

[4] Červenka, M., Bednařík, M., Acoustic particle displacement resonator, Applied Acoustics 99, 155-160, (2015) – Appendix A.4.

[5] Bálek, R., Červenka, M., Pekárek, S., Acoustic field effects on a negative corona discharge, Plasma Sources Sci. T. 23(3), 1-9, (2014) – Appendix A.5.

[6] Červenka, M., Bednařík, M., Variety of acoustic streaming in 2D resonant channels, Wave Motion 66, 21-30, (2016) – Appendix A.6.

[7] Červenka, M., Bednařík, M., Effect of inhomogeneous temperature fields on acoustic streaming structures in resonators, J. Acoust. Soc. Am. 141(6), 4418-4426, (2017) – Appendix A.7.

[8] Červenka, M., Bednařík, M., Numerical study of the influence of the convective heat transport on acoustic streaming in a standing wave, J. Acoust. Soc. Am. 143(2), 727-734, (2018) – Appendix A.8.

[9] Červenka, M., Bednařík, M., Non-paraxial model for a parametric acoustic array, J. Acoust. Soc. Am. 134(2), 933-938, (2013) – Appendix A.9.

[10] Červenka, M., Bednařík, M., On the structure of multi-Gaussian beam expansion coefficients, Acust. Acta Acust. 101(1), 15-23, (2015) – Appendix A.10.

[11] Červenka, M., Bednařík, M., A versatile computational approach for the numerical modelling of parametric acoustic array, J. Acoust. Soc. Am. 146(4), 2163-2169, (2019) – Appendix A.11.

A.1 On the optimization of an acoustic resonator shape with respect to acoustic pressure amplitude

Červenka, M., Bednařík, M., On the optimization of an acoustic resonator shape with respect to acoustic pressure amplitude, Acta Acustica United with Acustica 99(2), 183-191, (2013).

ACTA ACUSTICA UNITED WITH ACUSTICA
Vol. 99 (2013) 183 – 191

DOI 10.3813/AAA.918601

On the Optimization of an Acoustic Resonator Shape with Respect to Acoustic Pressure Amplitude

Milan Cervenka, Michal Bednarik
Czech Technical University in Prague, Faculty of Electrical Engineering, Technicka 2, 166 27 Prague 6, Czech Republic. [milan.cervenka, bednarik]@fel.cvut.cz

Summary
This paper deals with the optimization of an acoustic resonator shape in order to maximize acoustic pressure amplitude. The resonator shape is described using the cubic splines which interconnect a set of control points whose positions are determined using an evolutionary algorithm. As an objective function, numerical solution of modified Webster's equation is used. Numerical results show that the optimized resonators are rather simple-shaped, they differ for a piston- or shaker-driving and the fundamental resonance frequencies are lower than in the case of a constant-cross-section resonator. A nonlinear theory is used for assessment of finite-amplitude fields in the optimized resonators.

PACS no. 43.20.Ks, 43.25.Gf

1. Introduction

Many studies so far published have shown that it is possible to generate standing acoustic waves of such high amplitudes which enable their utilization in practical applications.

Gaitan and Atchley [1] showed that introduction of the cross-section variability in a piston-driven resonator can significantly reduce energy transfer from the fundamental to the higher modes, prevent shock-formation and increase amplitude of the standing wave.

Lawrenson *et al.* [2] presented in their experimental paper concept of Resonant Macrosonic Synthesis (RMS) whereby they obtained acoustic pressure amplitude more than an order larger than it had been possible previously. The concept is based on so-called dissonant resonators, whose varying-cross-section cavities don't have the higher eigenfrequencies coincident with the harmonics of the nonlinearly distorted waveform which results in the suppression of a shock-wave formation. The authors demonstrated a strong dependence of obtained maximum amplitude on the resonator shape (cylindrical, conical, horn-cone hybrid and bulb).

Ilinskii *et al.* [3] presented in their theoretical paper a quasi-one-dimensional model equation expressed in terms of the velocity potential for description of high-amplitude standing waves in axi-symmetric but otherwise arbitrarily shaped acoustic resonators. The model comprises nonlinearity, viscous bulk attenuation and entire-resonator driving by an external force (shaker-driving). A numerical algorithm was proposed for integration of the model equation in the frequency domain, the numerical simulations were conducted in the case of a cylindrical, conical and bulb-shaped resonator. The numerical results were in good agreement with the experimental ones. The model was subsequently fulfilled [4] to account for energy losses in the boundary-layer and the losses due to acoustically generated turbulence.

Hamilton *et al.* [5] investigated theoretically dependence of the resonance frequencies of the varying-cross-sectioned resonators and their nonlinear shifts.

Chun and Kim [6] investigated numerically the influence of an entirely-driven resonant cavity shape on the compression ratio (ratio of the maximum and minimum pressure attained at one point in the resonator cavity during one period) using a quasi-one-dimensional model equation based on the conservation laws integrated in the time-domain using a high-order finite-difference scheme. From the several simple shapes (cylindrical, conical, 1/2-cosine and 3/4-cosine) studied, the 1/2-cosine offered the best performance.

Erickson and Zinn [7] developed a Galerkin-method-based algorithm for time-domain integration of the model equation proposed in Ilinskii's *et. al.* paper [3]. They also showed that the exponentially shaped resonator's compression ratio strongly and non-trivially depends on its geometrical parameters.

Luo *et al.* [8] studied theoretically effect of the resonator shape and dimension on its compression ratio in the case of axi-symmetric and low-aspect-ratio exponential geometry, observing its decrease with decreasing resonator length and smaller-radius-to-length ratio.

Received 1 August 2012,
accepted 17 December 2012.

Li *et al.* [9] optimized by means of numerical simulations the parameters of simple-shaped resonator cavities in order to maximize the compression ratio. They achieved the value of 48 in the case of an optimized horn-cone shape.

Luo *et al.* [10] conducted numerical experiments in order to compare piston- or entire-driving of exponentially shaped cavity finding similar results.

In all the above-mentioned papers, the same approach was utilized, i.e., the resonator shapes were described using a smooth elementary function with fixed or adjustable (Erickson and Zinn [7], Li *et al.* [9]) parameters, e.g., all the resonator cavities were non-symmetrical, wide at one end and narrow at the other one, where the maximum pressure (or compression ratio) were obtained.

In this paper, a more general approach is used as a starting point. The axi-symmetric resonator shapes are not restricted to a-few-parameter elementary functions, they are rather parametrized using a set of control points which are interconnected using the cubic splines.

The appropriate shapes are determined in order that acoustic pressure at one resonator's end were maximized either in the case of a piston- or shaker-driving. Even if the optimization is performed using a linear theory, the results are verified using a nonlinear model.

Section 2 deals with description of the linearized model equations describing the acoustic field in an axi-symmetric resonator and their solutions. The optimization algorithm is described in section 3. The numerical results are then presented in section 4.

2. Description of Acoustic Field in a Resonator Using Linear Theory

2.1. Model Equation

For description of the acoustic field in a variable-cross-section resonator driven by an external (inertial) force, we can issue from the quasi-one-dimensional model equation derived in [3], which has the form

$$\begin{aligned}&\frac{c_0^2}{r^2}\frac{\partial}{\partial x}\left(r^2\frac{\partial\varphi}{\partial x}\right)-\frac{\partial^2\varphi}{\partial t^2}+\frac{\delta}{r^2}\frac{\partial^2}{\partial x\partial t}\left(r^2\frac{\partial\varphi}{\partial x}\right)=\\ &\quad x\frac{\mathrm{d}a_\mathrm{s}}{\mathrm{d}t}+a_\mathrm{s}(t)\frac{\partial\varphi}{\partial x}+\frac{\gamma-1}{r^2}a_\mathrm{s}(t)x\frac{\partial}{\partial x}\left(r^2\frac{\partial\varphi}{\partial x}\right)\\ &\quad+2\frac{\partial\varphi}{\partial x}\frac{\partial^2\varphi}{\partial x\partial t}+\frac{\gamma-1}{r^2}\frac{\partial\varphi}{\partial t}\frac{\partial}{\partial x}\left(r^2\frac{\partial\varphi}{\partial x}\right)\qquad(1)\\ &\quad+\frac{1}{3}\frac{\partial}{\partial x}\left(\frac{\partial\varphi}{\partial x}\right)^3+\frac{\gamma-1}{2r^2}\left(\frac{\partial\varphi}{\partial x}\right)^2\frac{\partial}{\partial x}\left(r^2\frac{\partial\varphi}{\partial x}\right),\end{aligned}$$

where φ is the velocity potential, x is the spatial coordinate along the resonator cavity, t is time, $r = r(x)$ is the varying resonator radius, c_0 is small-signal speed of sound, $a_\mathrm{s} = a_\mathrm{s}(t)$ is the driving acceleration (the acceleration with which the entire resonator cavity attached to a shaker oscillates), $\delta = (\zeta + 4\eta/3)/\rho_0$ is an attenuation coefficient, where ζ and η are bulk and shear viscosities, respectively, ρ_0 is ambient fluid density and γ is the Poisson's constant.

After linearization, equation (1) reduces into the form

$$\begin{aligned}&\frac{c_0^2}{r^2}\frac{\partial}{\partial x}\left(r^2\frac{\partial\varphi}{\partial x}\right)-\frac{\partial^2\varphi}{\partial t^2}=\\ &\quad-\frac{\delta}{r^2}\frac{\partial^2}{\partial t\partial x}\left(r^2\frac{\partial\varphi}{\partial x}\right)+\frac{\mathrm{d}a_\mathrm{s}}{\mathrm{d}t}x.\qquad(2)\end{aligned}$$

Left side of equation (2) represents the Webster's equation. In the first approximation, an acoustic pressure p' can be calculated from the velocity potential using formula

$$p'=-\rho_0\frac{\partial\varphi}{\partial t}-\rho_0 a_\mathrm{s}x.\qquad(3)$$

For the sake of the subsequent analysis, it is convenient to introduce dimensionless variables, e.g. in form

$$\begin{aligned}&X=\frac{x}{l},\quad T=\omega t,\quad R=\frac{r}{l},\\ &A=\frac{a}{l\omega_0^2},\quad \Phi=\frac{\varphi}{l^2\omega_0},\quad P=\frac{p'}{\pi^2\rho_0c_0^2},\end{aligned}$$

where l is the resonator length, ω is the driving frequency and $\omega_0 = \pi c_0/l$ is the first eigenfrequency for a constant-cross-section resonator. Using these new variables, equations (2) and (3) have the form

$$\begin{aligned}&\frac{1}{\pi^2R^2}\frac{\partial}{\partial X}\left(R^2\frac{\partial\Phi}{\partial X}\right)-\Omega^2\frac{\partial^2\Phi}{\partial T^2}=\\ &\quad-\frac{G\Omega}{\pi^3R^2}\frac{\partial^2}{\partial T\partial X}\left(R^2\frac{\partial\Phi}{\partial X}\right)+D_\mathrm{s},\qquad(4)\end{aligned}$$

where

$$D_\mathrm{s}=\Omega\frac{\mathrm{d}A_\mathrm{s}}{\mathrm{d}T}X,$$

and

$$P=-\Omega\frac{\partial\Phi}{\partial T}-A_\mathrm{s}X,\qquad(5)$$

where $\Omega = \omega/\omega_0$ and $G = \pi\omega_0\delta/c_0^2$.

As it is assumed that the resonator cavity has rigid walls and end caps, the boundary conditions for the velocity potential have form

$$V(0,T)=\left.\frac{\partial\Phi}{\partial X}\right|_{X=0}=V(1,T)=\left.\frac{\partial\Phi}{\partial X}\right|_{X=1}=0.\qquad(6)$$

If the resonator cavity is driven using a vibrating piston positioned at $X = 1$ (instead of entire-driving) having dimensionless velocity $U_\mathrm{p} = U_\mathrm{p}(T)$, it holds true that in equation (4) $D_\mathrm{s} = 0$ and the inhomogeneous boundary conditions have the form[1]

$$\begin{aligned}&V(0,T)=\left.\frac{\partial\Phi}{\partial X}\right|_{X=0}=0,\\ &V(1,T)=\left.\frac{\partial\Phi}{\partial X}\right|_{X=1}=U_\mathrm{p}.\qquad(7)\end{aligned}$$

---

[1] Within the scope of the linear approximation, it is assumed that the velocity $U_\mathrm{p}(T)$ has such a small amplitude that the position of the piston can be assumed to be constant [$X_\mathrm{p}(T) = 1$].

It is further advantageous to homogenize the boundary conditions (7) introducing new variable $\Psi(X,T)$ obeying relation

$$\Phi = \Psi + \frac{X^2}{2} U_\mathrm{p} \quad \Rightarrow \quad V = \frac{\partial \Phi}{\partial X} = \frac{\partial \Psi}{\partial X} + X U_\mathrm{p} \tag{8}$$

Substituting the relations (8) into equation (4) results in

$$\begin{aligned} &\frac{1}{\pi^2 R^2}\frac{\partial}{\partial X}\left(R^2 \frac{\partial \Psi}{\partial X}\right) - \Omega^2 \frac{\partial^2 \Psi}{\partial T^2} = \\ &\quad - \frac{G\Omega}{\pi^3 R^2}\frac{\partial^2}{\partial T \partial X}\left(R^2 \frac{\partial \Psi}{\partial X}\right) + D_\mathrm{p}, \end{aligned} \tag{9}$$

where

$$\begin{aligned} D_\mathrm{p} &= -\frac{1}{\pi^2 R^2}\frac{\mathrm{d}(XR^2)}{\mathrm{d}X} U_\mathrm{p} + \Omega^2 \frac{X^2}{2}\frac{\mathrm{d}^2 U_\mathrm{p}}{\mathrm{d}T^2} \\ &\quad - \frac{G\Omega}{\pi^3 R^2}\frac{\mathrm{d}(XR^2)}{\mathrm{d}X}\frac{\mathrm{d}U_\mathrm{p}}{\mathrm{d}T} \\ &\approx -\left(1 + \frac{2X}{R}\frac{\mathrm{d}R}{\mathrm{d}X}\right)\frac{U_\mathrm{p}}{\pi^2} + \Omega^2 \frac{X^2}{2}\frac{\mathrm{d}^2 U_\mathrm{p}}{\mathrm{d}T^2}, \end{aligned} \tag{10}$$

because $G \ll 1$. The boundary conditions for equation (9) then have the form

$$\left.\frac{\partial \Psi}{\partial X}\right|_{X=0} = \left.\frac{\partial \Psi}{\partial X}\right|_{X=1} = 0. \tag{11}$$

If the driving acceleration is harmonic, having the form $A_\mathrm{s}(T) = A_\mathrm{s0}\cos(T) = \Re\left[A_\mathrm{s0}\exp(\mathrm{i}T)\right]$ and we are only looking for the stationary solutions $\Phi(X,T) = \Re\left[\tilde{\Phi}(X)\exp(\mathrm{i}T)\right]$, then equation (4) can be rewritten into the form

$$\begin{aligned} &\frac{1}{\pi^2 R^2}\frac{\mathrm{d}}{\mathrm{d}X}\left(R^2 \frac{\mathrm{d}\tilde{\Phi}}{\mathrm{d}X}\right) + \Omega^2 \tilde{\Phi} = \\ &\quad - \frac{\mathrm{i}G\Omega}{\pi^3 R^2}\frac{\mathrm{d}}{\mathrm{d}X}\left(R^2 \frac{\mathrm{d}\tilde{\Phi}}{\mathrm{d}X}\right) + \mathrm{i}\Omega A_\mathrm{s0} X. \end{aligned} \tag{12}$$

Similarly, equation (9) can be recast into the form

$$\begin{aligned} &\frac{1}{\pi^2 R^2}\frac{\mathrm{d}}{\mathrm{d}X}\left(R^2 \frac{\mathrm{d}\tilde{\Psi}}{\mathrm{d}X}\right) + \Omega^2 \tilde{\Psi} = \\ &\quad - \frac{\mathrm{i}G\Omega}{\pi^3 R^2}\frac{\mathrm{d}}{\mathrm{d}X}\left(R^2 \frac{\mathrm{d}\tilde{\Psi}}{\mathrm{d}X}\right) \\ &\quad - \left(1 + \frac{2X}{R}\frac{\mathrm{d}R}{\mathrm{d}X} + \pi^2\Omega^2\frac{X^2}{2}\right)\frac{U_\mathrm{p0}}{\pi^2}. \end{aligned} \tag{13}$$

2.2. Solution of the Model Equations

Equations (12) and (13) can be solved using the method of eigenfunction expansions [11]. Nontrivial solutions $\{F_k, k = 1, 2, \dots\}$ of equation (Sturm-Liouville problem)

$$\frac{1}{\pi^2 R^2}\frac{\mathrm{d}}{\mathrm{d}X}\left(R^2 \frac{\mathrm{d}F}{\mathrm{d}X}\right) + \Omega^2 F = 0 \tag{14}$$

with homogeneous boundary conditions

$$\left.\frac{\mathrm{d}F}{\mathrm{d}X}\right|_{X=0} = \left.\frac{\mathrm{d}F}{\mathrm{d}X}\right|_{X=1} = 0$$

exist for certain values (eigenfrequencies) $\{\Omega_k\}$. These eigenfunctions (eigenmodes) are orthogonal for individual eigenfrequencies Ω_k, which in this case means that

$$\left\langle F_k | F_j \right\rangle = \int_0^1 R^2(X) F_k(X) F_j(X)\,\mathrm{d}X = 0 \tag{15}$$

for $k \neq j$ and because the functions $\{F_k\}$ form a complete set, the solution of equation (12) can be written as

$$\tilde{\Phi}(X) = \sum_{k=1}^{\infty} \tilde{\alpha}_k F_k(X), \tag{16}$$

where $\tilde{\alpha}_k$ are complex coefficients. Substituting the above relation into equation (12) yields

$$\sum_{k=1}^{\infty}\left(\pi\Omega^2 - \pi\Omega_k^2 - \mathrm{i}G\Omega\Omega_k^2\right)\tilde{\alpha}_k F_k = \mathrm{i}\pi\Omega A_\mathrm{s0} X.$$

Multiplication of both the sides of the above equation by function $R^2 F_j$, integration in limits $\langle 0, 1\rangle$ with respect to X and utilization of the orthogonality relation yields

$$\tilde{\alpha}_j = \frac{\mathrm{i}\pi\Omega A_\mathrm{s0}}{\pi\Omega^2 - \pi\Omega_j^2 - \mathrm{i}G\Omega\Omega_j^2}\frac{\langle X | F_j\rangle}{\langle F_j | F_j\rangle}. \tag{17}$$

Substitution of equation (17) into equation (16) then results in the solution of equation (12) in the form

$$\tilde{\Phi}(X) = \mathrm{i}\pi\Omega A_\mathrm{s0}\sum_{j=1}^{\infty}\frac{\langle X | F_j\rangle F_j(X)}{(\pi\Omega^2 - \pi\Omega_j^2 - \mathrm{i}G\Omega\Omega_j^2)\langle F_j | F_j\rangle}. \tag{18}$$

Because $G \ll 1$, for $\Omega = \Omega_j$ (at resonance) the result can be simplified as

$$\tilde{\Phi}(X, \Omega = \Omega_j) \approx -\frac{\pi A_\mathrm{s0}}{G\Omega_j^2}\frac{\langle X | F_j\rangle}{\langle F_j | F_j\rangle}F_j(X). \tag{19}$$

Application of the same procedure to equation (13) yields in

$$\begin{aligned} &\tilde{\Phi}(X) = \\ &\quad \frac{\mathrm{i}A_\mathrm{p0}}{\pi\Omega}\sum_{j=1}^{\infty}\frac{\langle 1 + 2X(\mathrm{d}R/\mathrm{d}X)/R + \pi^2\Omega^2X^2/2 | F_j\rangle F_j(X)}{(\pi\Omega^2 - \pi\Omega_j^2 - \mathrm{i}G\Omega\Omega_j^2)\langle F_j | F_j\rangle} \\ &\quad - \frac{\mathrm{i}A_\mathrm{p0}X^2}{2\Omega}, \end{aligned} \tag{20}$$

where $A_\mathrm{p0} = \mathrm{i}\Omega U_\mathrm{p0}$ is a dimensionless amplitude of acceleration of the driving piston. At the resonance, equation (20) reduces to

$$\begin{aligned} &\tilde{\Phi}(X, \Omega = \Omega_j) \approx \\ &\quad - \frac{A_\mathrm{p0}}{\pi G\Omega_j^4}\frac{\langle 1 + 2X(\mathrm{d}R/\mathrm{d}X)/R + \pi^2\Omega_j^2X^2/2 | F_j\rangle}{\langle F_j | F_j\rangle}F_j(X) \\ &\quad - \frac{\mathrm{i}A_\mathrm{p0}X^2}{2\Omega_j}. \end{aligned} \tag{21}$$

2.3. Finding the Eigenmodes and Eigenfrequencies

Nontrivial solutions of equation (14) are known in an analytical form for some functions $R(X)$ (constant, linear, exponential, ...), in the other cases, they can be looked for numerically [12]. The equation (14) can be rewritten into the form

$$\frac{\mathrm{d}F}{\mathrm{d}X} = \frac{W}{R^2}, \qquad \frac{\mathrm{d}W}{\mathrm{d}X} = -\pi^2\Omega^2 R^2 F \tag{22}$$

and integrated numerically [12] with initial conditions $\{F(0) = 1, W(0) = 0\}$. An eigenfrequency Ω_k is calculated numerically as a solution of the following equation

$$W(X = 1; \Omega_k) = 0, \qquad \Omega_k \in \langle \Omega_{\min}, \Omega_{\max} \rangle. \tag{23}$$

Once the eigenfrequency Ω_k is known, the corresponding eigenfunction F_k is also known, because it is the solution of equation (22) with the corresponding initial conditions and $\Omega = \Omega_k$.

3. Optimization of the Resonator Shape

3.1. Description of the Resonator Shape and Its Eligibility

So as not to restrict the resonator's shape to a specific predefined elementary function with only a few adjustable parameters, it is defined using N control points distributed regularly at positions

$$X_i = \frac{i}{N-1}, \qquad i = 0, 1, \ldots, N-1,$$

whose corresponding values $R(X_i) = R_i$ are found in predefined interval $R_i \in \langle R_{\min}, R_{\max} \rangle$.

The function $R(X)$ is obtained using the cubic-spline-interpolation of the control points (the function and its first and second derivatives are continuous) with zero derivatives at the ends of the interval. The values R_i are chosen in order that $R_{\min} \le R(X) \le R_{\max}$ for any $X \in \langle 0, 1 \rangle$.

With the resonator shape defined, an eigenfrequency Ω_k is looked for numerically in an interval $\langle \Omega_{\min}, \Omega_{\max} \rangle$ using equation (23). If there is not any solution found, the control-points set is rejected and a new set of values R_i is generated and the procedure repeats.

Once an eigenfrequency Ω_k is found, corresponding eigenmode $F_k(X)$ is also known as it is a solution of equations (22) for $\Omega = \Omega_k$. With use of this information, a suitable objective function can be evaluated for assessment of the resonator shape eligibility (quality).

As an objective function, the acoustic pressure amplitude at $X = 0$ is chosen. In the sake of a shaker-driven resonator we can, using equations (19) and (5), write

$$P_{\mathrm{s}0} = K_{\mathrm{s}} \frac{|A_{\mathrm{s}0}|}{G}, \text{ where } K_{\mathrm{s}} = \frac{\pi}{\Omega_k} \left| \frac{\langle X|F_k \rangle}{\langle F_k|F_k \rangle} F_k(0) \right|, \tag{24}$$

thus the resonator shape is searched for in order that the quantity K_{s} (which will be called in the following text as the *eligibility factor*) were maximized. In the case of a piston-driven resonator, we can similarly [using equations (21) and (5)] write

$$P_{\mathrm{p}0} = K_{\mathrm{p}} \frac{|A_{\mathrm{p}0}|}{G}, \tag{25}$$

$$K_{\mathrm{p}} = \frac{1}{\pi\Omega_k^3} \cdot \left| \frac{\langle 1 + 2X(\mathrm{d}R/\mathrm{d}X)/R + \pi^2\Omega_k^2 X^2/2|F_k \rangle}{\langle F_k|F_k \rangle} F_k(0) \right|.$$

Again, the resonator shape is searched for in order that the eligibility factor K_{p} were maximized.

The above-described procedure is schematically depicted in Figure 1.

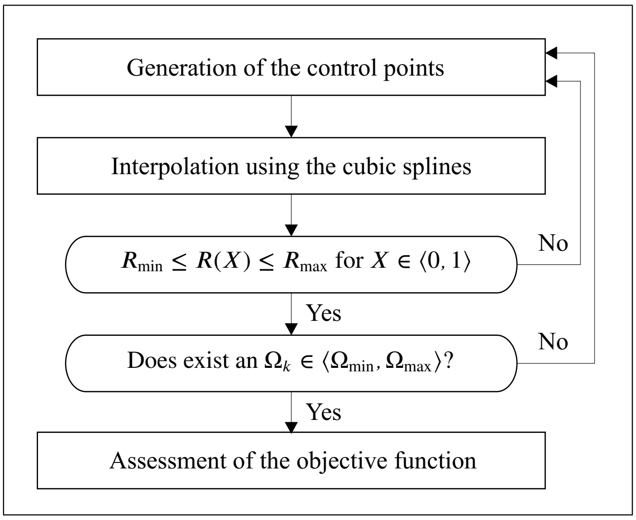

Figure 1. Flowchart of the algorithm for assessment of the resonator shape eligibility.

3.2. The Optimization Method

As the parameter search space for the objective function is many- (N-) dimensional ($\mathbb{R}^N$) and moreover, it is not continuous (some control-points sets lead to $R(X)$ that does not lie in pre-defined interval $\langle R_{\min}, R_{\max} \rangle$, possibly there is no eigenfrequency $\Omega_k \in \langle \Omega_{\min}, \Omega_{\max} \rangle$), a heuristic optimization method seems to have reasonable use for this type of problem. In this concrete case, a variant of Evolution Strategies [13] $(\mu + \lambda)$-ES was utilized.

The algorithm works as follows. Firstly, a population of M parents (randomly-generated sets of control points) is generated. For each member of the population, its objective function is evaluated according to the procedure described in Figure 1. Then, μ members with the highest values of the objective function are used as parents for the next generation. Each of the μ parents generates μ offspring by mutation (addition of a random number with Gaussian distribution and standard deviation σ (mutation strength) to individual R_i) using the formula

$$R_{i\mathrm{offspring}} = R_{i\mathrm{parent}} + \sigma \mathcal{N}_i(0, 1), \qquad i = 0, 1, \ldots, N-1.$$

These $\lambda = \mu \times \mu$ offspring together with their μ parents are supplemented with $M - \mu(\mu+1)$ randomly generated specimen, all these are evaluated and the cycle repeats. During the evolution, the mutation strength σ is slowly decreased in order to maintain the algorithm effective.

4. Numerical Results

4.1. Optimization of the Resonator Shape

Within the numerical experiments, the resonant cavities were parametrized using $N = 10$ control points. As it seems to be reasonable to suppose that for the fixed number of control points, the maximum resonator eligibility factor depends on the ratio of minimum and maximum radius, the resonant cavities were optimized for $R_{\min}/R_{\max} = 2/5$ and $1/5$, both, for shaker and piston driving.

In all the cases, parameters of the evolutionary algorithm were set as follows: $M = 500$, $\mu = 20$, evolution ran for 500 generations with the mutation strength decreasing from $\sigma_1 = 0.01$ to $\sigma_2 = 0.0001$. In all the cases, the algorithm was run repeatedly many rimes with reached dispersion of the maximized objective function in a level of fractions of one percent.

The numerical results are summarized in Table I and in Figures 2–7. For comparison, results for a constant-cross-section resonator and a conical resonator with $R_{\min}/R_{\max} = 1/9$ (similar to the one presented by Ilinskii *et al.* [3]) are included.

In the case of the constant-cross-section resonator, the eligibility factor for the shaker-driven resonator attains value of $K_s = 1.27$, the one for the piston driving $K_p = K_s/2$, which means, that with the same acceleration amplitude, the piston-driving provides half an acoustic pressure amplitude than in the case of the shaker-driving. Major disadvantage of this simple shape is the fact, that the higher eigenfrequencies are the integer multiples of the fundamental eigenfrequency which results in substantial nonlinear distortion in the high-amplitude fields and evolution of the shock-wave.

In the case of the conical resonator, see Table I, the factors K_s and K_p attain higher values than in the previous case and again, the shaker-driving is more effective. What is also important is the fact that the higher eigenfrequencies are not the integer multiples of the eigenfrequency fundamental, so that the nonlinearly generated higher harmonics are not coincident with the eigenfrequencies and thus they are suppressed. The shape of the resonator cavity and the first eigenmode are depicted in Figure 2.

The shapes of the acoustic resonators with $R_{\min}/R_{\max} = 2/5$ optimized for shaker- and piston-driving together with the corresponding eigenmodes are shown in Figure 3, the eligibility factors and eigenfrequencies are summarized in the second row of Table I. The optimum shapes were searched for in the frequency interval $\Omega \in \langle 0.2, 2.0\rangle$ in all the cases.

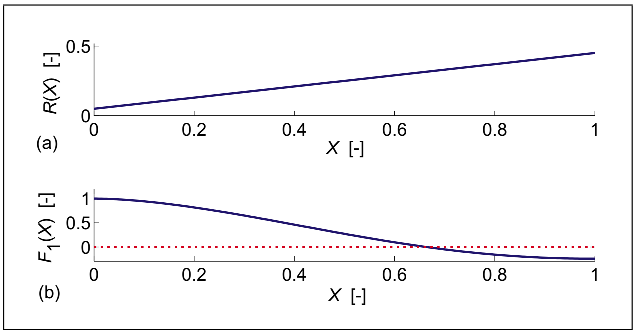

Figure 2. Conical cavity with $R_{\min}/R_{\max} = 1/9$, $\Omega_1 = 1.282$. (a) Cavity shape, (b) Eigenmode shape.

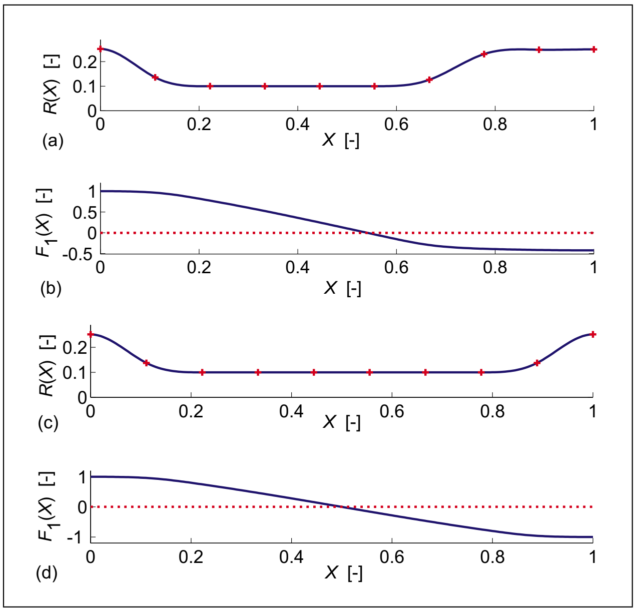

Figure 3. Optimized resonator shapes and corresponding eigenmodes for $R_{\min}/R_{\max} = 2/5$. (a,b): optimization for a shaker driving, $\Omega_1 = 0.606$; (c,d): optimization for a piston driving, $\Omega_1 = 0.642$. (a) Cavity shape (shaker-optimized), (b) Eigenmode shape (shaker-optimized), (c) Cavity shape (piston-optimized), (d) Eigenmode shape (piston-optimized).

In both the cases, the optimum resonator shapes are rather simple and similar, they have the maximum allowed radius at both the ends, the resonator optimized for a piston-driving is symmetric. Due to the frequency-dependence of the viscous attenuation, the optimum shapes are connected with very low fundamental eigenfrequencies ($\Omega_1 = 0.606$ in the shaker- and $\Omega_1 = 0.642$ in the piston-driving case). In both the cases, the higher eigenfrequencies are not integer multiples of the fundamental eigenfrequencies, which is important in the case of high-amplitude fields. The eligibility factors in Table I show that piston-driving is more effective even if the resonator is optimized for the shaker-driving, the maximum eligibility factor $K_p = 6.08$ in the case of piston-driven piston-optimized resonator, which is 9.6× more than in the case of a piston-driven cylindrical resonator.

Similarly, shapes of the acoustic resonators with $R_{\min}/R_{\max} = 1/5$ optimized for a shaker- or piston-driving together with the corresponding fundamental eigenmodes are shown in Figure 4, the eligibility factors and eigenfrequencies are summarized in the third row of Table I. Comparison of Figures 3 and 4 reveals that the optimum-resonator shapes are very similar as in the pre-

Table I. Parameters of individual resonant cavities.

Cylindrical, $R(X) = const.$ $K_\mathrm{s} = 1.27,\ K_\mathrm{p} = K_\mathrm{s}/2,\ \Omega_i = 1, 2, 3, 4, 5, \ldots$	Conical, $R_\mathrm{min}/R_\mathrm{max} = 1/9$ $K_\mathrm{s} = 1.77,\ K_\mathrm{p} = 1.14,\ \Omega_i = 1.28, 2.23, 3.19, 4.15, 5.13, \ldots$
Opt. for shaker, $R_\mathrm{min}/R_\mathrm{max} = 2/5$ $K_\mathrm{s} = 2.98,\ K_\mathrm{p} = 4.09,\ \Omega_i = 0.61, 1.90, 3.14, 3.90, 5.05, \ldots$	Opt. for piston, $R_\mathrm{min}/R_\mathrm{max} = 2/5$ $K_\mathrm{s} = 2.14,\ K_\mathrm{p} = 6.08,\ \Omega_i = 0.64, 1.61, 2.75, 3.93, 5.07, \ldots$
Opt. for shaker, $R_\mathrm{min}/R_\mathrm{max} = 1/5$ $K_\mathrm{s} = 5.46,\ K_\mathrm{p} = 20.43,\ \Omega_i = 0.36, 1.95, 3.43, 3.96, 5.41, \ldots$	Opt. for piston, $R_\mathrm{min}/R_\mathrm{max} = 1/5$ $K_\mathrm{s} = 3.69,\ K_\mathrm{p} = 38.38,\ \Omega_i = 0.38, 1.48, 2.78, 4.08, 5.33, \ldots$
Opt. for shaker, $R_\mathrm{min}/R_\mathrm{max} = 2/5, \Omega_1 = 1$ $K_\mathrm{s} = 2.27,\ K_\mathrm{p} = 1.15,\ \Omega_i = 1.00, 1.82, 3.03, 3.90, 4.99, \ldots$	Opt. for piston, $R_\mathrm{min}/R_\mathrm{max} = 2/5, \Omega_1 = 1$ $K_\mathrm{s} = 1.68,\ K_\mathrm{p} = 2.85,\ \Omega_i = 1.00, 1.50, 3.10, 3.58, 5.12, \ldots$
Opt. for shaker, $R_\mathrm{min}/R_\mathrm{max} = 1/5, \Omega_1 = 1$ $K_\mathrm{s} = 3.03,\ K_\mathrm{p} = 2.05,\ \Omega_i = 1.00, 1.34, 3.37, 4.20, 5.13, \ldots$	Opt. for piston, $R_\mathrm{min}/R_\mathrm{max} = 1/5, \Omega_1 = 1$ $K_\mathrm{s} = 2.18,\ K_\mathrm{p} = 6.65,\ \Omega_i = 1.00, 1.19, 3.01, 4.08, 5.22, \ldots$

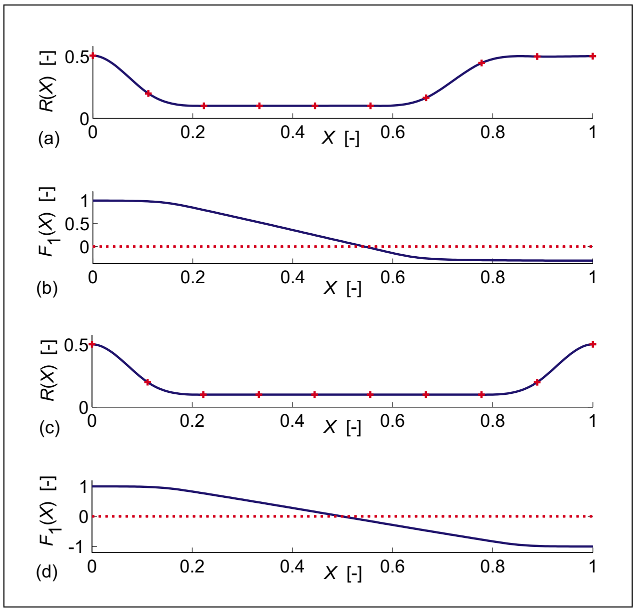

Figure 4. Optimized resonator shapes and corresponding eigenmodes for $R_\mathrm{min}/R_\mathrm{max} = 1/5$. (a,b): optimization for a shaker driving, $\Omega_1 = 0.361$; (c,d): optimization for a piston driving, $\Omega_1 = 0.382$. (a) Cavity shape (shaker-optimized), (b) Eigenmode shape (shaker-optimized), (c) Cavity shape (piston-optimized), (d) Eigenmode shape (piston-optimized).

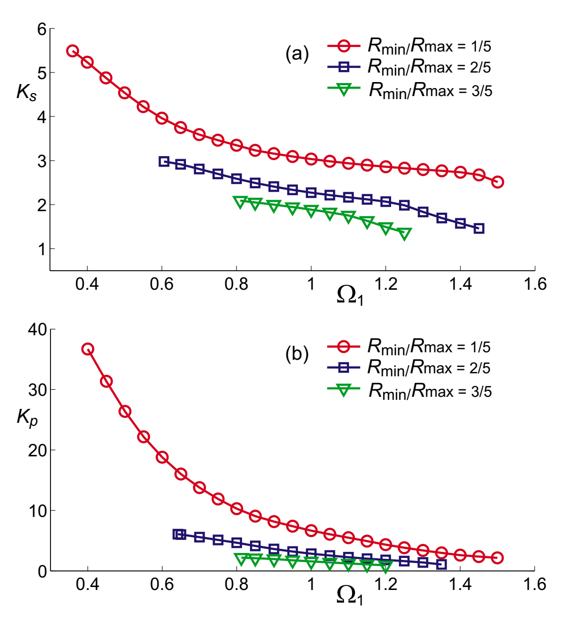

Figure 5. Eligibility factors for different ratios $R_\mathrm{min}/R_\mathrm{max}$ optimized in individual frequency intervals delimited by a minimum frequency Ω_1. (a) Shaker-optimized, shaker-driving, (b) Piston-optimized, piston-driving.

vious case. In this case, the higher ratio of the maximum and minimum radii allows further decrease of the fundamental eigenfrequencies ($\Omega_1 = 0.361$ in the shaker- and $\Omega_1 = 0.382$ in the piston-driving case). Again, the higher eigenfrequencies are not integer multiples of the fundamental ones and the piston driving is more efficient than the shaker driving, the eligibility factor for the piston-optimized piston-driven resonator attains value of $K_\mathrm{p} = 38.38$. Comparison of the eligibility factors in Table I clearly reveals, that increase of the ratio $R_\mathrm{max}/R_\mathrm{min}$ results in much bigger increase of the eligibility factor for the piston-driven resonator than for the shaker-driven one.

In some cases, the low eigenfrequencies of the optimum-shaped cavities need not be preferable. If the resonator shape is optimized in the frequency range $\Omega \in \langle\Omega_\mathrm{min}, \Omega_\mathrm{max}\rangle$, where $\Omega_\mathrm{min} > \Omega_\mathrm{opt}$, the algorithm finds quasi-optimum shape with eigenfrequency $\Omega = \Omega_\mathrm{min}$, however, the appropriate eligibility factor is smaller than in the case of the optimum-shaped resonator. The dependence of the eligibility factor on the lowest allowed frequency for individual $R_\mathrm{min}/R_\mathrm{max}$ ratios are depicted in Figure 5. It can be seen in all the cases that the lower $\Omega_\mathrm{min} > \Omega_\mathrm{opt}$ is allowed, the higher eligibility factor is attained. Higher ratio $R_\mathrm{max}/R_\mathrm{min}$ always causes higher eligibility factor for the given frequency. It can be observed in Figure 5 that the frequency-dependence of the eligibility factor value increases with $R_\mathrm{max}/R_\mathrm{min}$ ratio and the increase is stronger in the case of a piston-driven resonator.

In Figures 6 and 7 there are the quasi-optimum resonator shapes and the corresponding fundamental eigenmodes depicted for $\Omega_\mathrm{min} = \Omega_1 = 1$. The corresponding eligibility factors and the eigenfrequencies can be found

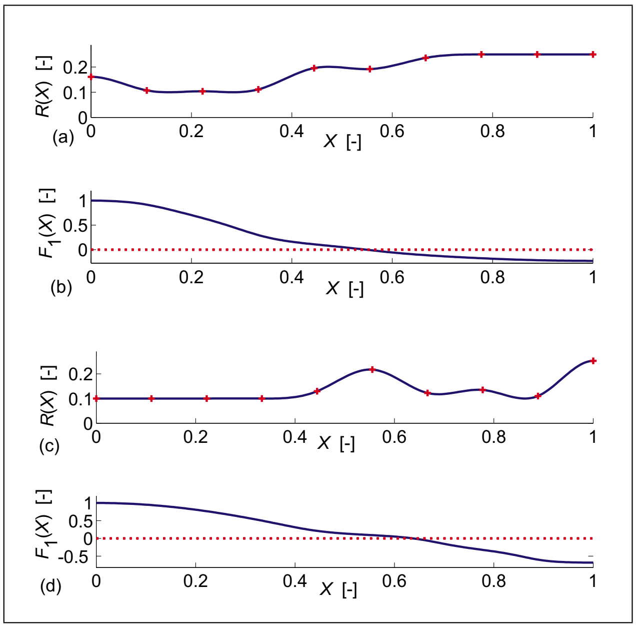

Figure 6. Quasi-optimum resonator shapes and corresponding eigenmodes for $R_{\min}/R_{\max} = 2/5$. (a,b): optimization for a shaker driving, (c,d): optimization for a piston driving, in both the cases $\Omega_1 = 1$. (a) Cavity shape (shaker-optimized), (b) Eigenmode shape (shaker-optimized), (c) Cavity shape (piston-optimized), (d) Eigenmode shape (piston-optimized).

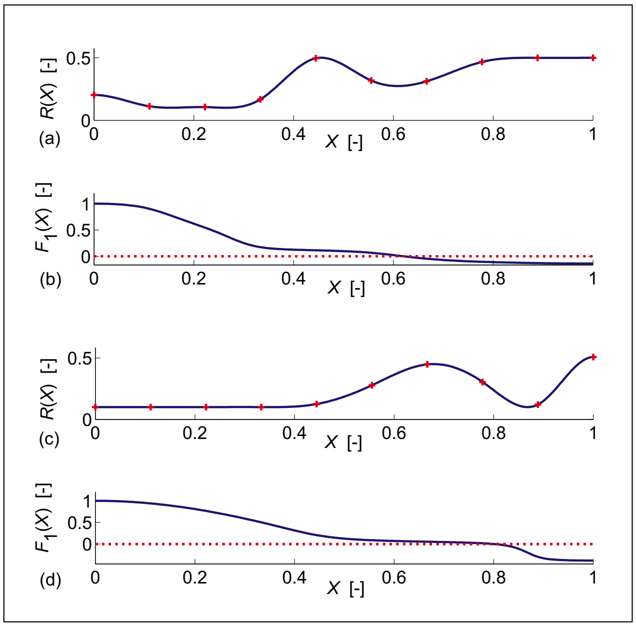

Figure 7. Quasi-optimum resonator shapes and corresponding eigenmodes for $R_{\min}/R_{\max} = 1/5$. (a,b): optimization for a shaker driving, (c,d): optimization for a piston driving, in both the cases $\Omega_1 = 1$. (a) Cavity shape (shaker-optimized), (b) Eigenmode shape (shaker-optimized), (c) Cavity shape (piston-optimized), (d) Eigenmode shape (piston-optimized).

in the last two rows in Table I. It can be observed that in these cases, the resonator shapes are slightly more complicated. Again, the higher eigenfrequencies are not integer multiples of the fundamental ones. Moreover, driving the resonator cavity in different way than it was designed for, results in significant decrease of the eligibility factor.

4.2. Finite-amplitude Acoustic Field in Optimized Resonators

High-amplitude acoustic fields were studied using the nonlinear model equation (1) proposed by Ilinskii *et al.* [3]. As in the original paper, the model equation was integrated numerically in the frequency domain; the two-point boundary value problem was solved using the shooting method, see e.g. [12].

As medium, air at normal atmospheric conditions was assumed ($\rho_0 = 1.2\,\mathrm{kg/m^3}$, $c_0 = 345\,\mathrm{m/s}$, $\gamma = 1.4$). The value of the attenuation coefficient $G = 10^{-2}$ was used [3, 9].

Figure 9 shows the frequency characteristics (amplitude of the fundamental harmonics at $X = 0$ – one-sided spectrum) of the piston-optimized piston-driven acoustic resonator with $R_{\min}/R_{\max} = 2/5$ (see Figure 8 c)) for different piston acceleration amplitudes. The frequency characteristics exhibits softening behavior with hysteresis for higher driving accelerations.

Figure 10 (top) shows distribution of amplitudes of the first three harmonics of acoustic pressure along the same resonator as in the previous case for $A_{p0} = 5 \times 10^{-4}$ and $\Omega = 0.586$. This frequency is reached using slow downwards frequency-sweep, at this point, maximum amplitude of the acoustic pressure is attained (see Figure 9). The small-amplitude resonance frequency for this resonator (see above) is $\Omega_{\mathrm{lin}} = 0.642$. It can be seen that the acoustic field is strongly nonlinearly distorted and that the 2nd harmonics attains similar amplitudes as the fundamental one. The bottom part of the figure shows distribution of the static (dc) pressure change caused by the nonlinear effects. The static pressure increases by 5 kPa at the ends of the resonator cavity and decreases by 7.5 kPa at its center.

Figure 11 shows for comparison the same data as Figure 10 but for a conical resonator with $R_{\min}/R_{\max} = 1/9$ (see Figure 8 b)) driven at the resonance frequency $\Omega = 1.285$ with the piston acceleration amplitude $A_{p0} = 5 \times 10^{-4}$. It can be observed that the 1st harmonics attains approximately half an amplitude at $X = 0$ compared with the optimized resonator and the higher harmonics are much less developed. Due to this fact, the dc pressure change is also smaller (it attains $\Delta p_{\mathrm{dc}} = 1.2\,\mathrm{kPa}$, compared with $\Delta p_{\mathrm{dc}} = 12.5\,\mathrm{kPa}$ in the case of the optimized resonator).

5. Discussion

An optimization algorithm was proposed for maximizing the standing-wave acoustic pressure amplitude by shaping of axi-symmetric resonator cavities. The algorithm is based on the Webster's equation supplemented with a term including viscous attenuation and driving. Within this model, there is one important parameter ($R_{\min}/R_{\max}$ ratio) affecting the acoustic field properties.

It has been shown that the optimum resonators are rather simple-shaped, symmetric in the case of the piston-driving

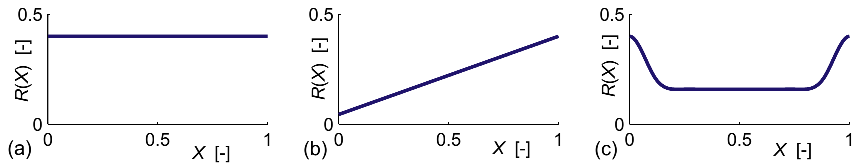

Figure 8. Comparison of shapes of resonators: (a) constant-cross-section resonator, (b) conical resonator, (c) resonator optimized for piston-driving.

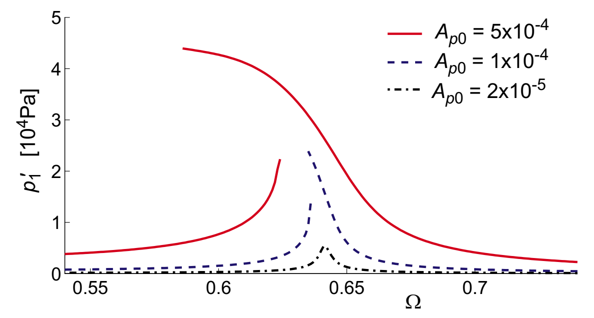

Figure 9. Frequency characteristics of the piston-optimised piston-driven resonator with $R_{\min}/R_{\max} = 2/5$ for different driving acceleration amplitudes $A_{\mathrm{p}0}$.

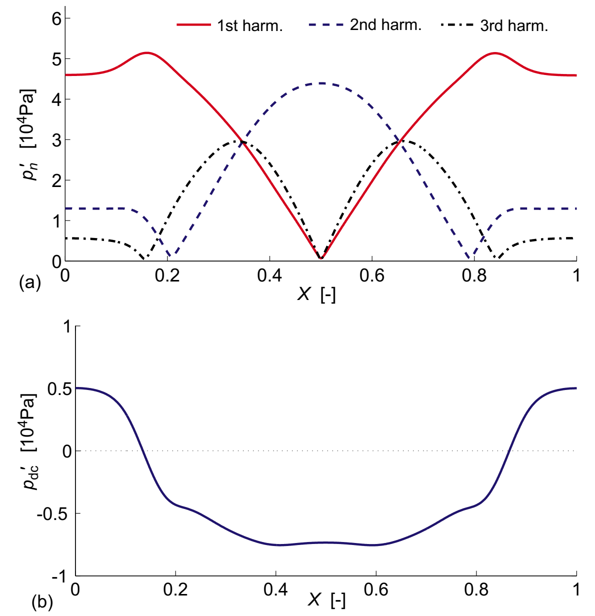

Figure 10. Top: distribution of acoustic pressure amplitude spectrum (one-sided) along the optimized-resonator axis; bottom: distribution of dc-pressure change (piston-optimized, piston-driven, $A_{\mathrm{p}0} = 5 \times 10^{-4}$, $\Omega = 0.586$). (a) Individual harmonics, (b) DC pressure change.

and non-symmetric in the case of the shaker-drivng. In both the cases, the optimum shape shifts the resonant frequency downwards (compared with a cylindrical resonator, where $\Omega_1 = 1$), the resonance frequency is the lower, the lower the ratio $R_{\min}/R_{\max}$ is. This behavior can be advantageous for practical applications, because for the given frequency (in Hertz), the resonant cavity length

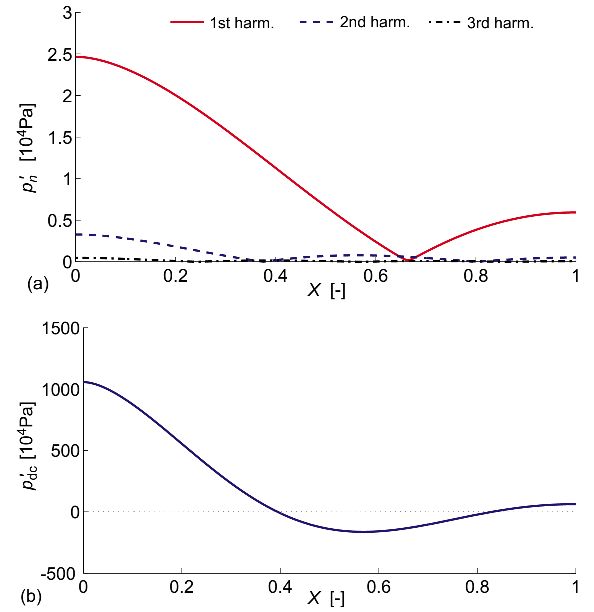

Figure 11. Top: distribution of acoustic pressure amplitude spectrum (one-sided) along the conical-resonator ($R_{\min}/R_{\max} = 1/9$) axis; bottom: distribution of dc-pressure change (piston-driven, $A_{\mathrm{p}0} = 5 \times 10^{-4}$, $\Omega = 1.285$). (a) Individual harmonics, (b) DC pressure change.

is smaller and for the given resonant cavity length, the resonance frequency is lower which can be applicable in pumping applications, where fast valves are used. The numerical results also show that optimum driving is always connected with driving of the lowest (fundamental) mode.

It has been shown that the piston driving gives rise to higher acoustic pressure amplitudes than the shaker driving when the optimized resonant cavities are used with the same driving acceleration amplitudes. Even if the shaker-driven cavity is technically much simpler in the concrete applications (there is no need of tightening of the moving piston), it requires more powerful (and thus more expensive) driving system. Replacement of the moving piston with e.g. a horn-driver thus seems to show a direction to low-cost applications utilizing high-amplitude acoustic fields.

Conducted numerical experiments indicate that the optimized acoustic resonators provide high-amplitude acoustic fields also in the nonlinear regime, even if the higher harmonics components are excited. The nonlinear interactions, on the other hand, generate strong change of the static pressure along the resonator axis which can be utilized in no-valve pumping of fluids.

It is important to emphasize that the used model is rather simplified, e.g., all the dissipation mechanisms are included in an experimentally justified [3, 9] parameter G. However, this approach allows to formulate simple results which have, on the other hand, limited validity. In the future work, the authors intend to propose more realistic optimization model including the dissipation effect of the boundary layer as well as the non-acoustic dissipation mechanisms. The interest will be e specially focused on the optimization of a complex system consisting of a resonant cavity connected to a horn-driver.

Acknowledgments

This work has been supported by GA CR grant project P101/12/1925.

References

[1] D. F. Gaitan, A. A. Atchley: Finite amplitude standing waves in harmonic and anharmonic tubes. J. Acoust. Soc. Am. **93** (1993) 2489–2495.

[2] C. C. Lawrenson, B. Lipkens, T. S. Lucas, D. K. Perkins, T. W. Van Doren: Measurements of macrosonic standing waves in oscillating closed cavities. J. Acoust. Soc. Am. **104** (1998) 623–636.

[3] Y. A. Ilinskii, B. Lipkens, T. S. Lucas, T. W. Van Doren, E. A. Zabolotskaya: Nonlinear standing waves in an acoustical resonator. J. Acoust. Soc. Am. **104** (1998) 2664–2674.

[4] Y. A. Ilinskii, B. Lipkens, E. A. Zabolotskaya: Energy losses in an acoustical resonator. J. Acoust. Soc. Am. **109** (2001) 1859–1870.

[5] M. F. Hamilton, Y. A. Ilinskii, E. A. Zabolotskaya: Linear and nonlinear frequency shifts in acoustical resonators with varying cross sections. J. Acoust. Soc. Am. **110** (2001) 109–119.

[6] Y.-D. Chun, Y.-H. Kim: Numerical analysis for nonlinear resonant oscillations of gas in axisymmetric closed tubes. J. Acoust. Soc. Am. **108** (2000) 2765–2774.

[7] R. R. Erickson, B. T. Zinn: Modeling of finite amplitude acoustic waves in closed cavities using the Galerkin method. J. Acoust. Soc. Am. **113** (2003) 1863–1870.

[8] C. Luo, X. Y. Huang, N. T. Nguyen: Effect of resonator dimensions on nonlinear standing waves. J. Acoust. Soc. Am. **117** (2005) 96–103.

[9] X. Li, J. Finkbeiner, G. Raman, C. Danielsb, B. M. Steinetz: Optimized shapes of oscillating resonators for generating high-amplitude pressure waves. J. Acoust. Soc. Am. **116** (2004) 2814–2821.

[10] C. Luo, X. Y. Huang, N. T. Nguyen: Generation of shock-free pressure waves in shaped resonators by boundary driving. J. Acoust. Soc. Am. **121** (2007) 2515–2521.

[11] D. Zwillinger: Handbook of differential equations. Academic Press, San Diego, 1997.

[12] W. H. Press, S. A. Teukolsky, W. T. Vetterling, B. P. Flannery: Numerical recipes 3rd edition: The art of scientific computing. Cambridge University Press, Cambridge, 2007.

[13] A. E. Eiben, J. E. Smith: Introduction to evolutionary computing. Springer, Berlin, 2010.

A.2 Optimal shaping of acoustic resonators for the generation of high-amplitude standing waves

Červenka, M., Šoltés, M., Bednařík, M., Optimal shaping of acoustic resonators for the generation of high-amplitude standing waves, Journal of the Acoustical Society of America 136(3), 1003-1012, (2014).

Optimal shaping of acoustic resonators for the generation of high-amplitude standing waves

Milan Červenka,[a)] Martin Šoltés, and Michal Bednařík
Faculty of Electrical Engineering, Czech Technical University in Prague, Technická 2, 166 27 Prague 6, Czech Republic

(Received 27 September 2013; revised 2 June 2014; accepted 8 July 2014)

Within this paper, optimal shaping of acoustic resonators for the generation of high-amplitude standing waves through the use of evolutionary algorithms is discussed. The resonator shapes are described using sets of control points interconnected with cubic-splines. Positions of the control points are calculated by means of an evolutionary algorithm in order to maximize acoustic pressure amplitude at a given point of the resonator cavity. As an objective function for the optimization procedure, numerical solution of one-dimensional linear wave equation taking into account boundary-layer dissipation is used. Resonator shapes maximizing acoustic pressure amplitude are found in case of a piston, shaker, or loudspeaker driving. It is shown that the optimum resonator shapes depend on the method of driving. In all the cases, acoustic field attains higher amplitude in the optimized resonators than in simple-shaped non-optimized resonators of similar dimensions. Theoretical results are compared with experimental data in the case of a loudspeaker driving, good agreement of which is achieved. © *2014 Acoustical Society of America*.

[http://dx.doi.org/10.1121/1.4892751]

PACS number(s): 43.25.Cb, 43.25.Gf [MDV] Pages: 1003–1012

I. INTRODUCTION

Many studies so far published have shown that it is possible to generate effectively standing acoustic waves even with overpressure exceeding the ambient pressure several times, which enables their utilization in a variety of practical applications. Pumping of fluids, stabilization of electric discharges[1] for plasma-chemical reactors, or thermoacoustics[2] can be given as examples.

Gaitan and Atchley[3] showed that introduction of the cross-section variability in a piston-driven resonator can significantly reduce energy transfer from the fundamental to the higher modes, prevent shock-formation, and increase an amplitude of the standing wave.

Lawrenson *et al.*[4] presented in their experimental paper concept of Resonant Macrosonic Synthesis (RMS) whereby they obtained acoustic pressure amplitude more than an order larger than it had been possible before. The concept is based on so-called dissonant resonators, whose varying cross-section cavities do not have the higher eigenfrequencies coincident with the harmonics of the nonlinearly distorted waveform which results in the suppression of a shock-wave formation. The authors demonstrated a strong dependence of obtained maximum amplitude on the resonator shape (cylindrical, conical, horn-cone hybrid, and bulb).

Ilinskii *et al.*[5] presented in their seminal theoretical paper a quasi-one-dimensional model equation expressed in terms of the velocity potential for description of high-amplitude standing waves in axisymmetric but otherwise arbitrarily shaped acoustic resonators. The model comprises nonlinearity, viscous bulk attenuation, and entire-resonator driving by an external force (shaker-driving). A numerical algorithm was proposed for integration of the model equation in the frequency domain, the numerical simulations were conducted in case of a cylindrical, conical, and bulb-shaped resonator. The numerical results were in good agreement with the experimental ones. The model was subsequently supplemented[6] to account for energy losses in the boundary-layer and the losses due to acoustically generated turbulence.

Hamilton *et al.*[7] and Mortell and Seymour[8] investigated theoretically dependence of the resonance frequencies of the varying cross-sectioned resonators on their shapes and their nonlinear shifts.

Chun and Kim[9] investigated numerically the influence of an entirely-driven resonant cavity shape on the compression ratio (ratio of the maximum and minimum pressure attained at a chosen point in the resonator cavity during one period) using a quasi-one-dimensional model equation based on the conservation laws integrated in the time-domain using a high-order finite-difference scheme. From the several simple studied shapes (cylindrical, conical, 1/2-cosine, and 3/4-cosine), the 1/2-cosine offered the best performance.

Erickson and Zinn[10] developed a Galerkin-method-based algorithm for time-domain integration of the model equation proposed in paper.[5] They also showed that the exponentially shaped resonator's compression ratio strongly and non-trivially depends on its geometrical parameters.

Luo *et al.*[11] studied theoretically the effect of the resonator shape and dimension on its compression ratio in the case of axisymmetric and low-aspect-ratio exponential geometry, observing its decrease with shortening the resonator length and smaller radius-to-length ratio.

Li *et al.*[12] optimized the parameters of simple-shaped resonator cavities in order to maximize the compression ratio

---

[a)] Author to whom correspondence should be addressed. Electronic mail: milan.cervenka@fel.cvut.cz by means of numerical simulations based on a nonlinear wave equation with volume acoustic energy attenuation model.[5] Within the numerical experiments, they achieved the value of 48 in the case of an optimized horn-cone shape.

Luo *et al.*[13] conducted numerical experiments in order to compare piston- or entire-driving of exponentially shaped cavity finding similar results.

Min *et al.*[14] demonstrated experimentally the possibility of generating strong nonlinear acoustic fields in loudspeaker-driven dissonant tubes.

High-amplitude acoustic fields in shaped resonators were also studied numerically using conservation laws in Refs. 15 and 16.

In all the above-mentioned papers, the same approach was employed, i.e., the resonator shapes were described using smooth elementary functions with fixed or adjustable (Erickson and Zinn,[10] Li *et al.*[12]) parameters, e.g., all the resonator cavities were non-symmetrical, wide at one end and narrow at the other one, where the maximum pressure (or compression ratio) was obtained.

Červenka and Bednařík[17] used a more general approach of parameterizing acoustic resonator shapes using control points interconnected with cubic-splines. Using a linear theory with a model of volume losses, they found a family of shapes maximizing acoustic pressure at one of the cavity ends.

This work follows-up and further develops paper[17] in two principal aspects. First, a model of dissipation of acoustic energy in an acoustic boundary layer was introduced as the experiments conducted by the authors had shown limited validity of results obtained using the model based on only volume losses, and second, optimization for driving by a loudspeaker driver was performed as this is probably the most interesting case with respect to applications.

Similarly, as in Ref. 17 the optimization procedure is based on a linear theory which means that the model cannot predict the amplitudes and phases of the higher harmonics, which is the cornerstone of the RMS technique. However, cross-section variability makes the optimized resonator shapes dissonant and therefore shock-wave formation is suppressed. As a result, the optimized resonator shapes provide higher amplitudes of acoustic pressure than the ones proposed previously provided that the higher harmonics are not excited too much.

Section II of this paper describes the mathematical model used for description of the acoustic field in a variable cross-section resonator together with the model of a loudspeaker driver. Details of the numerical optimization procedure are given in Sec. III. The results of numerical experiments are discussed in Sec. IV and a comparison of numerical and experimental data is provided in Sec. V to validate the proposed approach. Section VI concludes the paper.

II. MATHEMATICAL MODEL

A. Acoustic field in a resonant cavity

For a description of finite-amplitude standing waves in axisymmetric variable cross-section resonators, the following model equation derived in the second approximation was used:

$$\begin{aligned}\frac{\partial^2\varphi}{\partial t^2}-\frac{c_0^2}{r^2}\frac{\partial}{\partial x}\left(r^2\frac{\partial\varphi}{\partial x}\right)&=-\frac{\partial}{\partial t}\left(\frac{\partial\varphi}{\partial x}\right)^2-\frac{\gamma-1}{2c_0^2}\frac{\partial}{\partial t}\left(\frac{\partial\varphi}{\partial t}\right)^2-x\frac{\mathrm{d}a_\mathrm{s}}{\mathrm{d}t}\\&\quad+\frac{\delta}{c_0^2}\frac{\partial^3\varphi}{\partial t^3}-\frac{2c_0^2\varepsilon}{\sqrt{\pi}r^2}\int_{-\infty}^{t}\frac{1}{\sqrt{t-\tau}}\frac{\partial}{\partial x}\left[r\frac{\partial\varphi(x,\tau)}{\partial x}\right]\mathrm{d}\tau,\end{aligned}\tag{1}$$

where φ is the velocity potential, a_s is the acceleration of the resonant cavity, t is the time, x is the spatial coordinate along the resonator cavity, $r=r(x)$ is its radius, c_0 is the small-signal sound speed, γ is the adiabatic exponent, $\delta=[\zeta+4\eta/3+\kappa(1/c_V-1/c_p)]/\rho_0$ is the diffusivity of sound, where η, ζ are the coefficients of shear and bulk viscosity, respectively, κ is the coefficient of thermal conduction, c_p, c_V are the specific heats at constant pressure and volume, respectively, and ρ_0 is the ambient fluid density. Coefficient ε is defined as $\varepsilon=\sqrt{\nu_0}[1+(\gamma-1)/\sqrt{\mathrm{Pr}}]$, where $\nu_0=\eta/\rho_0$ is the kinematic viscosity and $\mathrm{Pr}=\eta c_\mathrm{p}/\kappa$ is the Prandtl number.

Derivation of the model Eq. (1) is briefly outlined in the Appendix. The terms on the left-hand side represent the linear wave equation describing one-dimensional wave motion in a rigid-walled waveguide filled with non-dissipative fluid, the first two terms on the right-hand side represent the nonlinear effects, the third term represents driving by the entire-resonator shaking, the fourth term represents the thermo-viscous bulk attenuation and finally, the last term represents the thermo-viscous attenuation due to the boundary layer. Additional losses due to acoustically generated turbulence[6] can be incorporated into this term in a straightforward way.

The applicability of Eq. (1) is limited by the second-order approximation, by condition of a small fractional change of the velocity potential over the cross-section, which can be formulated as $kr|\mathrm{d}r/\mathrm{d}x|/2\ll 1$, see Pierce,[18] where k is the wavenumber and further, by small thickness of the boundary layer $\delta_\mathrm{bl}\sim\sqrt{\nu_0/\omega}\ll r$.

As the aim of this work is to optimize the acoustic-resonator cavities for *moderate acoustic fields* and because the nonlinearly generated higher-harmonic components are usually suppressed in shaped resonators, the second-order nonlinear terms in Eq. (1) are omitted (the equation is linearized) so that the equation reads

$$\begin{aligned}\frac{\partial^2\varphi}{\partial t^2}-\frac{c_0^2}{r^2}\frac{\partial}{\partial x}\left(r^2\frac{\partial\varphi}{\partial x}\right)-\frac{\delta}{c_0^2}\frac{\partial^3\varphi}{\partial t^3}+\frac{2c_0^2\varepsilon}{\sqrt{\pi}r^2}\\\times\int_{-\infty}^{t}\frac{1}{\sqrt{t-\tau}}\frac{\partial}{\partial x}\left[r\frac{\partial\varphi(x,\tau)}{\partial x}\right]\mathrm{d}\tau=-x\frac{\mathrm{d}a_\mathrm{s}}{\mathrm{d}t}.\end{aligned}\tag{2}$$

Acoustic velocity v and acoustic pressure p' (in the first approximation) can be calculated from the velocity potential using the well-known formulas

$$v=\frac{\partial\varphi}{\partial x},\quad p'=-\rho_0\frac{\partial\varphi}{\partial t}.$$

As we are further focused on harmonically-driven steady-state acoustic fields, we can represent all the acoustic quantities as $q(x, t) = \Re[\hat{q}(x)\mathrm{e}^{\mathrm{i}\omega t}]$. Substitution into Eq. (2) results in

$$\left(1-\frac{2\varepsilon}{\sqrt{\mathrm{i}\omega r}}\right)\frac{\mathrm{d}}{\mathrm{d}x}\left(r^2\frac{\mathrm{d}\hat{\varphi}}{\mathrm{d}x}\right)+\frac{2\varepsilon}{\sqrt{\mathrm{i}\omega}}\frac{\mathrm{d}r}{\mathrm{d}x}\frac{\mathrm{d}\hat{\varphi}}{\mathrm{d}x}$$
$$+\frac{\omega^2}{c_0^2}\left(1-\frac{\mathrm{i}\omega\delta}{c_0^2}\right)r^2\hat{\varphi}=\frac{\mathrm{i}\omega x r^2\hat{a}_{\mathrm{s}}}{c_0^2}. \quad (3)$$

Depending on the manner of driving, the following boundary conditions are imposed. Driving by the entire-resonator-body shaking

$$\left.\frac{\mathrm{d}\hat{\varphi}}{\mathrm{d}x}\right|_{x=0}=\left.\frac{\mathrm{d}\hat{\varphi}}{\mathrm{d}x}\right|_{x=l}=0, \quad (4)$$

where l is the resonator cavity length; driving by a vibrating piston at $x = l$ [in Eq. (3), $\hat{a}_{\mathrm{s}} = 0$]

$$\left.\frac{\mathrm{d}\hat{\varphi}}{\mathrm{d}x}\right|_{x=0}=0, \quad \left.\frac{\mathrm{d}\hat{\varphi}}{\mathrm{d}x}\right|_{x=l}=\frac{\hat{a}_{\mathrm{p}}}{\mathrm{i}\omega}, \quad (5)$$

where $\hat{a}_{\mathrm{p}}$ is a phasor of the piston acceleration; and driving by a loudspeaker driver at $x = l$ [in Eq. (3), $\hat{a}_{\mathrm{s}} = 0$]

$$\left.\frac{\mathrm{d}\hat{\varphi}}{\mathrm{d}x}\right|_{x=0}=0, \quad \mathcal{L}\left[\hat{p}'(x=l),\, \hat{v}(x=l),\, \hat{u}\right]=0, \quad (6)$$

where $\mathcal{L}$ is a linear function of an acoustic pressure phasor $\hat{p}'$, an acoustic velocity phasor $\hat{v}$, and a driving voltage phasor $\hat{u}$ describing (modeling) the driver (loudspeaker), see below.

As a general analytical solution of Eq. (3) is not known for general $r(x)$, it has to be solved numerically. For this reason, dimensionless variables are convenient to introduce, e.g., in the form

$$X=\frac{x}{l}, \quad R=\frac{r}{l}, \quad A=\frac{\hat{a}}{l\omega_0^2}, \quad \Phi=\frac{\hat{\varphi}}{l^2\omega_0}, \quad \Omega=\frac{\omega}{\omega_0},$$

where $\omega_0 = \pi c_0/l$ corresponds to the first eigenfrequency of a constant cross-section resonator ended with rigid caps.

Using these new variables, Eq. (3) can be rewritten as

$$\frac{\mathrm{d}\Phi}{\mathrm{d}X}=\frac{W}{R^2}, \quad (7a)$$

$$\left(1-\frac{\Gamma}{\sqrt{\mathrm{i}\Omega R}}\right)\frac{\mathrm{d}W}{\mathrm{d}X}=-\pi^2\Omega^2R^2\left(1-\frac{\mathrm{i}G\Omega}{\pi}\right)\Phi$$
$$-\frac{\Gamma}{\sqrt{\mathrm{i}\Omega}R^2}\frac{\mathrm{d}R}{\mathrm{d}X}W+\mathrm{i}\pi^2\Omega R^2XA, \quad (7b)$$

where $G = \pi\omega_0\delta/c_0^2$ is a coefficient accounting for thermoviscous volume dissipation and $\Gamma = 2\varepsilon/\sqrt{\pi c_0 l}$ is a coefficient accounting for influence of the boundary layer.

Equations (7a) and (7b) form a set of four first-order linear ordinary differential equations for real and imaginary parts of the variables Φ and W. The equations were integrated numerically using the adaptive-stepsize eight-order Runge-Kutta method; the boundary-value problem was solved using the shooting method.[19]

B. Loudspeaker driver

Driving the resonator by a loudspeaker driver is modeled using Eq. (6). In this case, the used relation has the form

$$\left[Z_{\mathrm{e}}Z'_{\mathrm{m}}+(Bl_{\mathrm{vc}})^2\right]\hat{v}-Z_{\mathrm{e}}S_{\mathrm{d}}\hat{p}'-Bl_{\mathrm{vc}}\hat{u}=0, \quad (8)$$

see Fig. 1 and, e.g., Merhaut,[20] where $Z_{\mathrm{e}} = R_{\mathrm{e}} + \mathrm{i}\omega L_{\mathrm{e}}$ is the electrical impedance of the driver voice coil, R_{e} is the electrical resistance, and L_{e} is the electrical inductance; $Z'_{\mathrm{m}} = Z_{\mathrm{m}} + S_{\mathrm{d}}^2/\mathrm{i}\omega C_{\mathrm{a}}$, where $Z_{\mathrm{m}} = R_{\mathrm{m}} + \mathrm{i}\omega M + 1/\mathrm{i}\omega C_{\mathrm{m}}$ is the driver mechanical impedance, R_{m} is the mechanical resistance of the driver diaphragm suspension, M is the moving mass of the driver diaphragm assembly, C_{m} is the mechanical compliance of the driver diaphragm suspension; S_{d} is the effective piston area of the diaphragm, $C_{\mathrm{a}} = V_{\mathrm{b}}/\rho_0 c_0^2$ is the acoustic compliance of the enclosure behind the diaphragm, where V_{b} is its volume; B is the magnetic flux density in the driver air gap and l_{vc} is the length of the voice coil in the magnetic field.

III. OPTIMIZATION OF A RESONATOR SHAPE

A. Description of a resonator shape and its eligibility

So as not to restrict a resonator shape to a specific pre-defined elementary function with only a few adjustable parameters, it is defined using N control points distributed regularly at positions

$$X_i=\frac{iL}{N-1}, \qquad i=0,\,1,\,\ldots,\,N-1,$$

where $L = 1$ in case of a piston- or shaker-driven resonator (entire resonator body is optimized) and $L < 1$ in case of a loudspeaker-driven resonator (part of the resonator cavity is constituted by the internal waveguide of the loudspeaker driver). The corresponding values $R(\{X_i\}) = \{R_i\}$ are searched for within a pre-defined interval $R_i \in \langle R_{\min}, R_{\max}\rangle$. The function $R(X) = R(X, \{[X_i, R_i]\})$ is then constructed using the cubic-spline-interpolation of the control point pairs $[X_i, R_i]$ (the function and its first and second derivatives are continuous) with zero derivatives at the ends of the interval. The values R_i are further required to guarantee the condition

$$R_{\min}\le R(X)\le R_{\max} \quad \text{for any} \quad X\in\langle 0,\,L\rangle. \quad (9)$$

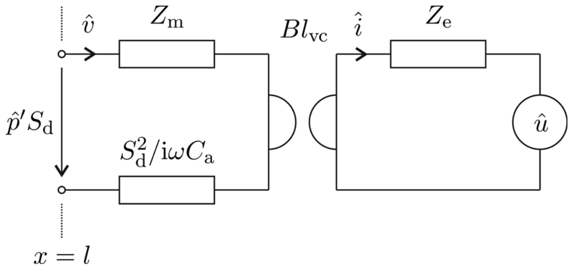

FIG. 1. Lumped-element circuit model of a loudspeaker driver.

The used optimization criterion (objective function) was the one for maximization of the acoustic pressure amplitude at resonance frequency at one of the ends $(x = 0)$ of the acoustic resonator; in case of a piston- or a shaker-driving, it is defined as

$$k_{pa} = \frac{|\hat{p}'(x = 0,\, \Omega = \Omega_{\text{resonance}})|}{|\hat{a}|}, \qquad (10)$$

where $\hat{a} = \hat{a}_{\text{p}}$ for piston-driving and $\hat{a} = \hat{a}_{\text{s}}$ for shaker-driving. In case of a loudspeaker-driving, it is defined as

$$k_{pu} = \frac{|\hat{p}'(x = 0,\, \Omega = \Omega_{\text{resonance}})|}{|\hat{u}|}. \qquad (11)$$

The parameters k_{pa} and k_{pu} are further called *the eligibility factors*. It is necessary to note that the value of the eligibility factor depends on the resonator length (due to frequency-dependence of the losses), maximum and minimum allowed resonator radii $R_{\max}$, $R_{\min}$ and, in case of loudspeaker-driving, on the physical parameters of the driver's model. As it is further shown, it is useful in some cases to restrict the allowed resonance frequency (which depends on the resonator shape) in certain limits $\Omega_{\text{resonance}} \in \langle \Omega_{\min}, \Omega_{\max} \rangle$. Using this restriction, the resonator shape can be optimized for being driven at a certain pre-defined resonance frequency.

B. Optimization procedure

For given model parameters and constraint conditions, the eligibility factor $k_{px} = k_{px}(\{R_i\})$ is a function of N variables $\mathbb{R}^N \rightarrow \mathbb{R}$, whose maximum is to be found. As the maximized function probably possesses a multimodal topology and as the definition domain of k_{px} is discontinuous [some $\{R_i\}$ sets do not comply with the condition (9), especially at the vicinity of the maximum], heuristic optimization methods seem to have reasonable use for this problem. In this case, an uncorrelated-mutation-with-one-step-size variant of self-adaptive (μ, λ)-ES Evolution Strategies[21] was used.

In short, the procedure works as follows. A population of λ individuals is generated, each of whom is characterized by its *genome*, namely, the set of control points $\{R_i\}$. For the first time, the control point sets are generated randomly. The individuals are assessed and μ best of them (the ones with the highest values of the objective function k_{px}) are employed as *parents*. From the set of parents, pairs are randomly drawn, recombined and mutated until a new generation of λ offspring is generated. The process continues until the objective function value of the best offspring increases. In this case, these values were used: $\mu = 20$, $\lambda = 7\mu$.

Assessment of the objective function (the eligibility factor) works as follows, see Fig. 2. First, a control points set is randomly generated in a specified range (the first generation) or it is obtained by recombination and mutation within the process of evolution (the following generations). In the second case, it is checked whether the control points lie within the pre-defined interval; if not, the control points set is discarded. Then, after interpolation by cubic splines, it is checked whether condition (9) is fulfilled; if not, the control points set is discarded. Subsequently, it is checked whether a resonance occurs in a pre-defined interval $\langle \Omega_{\min}, \Omega_{\max} \rangle$. For this purpose, Brent's method[22] is used for searching for a resonance maximum in the given frequency interval. If found, the resonator's eligibility is calculated using Eq. (10) or (11).

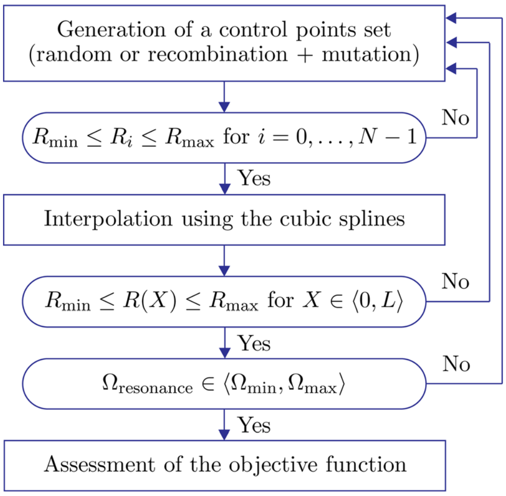

FIG. 2. (Color online) Flowchart of the algorithm for assessment of the resonator shape eligibility.

Because of its stochastic character, the process of maximization of the eligibility factor was repeated many times so that the dispersion of the results could be assessed.

IV. NUMERICAL RESULTS

The numerical experiments were conducted for hard-walled axisymmetric cavities filled with air at room conditions ($c_0 = 345.2$ m/s, $\rho_0 = 1.193$ kg/m^3, $\gamma = 1.402$, $c_{\text{p}} = 1004$ J/kg K, $\eta = 1.827 \times 10^{-5}$ kg/ms, $\zeta = 1.096 \times 10^{-5}$ kg/ms, $\kappa = 25.87 \times 10^{-3}$ J/K ms). In all cases, the cavities were parametrized using $N = 10$ control points.

A. Piston or shaker driving

Here, it is assumed that the resonator cavity is driven by entire-shaking of its body with acceleration a_{s} or by a piston positioned at $x = l$ vibrating with acceleration a_{p}.

1. Frequency dependence

The optimization method allows searching for an optimum shape of the resonant cavity in given frequency interval $\langle \Omega_x, \Omega_x + \Delta\Omega \rangle$ which allows studying also the quasi-optimum cases and frequency dependence of the resonator shape and eligibility. In this case, the optimum shape is defined as the one maximizing the eligibility factor defined using Eq. (10).

Figure 3 shows results for $\Delta\Omega = 0.1$, the resonator length $l = 30$ cm, maximum allowed radius $r_{\max} = 2.5$ cm, and individual minimum allowed radii such that $r_{\min}/r_{\max} = 1/5$, $2/5$ and $3/5$. The courses in the left part of the figure are related to driving at the first eigenfrequency, the ones in the right part are related to driving at the second eigenfrequency.

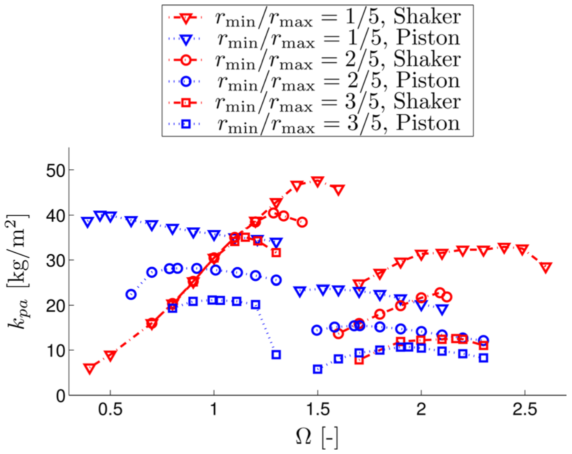

FIG. 3. (Color online) Eligibility factors calculated in individual intervals $\langle \Omega_x,\ \Omega_x + \Delta\Omega\rangle$ in the case of piston- and shaker-driving.

The figure clearly shows that decreasing ratio $r_{\min}/r_{\max}$ allows to attain higher values of k_{pa} and to decrease the minimum resonance frequency. In case of the piston-driving, k_{pa} for the first eigenfrequency depends on the allowed frequency interval $\langle \Omega_x,\ \Omega_x + \Delta\Omega\rangle$ only moderately, whereas in case of the shaker-driving, higher values of k_{pa} are attained at higher frequencies.

In case of the piston-driving, the optimum shapes (for individual frequency ranges) have maximum allowed radius $r_{\max}$ at the piston-end ($x = l$) and they attain the minimum allowed radius $r_{\min}$, not necessarily at the place where the acoustic pressure is maximized ($x = 0$). The resonator shapes change substantially according to the frequency interval of optimization. Two examples for $r_{\min}/r_{\max} = 1/5$ can be seen in Fig. 4. The top two figures show the resonator shape (crosses denote the positions of the control points) and distribution of amplitude of acoustic pressure divided by amplitude of the driving acceleration at the global maximum ($\Omega_1 = 0.450$, $k_{pa} = 40.07$ kg/m^2). It can be seen that the resonator shape is rather symmetric and very simple, similar to the corresponding case studied in Ref. 17. The bottom two figures show a high-frequency quasi-optimum case ($\Omega_1 = 1.300$, $k_{pa} = 34.06$ kg/m^2), the shape is non-symmetric with minimum radius at $x = 0$.

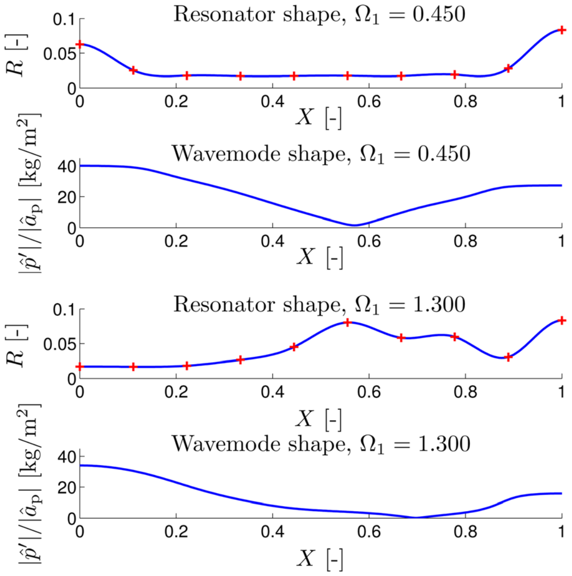

FIG. 4. (Color online) Optimized resonator shape and distribution of normalized acoustic pressure amplitude along the resonator cavity for $r_{\min}/r_{\max} = 1/5$ and piston-driving. Top two figures—global optimum ($\Omega_1 = 0.450$, $k_{pa} = 40.07$ kg/m^2); bottom two figures—high-frequency quasi-optimum ($\Omega_1 = 1.300$, $k_{pa} = 34.06$ kg/m^2).

As was mentioned above, the maximum value k_{pa} obtained in case of the shaker-driven resonators strongly depends on the frequency interval of optimization. The lower the value of $r_{\min}/r_{\max}$ the lower resonance frequency can be obtained, but the maximum k_{pa} values are substantially smaller than at higher frequencies. It can be seen in Fig. 3 that for lower frequencies, the maximum values k_{pa} are the same for different minimum allowed values of $r_{\min}/r_{\max}$, the smallest values of resonator radii do not attain the minimum allowed radius $r_{\min}$.

Figure 5 shows the optimum shape of the shaker-driven resonator for $r_{\min}/r_{\max} = 1/5$ and distribution of the acoustic pressure amplitude divided by amplitude of the driving acceleration for driving at resonance ($\Omega_1 = 1.488$, $k_{pa} = 49.45$ kg/m^2). The resonator is bottle-shaped and dissimilar to the optimum shapes for piston-driving.

The numerical results show that either in the case of shaker- or piston-driving, the driving at the first eigenfrequency provides a higher value of k_{pa}; for the same ratio $r_{\min}/r_{\max}$, shaker-driving offers higher maximum k_{pa} than the piston-driving. Optimum resonator shapes are different for shaker- and piston-driving. The numerical results obtained for the optimized resonators and some simple-shaped resonators are listed in Table I for comparison. It can be noticed that the dimensionless resonance frequencies of the shaped resonators are not integer multiples of the first one—the resonators are dissonant. This fact prevents formation of a shock wave even at high amplitudes of acoustic field. The dissonance in the case of the cylindrical resonator is caused by the boundary-layer dispersion.

2. Sizing

Figure 6 shows the dependence of k_{pa} for piston- and shaker-optimized resonators on their dimensions. In both cases, $R_{\max} = 1/12$ and $R_{\min} = R_{\max}/5$ and $l = 0.2$ m–0.4 m. The k_{pa} parameter increases with the resonator dimensions in a super-linear way $\sim l^{3/2}$, because (1) with the increasing

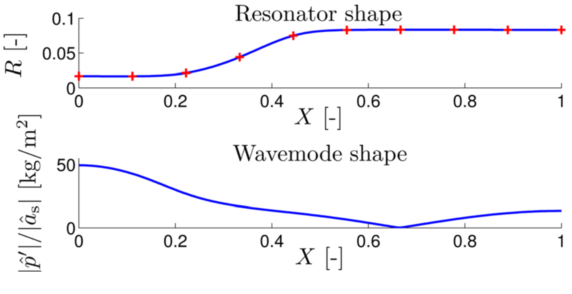

FIG. 5. (Color online) Optimized resonator shape and distribution of normalized acoustic pressure amplitude along the resonator cavity for $r_{\min}/r_{\max} = 1/5$ and shaker-driving; global optimum ($\Omega_1 = 1.488$, $k_{pa} = 49.45$ kg/m^2).

TABLE I. Parameters of some simple-shaped and optimized resonators with $l = 30$ cm. In variable-cross-section resonators, $r_{\min} = 0.5$ cm, $r_{\max} = 2.5$ cm.

Cylindrical, $r = 2.5$ cm
$\Omega_i = 0.997, 1.996, 2.995, 3.995, 4.994, \ldots$
Piston-driving: $k_{pa} = 13.24$ kg/m^2
Shaker-driving: $k_{pa} = 26.47$ kg/m^2

Conical
$\Omega_i = 1.188, 2.126, 3.089, 4.065, 5.050, \ldots$
Piston-driving: $k_{pa} = 18.40$ kg/m^2
Shaker-driving: $k_{pa} = 28.45$ kg/m^2

Piston-driving optimized, global optimum
$\Omega_i = 0.450, 1.454, 2.605, 3.728, 5.147, \ldots$
$k_{pa} = 40.07$ kg/m^2

Piston-driving optimized, high-frequency quasi-optimum
$\Omega_i = 1.300, 1.597, 2.893, 3.615, 5.155, \ldots$
$k_{pa} = 34.06$ kg/m^2

Shaker-driving optimized, global optimum
$\Omega_i = 1.488, 1.992, 3.080, 4.157, 5.101, \ldots$
$k_{pa} = 47.70$ kg/m^2

resonator length, its resonance frequency decreases and the boundary-layer absorption is proportional to $\sqrt{\omega}$, and (2) with increasing resonator dimensions, the ratio of section to circumference increases which decreases the influence of the boundary-layer absorption. In the studied interval of resonator dimensions, the optimization algorithm always converged to the same resonator shapes (depicted in the top part of Fig. 4 and in Fig. 5.

Similar characteristics can be found for variable resonator length l and fixed values of $r_{\min}$ and $r_{\max}$. Because in this case the ratios of section to circumference do not change with the resonator length, the ratio k_{pa} increases as $\sim\sqrt{l}$.

3. Comparison with previously-used shapes

In this section, parameters of acoustic fields generated in optimized resonators are compared with the ones used by Lawrenson *et al.*[4] (cone, horn-cone, and bulb—in this case only the central part for $0 \leq x \leq 28$ cm is taken). In all the cases, the individual optimized shapes have the same length and the minimum and maximum radii as their counterparts; the optimization is performed for shaker-driving. A comparison of the individual shapes can be seen in Fig. 7. Table II summarizes the parameters of the original shapes and their optimized equivalents. It can be seen that in the case of cone and horn-cone, the optimization results in about a twofold increase of the $k_{\rm pa}$ parameter, in the case of the bulb-shaped cavity, the increase is not so significant as the shapes are similar.

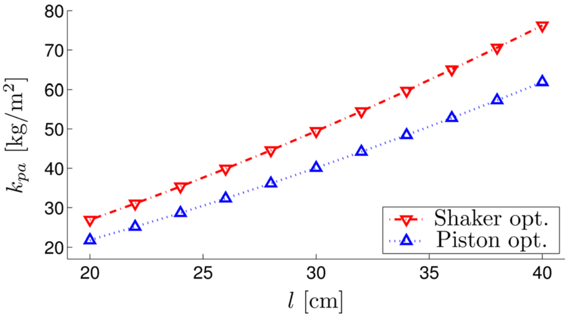

FIG. 6. (Color online) Dependence of k_{pa} on the resonator dimensions in the case of piston- and shaker-optimization. In both cases, $R_{\max} = 1/12$ and $R_{\min} = R_{\max}/5$.

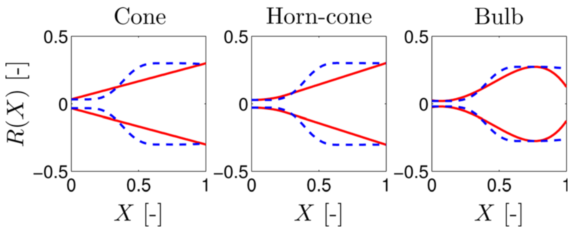

FIG. 7. (Color online) Resonator shapes used by Lawrenson *et al.* (Ref. 4) and their equivalents optimized for shaker-driving.

Figure 8 shows the dependence of the first harmonics of acoustic pressure at the small end of the horn-cone and the corresponding optimized cavity on the amplitude of driving acceleration calculated at resonance using numerical solution of Eq. (1). It can be observed that the optimized resonator provides higher amplitudes of acoustic pressure even in the case of relatively strong fields. Due to dissonance, nonlinear distortion is small in both cases, e.g., for the optimized shape and $|\hat{a}_s| = 400$ m/s^2, $|\hat{p}_2/\hat{p}_1| = 5.6\%$ and $|\hat{p}_3/\hat{p}_1| = 6.7\%$. It can also be seen in Fig. 8 that the slope of the characteristics for the optimized cavity decreases with increasing driving amplitude mainly as a result of increasing losses due to transition to turbulence[6] in the boundary layer in the longer narrow part of the resonator cavity.

TABLE II. Comparison of parameters of resonator shapes used by Lawrenson *et al.* (Ref. 4) with the corresponding ones optimized for shaker-driving.

Cone, Lawrenson *et al.* (Ref. 4), Eq. (3)
$\Omega_i = 1.282, 2.230, 3.185, 4.151, 5.126, \ldots$
Shaker-driving: $k_{pa} = 45.51$ kg/m^2

Optimized equivalent
$l = 17$ cm, $r_{\min} = 0.56$ cm, $r_{\max} = 5.12$ cm
$\Omega_i = 1.648, 2.076, 3.164, 4.261, 5.205, \ldots$
Shaker-driving: $k_{pa} = 91.82$ kg/m^2

Horn-cone, Lawrenson *et al.* (Ref. 4), Eq. (4)
$\Omega_i = 1.444, 2.258, 3.083, 4.067, 5.067, \ldots$
Shaker-driving: $k_{pa} = 87.75$ kg/ m^2

Optimized equivalent
$l = 24$ cm, $r_{\min} = 0.68$ cm, $r_{\max} = 7.27$ cm
$\Omega_i = 1.681, 2.084, 3.206, 4.298, 5.210, \ldots$
Shaker-driving: $k_{pa} = 163.34$ kg/m^2

Bulb, Lawrenson *et al.* (Ref. 4), Eq. (5)
$\Omega_i = 1.811, 2.475, 3.213, 4.181, 5.168, \ldots$
Shaker-driving: $k_{pa} = 161.94$ kg/m^2

Optimized equivalent
$l = 28$ cm, $r_{\min} = 0.56$ cm, $r_{\max} = 7.70$ cm
$\Omega_i = 1.739, 2.104, 3.276, 4.383, 5.242, \ldots$
Shaker-driving: $k_{pa} = 203.01$ kg/m^2

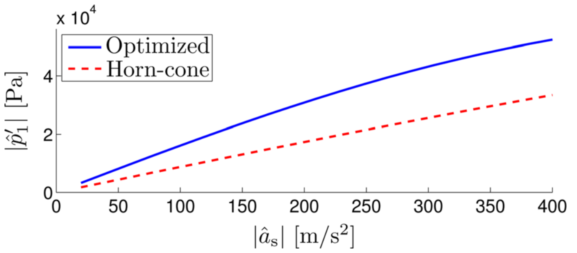

FIG. 8. (Color online) Amplitude of the first harmonics of acoustic pressure at the small end of the horn-cone and corresponding optimized resonator as a function of driving acceleration amplitude; calculated at resonance frequency.

B. Driving by a loudspeaker driver

For both numerical and real experiments with a loudspeaker driver, a Selenium (Brasil) D405Ti compression driver was used, from which the phase-plug was removed. Parameters of its lumped-element-circuit model were determined by measurement as follows: $R_\mathrm{e} = 6.5\Omega$, $L_\mathrm{e} = 6.7 \times 10^{-5}$ H, $R_\mathrm{m} = 7.48$ kg/s, $M = 4.1$ g, $C_\mathrm{m} = 1.24 \times 10^{-5}$ s^2/kg, $V_\mathrm{b} = 187$ cm^3, $S_\mathrm{d} = 90$ cm^2, and $Bl_\mathrm{vc} = 9.6$ Tm. The driver contains a variable-cross-section axisymmetric internal waveguide of length $l_\mathrm{int} = 59$ mm and $r_1 = 25$ mm output radius. Its geometrical model is depicted in Fig. 9.

Due to the internal waveguide, the entire resonator length is given as

$$l = l_\mathrm{int} + l_\mathrm{ext},$$

where l_ext is the length of the external waveguide whose shape is optimized.

Because of the internal waveguide and acoustic impedance of the driver's mechanism, the optimum resonator shapes substantially differ from the ones found for the case of the piston-driving.

Figure 10 shows the optimum shape for $l_\mathrm{ext} = 30$ cm, $r_\mathrm{max} = r(x = l_\mathrm{int}) = r_1 = 2.5$ cm (the external resonator radius matches the internal waveguide output), and $r_\mathrm{min} = r_\mathrm{max}/5$ and the corresponding wavemode. Its parameters, together with the ones for some simple-shaped non-optimized resonator cavities attached to the driver are shown in Table III. It can be observed that the acoustic pressure amplitude in the optimized cavity attains almost 6× higher amplitude than in the case of a cylindrical cavity and 2.4× higher amplitude than in the case of a conical cavity (with the same $r_\mathrm{min}/r_\mathrm{max}$ ratio).

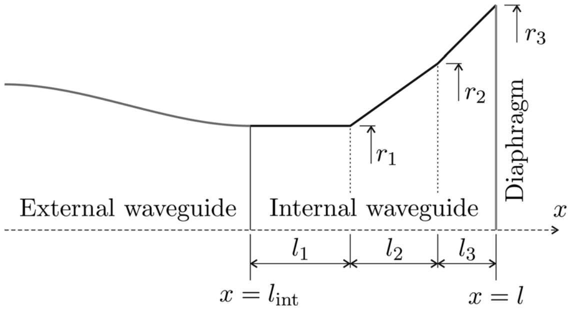

FIG. 9. Model geometry of the internal waveguide of loudspeaker driver Selenium D405Ti; $l_1 = 24$ mm, $l_2 = 21$ mm, $l_3 = 14$ mm, $r_1 = 25$ mm, $r_2 = 39.5$ mm, and $r_3 = 53.5$ mm.

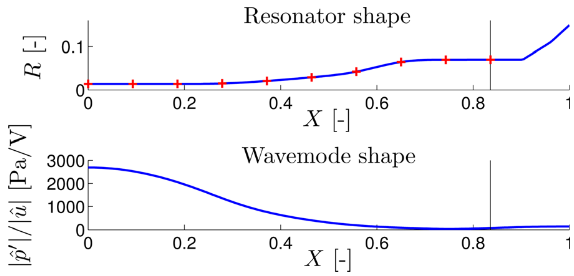

FIG. 10. (Color online) Optimized resonator shape and distribution of normalized acoustic pressure amplitude along the resonator cavity for $r_\mathrm{min}/r_\mathrm{max} = 1/5$ and driving with a loudspeaker driver. The vertical line denotes the beginning of the driver's internal waveguide. ($\Omega_1 = 1.188$, $k_{pu} = 2693$ Pa/V).

It can be observed that even in the case of the cylindrical resonator, the resonance frequencies are not integer multiples of the first one which is caused mainly because of the driver's variable-cross-section internal waveguide and output impedance of the driving mechanism.

V. EXPERIMENTAL VALIDATION

To validate the numerical results, some experiments with loudspeaker-driven resonators were conducted. The above-mentioned Selenium D405Ti compression driver with removed phase-plug was utilized together with three axisymmetric resonators: (a) cylindrical one with $r = 2.5$ cm and $l_\mathrm{ext} = 29.8$ cm; (b) conical one with $r_\mathrm{min} = 0.5$ cm, $r_\mathrm{max} = 2.5$ cm, and $l_\mathrm{ext} = 30$ cm, and (c) the driver-optimized one depicted in Fig. 10. The variable cross-section resonators were milled in two pieces of a duralumin block and stuck together. Acoustic pressure was measured using 1/8 in. G.R.A.S. (Denmark) Type 40DP microphone placed at the symmetry-axis at the end of the resonators opposite the driver. All the measurements were conducted in air at room conditions. The experimental results were compared with the numerical ones obtained using Eq. (1). The model of additional losses due to acoustically generated turbulence in boundary layer[6] provided good agreement of theoretical and experimental data in the case of the strongest driving of the optimized resonator. The parameter ξ characterizing the ratio between the dynamic viscosity and the eddy viscosity[6] was set to $\xi = 1$.

TABLE III. Parameters of some simple-shaped and optimized resonators with $l_\mathrm{ext} = 30$ cm driven by the loudspeaker driver. In variable-cross-section resonators, $r_\mathrm{max} = 2.5$ cm, $r_\mathrm{min} = r_\mathrm{max}/5$.

Cylindrical, $r = 2.5$ cm
$\Omega_i = 0.828, 1.783, 2.869, 3.883, 4.909, \ldots$
$k_{pu} = 451$ Pa/V

Conical
$\Omega_i = 1.089, 2.012, 3.012, 3.983, 4.982, \ldots$
$k_{pu} = 1133$ Pa/V

Optimized
$\Omega_i = 1.188, 1.789, 2.916, 4.064, 4.921, \ldots$
$k_{pu} = 2693$ Pa/V

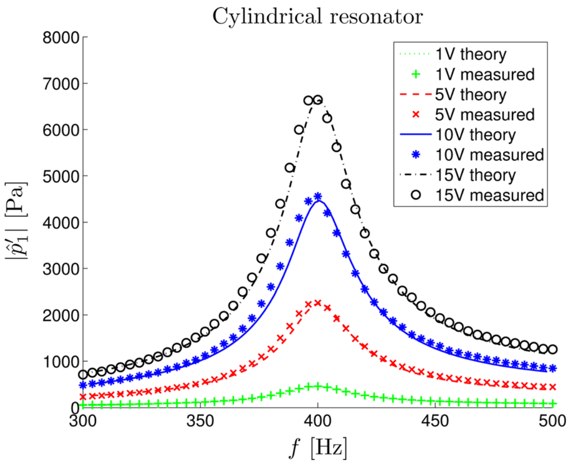

FIG. 11. (Color online). Frequency characteristics of amplitude of the first harmonics of acoustic pressure in loudspeaker-driven cylindrical resonator—comparison of theoretical and experimental data.

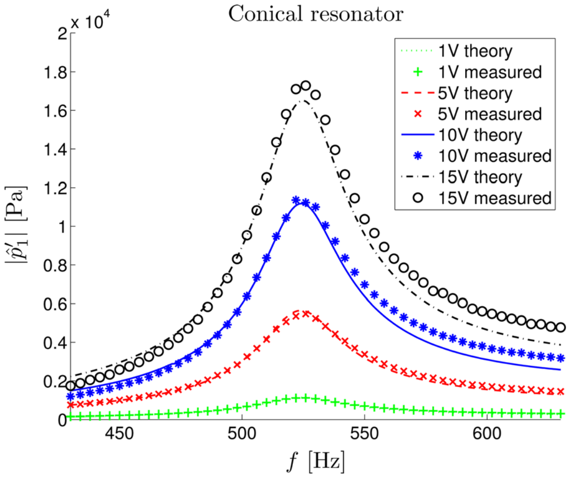

FIG. 12. (Color online) Frequency characteristics of amplitude of the first harmonics of acoustic pressure in loudspeaker-driven conical resonator—comparison of theoretical and experimental data.

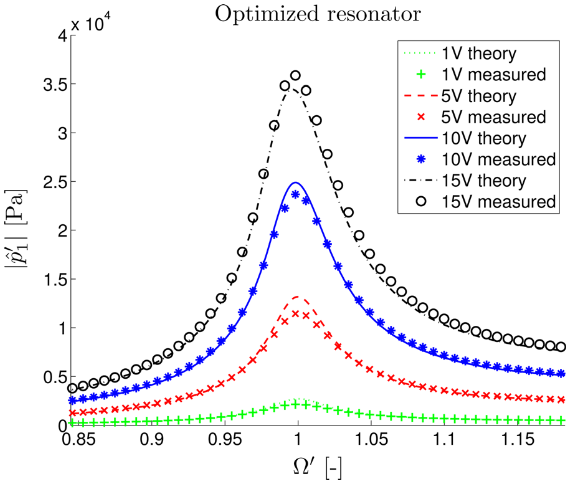

FIG. 13. (Color online) Frequency characteristics of amplitude of the first harmonics of acoustic pressure in loudspeaker-driven optimized resonator—comparison of theoretical and experimental data.

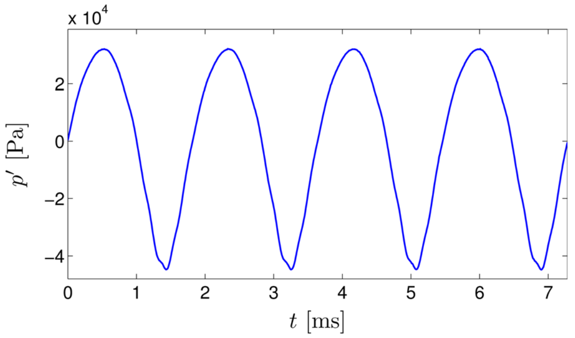

FIG. 14. (Color online) Time course of acoustic pressure measured in the optimized resonator at $f = 549$ Hz (resonance), driving voltage amplitude $U_0 = 15$ V.

Figures 11–13 show frequency characteristics of amplitude of the first harmonics of acoustic pressure measured and calculated in the case of individual resonators for different driving voltage amplitudes. The agreement of the experimental and numerical data is quite good in the case of the cylindrical (Fig. 11) and conical resonator (Fig. 12) even for higher driving voltages.

In the case of the driver-optimized resonator, the agreement is a little worse. For driving voltage amplitude of 1 V, the resonance frequency calculated $f_{\mathrm{r\,calc}} = 571$ Hz differs from the resonance frequency measured $f_{\mathrm{r\,meas}} = 551$ Hz by 3.6%. This discrepancy can possibly be attributed to differences between the mathematical description of the resonator shape and the actual shape of the manufactured resonator. Considering this fact, the frequencies in Fig. 13 were normalized to individual resonance frequencies $\Omega' = f/f_{\mathrm{r}x}$. Resonance frequency of the system decreases with increasing driving voltage amplitude, the value of 549 Hz was measured when 15 V driving voltage amplitude was used. The numerical results also predict this softening-spring-like behavior.

For driving voltage amplitude of 15 V the first harmonics in the optimized resonator attains an amplitude of $|\hat{p}'_1| = 36\,000$ Pa at resonance, which is 2× more than in the case of the conical resonator and 5.4× more than in case of the cylindrical resonator. It can be seen in Fig. 14 that the time-course of the acoustic pressure is distorted but a shock-wave is not present.

VI. CONCLUSIONS

A new method was proposed for optimization the acoustic-resonator shapes for generation of high-amplitude acoustic fields driven by a piston, shaker, or a loudspeaker driver. The numerical results show that the optimum shapes differ for individual manners of driving and that use of a properly optimized resonant cavity results in substantially stronger acoustic field compared with simple-shaped resonators of similar dimensions. Good agreement of the numerical results with the experimental data confirms the necessity of introduction of the model of boundary-layer acoustic energy dissipation in the governing equations used for the optimization procedure. The numerical experiments indicate that similar results can be obtained either in case of piston- or shaker-driving, if correspondingly optimized resonators are used and, moreover, a resonant cavity for piston-driving can be tuned in a wide range of frequencies.

It has been shown that even if the optimization procedure is based on a linear theory (and thus it cannot predict behavior of strongly nonlinear acoustic fields), it provides a systematic means of design of resonant cavities for high-amplitude acoustic applications such as, e.g., thermoacoustic devices or plasma-chemical reactors. Utilizing the appropriately optimized resonant cavities together with commercially available loudspeakers could increase economic attractiveness of these promising applications.

ACKNOWLEDGMENTS

This work was supported by GACR Grant No. P101/12/1925. The numerical calculations were performed at Computing and Information Centre of CTU.

APPENDIX: DERIVATION OF THE MODEL EQUATION

The second-order nonlinear model Eq. (1) is similar to the one published in Ref. 23. It issues from the gas-dynamics equations for one-dimensional flow in axisymmetric variable-cross-section hard-walled waveguide which have the following form (meaning of the individual symbols is explained in Sec. II).

The continuity equation

$$\frac{\partial \rho}{\partial t}+\frac{1}{r^2}\frac{\partial}{\partial x}\left(r^2\rho v\right)=\frac{2\varepsilon\rho}{\sqrt{\pi}r^2}\frac{\partial}{\partial x}\int_{-\infty}^{t}\frac{rv(x,\,\tau)}{\sqrt{t-\tau}}\mathrm{d}\tau, \tag{A1}$$

where ρ is the total fluid density. The term on the right-hand side describes the influence of the acoustic boundary layer on the fluid flow. Equation (A1) corresponds to the continuity equation used by Ilinskii *et al.*,[6] the model based on this equation provides better agreement between numerical and experimental data than the variant of the continuity equation used by Chester,[24] especially in the case of higher values of $|\mathrm{d}r/\mathrm{d}x|$.

In the case of high-amplitude acoustic fields, the model of increasing effective viscosity and thermal conductivity due to turbulence generated in the boundary layer[6] describes the well observed increase of acoustic energy dissipation.

The momentum equation, see, e.g., Ilinskii *et al.*,[5] reads

$$\rho\left(\frac{\partial v}{\partial t}+v\frac{\partial v}{\partial x}\right)=-\rho a_{\mathrm{s}}-\frac{\partial p}{\partial x}+\left(\zeta+\frac{4}{3}\eta\right)\frac{\partial}{\partial x}\left[\frac{1}{r^2}\frac{\partial}{\partial x}(r^2v)\right], \tag{A2}$$

where p is the total fluid pressure.

The state equation for an ideal gas in the second approximation can be written in the form

$$p'=c_0^2\rho'+\frac{c_0^2}{2\rho_0}(\gamma-1)\rho'^2-\kappa\left(\frac{1}{c_V}-\frac{1}{c_p}\right)\frac{1}{r^2}\frac{\partial}{\partial x}(r^2v), \tag{A3}$$

see, e.g., Makarov and Ochman,[25] where $\rho'=\rho-\rho_0$ is the acoustic density.

In the following text, it is assumed that the acoustic quantities p', ρ', and v together with the fluid parameters η, ζ, and κ are the first order of smallness and the driving acceleration a_{s} is the second order of smallness.

Within the second approximation, terms of the third and higher orders are discarded in the respective equations and the first-order approximations are substituted into the second-order terms. In the first approximation, the momentum equation (A2) integrated with respect to the spatial coordinate x and the state equation (A3) have form

$$p'=-\rho_0\frac{\partial\varphi}{\partial t}, \tag{A4}$$

$$p'=c_0^2\rho'. \tag{A5}$$

The first-order wave equation

$$\frac{1}{r^2}\frac{\partial}{\partial x}\left(r^2\frac{\partial\varphi}{\partial x}\right)=\frac{1}{c_0^2}\frac{\partial^2\varphi}{\partial t^2} \tag{A6}$$

is substituted into the second-order terms so that we can eliminate the spatial derivatives.

Introducing the velocity potential in Eq. (A2), dropping the third-order terms and substituting for acoustic density from Eqs. (A4) and (A5) yields after integration with respect to the spatial coordinate x in

$$p'=-\rho_0\frac{\partial\varphi}{\partial t}-\rho_0ax+\frac{\rho_0}{2c_0^2}\left(\frac{\partial\varphi}{\partial t}\right)^2-\frac{\rho_0}{2}\left(\frac{\partial\varphi}{\partial x}\right)^2+\frac{1}{c_0^2}\left(\zeta+\frac{4}{3}\eta\right)\frac{\partial^2\varphi}{\partial t^2}. \tag{A7}$$

Equation (A6) was used for the further simplification in one of the second-order terms.

Introducing the acoustic quantities together with the velocity potential in the continuity equation (A1), employing relations (A4), (A5), and (A6) in the second-order terms and dropping the higher-order terms results in

$$\frac{\partial\rho'}{\partial t}=-\frac{\rho_0}{r^2}\frac{\partial}{\partial x}\left(r^2\frac{\partial\varphi}{\partial x}\right)+\frac{\rho_0}{2c_0^4}\frac{\partial}{\partial t}\left(\frac{\partial\varphi}{\partial t}\right)^2+\frac{\rho_0}{2c_0^2}\frac{\partial}{\partial t}\left(\frac{\partial\varphi}{\partial x}\right)^2+\frac{2\varepsilon\rho_0}{\sqrt{\pi}r^2}\int_{-\infty}^{t}\frac{1}{\sqrt{t-\tau}}\frac{\partial}{\partial x}\left[r\frac{\partial\varphi(x,\,\tau)}{\partial x}\right]\mathrm{d}\tau. \tag{A8}$$

Taking the time derivative of Eq. (A3), introducing the velocity potential and employing relations (A4), (A5), and (A6) in the second-order term results in

$$\frac{\partial p'}{\partial t}=c_0^2\frac{\partial\rho'}{\partial t}+\frac{\rho_0}{2c_0^2}(\gamma-1)\frac{\partial}{\partial t}\left(\frac{\partial\varphi}{\partial t}\right)^2-\frac{\kappa}{c_0^2}\left(\frac{1}{c_{\mathrm{V}}}-\frac{1}{c_{\mathrm{p}}}\right)\frac{\partial^3\varphi}{\partial t^3}. \tag{A9}$$

The time-derivative of Eq. (A7) together with Eqs. (A8) and (A9) can be used to eliminate the acoustic pressure and density resulting in the second-order model equation (1).

Compared to the third-order model equation used by Ilinskii *et al.*,[5] Eq. (1) can be used for calculation of moderate acoustic fields with much less numerical effort.

Acoustic pressure can be calculated from the solution of Eq. (1) using Eq. (A7). The model equation (1) can be integrated numerically in frequency domain as was proposed in Ref. 5.

[1] T. Nakane, "Discharge phenomenon in high-intensity acoustic standing wave field," IEEE Trans. Plasma Sci. **33**(2), 356–357 (2005).

[2] G. W. Swift, "Thermoacoustic engines," J. Acoust. Soc. Am. **84**, 1145–1180 (1988).

[3] D. F. Gaitan and A. A. Atchley, "Finite amplitude standing waves in harmonic and anharmonic tubes," J. Acoust. Soc. Am. **93**, 2489–2495 (1993).

[4] Ch. C. Lawrenson, B. Lipkens, T. S. Lucas, D. K. Perkins, and T. W. Van Doren, "Measurements of macrosonic standing waves in oscillating closed cavities," J. Acoust. Soc. Am. **104**, 623–636 (1998).

[5] Yu. A. Ilinskii, B. Lipkens, T. S. Lucas, T. W. Van Doren, and E. A. Zabolotskaya, "Nonlinear standing waves in an acoustical resonator," J. Acoust. Soc. Am. **104**, 2664–2674 (1998).

[6] Yu. A. Ilinskii, B. Lipkens, and E. A. Zabolotskaya, "Energy losses in an acoustical resonator," J. Acoust. Soc. Am. **109**, 1859–1870 (2001).

[7] M. F. Hamilton, Yu. A. Ilinskii, and E. A. Zabolotskaya, "Linear and nonlinear frequency shifts in acoustical resonators with varying cross sections," J. Acoust. Soc. Am. **110**, 109–119 (2001).

[8] M. P. Mortell and B. R. Seymour, "Nonlinear resonant oscillations in closed tubes of variable cross-section," J. Fluid Mech. **519**, 183–199 (2004).

[9] Y.-D. Chun and Y.-H. Kim, "Numerical analysis for nonlinear resonant oscillations of gas in axisymmetric closed tubes," J. Acoust. Soc. Am. **108**, 2765–2774 (2000).

[10] R. R. Erickson and B. T. Zinn, "Modeling of finite amplitude acoustic waves in closed cavities using the Galerkin method," J. Acoust. Soc. Am. **113**, 1863–1870 (2003).

[11] C. Luo, X. Y. Huang, and N. T. Nguyen, "Effect of resonator dimensions on nonlinear standing waves," J. Acoust. Soc. Am. **117**, 96–103 (2005).

[12] X. Li, J. Finkbeiner, G. Raman, Ch. Danielsb, and B. M. Steinetz, "Optimized shapes of oscillating resonators for generating high-amplitude pressure waves," J. Acoust. Soc. Am. **116**, 2814–2821 (2004).

[13] C. Luo, X. Y. Huang, and N. T. Nguyen, "Generation of shock-free pressure waves in shaped resonators by boundary driving," J. Acoust. Soc. Am. **121**, 2515–2521 (2007).

[14] Q. Min, Q.-Y. Zhang, J.-J. Tian, Q.-B. Wang, and W.-Q. He, "A study on the dissonant standing-wave tube with variable section and its extremely nonlinear standing-wave field," Phys. Lett. A **377**, 99–106 (2012).

[15] M. Červenka and M. Bednařík, "Description of finite-amplitude standing acoustic waves using convection-diffusion equations," Czech. J. Phys. **55**(6), 673–680 (2005).

[16] F. Ning and X. Li, "Numerical simulation of finite amplitude standing waves in acoustic resonators using finite volume method," Wave Motion **50**, 135–145 (2013).

[17] M. Červenka and M. Bednařík, "On the optimization of an acoustic resonator shape with respect to acoustic pressure amplitude," Acust. Acta Acust. **99**, 183–191 (2013).

[18] A. D. Pierce, *Acoustics: An Introduction to its Physical Principles and Applications*, first published 1981 (currently published by Acoustical Society of America, Melville, NY, 1994), Chap. 7, pp. 360–361.

[19] W. H. Press, S. A. Teukolsky, W. T. Vetterling, and B. P. Flannery, *Numerical Recipes 3rd Edition: The Art of Scientific Computing* (Cambridge University Press, Cambridge, 2007), Chap. 17, pp. 899–964.

[20] J. Merhaut, *Theory of Electroacoustics* (McGraw-Hill, New York, 1981), Chap. 6, pp. 209–218.

[21] A. E. Eiben and J. E. Smith, *Introduction to Evolutionary Computing* (Springer, Berlin, 2010), Chap. 4, pp. 71–87.

[22] W. H. Press, S. A. Teukolsky, W. T. Vetterling, and B. P. Flannery, *Numerical Recipes 3rd Edition: The Art of Scientific Computing* (Cambridge University Press, Cambridge, 2007), Chap. 10, pp. 487–499.

[23] M. Červenka and M. Bednařík, "Nonlinear waves in resonators," in *Nonlinear Acoustics at the Turn of the Millennium, Goettingen, September 1–4, 1999, 15th International Symposium on Nonlinear Acoustics*, edited by W. Lauterborn and T. Kurz (AIP, New York, 2000), pp. 165–168.

[24] W. Chester, "Nonlinear resonant oscillations of a gas in a tube of varying cross-section," Proc. R. Soc. London, Ser. A **444**, 591–604 (1994).

[25] S. Makarov and M. Ochmann, "Nonlinear and thermoviscous phenomena in acoustics, Part I," Acust. Acta Acust. **82**, 579–606 (1996).

A.3 Equations for description of nonlinear standing waves in constant-cross-sectioned resonators

Bednařík, M., Červenka, M., Equations for description of nonlinear standing waves in constant-cross-sectioned resonators, Journal of the Acoustical Society of America 135(3), EL134-EL139, (2014).

Equations for description of nonlinear standing waves in constant-cross-sectioned resonators

Michal Bednarik and Milan Cervenka
Czech Technical University in Prague, Faculty of Electrical Engineering, Technicka 2,
166 27 Prague, Czech Republic
bednarik@fel.cvut.cz; cervenm3@fel.cvut.cz

Abstract: This work is focused on investigation of applicability of two widely used model equations for description of nonlinear standing waves in constant-cross-sectioned resonators. The investigation is based on the comparison of numerical solutions of these model equations with solutions of more accurate model equations whose validity has been verified experimentally in a number of published papers.

PACS numbers: 43.25.Gf [MH]
Date Received: September 13, 2013 **Date Accepted:** January 19, 2014

1. Introduction

The description of the behavior of nonlinear standing waves in constant-cross-sectioned resonators represents an interesting problem both from a theoretical and practical point of view. There are a number of model equations which can be used for this purpose but limits of their applicability are not obvious.

This study aims to assess the validity of the Kuznetsov and inhomogeneous Burgers model equations [see, e.g., Kuznetsov (1970), Gusev (1984), Rudenko *et al.* (2001), Bednarik and Konicek (2004)] that include only nonlinear terms of second order. These equations are widely used for analysis of nonlinear processes in constant-cross-sectioned resonators, in particular in cylindrical ones. Our approach is based on the comparison of the above-mentioned simpler model equations with a more accurate equation containing the third-order terms [see Ilinskii *et al.* (1998)] whose validity has been verified experimentally, see, e.g., Lawrenson *et al.* (1998).

2. Model equation

A one-dimensional wave equation describing the high-amplitude acoustic field in a constant-cross-sectioned waveguide can be written, see Ilinskii *et al.* (1998), in the form

$$c_0^2\frac{\partial^2\varphi}{\partial x^2}-\frac{\partial^2\varphi}{\partial t^2}+\frac{b}{\rho_0}\frac{\partial^3\varphi}{\partial x^2\partial t}=2\frac{\partial\varphi}{\partial x}\frac{\partial^2\varphi}{\partial x\partial t}+(\gamma-1)\frac{\partial\varphi}{\partial t}\frac{\partial^2\varphi}{\partial x^2}+\frac{(\gamma+1)}{2}\left(\frac{\partial\varphi}{\partial x}\right)^2\frac{\partial^2\varphi}{\partial x^2}, \tag{1}$$

where φ is the velocity potential, $v=\partial\varphi/\partial x$ is the acoustic velocity, x is the spatial coordinate along the waveguide axis, t is the time, c_0 is the small-signal speed of sound, ρ_0 is the ambient fluid density, γ is the Poisson's exponent, and $b=\zeta+4\eta/3$ is an attenuation constant, where ζ and η are the bulk and shear viscosities. The first two terms on the left-hand side of Eq. (1) represent the linear lossless wave equation and the third term on the left-hand side describes the viscous volume attenuation. The first two terms on the right-hand side are quadratic-nonlinear ones and the last one is a cubic-nonlinear term. If $b=0$, Eq. (1) represents an exact wave equation for plane-waves in perfect gas, see, e.g., Hamilton and Morfey (1998). Acoustic pressure can be calculated from the solution of Eq. (1) as

$$p'=\frac{\rho_0c_0^2}{\gamma}\left\{1-\frac{\gamma-1}{c_0^2}\left[\frac{\partial\varphi}{\partial t}+\frac{1}{2}\left(\frac{\partial\varphi}{\partial x}\right)^2-\frac{b}{\rho_0}\frac{\partial^2\varphi}{\partial x^2}\right]\right\}^{\gamma/(\gamma-1)}-\frac{\rho_0c_0^2}{\gamma}, \tag{2}$$

see Ilinskii *et al.* (1998). If the cubic-nonlinear term in Eq. (1) is dropped and $\partial^2\varphi/\partial t^2 = c_0^2\partial^2\varphi/\partial x^2$ is substituted into the corresponding terms (the third one on the left-hand side and the second one on the right-hand side), the error is a third-order small and the resulting equation reads

$$c_0^2\frac{\partial^2\varphi}{\partial x^2} - \frac{\partial^2\varphi}{\partial t^2} = \frac{\partial}{\partial t}\left[\left(\frac{\partial\varphi}{\partial x}\right)^2 + \frac{\gamma-1}{2c_0^2}\left(\frac{\partial\varphi}{\partial t}\right)^2 - \frac{b}{\rho_0 c_0^2}\frac{\partial^2\varphi}{\partial t^2}\right], \tag{3}$$

which is the well-known Kuznetsov equation,[1] see Kuznetsov (1970).

Acoustic pressure can be calculated from the solution of Eq. (3) using Eq. (2) or, for consistency, it can be recast in the second approximation using the Taylor series expansion into the form

$$p' = -\rho_0\frac{\partial\varphi}{\partial t} - \frac{\rho_0}{2}\left(\frac{\partial\varphi}{\partial x}\right)^2 + \frac{\rho_0}{2c_0^2}\left(\frac{\partial\varphi}{\partial t}\right)^2 + b\frac{\partial^2\varphi}{\partial x^2}. \tag{4}$$

If Eq. (1) or (3) is used for calculation of acoustic field in an acoustic resonator driven by a vibrating piston, they can be supplemented with the following boundary conditions:

$$\left(\frac{\partial\varphi}{\partial x}\right)_{x=0} = 0, \quad \left(\frac{\partial\varphi}{\partial x}\right)_{x=L} = v_p(t), \tag{5}$$

where L is the length of the resonant cavity and $v_p(t)$ is the velocity of the vibrating piston.

The inhomogeneous Burgers equation is another model equation which can be used for the description of nonlinear standing waves in the cylindrical resonator. The inhomogeneous Burgers equation can be derived from the Kuznetsov equation (3). There are several ways how to derive this model equation [see, e.g., Gusev (1984), Rudenko *et al.* (2001), Enflo and Hedgerg (2002)]. However, all of these derivation-procedures follow from the assumption that the acoustic field inside the cylindrical resonator can be described as a superposition of two nonlinear counter-propagating waves $\varphi_\pm$ which are coupled only by conditions on the resonator side-walls. This assumption means that we can ignore a mutual interaction of the counter-propagating waves. To justify the assumption we can use the method which has been sketched, e.g., in Gusev (2005) and Gusev *et al.* (1999).

Within the framework of the second order approximation of the nonlinear acoustics we can suppose that each of the counter-propagating waves is relatively weak in its amplitude and therefore the nonlinear processes are also weak. The relative weakness of the nonlinear processes allows us to suppose that wave profiles of the counter-propagating waves vary slowly with time and propagation distance, i.e., the changes in the wave profiles are assumed to be small for distances of order $O(\lambda)$ and times of order $O(T)$, where λ is the wavelength and T is the wave period. We can formalize the mentioned statement by the fact that we will search for the solution of the Kuznetsov equation (3) in the following form:

$$\varphi = \mu\varphi_+(t_1 = \mu t, x_1 = \mu x, \tau_+ = t - x/c_0) - \mu\varphi_-(t_1 = \mu t, x_1 = \mu x, \tau_- = t + x/c_0), \tag{6}$$

where $\mu < 1$ is a small scaling parameter and t_1 and x_1 represent slow time and space coordinates. After substituting the expression (6) into Eq. (3), considering $b \sim \mu$ and ignoring the terms of the order 3 and higher we obtain

$$\mu\frac{\partial^2\varphi_\pm}{\partial\tau_\pm\partial t_1} \pm c_0\mu\frac{\partial^2\varphi_\pm}{\partial\tau_\pm\partial x_1} \pm \frac{\beta}{2c_0^2}\left[\frac{\partial}{\partial\tau_\pm}\left(\frac{\partial\varphi_\pm}{\partial\tau_\pm}\right)^2 - \frac{\partial\varphi_+}{\partial\tau_+}\frac{\partial\varphi_-}{\partial\tau_-}\right] - \frac{b}{2\rho_0 c_0^2}\frac{\partial^3\varphi_\pm}{\partial\tau_\pm^3} = 0, \tag{7}$$

where $\beta = (\gamma + 1)/2$. The second term in square brackets in Eq. (7) represents the interaction of the counterpropagating waves.

Equation (7) formally contains two unknowns ($\varphi_\pm$), two fast variables ($\tau_\pm$), and two slow variables (t_1, x_1). The fast variables are not independent because they are connected by the relation $\tau_- = \tau_+ + 2x/c_0$. Therefore in the coordinate system (t_1, x_1, τ_+), accompanying the wave propagating to the right, the function $\varphi_-(t_1, x_1, \tau_-) = \varphi_-(t_1, x_1, \tau_+ + 2x/c_0)$ is a fast varying function of coordinate x. After using the following operator:

$$\langle \cdots \rangle \equiv \frac{1}{\lambda}\int_{x-\lambda/2}^{x+\lambda/2} (\cdots)\mathrm{d}x, \tag{8}$$

we can conduct the formal procedure of the separation of the counter-propagating waves because φ_+ does not depend on the fast coordinate x and consequently the operator (8) does not influence φ_+ and its derivatives. Assuming the absence of an average directional motion of fluid and the wave periodicity we can write

$$\langle \varphi_- \rangle \equiv \frac{1}{\lambda}\int_{x-\lambda/2}^{x+\lambda/2} \varphi_-\left(t_1, x_1, \tau_+ + \frac{2x'}{c_0}\right)\mathrm{d}x' = \frac{1}{T}\int_{t-T/2}^{t+T/2} \varphi_-(t_1, x_1, \tau_+ + 2t')\,\mathrm{d}t' = 0. \tag{9}$$

Therefore by the averaging we obtain

$$\langle \varphi_- \rangle = 0, \quad \left\langle \frac{\partial \varphi_-}{\partial \tau_-} \right\rangle = 0, \quad \left\langle \frac{\partial}{\partial \tau_-}\left(\frac{\partial \varphi_-}{\partial \tau_-}\right)^2 \right\rangle = 0.$$

After application of the operator (8) in the coordinate system (t_1, x_1, τ_+) for Eq. (7) we obtain an equation only for φ_+. Repeating this procedure for the coordinate system (t_1, x_1, τ_-) accompanying the wave propagating to the left, we get an equation only for φ_-.

The separated equations have the form

$$\mu\frac{\partial^2 \varphi_\pm}{\partial \tau_\pm \partial t_1} \pm c_0 \mu \frac{\partial^2 \varphi_\pm}{\partial \tau_\pm \partial x_1} \pm \frac{\beta}{2c_0^2}\frac{\partial}{\partial \tau_\pm}\left(\frac{\partial \varphi_\pm}{\partial \tau_\pm}\right)^2 - \frac{b}{2\rho_0 c_0^2}\frac{\partial^3 \varphi_\pm}{\partial \tau_\pm^3} = 0. \tag{10}$$

Within the framework of second order theory it is possible to consider the interactions of the counter-propagating waves to be ineffective, which means that effects of the interactions do not accumulate. Consequently, the operator (8) retains in Eq. (7) only the terms which provide the influence accumulating with propagation distance [Gusev *et al.* (1999)]. This conclusion has been clarified in the works Rudenko *et al.* (2001) and Rudenko (2009) whose explanation is based on an approximate solution of the one-dimensional Westervelt equation for ideal fluids. Taking into account the relation

$$v_\pm = \frac{\partial \varphi_\pm}{\partial x} = \mp \frac{1}{c_0}\frac{\partial \varphi_\pm}{\partial \tau_\pm} + \mu \frac{\partial \varphi_\pm}{\partial x_1} \tag{11}$$

and keeping the assumed second order of accuracy of Eq. (10) we can rewrite it for acoustic velocities as

$$\frac{\partial v_\pm}{\partial t} \pm c_0 \frac{\partial v_\pm}{\partial x} - \frac{\beta}{c_0} v_\pm \frac{\partial v_\pm}{\partial \tau_\pm} - \frac{b}{2\rho_0 c_0^2}\frac{\partial^2 v_\pm}{\partial \tau_\pm^2} = 0. \tag{12}$$

Here Eq. (12) is expressed in the original physical coordinates t and x.

As the nonlinear standing wave in a resonator is given as the superposition of two nonlinear counter-propagating waves we can write

$$v = \frac{\partial \varphi}{\partial x} = \frac{\partial \varphi_+}{\partial x} - \frac{\partial \varphi_-}{\partial x} = v_+ - v_-. \tag{13}$$

The boundary conditions (5) can be formulated in this case as

$$v = (v_+ - v_-)_{x=0} = 0, \tag{14}$$

$$v = (v_+ - v_-)_{x=L} = v_p(t) = -v_0 \sin(\omega t), \tag{15}$$

and an initial condition can be given as

$$v_\pm(t=0) = 0, \tag{16}$$

where v_0 is the velocity amplitude of the exciting piston which vibrates with an angular frequency ω. The angular frequency is assumed to be equal to one of the resonator eigenfrequencies (the resonance condition) that is given as

$$\omega_n = \frac{n\pi c_0}{L}, \quad n = 1, 2.3, \ldots . \tag{17}$$

With respect to the conditions (14)–(16) it is possible to apply the method of successive-approximations to Eqs. (12) which leads to the following forced model equations [see, e.g., Gusev (1984)]:

$$\frac{\partial \bar{v}_\pm}{\partial t} - \frac{\beta}{c_0}\bar{v}_\pm \frac{\partial \bar{v}_\pm}{\partial \tau_\pm} - \frac{b}{2\rho_0 c_0^2}\frac{\partial^2 \bar{v}_\pm}{\partial {\tau_\pm}^2} = \frac{v_0 c_0}{2L}\sin(\omega\tau_\pm), \tag{18}$$

where $\bar{v}_\pm$ represents the acoustic velocity of the counter-propagating waves in the first approximation, see, e.g., Gusev (1984). Equation (18) represents the inhomogeneous Burgers equation.

The acoustic velocity of the standing wave can be calculated from solution of Eq. (18) [see Bednarik and Konicek (2004)] as

$$v(t,x) = \bar{v}_+(t,\tau_+) - \bar{v}_-(t,\tau_-) - \frac{v_0 x}{L}\cos\left(\frac{\omega x}{c_0}\right)\sin(\omega\tau). \tag{19}$$

3. Comparison of numerical solutions of individual model equations

The model equations (1) and (3) were solved numerically in the time domain using the algorithm proposed in Cervenka (2007) whereas Eq. (18) was solved numerically in the frequency domain, see, e.g., Ginsberg and Hamilton (1998). For all the numerical

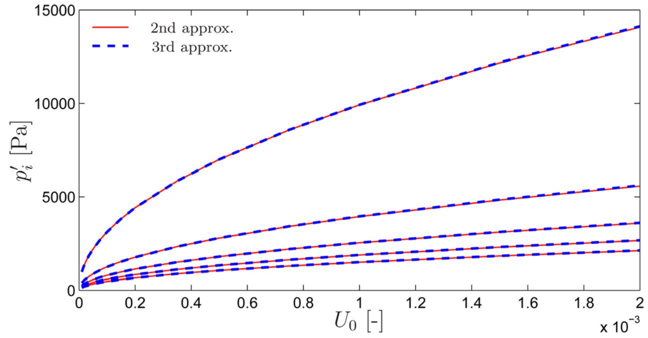

Fig. 1. (Color online) Comparison of amplitudes of the first five harmonics (one-side spectrum) of acoustic pressure at $x=0$ calculated using Eqs. (1) and (3).

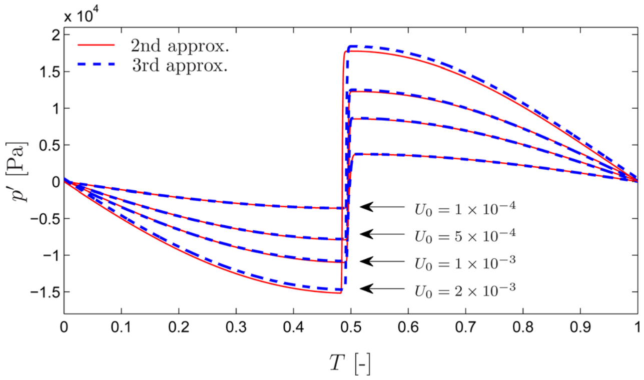

Fig. 2. (Color online) One period of steady-state acoustic pressure at $x = 0$ calculated using Eqs. (1) and (3).

calculations the driving piston vibrated at the fundamental eigen-frequency of ($\omega = \omega_1$) and air at room conditions was assumed as fluid and $G = \pi\omega b/(\rho_0 c_0^2) = 10^{-3}$. Numerical results are compared in Figs. 1–3. From these figures it is evident that there are only slight differences between the results of numerical solutions of the assumed model equations, even for relatively strong excitation of acoustic waves.

The comparison of numerical solutions of Eqs. (1) and (3) for the acoustic pressure is depicted in Figs. 1 and 2. It is obvious from Fig. 1 that the amplitudes of the first five harmonics are practically identical. One can observe a small discrepancy between the numerical solutions for $U_0 = v_0/(\pi c_0) = 2 \times 10^{-3}$ in Fig. 2 which is caused by the fact that a bit higher value of a dc-pressure follows from the model equation (1). The numerical solution for the acoustic velocity of all the model equations are sketched in Fig. 3. Again we can observe a slight difference of the solution of Eq. (1) with respect to the other solutions. This slight difference is reflected in a small shape asymmetry of the standing wave and is caused by a fine nonlinear resonance frequency shift following from the model equation (1). The numerical results show that unlike Eqs. (1) and (3), the inhomogeneous Burgers equation (18) does not capture this effect, however, relatively high nonlinear attenuation causes that the influence of the nonlinear resonance frequency shift can be ignored for acoustic fields up to the acoustic Mach number of about 0.1. The numerical solutions of Eqs. (3) and (18) are almost identical for all the driving amplitudes excluding the Gibbs oscillations.

4. Conclusion

In this work we presented three widely used model equations for the description of nonlinear standing waves in constant-cross-sectioned resonators with rigid ends. One

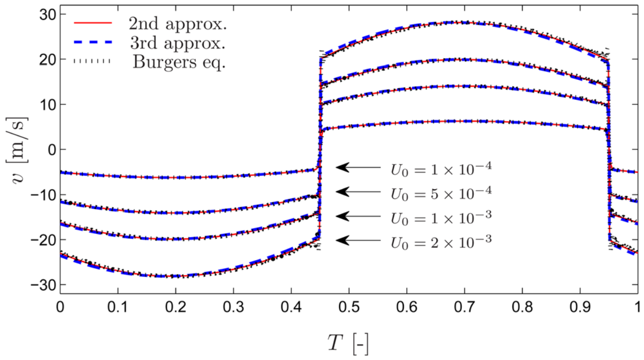

Fig. 3. (Color online) One period of steady-state acoustic velocity at $x = L/2$ calculated using Eqs. (1), (3), and (18).

of the model equations is more accurate by taking into account nonlinear effects of the third order. The remaining two model equations (3) and (18) can be derived from this more accurate one under certain assumptions. The model equations were solved numerically and numerical results were compared to each other to check whether acoustic fields inside the constant-cross-sectioned resonators satisfy the conditions under which the simpler model equations have been derived. By comparing the results of the model equations it can be stated that it is possible to use both the Kuznetsov and inhomogeneous Burgers equations for the description of nonlinear standing waves in the constant-cross-sectioned resonators even for relatively high sound pressure levels of practical interest (the acoustic Mach number of about 0.1). Unlike Eqs. (1) and (3), the inhomogeneous Burgers equation (18) does not capture the resonance frequency shift. If generation of higher harmonics is not suppressed, relatively high nonlinear attenuation prevents the effect of nonlinear resonance frequency shift to manifest itself in a substantial way. In the case of any method used for suppression of the higher harmonics it would probably be necessary to take into account this effect and to verify the applicability of the inhomogeneous Burgers equation using a more complex model.

From this conclusion it follows that in the case of relatively high nonlinear attenuation, an acoustic field inside the constant-cross-sectioned resonators can be described as a superposition of two nonlinear counter-propagating waves. It is also possible to ignore their mutual interactions because these waves couple only weakly and their coupling does not have cumulative character. For this reason we can use the far simpler inhomogeneous Burgers equation in comparison with Eq. (1) for analysis of nonlinear acoustic fields and a possible derivation of approximate analytical solutions.

Acknowledgments

This work was supported by GACR Grant No. P101/12/1925. The numerical calculations were performed at the Computing and Information Centre of CTU.

References and links

[1] The original derivation of this equation Kuznetsov (1970) also takes into account the influence of losses due to thermal conductivity which are incorporated into the parameter *b*.

Bednarik, M., and Konicek, P. (**2004**). "Asymptotic solutions of the inhomogeneous Burgers equation," J. Acoust. Soc. Am. **115**, 91–98.

Cervenka, M. (**2007**). "Numerical simulation of two-dimensional high-amplitude acoustic field in cylindrical resonators using Kuznetsov's equation," *19th International Congress on Acoustics*, Madrid, CD-ROM.

Enflo, B. O., and Hedberg, C. M. (**2002**). *Theory of Nonlinear Acoustics in Fluids* (Kluwer Academic, Dordrecht), Chap. 8.2, pp. 226–231.

Ginsberg, J. H., and Hamilton, M. F. (**1998**). "Computational methods," in *Nonlinear Acoustics*, edited by M. F. Hamilton and D. T. Blackstock (Academic, San Diego), Chap. 11, pp. 309–316.

Gusev, V. E. (**1984**). "Buildup of forced oscillations in acoustic resonator," Sov. Phys. Acoust. **30**, 121–125.

Gusev, V. E. (**2005**). "On the interaction of counterpropagating acoustic waves in resonant rods composed of materials with hysteretic quadratic nonlinearity," J. Acoust. Soc. Am. **117**, 1850–1857.

Gusev, V. E., Bailliet, H., Lotton, P., and Bruneau, M. (**1999**). "Interaction of counterpropagating acoustic waves in media with nonlinear dissipation and in hysteretic media," Wave Motion **29**, 211–221.

Hamilton, M. F., and Morfey, C. L. (**1998**). "Model equations," in *Nonlinear Acoustics*, edited by M. F. Hamilton and D. T. Blackstock (Academic, San Diego), Chap. 3, pp. 47–49.

Ilinskii, Yu. A., Lipkens, B., Lucas, T. S., Van Doren, T. W., and Zabolotskaya, E. A. (**1998**). "Nonlinear standing waves in an acoustical resonator," J. Acoust. Soc. Am. **104**, 2664–2674.

Kuznetsov, V. P. (**1970**). "Equation of nonlinear acoustics," Sov. Phys. Acoust. **16**, 467–468.

Lawrenson, Ch. C., Lipkens, B., Lucas, T. S., Perkins, D. K., and Van Doren, T. W. (**1998**). "Measurements of macrosonic standing waves in oscillating closed cavities," J. Acoust. Soc. Am. **104**, 623–637.

Rudenko, O. V. (**2009**). "Nonlinear standing waves, resonance phenomena, and frequency characteristics of distributed systems," Acoust. Phys. **55**, 27–54.

Rudenko, O. V., Hedberg, C. M., and Enflo, B. O. (**2001**). "Nonlinear standing waves in a layer excited by the periodic motion of its boundary," Acoust. Phys. **47**, 452–460.

A.4 Acoustic particle displacement resonator

Červenka, M., Bednařík, M., Acoustic particle displacement resonator, Applied Acoustics 99, 155-160, (2015).

Applied Acoustics 99 (2015) 155–160

Contents lists available at ScienceDirect

Applied Acoustics

journal homepage: www.elsevier.com/locate/apacoust

Acoustic particle displacement resonator

M. Červenka *, M. Bednařík

Czech Technical University in Prague, Faculty of Electrical Engineering, Technická 2, 166 27 Prague 6, Czech Republic

A R T I C L E   I N F O

Article history:
Received 21 January 2015
Received in revised form 4 June 2015
Accepted 15 June 2015
Available online 26 June 2015

Keywords:
High amplitude
Particle displacement
Resonator
Loudspeaker
Minor losses

A B S T R A C T

A simple device consisting of a waveguide and two loudspeakers is proposed for generation of low-frequency standing acoustic field with high amplitude of acoustic velocity and particle displacement, which is primarily intended to be used for stabilization of electric discharges in acoustic field. A coupled model of loudspeakers and nonlinear wave equation including waveguide radius variability, thermoviscous attenuation in boundary layer and minor losses is developed. The results of the conducted experiments validate the model revealing that the minor losses and acoustically generated turbulence in the boundary layer represent an important means of acoustic energy dissipation in this and similar applications.

1. Introduction

In recent years, some non-conventional applications utilizing high-amplitude acoustic fields have begun to develop; acoustic compressors, mixers, thermoacoustic engines or refrigerators can serve as an example. Another example is stabilization of electric discharge in acoustic pressure node of a high-amplitude standing wave, see e.g. [1,2], which finds its application in plasma-chemical reactors increasing the efficiency of the processes leading to the destruction of toxic pollutants, decomposition of volatile organic compounds, etc. It has been found in work [2] that acoustic field with high amplitude of particle displacement plays a key role in these processes so it is desirable to find an effective way of its generation. As the acoustic displacement amplitude is for given acoustic velocity amplitude inversely proportional to frequency, it is necessary, in case of standing waves, to pay an attention to reasonable dimensions of the used machinery.

For this reason (and we are convinced that there would also be other applications) a simple device has been proposed for generation of standing acoustic field with high amplitudes of acoustic particle displacement, which is the subject of this article. Section 2 describes its construction and experimental techniques used, Section 3 deals with a theoretical model which is needed in order to understand the underlying physics. Section 4 presents the obtained results and comparison of experimental data with the model predictions, Section 5 then concludes the article.

2. Experimental setup

2.1. Low-frequency acoustic resonator

The proposed device allowing generation of acoustic field with high amplitude of acoustic velocity and displacement is schematically depicted in Fig. 1. It consists of two electrodynamic transducers (loudspeakers) B&C 6MD38-8 (power handling 240 W), enclosed in small loudspeaker-boxes, connected in antiphase in series, which drive acoustic field in a waveguide (plexiglass tube with inner radius $r_1 = 12$ mm, length $2 \times l_1 = 300$ mm and thickness 2 mm) through conical segments (made from plastic funnels, small inner radius $r_1 = 12$ mm, large inner radius $r_2 = 75$ mm, length $l_2 = 60$ mm) and short segments with inner radius r_2 and length $l_3 = 40$ mm. Due to the antiphase driving of the loudspeakers, the primary acoustic field (the first harmonics) has node of acoustic pressure and anti-node of acoustic velocity and particle displacement at the centre of the waveguide. The loudspeakers are driven by a harmonic signal which is amplified using power amplifier Akiyama AMD400.

2.2. Measurements

Electrical and acoustical measurements on the proposed device were conducted as follows.

Input electrical impedance was measured using a home-made program written in LabView which controls a sine-wave generator (Agilent U2761A) and AC voltmeter and ammeter (Agilent U2741A). The generated signals were amplified by a power

---

* Corresponding author.
E-mail address: milan.cervenka@fel.cvut.cz (M. Červenka).

http://dx.doi.org/10.1016/j.apacoust.2015.06.009
0003-682X/

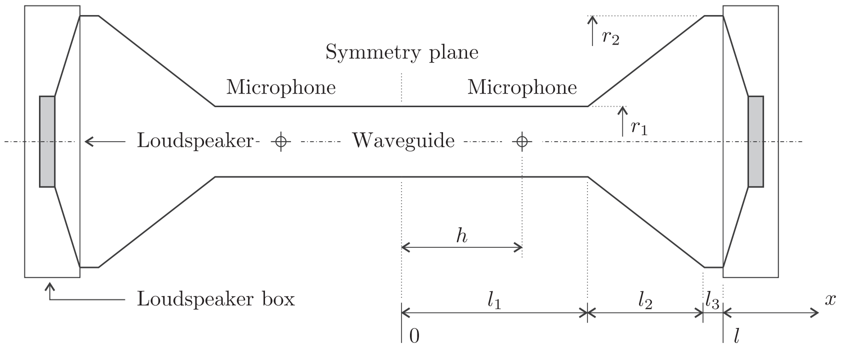

Fig. 1. Arrangement of the device.

amplifier, the measurements were conducted at constant voltage amplitude. The same equipment was used for measurement of impedance characteristics of the loudspeakers in vacuum in order to determine their parameters, see e.g. [3], using the nonlinear least-squares fit.

Acoustic velocity and particle displacement at the centre of the device were determined using the two-microphone method, see e.g. [4]. Two 1/8" microphones (G.R.A.S. Type 40DP) were placed symmetrically along the centre in the waveguide wall separated by the distance of $2 \times h = 160$ mm, measuring acoustic pressures $p'_{\rm A}(t)$ and $p'_{\rm B}(t)$. If the microphones separation $2 \times h \ll \lambda$, where λ is the wavelength, acoustic velocity v between the microphones can be calculated using the linearised Euler's equation as

$$v(t) = \frac{1}{\rho_0} \int \frac{p'_{\rm B}(t) - p'_{\rm A}(t)}{2h} {\rm d}t, \tag{1}$$

where ρ_0 is the ambient fluid density. Acoustic particle displacement $\xi(t)$ can be then calculated as

$$\xi(t) = \int v(t) {\rm d}t. \tag{2}$$

The microphone signals were amplified (G.R.A.S. Type 26AC Preamplifiers + G.R.A.S. Type 12AB Microphone Power Module) and digitized using DAQ card (National Instruments PCI-6251) controlled by a LabView-written program; the integrals in Eqs. (1) and (2) were calculated using the FFT method implemented in Matlab.

3. Theoretical model

3.1. Model equation for acoustic field in a waveguide

High-amplitude acoustic field inside a variable-cross-section waveguide can be described using a set of two quasi-one-dimensional equations

$$\frac{\partial p'}{\partial x} = -\rho_0 \frac{\partial v}{\partial t} - \frac{p'}{c_0^2}\frac{\partial v}{\partial t} + \frac{v}{c_0^2}\frac{\partial p'}{\partial t} + \frac{2}{r}\frac{{\rm d}r}{{\rm d}x}\rho_0 v^2 + \frac{\rho_0 \delta_{\rm v}}{c_0^2}\frac{\partial^2 v}{\partial t^2}, \tag{3a}$$

$$\frac{\partial v}{\partial x} - \frac{2\varepsilon}{r^2}\frac{\partial^{1/2}(rv)}{\partial t^{-1/2}\partial x} = -\frac{1}{\rho_0 c_0^2}\frac{\partial p'}{\partial t} - \frac{2}{r}\frac{{\rm d}r}{{\rm d}x} v + \frac{\gamma}{2\rho_0^2 c_0^4}\frac{\partial p'2}{\partial t} + \frac{1}{2c_0^2}\frac{\partial v^2}{\partial t} + \frac{\delta_{\rm t}}{\rho_0 c_0^4}\frac{\partial^2 p'}{\partial t^2}, \tag{3b}$$

where $p' = p - p_0$ is the acoustic pressure, p is the total pressure, p_0 is the ambient pressure, v is the acoustic velocity, t is the time, x is the spatial coordinate along the waveguide, $r = r(x)$ is its radius, c_0 is the small-signal speed of sound, γ is the adiabatic exponent, $\delta_{\rm v} = (\zeta + 4\eta/3)/\rho_0$ is the diffusivity of sound due to viscosity, where η, ζ are the coefficients of shear and bulk viscosity, respectively, $\delta_{\rm t} = \kappa(1/c_V - 1/c_p)/\rho_0$ is the diffusivity of sound due to thermal conduction, where κ is the coefficient of thermal conduction and $c_{\rm p}$, $c_{\rm V}$ are the specific heats at constant pressure and volume, respectively. Further, $\varepsilon = \sqrt{\nu_0}[1 + (\gamma - 1)/\sqrt{Pr}]$, where $\nu_0 = \eta/\rho_0$ is the kinematic viscosity and $Pr = \eta c_p/\kappa$ is the Prandtl number. The term with coefficient ε describes the acoustic energy dissipation in the boundary layer; additional losses due to acoustically generated turbulence, which appear to play an important role in this case, are incorporated into the coefficient ε in a straightforward way, see Appendix A and [5].

Eq. (3) are derived in the second approximation, they account for waveguide cross-section spatial variability, nonlinearity, thermoviscous volume attenuation and thermoviscous attenuation in the boundary layer. The derivation is briefly sketched in Appendix A. Use of Eq. (3) in this case is more advantageous than employing the model equations used e.g. in works [6,7], as Eq. (3) are formulated using the primary acoustic variables p', v and it is thus simple and straightforward to couple them to a model of an electro-acoustic transducer or to a model of the minor losses.

As we are further focused on periodic steady-state acoustic fields, the acoustic quantities are represented as

$$q(x,t) = \frac{1}{2}\sum_{n=-N}^{N} \hat{q}_n(x) {\rm e}^{{\rm i}n\omega t}, \tag{4}$$

where $q(x,t)$ stands for $p'(x,t)$, $v(x,t)$ and $\hat{q}_n(x)$ represents individual (complex) harmonics. Further, ω is the driving frequency, N is the number of harmonics taken into account and $\hat{q}_{-n}(x) = \hat{q}_n^*(x)$, where the asterisk denotes the complex conjugate, because of the fact that physical quantities are represented by real functions. Substituting expansion (4) into Eq. (3) results in a set of $2N + 1$ ordinary differential equations (ODEs) for phasors $\hat{p}'_0, \ldots, \hat{p}'_N$, $\hat{v}_1, \ldots, \hat{v}_N$. The ODEs were integrated numerically using the adaptive-step-size eight-order Runge–Kutta method, see e.g. [8].

3.2. Model of the loudspeakers

The loudspeakers situated at the ends of the waveguide, see Fig. 1, are modelled using lumped-element circuits, see e.g. [3], the corresponding equations represent the boundary conditions for Eq. (3) at $x = -l$ (the left loudspeaker) and $x = l$ (the right loudspeaker) and have the form

$$\left[Z_{\rm e} Z'_{\rm m} + (Bl_{\rm vc})^2\right] \hat{v}_n + Z_{\rm e} S_{\rm d} \hat{p}'_n - Bl_{\rm vc} \hat{u}_n^{\rm L} = 0 \quad \text{for} \quad x = -l, \tag{5a}$$

$$-\left[Z_{\rm e} Z'_{\rm m} + (Bl_{\rm vc})^2\right] \hat{v}_n + Z_{\rm e} S_{\rm d} \hat{p}'_n - Bl_{\rm vc} \hat{u}_n^{\rm R} = 0 \quad \text{for} \quad x = l, \tag{5b}$$

where $Z_{\rm e} = R_{\rm e} + {\rm i}n\omega L_{\rm e}$ is the electrical impedance of the loudspeaker voice coil, $R_{\rm e}$ is the electrical resistance and $L_{\rm e}$ is the electrical inductance; $Z'_{\rm m} = Z_{\rm m} + S_{\rm d}^2/{\rm i}n\omega C_{\rm a}$, where $Z_{\rm m} = R_{\rm m} + {\rm i}n\omega M + 1/{\rm i}n\omega C_{\rm m}$ is the loudspeaker mechanical impedance, $R_{\rm m}$ is the mechanical resistance of the diaphragm suspension, M is the moving mass of the diaphragm assembly, C_m is the mechanical compliance of the diaphragm suspension; S_d is the effective piston area of the diaphragm, $C_\mathrm{a} = V_\mathrm{b}/\rho_0 c_0^2$ is the acoustic compliance of the enclosure behind the diaphragm, where V_b is its volume; B is the magnetic flux density in the loudspeaker's air gap and l_vc is the length of the voice coil in the magnetic field. Finally, $\hat{u}_n^\mathrm{L}$, $\hat{u}_n^\mathrm{R}$ represent the driving voltage of the left and the right loudspeaker.

The two-point boundary-value problem (5) for Eq. (3) was solved using the shooting method, see e.g. [8].

3.3. Minor losses

It is well-known from hydraulics that pressure drops appear in high-Reynolds-number flows through channels with cross-section changes (junctions). These effects are called the minor losses, they result from flow separation, vorticity generation, turbulence and other effects. For a steady flow, the pressure drop resulting from the minor losses is characterized by the dimensionless parameter K as

$$\Delta p = \frac{1}{2} K \rho v^2, \tag{6}$$

where ρ is the fluid density and v is the flow velocity. The values of K for variety of geometries are tabulated, see e.g. [9].

Relation (6) can according to Iguchi's hypothesis, see e.g. [10], be used even in case of unsteady flows represented by acoustic waves, if $|\hat{\xi}_1|$ is larger than all other dimensions in the vicinity [10–12]. The minor loss coefficients for oscillatory flows have been studied both theoretically and experimentally, see e.g. [13,14]. According to [10,11], Eq. (6) can be in case of oscillatory flows rewritten as

$$\Delta p'(t) = -\frac{1}{2} K \rho_0 |v(t)| v(t), \tag{7}$$

where $v(t)$ now stands for the acoustic velocity. The minus sign in Eq. (7) provides the correct sign of the pressure drop with respect to the flow orientation. It is known that the value of K differs in case of *contracting* flow (the fluid flows in the direction of decreasing pipe radius), $K = K_\mathrm{con}$, and *expanding* flow (the fluid flows in the direction of increasing pipe radius), $K = K_\mathrm{exp}$. In the case of acoustic field, the flow changes its orientation twice every cycle. Here, the values of K_con and K_exp are assumed to be constant. In this case, minor losses are modelled at the junctions of the constant-cross-section part of the waveguide (with radius r_1) and the conical segments.

The model of minor losses (7) is included into the model of acoustic field in the waveguide as follows. Model Eq. (3) is integrated in frequency domain along the spatial coordinate x from $x = -l$ to $x = -l_1$, which means that values of $\hat{v}_n(-l_1)$ and $\hat{p}'_n(-l_1)$ are known here. Then, time course of one period of acoustic velocity $v(-l_1, t_m), m = 0, \ldots, M$ is calculated using Eq. (4), subsequently, and the time course of the pressure drop is calculated using Eq. (7), where K_con or K_exp are chosen according to the sign of $v(-l_1, t_m)$ at the particular times t_m. Finally, $\Delta\hat{p}'_n$ are calculated numerically using the Fourier integral (which is implemented using the Simpson's rule) and values of $\hat{v}_n(-l_1)$, $\hat{p}'_n(-l_1) + \Delta\hat{p}'_n$ are used as an initial condition for numerical integration of Eq. (3) from $x = -l_1$ to $x = l_1$ where the same procedure is repeated.

4. Results and discussion

All experiments were conducted in air at room conditions. Corresponding parameters were used in the numerical model. According to [9], the minor loss coefficients for given geometry were determined as $K_\mathrm{exp} = 0.87$ and $K_\mathrm{con} = 0.28$.

Frequency characteristics of input electrical impedance of the device measured with loudspeakers connected in series in antiphase and in-phase (shown only for reference) are presented in Fig. 2. In both the cases, amplitude of the driving voltage was set to 1 V. The vertical arrow marks the resonance peak (operating point) in vicinity of which maximum values of acoustic velocity and particle displacement are attained; here, the local maximum of input impedance is found at $f_\mathrm{rez} = 64.3$ Hz. This resonance is associated with the first antisymmetric mode of the waveguide with acoustic pressure node at the centre (the corresponding resonance frequency of this waveguide ended by rigid caps, according to eigenfrequency analysis made using COMSOL Multiphysics, equals to 86.5 Hz). The main resonance peak (for both the loudspeaker connections) is associated with the electro-mechanical resonance of the loudspeakers, the resonance frequencies differ (392 Hz, 402 Hz) as in the individual cases, the loudspeakers are loaded by different input impedances of the waveguide. It can be seen that these resonance peaks are not symmetric which may be caused by the fact that the loudspeakers' diaphragms (cones) do not vibrate as rigid bodies any more at these frequencies, see e.g. [3]. The low-frequency resonance peak for the loudspeakers connected in-phase disappears as the acoustic resonance frequency of the first symmetric mode of the waveguide is 537 Hz (calculated using COMSOL Multiphysics).

Fig. 3 shows comparison of measured input electrical impedance modulus (connection in antiphase) with the model data in the vicinity of the operating point. The volume V_b (associated with the acoustic compliance) of the loudspeaker-boxes as well as the acoustic resistance of the boxes were slightly adjusted to fit the measured data; especially the value of V_b is hard to determine due to complicated geometry of the rear-side of the loudspeakers. It can be seen that the measured and theoretical results correspond to each other well; the agreement of measured and theoretical data decreases with increasing frequency as the membrane vibration at

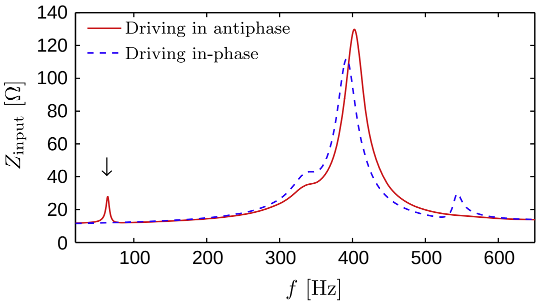

Fig. 2. Input electrical impedance of the device measured with loudspeakers connected in antiphase and in-phase.

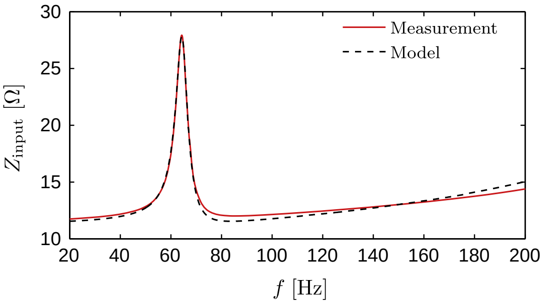

Fig. 3. Input electrical impedance of the device with loudspeakers connected in antiphase; comparison of measured data and model.

higher frequencies cannot be described using a lumped-element model.

Fig. 4 shows frequency characteristics of amplitude of the first harmonics of acoustic velocity measured using the two-microphone technique at the centre of the waveguide for several driving voltages (in this and all the remaining cases, the loudspeakers are connected in series in antiphase). It can be observed that for $U = 35$ V, the velocity amplitude reaches the value of 36.3 m/s at resonance frequency of 66 Hz. In this case, the power input of the device is 29 W. Even in this case, the time-course of acoustic velocity is almost distortion-free (amplitude of the second harmonics is 0.07 m/s, amplitude of the third harmonics is 0.27 m/s). It is also apparent that due to nonlinear losses, the maximum velocity amplitude is not proportional to the driving amplitude and that there is small resonance-frequency shift–the resonance frequency increases with the driving voltage amplitude.

Acoustic velocity in the waveguide is almost distortion free even if the acoustic pressure in the narrow tube is distorted by the second harmonics, see Fig. 5. The reason is that unlike the first harmonics of acoustic pressure spatial distribution along the waveguide is antisymmetric, i.e. $\hat{p}'_1(x) \approx -\hat{p}'_1(-x)$, as the loudspeakers are driven in antiphase, the second harmonics distribution is symmetric, i.e. $\hat{p}'_2(x) \approx \hat{p}'_2(-x)$, and almost constant along the narrow tube which results in negligible gradient and thus velocity.

Fig. 6 shows frequency characteristics of amplitude of the first harmonics of acoustic particle displacement measured at the centre of the waveguide for several driving voltages. The characteristics are similar as those shown in Fig. 4 as the resonance peaks are rather broad, the decrease of amplitude above the resonance frequency is faster as $|\hat{\xi}_1| = |\hat{v}_1|/\omega$; the maximum displacement amplitude reaches value of 8.8 cm for $U = 35\,V$ and $f = 64.5$ Hz.

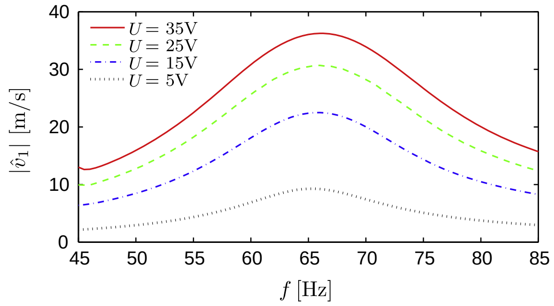

Fig. 4. Frequency characteristics of amplitude of the first harmonics of acoustic velocity measured at the centre of the waveguide for various driving voltage amplitudes.

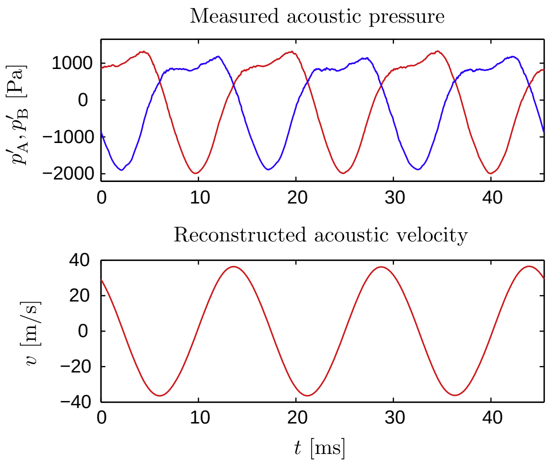

Fig. 5. Top: acoustic pressures p'_A, p'_B measured for $U = 35$ V and $f = 66$ Hz, bottom: corresponding acoustic velocity.

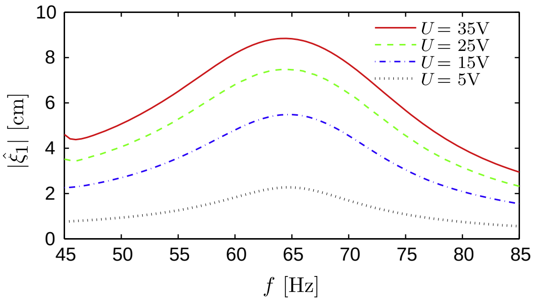

Fig. 6. Frequency characteristics of amplitude of the first harmonics of acoustic particle displacement measured at the centre of the waveguide for various driving voltage amplitudes.

Fig. 7 shows dependence of acoustic velocity amplitude at the centre of the waveguide on driving voltage amplitude for $f = 65$ Hz; measured and calculated using the proposed model with individual loss mechanisms taken into account.

It can be seen that if the minor losses and the losses due to turbulence in the boundary layer [5] are not taken into account (dotted line), the model predicts almost linear dependence of the acoustic velocity amplitude on the driving amplitude as the energy dissipation in higher harmonics is negligible. This is because of the fact that the higher harmonics are not resonantly amplified (their frequencies are not coincident with the higher eigenfrequencies due to varying radius of the waveguide, see e.g. [7], and the loudspeakers' acoustic impedance) and thus the acoustic energy transfer into them is ineffective. The dashed line corresponds to the situation when turbulent losses are taken into account and minor losses are not, again the model overestimates the velocity amplitude. When all the nonlinear loss mechanisms are taken into account, the model (solid line) fits the experimental data well. The small discrepancies for ca. $U > 25$ V may be caused by decreased loudspeakers' force factor Bl_{vc} due to high voice-coil excursion in the magnetic field, see e.g. [15].

Fig. 8 shows distribution of amplitudes of the first three harmonics of acoustic pressure calculated for $U = 35$ V and $f = 65$ Hz. The vertical lines delimit the central narrow part of the waveguide. It can be observed that in correspondence with the previously employed assumptions, the pressure gradient of the first harmonics is almost constant along the narrow part of the waveguide, whereas the second harmonics amplitude is almost constant (its gradient has almost zero value). In the central part, the amplitude of the second harmonics exceeds the first one. The jumps at the junctions of the central waveguide with the conical

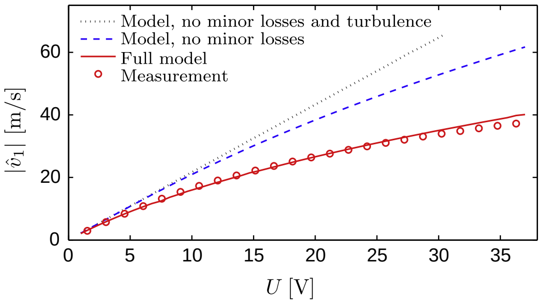

Fig. 7. Comparison of experimental results with model.

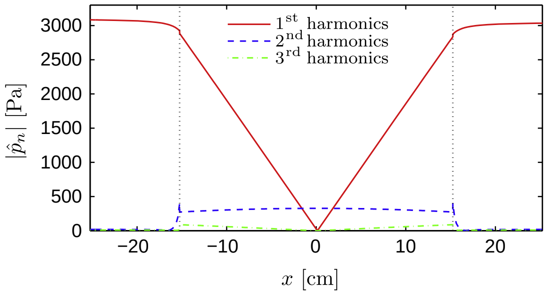

Fig. 8. Distribution of acoustic pressure harmonics amplitudes along the waveguide, $U = 35$ V, $f = 65$ Hz.

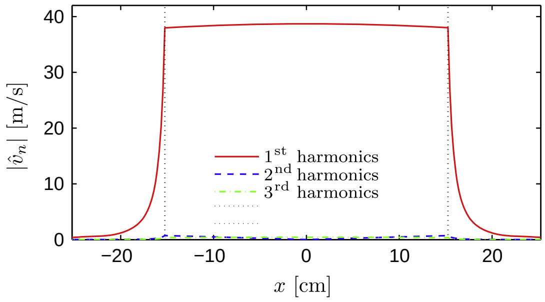

Fig. 9. Distribution of acoustic velocity harmonics amplitudes along the waveguide, $U = 35$ V, $f = 65$ Hz.

segments follow from the adopted “local” model of the minor losses.

Fig. 9 shows distribution of the first three harmonics of acoustic velocity calculated for the same conditions. It can be observed that the higher harmonics are negligible and that the amplitude of the first one is almost constant along the narrow part of the waveguide, which justifies using Eq. (1) for determination of acoustic velocity.

5. Conclusions

A simple resonant system for generation of low-frequency oscillatory flows with high amplitudes of acoustic velocity and particle displacement has been developed. The device was mainly aimed to be utilized for stabilization of electrical discharges for plasma-chemical reactors, but it can find its use in technological applications where strong acoustic fields are needed. Theoretical model has been proposed taking into account nonlinear effects (harmonics generation), losses in the acoustic boundary layer and the minor losses. Results of the conducted experiments are in good agreement with the theoretical ones validating the model, which can thus be employed for subsequent optimization of the resonant system. For example, the resonance frequency can be easily tuned by adjusting the central waveguide length or the volume of the loudspeaker boxes. As it has been shown that the minor losses due to relatively steep waveguide radius changes represent a significant means of the acoustic energy dissipation, the effectiveness of the device could be further improved by using e.g. exponential horns for coupling the loudspeakers to the central waveguide.

Acknowledgement

This work was supported by GACR – Czech Republic Grant P101/12/1925 and partially by GACR Grant 15-23079S.

Appendix A. Derivation of the model equations

The set of second-order nonlinear Eqs. (3) follows from the gas-dynamics equations for one-dimensional flow in an axisymmetric variable-cross-section hard-walled waveguide which have the following form (meaning of the individual symbols is explained in Section 3.1).

The continuity equation

$$\frac{\partial \rho}{\partial t} + \frac{1}{r^2}\frac{\partial}{\partial x}(r^2 \rho v) = \frac{2\varepsilon\rho}{r^2}\frac{\partial^{1/2}(rv)}{\partial x \partial t^{-1/2}}, \tag{A.1}$$

where ρ is the total fluid density and the Riemann–Liouville fractional integral of order $1/2$ of a function $f(t)$ on the right side of Eq. (A.1) is defined as

$$\frac{\partial^{-1/2} f}{\partial t^{-1/2}} = \frac{1}{\sqrt{\pi}}\int_{-\infty}^{t}\frac{f(\tau)}{\sqrt{t-\tau}}\mathrm{d}\tau. \tag{A.2}$$

In frequency domain, it describes losses proportional to $1/\sqrt{\mathrm{i}\omega}$.

The term on the right side of Eq. (A.1) describes the influence of the acoustic boundary layer on the fluid flow. Eq. (A.1) corresponds to the continuity equation introduced in [5].

Following [5], the model of additional losses due to the acoustically generated turbulence is incorporated into the coefficient ε by replacing the dynamic viscosity η by

$$\tilde{\eta} = \eta\left[1 + \zeta'\left(\sqrt{1 + \left(\frac{\mathrm{Re}}{\mathrm{Re}_0}\right)^2} - 1\right)\right],$$

where Re is the Reynolds number based on the boundary layer thickness and $\mathrm{Re}_0 = 400$ is the Reynolds number for which the transition to turbulence in the boundary layer of oscillating pipe flow occurs [16]. Further, $\zeta' \approx 1.75$ is a parameter that characterizes the ratio between the dynamic viscosity and the eddy viscosity; for further details, see [5].

The momentum equation see e.g. [7], reads

$$\rho\left(\frac{\partial v}{\partial t} + v\frac{\partial v}{\partial x}\right) = -\frac{\partial p}{\partial x} + \rho_0 \delta_{\mathrm{v}}\frac{\partial}{\partial x}\left[\frac{1}{r^2}\frac{\partial}{\partial x}(r^2 v)\right]. \tag{A.3}$$

The state equation for an ideal gas in the second approximation can be written in form

$$p' = c_0^2 \rho' + \frac{c_0^2}{2\rho_0}(\gamma - 1)\rho'^2 - \frac{\rho_0 \delta_{\mathrm{t}}}{r^2}\frac{\partial}{\partial x}(r^2 v), \tag{A.4}$$

see e.g. [17], where $\rho' = \rho - \rho_0$ is the acoustic density.

In the following text, it is assumed that the acoustic quantities p', ρ' and v together with the parameters δ_{v}, δ_{t} and ε are the first order of smallness. Within the second approximation, terms of the third and higher orders are discarded in the respective equations and the first-order approximations are substituted into the second-order terms.

In the first approximation, the continuity equation (A.1), the momentum Eq. (A.3) and the state Eq. (A.4) have the form

$$\frac{\partial \rho'}{\partial t} = -\frac{\rho_0}{r^2}\frac{\partial (r^2 v)}{\partial x}, \tag{A.5a}$$

$$\rho_0 \frac{\partial v}{\partial t} = -\frac{\partial p'}{\partial x}, \tag{A.5b}$$

$$p' = c_0^2 \rho'. \tag{A.5c}$$

It can be easily shown that in the first approximation, Eq. (A.5) can be combined into a wave equation

$$\frac{\partial}{\partial x}\left[\frac{1}{r^2}\frac{\partial}{\partial x}(r^2 v)\right] = \frac{1}{c_0^2}\frac{\partial^2 v}{\partial t^2}. \tag{A.6}$$

Eq. (3a) is derived as follows. Acoustic quantities are substituted into Eq. (A.3), the third-order term is discarded and the spatial derivatives in the dissipation terms are eliminated using Eq. (A.6) resulting in

$$\frac{\partial p'}{\partial x} = -\rho_0\frac{\partial v}{\partial t} - \rho'\frac{\partial v}{\partial t} - \rho_0 v\frac{\partial v}{\partial x} + \frac{\rho_0\delta_v}{c_0^2}\frac{\partial^2 v}{\partial t^2}.$$

Acoustic density can be eliminated from the second term on the right side using Eq. (A.5c), the derivative of the acoustic velocity in the third term using Eqs. (A.5a) and (A.5c), resulting in Eq. (3a).

Eq. (3b) is derived as follows. Substituting acoustic quantities into Eq. (A.1) results in

$$\frac{\partial v}{\partial x} - \frac{2\varepsilon}{r^2}\frac{\partial^{1/2}(rv)}{\partial x\partial t^{-1/2}} = -\frac{1}{\rho_0}\frac{\partial \rho'}{\partial t} - \frac{\rho'}{\rho_0}\frac{\partial v}{\partial x} - \frac{v}{\rho_0}\frac{\partial \rho'}{\partial x} - \frac{2}{\rho_0 r}\frac{\mathrm{d}r}{\mathrm{d}x}\rho' v - \frac{2}{r}\frac{\mathrm{d}r}{\mathrm{d}x}v. \tag{A.7}$$

To eliminate the acoustic density from the first term on the right side, Eq. (A.4) is rewritten using Eqs. (A.5a) and (A.5c) as

$$\rho' = \frac{p'}{c_0^2} - \frac{\gamma-1}{2\rho_0 c_0^4}p'^2 - \frac{\delta_t}{c_0^4}\frac{\partial p'}{\partial t}.$$

Acoustic density, its spatial derivative and the spatial derivative of the acoustic velocity are eliminated from the second, third and the fourth term using Eq. (A.5) which after some little algebra results in Eq. (3b).

References

[1] Nakane T. Discharge phenomenon in high-intensity acoustic standing wave field. IEEE Trans Plasma Sci 2005;33(2):356–7. http://dx.doi.org/10.1109/TPS.2005.845124.

[2] Bálek R, Červenka M, Pekárek S. Acoustic field effects on a negative corona discharge. Plasma Sources Sci Technol 2014;23(3):035005. http://dx.doi.org/10.1088/0963-0252/23/3/035005.

[3] Beranek LL, Mellow TJ. Acoustics: sound fields and transducers. Oxford: Academic Press; 2012.

[4] Fahy FJ. Sound intensity. London: Elsevier Applied Science; 1989.

[5] Ilinskii YA, Lipkens B, Zabolotskaya EA. Energy losses in an acoustical resonator. J Acoust Soc Am 2001;109(5):1859–70. http://dx.doi.org/10.1121/1.1359798.

[6] Červenka M, Šoltés M, Bednařík M. Optimal shaping of acoustic resonators for the generation of high-amplitude standing waves. J Acoust Soc Am 2014;136(3):1003–12. http://dx.doi.org/10.1121/1.4892751.

[7] Ilinskii YA, Lipkens B, Lucas TS, Doren TWV, Zabolotskaya EA. Nonlinear standing waves in an acoustical resonator. J Acoust Soc Am 1998;104(5):2664–74. http://dx.doi.org/10.1121/1.423850.

[8] Press WH, Teukolsky SA, Vetterling WT, Flannery BP. Numerical recipes: the art of scientific computing. 3rd ed. Cambridge: Cambridge University Press; 2007.

[9] Idelchik IE. Handbook of hydraulic resistance. Jaico Publishing House; 2005.

[10] Swift G. Thermoacoustics. Acoustical Society of America; 2002.

[11] Backhaus S, Swift GW. A thermoacoustic-stirling heat engine: detailed study. J Acoust Soc Am 2000;107(6):3148–66. http://dx.doi.org/10.1121/1.429343.

[12] Marx D, Mao X, Jaworski AJ. Acoustic coupling between the loudspeaker and the resonator in a standing-wave thermoacoustic device. Appl Acoust 2006;67(5):402–19. http://dx.doi.org/10.1016/j.apacoust.2005.08.001.

[13] Morris PJ, Boluriaan S, Shieh CM. Numerical simulation of minor losses due to a sudden contraction and expansion in high amplitude acoustic resonators. Acust Acta Acust 2004;90(3):393–409.

[14] Doller AJ. Acoustic minor losses in high amplitude resonators with single-sided junctions, PhD. Thesis, The Pennsylvania State University; 2004.

[15] Klippel W. Tutorial: loudspeaker nonlinearities – causes, parameters, symptoms. J Audio Eng Soc 2006;54(10):907–39.

[16] Merkli P, Thomann H. Transition to turbulence in oscillating pipe flow. J Fluid Mech 1975;68(3):567–76. http://dx.doi.org/10.1017/S0022112075001826.

[17] Makarov S, Ochmann M. Nonlinear and thermoviscous phenomena in acoustics, Part I. Acust Acta Acust 1996;82(5):579–606.

A.5 Acoustic field effects on a negative corona discharge

Bálek, R., Červenka, M., Pekárek, S., Acoustic field effects on a negative corona discharge, Plasma Sources Science and Technology 23(3), 1-9, (2014).

IOP Publishing Plasma Sources Science and Technology
Plasma Sources Sci. Technol. **23** (2014) 035005 (9pp) doi:10.1088/0963-0252/23/3/035005

Acoustic field effects on a negative corona discharge

R Bálek, M Červenka and S Pekárek

Czech Technical University in Prague, Faculty of Electrical Engineering, Technická 2, 166 27 Prague 6, Czech Republic

E-mail: balek@fel.cvut.cz

Received 28 November 2013, revised 26 February 2014
Accepted for publication 11 March 2014
Published 15 May 2014

Abstract

For a negative corona discharge under atmospheric pressure in different regimes, we investigated the effects of an acoustic field both on its electrical parameters and on the change in its visual appearance. We found that the application of an acoustic field on the true corona discharge, for particular currents, decreases the discharge voltage. The application of an acoustic field on the discharge in the filamentary streamer regime substantially extends the range of currents for which the discharge voltage remains more or less constant, i.e. it allows a substantial increase in the power delivered to the discharge. The application of an acoustic field on the discharge causes the discharge to spread within the discharge chamber and consequently, a highly reactive non-equilibrium plasma is created throughout the inter-electrode space. Finally, our experimental apparatus radiates almost no acoustic energy from the discharge chamber.

Keywords: negative corona discharge, acoustic field, discharge spread

(Some figures may appear in colour only in the online journal)

1. Introduction

From the standpoint of environment protection, increasing the efficiency of the processes leading to the destruction of toxic pollutants, decomposition of volatile organic compounds or combustion is an important task. One way to enhance these processes is using a non-thermal plasma. Therefore, the creation of a space- and time-homogeneous non-equilibrium low-temperature plasma in the entire discharge reactor volume is an important pre-requisite for triggering these processes and for increasing their efficiency. Space homogenization is usually understood as the creation of a plasma that is distributed more or less uniformly throughout the entire volume of the discharge reactor. Time homogenization means the creation of such conditions that allow obtaining an approximately regular train of current and voltage pulses, which are distributed uniformly in time.

The sources of low-temperature non-equilibrium plasmas are various types of electrical discharges, which also include the corona discharge. One of the drawbacks of this discharge is that with increasing current the discharge goes to a spark. However, in connection with the creation of a highly reactive non-equilibrium plasma throughout the entire volume of a discharge chamber, the attention of researchers has become focused on the filamentary streamer discharge regime, which precedes the spark. Different approaches can be used to prevent the transition to the spark. In addition to the pulse energization of the discharge, a gas flow [1–3], a magnetic field [4–6] and an acoustic or ultrasound field [7, 8] can be applied to the discharge. The key role of using the acoustic field is in the suppression of the thermal instability caused by the increased temperature of the gas, which is associated with the increased discharge current [9]. In addition, acoustic waves applied to the discharge can also enhance the chemical reactions occurring in the non-equilibrium plasma; this process is sometimes called sonification [10]. An interesting non-traditional application of ultrasonic waves on corona discharge is presented in [11]. In this paper, ultrasonic waves were used to improve the charging performance of a corona charger in electrophotography.

In the case of acoustic field application on the discharge, the pressure variations associated with the passage of the acoustic waves in the discharge volume affect the flow of charged particles between the discharge electrodes through collisions between neutral particles and ions [12, 13] and

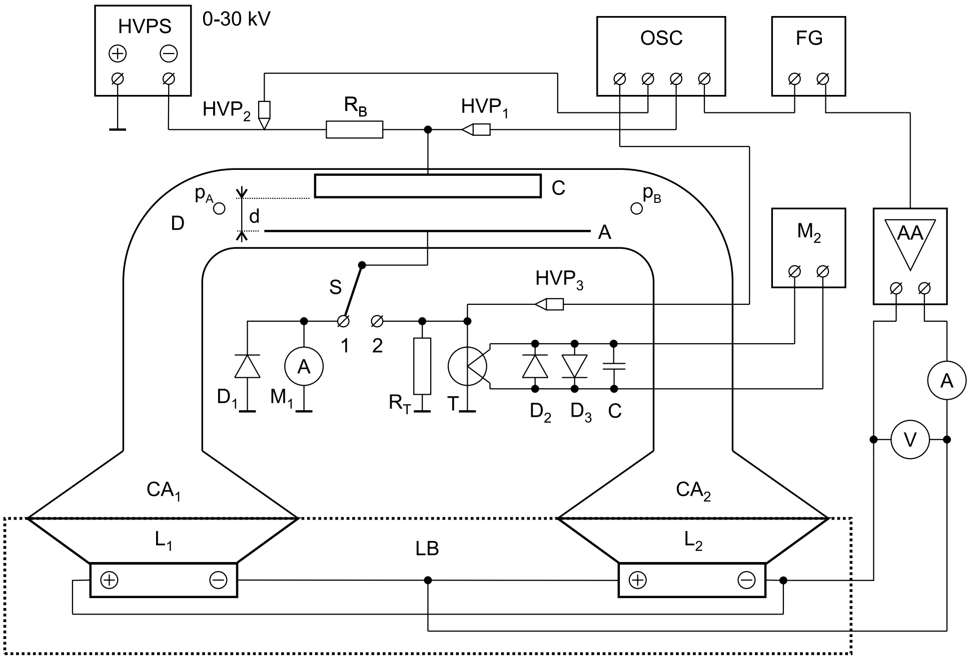

Figure 1. Experimental arrangement.

consequently, they influence not only the electrical parameters of the discharge but also its visual appearance.

A common problem arises if an acoustic field is utilized in sonification techniques or applied to a discharge; an audible sound of high intensity up to 160 dB [10] is used, which can affect human hearing. To tackle this issue, we have developed a special arrangement of sound-generating unit such that no sound is detected outside of the discharge chamber. In addition, our experimental arrangement solves another problem; that is associated with the dilution of the working gas, which occurs in cases where the gas flow is used to stabilize the discharge.

Our experiments were focused on the effects of an applied acoustic field on the volt–ampere characteristics of the razor blade to a wire discharge in air at atmospheric pressure and the corresponding changes in its visual appearance. The goal of our study was to stabilize the discharge and to obtain uniform distribution of the non-equilibrium plasma over the entire length of the electrodes. The obtained results could be used for increasing the efficiency of processes leading to the destruction of toxic pollutants, decomposition of volatile organic compounds or plasma-enhanced combustion.

2. Experimental arrangement and description of measurements

2.1. Experimental arrangement

The experimental arrangement used to study the interaction of an acoustic field with a negative corona discharge in different regimes is shown in figure 1. It comprises a cylindrical discharge chamber D, connected on each side to sound-generating unit equipped with loudspeakers L$_1$ and L$_2$. The discharge chamber D incorporates an electrode system; the cathode C is connected via the ballast resistor $R_B = 6.8$ MW to the high-voltage power source HVPS, 0–30 kV/5 mA. A stainless steel razor blade of length 37 mm is used as the cathode C and stainless steel wire of diameter 1.4 mm and length 80 mm serves as anode A. The distance d between the electrodes is 10.7 mm and the electrodes are positioned at the centre of the discharge chamber. An oscilloscope OSC, mA-meter M$_1$, mV-meter M$_2$, ac/dc thermocouple converter T, three high-voltage probes HVP$_{1-3}$ and ballast resistor R_B are used for electrical parameters diagnostics. A function generator FG with a power audio-amplifier AA serves for the excitation of the loudspeakers.

The acoustic field is generated by means of two loudspeakers L$_1$ and L$_2$ (B&C 6MD38-8) with membrane diameters of 150 mm, connected out of phase and placed in a loudspeaker box.

The generated acoustic waves are led into the discharge chamber D via two 80 mm-long conical adapters CA$_1$ and CA$_2$, which are made from polyvinyl chloride and match the loudspeaker diameter of 150 mm with the 24 mm diameter of the chamber. The loudspeakers generate an acoustic field with an acoustic velocity antinode (and acoustic pressure node) at the centre of the discharge electrodes. The wavelength of this low-frequency wave is of the order of several metres, so that the acoustic velocity vector in the entire discharge volume may be regarded as spatially uniform. Owing to this arrangement and the fact that the loudspeakers are connected out of phase, the air in the cylindrical chamber executes an oscillatory motion along its axis. In contrast with common applications of acoustic resonators in sonification techniques [10], the unique feature of the proposed arrangement is its almost absolute silence. This is because the acoustic pressure in the chamber attains relatively small amplitudes and the nearby out-of-phase loudspeakers radiate into the loudspeaker box as an acoustic dipole.

The loudspeakers are excited by the audio power amplifier AA and the delivered power is determined from the measurement of voltage (voltmeter V) and current

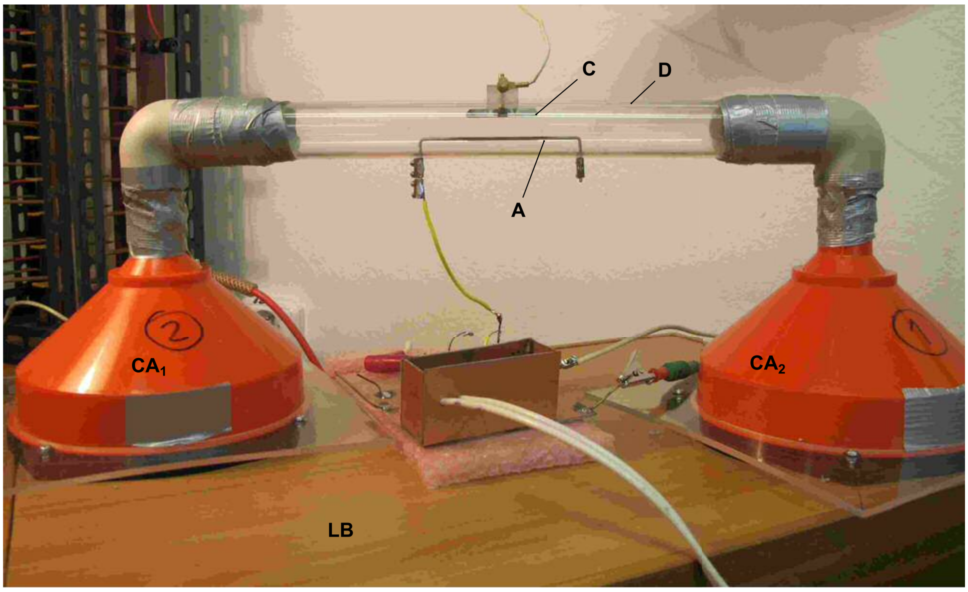

Figure 2. Photograph of the experimental apparatus.

(ammeter A). The input harmonic signal for the power audio-amplifier is supplied from the function generator FG, which is also used to synchronize the oscilloscope OSC. A photograph of the experimental apparatus is shown in figure 2.

2.2. Electrical measurements

To assess the effect of the acoustic field on the electrical characteristics of the discharge, we measured the discharge voltage and current and using these quantities, we constructed the V–A characteristics of the discharge. In the case of the true corona discharge, switch S is in position 1 (figure 1) and the anode A is grounded via the magneto-electric milliammeter M_1.

To measure the electrical parameters of the discharge in the filamentary streamer regime, the situation is more complicated because of the voltage and current pulsations. Typical time-resolved voltage and current signals are shown in figure 3 and details of the same picture for a different time scale are illustrated in figure 4.

The voltage and current pulses are caused by the discharging of the parasitic capacitor formed by the electrode system and components of the electric circuit (i.e. high-voltage probes, ballast resistor, wires). Small current pulses that appear before the main streamer and cause the decrease in the discharge voltage U can also be seen in figure 3. From our analysis based on the recorded current and voltage signals it can be concluded that the amplitudes of typical current pulses reach up to several amperes, they are irregularly distributed in time, and their number with increasing source voltage increases as far as the acoustic field causes sufficient time and spatial separation of the individual pulses. Typical duration of the current pulse is about 10 ns.

To avoid problems associated with large amounts of data, necessary for sampling the discharge current signal for the evaluation of the mean discharge current during relatively long acoustic wave periods (sampling 0.5 GS s^{-1} through 50 ms time), we measured the root mean square (RMS) value of the discharge current by means of an ac/dc thermocouple converter. In this case, switch S is in position 2 (figure 1) and anode A is grounded via the parallel combination of resistor R_T and a heated wire of the vacuum-type ac/dc thermocouple converter T. The thermocouple converter measures the discharge current RMS value irrespective of its time dependence. The resistance of R_T was chosen to match the current range of the ac/dc converter. The converter was calibrated correspondingly and the thermoelectric voltage was measured by the mV-meter M_2. Diodes D_1–D_3 are used to prevent overloading of the measuring devices and the capacitor C serves as a trap for parasitic signals.

The output voltage from the high-voltage power source HVPS and the discharge RMS voltage are also measured by an oscilloscope through the high-voltage probes HVP_2 and HVP_1, respectively.

2.3. Acoustic measurements

Our study focused on the effects of acoustic waves on the electrical parameters of the discharge and on the change in its visual appearance. In addition to the frequency, the amplitude of the acoustic velocity was also used as a parameter for the presentation of the effects of the acoustic field on the V–A characteristics of the discharge. The amplitude of the acoustic velocity was determined using measurements from two microphones. This approach is based on the linearized Euler equation

$$\rho_0 \frac{\partial \mathbf{v}}{\partial t} = -\nabla p, \qquad (1)$$

where ρ_0 is the density of air, $\boldsymbol{v}$ is the acoustic velocity vector, p is the acoustic pressure and t is time. The component of the gradient of acoustic pressure between two points of coordinates $(x_0 + h/2, y_0, z_0)$ and $(x_0 - h/2, y_0, z_0)$ can be approximated

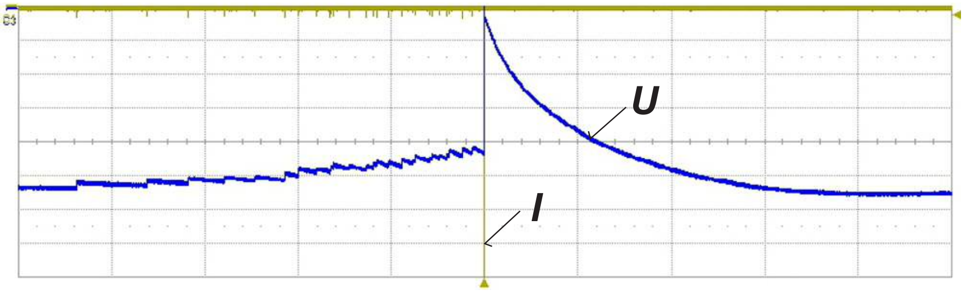

Figure 3. Time-resolved discharge current I (yellow, vertical scale 1A/div), discharge voltage U (blue, vertical scale 2.5 kV/div), time (horizontal scale 100 μs/div).

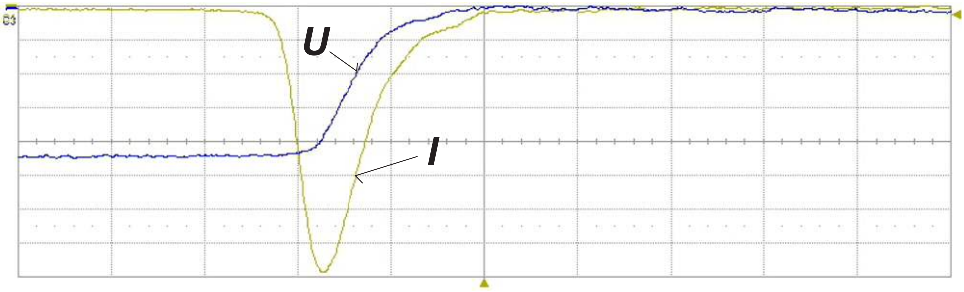

Figure 4. Time-resolved discharge current I (yellow, vertical scale 1 A/div), discharge voltage U (blue, vertical scale 2.5 kV/div), time (horizontal scale 20 ns/div).

using finite differences as

$$\left.\frac{\partial p}{\partial x}\right|_{x_0,y_0,z_0} \approx \frac{p(x_0 + h/2, y_0, z_0, t) - p(x_0 - h/2, y_0, z_0, t)}{h}. \tag{2}$$

We assume that $h \ll \lambda$, where λ is the wavelength of the acoustic wave and h is the distance between these points. If we denote

$$p_A = p(x_0 + h/2, y_0, z_0, t),\ p_B = p(x_0 - h/2, y_0, z_0, t) \tag{3}$$

as the acoustic pressures measured at positions p_A and p_B (see figure 1), separated by distance h and placed symmetrically to the discharge electrodes centre, the x-component (along the chamber axis) of the acoustic velocity vector can be written as

$$v_{ax} \approx \frac{1}{\rho_0 h}\int (p_B - p_A)\mathrm{d}t. \tag{4}$$

Thus, by measuring the acoustic pressures p_A and p_B in two different positions inside the cylindrical chamber, this component of acoustic velocity vector can be found [14].

For our experimental conditions we had $h = 16$ cm and the density of air at STP $\rho_0 = 1.2\,\mathrm{kg\,m^{-3}}$. Finally, the integral given by equation (4) was calculated using the Fast Fourier transform. The acoustic pressures were measured using 1/4 inch GRAS, type 40BP microphones. The maximum electric power applied to loudspeakers for frequency 50 Hz is 100 W. There is zero amplitude of the first harmonics of acoustic pressure at the centre of the discharge chamber and it slowly increases to about 830 Pa at a distance 8 cm from the centre. The amplitude of a second harmonics is about 190 Pa and is more or less spatially uniform along the discharge chamber. Amplitudes of the higher harmonics are negligible.

3. Experimental results and discussion

The experiments were performed with ambient air at a temperature of 24±2 °C, relative humidity of 40% and pressure of 1013 ± 20 hPa. The frequency of the applied acoustic field changed from 24 to 100 Hz. The amplitudes of the acoustic velocities varied up to 25 $\mathrm{m\,s^{-1}}$. The blade electrode was biased negatively. All photographs were taken with the same shutter speed of 1/5 s and aperture 5.6.

The V–A characteristics were studied both for the true corona as well as for the discharge in a filamentary streamer regime (transient spark). For the true corona, the V–A characteristics are given as the discharge voltage versus discharge current. For the discharge in the filamentary streamer regime, the V–A characteristics are presented as the RMS value of the discharge voltage versus the RMS value of the discharge current.

An acoustic field with various acoustic velocity amplitudes was used for the study of its effect on the discharge.

The visual appearance of the discharge in stationary air without the application of an acoustic field is shown in figure 5. It can be seen that the discharge is constricted into the channel between the edge of the razor blade and wire electrode, which corresponds to the filamentary mode of a non-stationary glow discharge at atmospheric pressure [15].

When we applied one-dimensional motion to the air, from right to left of the discharge chamber, the streamers were shifted in the direction of air motion (see figure 6). This is an illustrative example of the fact that the positions and shapes of the streamers can be affected efficiently by the oriented motion of the gas.

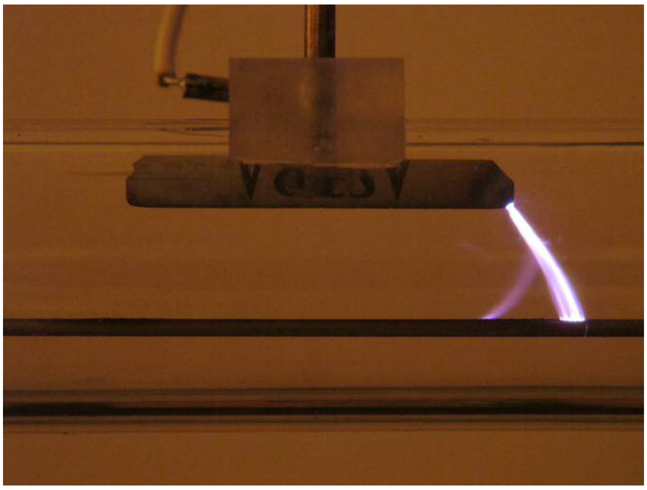

Figure 5. Discharge in stationary air without application of the acoustic field; discharge voltage 3.9 kV, discharge current 1.7 mA.

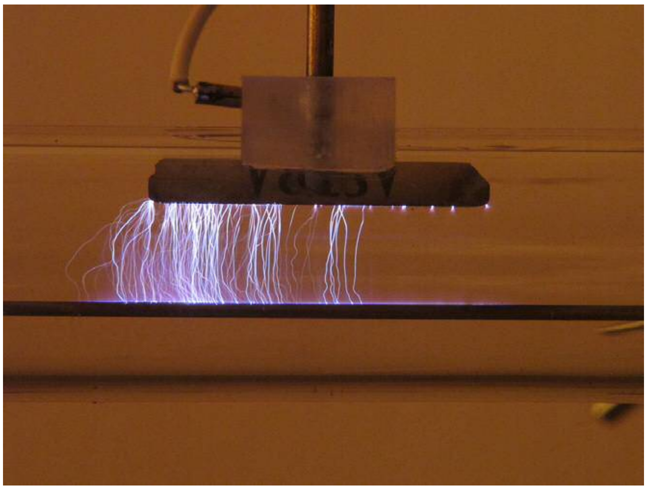

Figure 6. Discharge in air, which is moving from right to left; RMS of the discharge voltage: 13.7 kV, RMS of the discharge current: 12 mA, mean velocity of air: 40 m s^{-1}.

3.1. Effect of amplitude of acoustic velocity on discharge performance

Our research focused on the investigation of the effects of acoustic velocity amplitude and frequency on the electrical parameters of the discharge and on the change of its visual appearance in order to stabilize the discharge. The experiments were performed with frequencies of acoustic field ranging from 24 to 100 Hz. For the purposes of illustration, we present the results for the frequency of 50 Hz. For other frequencies, we obtained similar results when the ratio of acoustic velocity to frequency was the same.

Figure 7 shows the V–A characteristics of the true corona discharge both for the situation without the application of an acoustic field and for cases with the application of an acoustic field on the discharge.

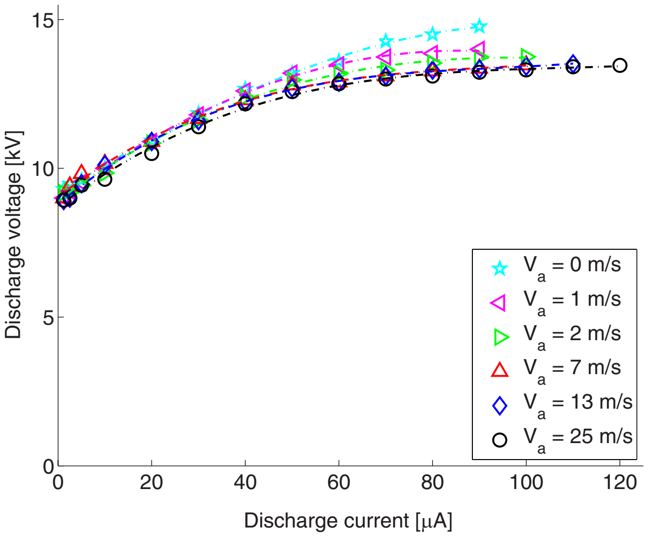

Figure 7. V–A characteristics of the true corona discharge for stationary air and for the discharge with an acoustic field with various amplitudes V_a of acoustic velocity.

It can be seen that if the current in the true corona discharge is very small (smaller than approximately 30 μA), the application of an acoustic field has almost no effect on the discharge voltage. When the discharge current exceeds this value, the application of an acoustic field for a particular current decreases the discharge voltage. It can also be seen that the decrease in the discharge voltage depends slightly on the amplitude V_a of the acoustic velocity. When this amplitude exceeds approximately 5 m s^{-1}, the decrease in the corona discharge voltage is no longer a function of this velocity.

The fact that for very small currents (smaller than approximately 30 μA) the application of the acoustic field does not affect the electrical parameters of the discharge can be explained based on the following considerations. When the current is restricted to a very small value, the discharge is in the Townsend regime. In this case, the discharge volume is customarily divided into an ionization (active) region and a drift region. Ionization, or production of charged particles, takes place only in the vicinity of an electrode where the electric field is sufficiently high. The ionization region, which is a relatively small region in the vicinity of the sharp electrode edge, is characterized by a strong non-uniform electric field. In the drift region of the corona discharge, the electric field distribution is more uniform and its magnitude is smaller than in the ionization region. The ionization processes, which determine the discharge current, occur mainly in the ionization region of the discharge. The effectiveness of these processes depends on the reduced electric field E/n, where E is the electric field strength and n is the concentration of neutral particles. As long as the thickness of the ionization region can be estimated roughly to be about 1 mm, which represents about one-tenth of the inter-electrode distance for our experimental conditions, the dominant effect on ionization is from the strong electric field in this region and the effect of changes in the concentration of neutral particles due to acoustic perturbations can be neglected.

This conclusion is supported by the fact that because of the shear friction, the acoustic particle velocity decreases from the maximum at the axis of the discharge chamber to zero at the chamber walls or electrodes. It can be shown that the thickness of this viscous acoustic boundary layer, see [16], can

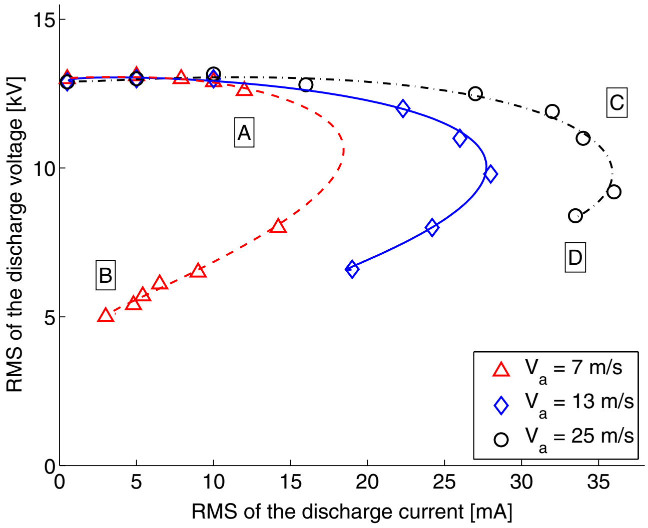

Figure 8. V–A characteristics of the discharge in the filamentary streamer regime for various amplitudes V_a of acoustic velocity.

be calculated as

$$\delta_v = \sqrt{\frac{2\nu}{\omega}},$$

where ν is the kinematic viscosity of the fluid and ω is the angular frequency of the acoustic field. For air at standard temperature and pressure and for a frequency of the acoustic field of 50 Hz, the thickness of the acoustic boundary layer is $\delta_v \approx 0.3$ mm. Therefore, it is obvious that the presence of an acoustic field in the entire volume of the discharge chamber has only marginal effects on the discharge current and consequently, on its V–A characteristics.

The situation is slightly different for currents exceeding a value of approximately 30 μA, when the application of an acoustic field for a particular current decreases the discharge voltage. In electronegative gases such as air, the main charge-carrying species are negative ions. The space charge of these ions limits the currents in the drift region [17]. The mass of negative ions is approximately the same as the mass of neutral particles, the motion of which we affect via the application of the acoustic field. In this case, the oscillatory bulk motion of air, which is perpendicular to the vector of current density, through collision of neutral particles with negative ions, affects the collision frequency, conductivity and consequently, the current density. Thus, for example, the application of an acoustic field on the discharge substantially extends the range of currents for the discharge in the diffuse glow regime. The typical discharge currents in this regime are higher compared with currents of the true negative corona [15]. With an increasing number of glow discharge channels along the razor edge, the total current increases and the discharge voltage decreases in comparison with the discharge at the same current without an acoustic field.

Figure 8 shows the V–A characteristics of the discharge in the filamentary streamer regime with an applied acoustic field of various acoustic velocity amplitudes V_a. From these characteristics, it can be seen that in the filamentary streamer regime, the acoustic field affects the discharge substantially.

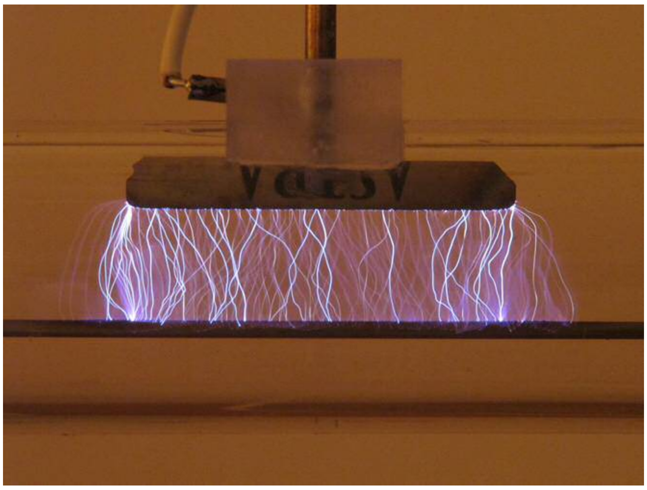

Figure 9. Photograph of the discharge corresponding to point A in figure 8; RMS value of the discharge voltage: 12.6 kV, RMS value of the discharge current: 12.0 mA, amplitude of acoustic velocity: $V_a = 7\,\mathrm{m\,s^{-1}}$.

First, the application of the acoustic field extends the range of currents for which the discharge voltage remains more or less constant, i.e. the application of the acoustic field allows a substantial increase in the power delivered to the discharge. This result is very useful from the standpoint of plasma-chemical applications. Second, it can also be seen from the V–A characteristics that with increasing amplitude of the acoustic velocity, the region in which the discharge in the filamentary streamer regime can survive is extended substantially.

Generally, the increase in discharge current causes an increase in heat produced by the discharge and consequently, the development of thermal instability, which is ultimately responsible for the transition of the discharge to a spark. However, from our results, it can be concluded that the application of the acoustic field prevents the transition to the spark. This can be understood by taking into account the visual appearance of the discharge, as shown in figures 9 and 11. The RMS value of the discharge voltage for the discharge in figure 9 (point A in figure 8) is 12.6 kV and for figure 11 (point C in figure 8), it is 11 kV. However, the RMS value of the discharge current is increased from 12 mA (figure 9) to 34 mA (figure 11). These photographs show that for the part of the V–A characteristics for which the discharge voltage remains more or less constant (for currents smaller than currents corresponding to points A and C in figure 8) with increasing current, the number of strong current streamers per unit length of the blade electrode increases. This causes an increase in heat production and consequently, without the acoustic field, it causes development of thermal instability.

In the case of an applied acoustic field, the increase in currents for which the discharge in the filamentary streamer regime can exist, as well as its increase with the increase in acoustic velocity amplitude, can be explained by a greater mixing of air in the inter-electrode volume due to the oscillatory bulk motion of the air perpendicular to the discharge current density. This more intense mixing of air results in more efficient heat transfer from the streamers to the surrounding air, followed by a decrease in the temperature of air, which leads to the suppression of thermal instability.

Thus, the increase in discharge current for a particular acoustic velocity amplitude, which can be seen in the V–A characteristics in figure 8, is caused by the increase in the number of strong current streamers. The conditions for thermal stability of the discharge must be fulfilled for point A as well as for point C.

Generally, thermal instability can be prevented if the gas residence time τ_{res} in the discharge is small compared with the heating time τ_{heat}, so that the neutral molecules are able to leave the volume of the discharge before they become too 'hot' [18], i.e. if

$$\tau_{\mathrm{res}} < \tau_{\mathrm{heat}}. \qquad (5)$$

In the true corona discharge, the heating time is long because of the small specific energy input. However, the situation is quite different in the case of the discharge in the filamentary streamer regime and it is even more complicated when the discharge is exposed to the acoustic field. In this case, we assume that a small volume element of air executes simple harmonic motion with a particular frequency.

The heating time τ_{heat} is also a variable quantity, which is determined mainly by the electrical parameters of the discharge.

According to [18], this time is for a single neutral given as the inverse of the electron–neutral heating collision frequency ν_{en}, which in turn is the electron density n_{e} times the rate constant for vibrational excitation of the neutral k_{en}, or $\tau_{\mathrm{heat}} = 1/(n_{\mathrm{e}}k_{\mathrm{en}})$. For molecular gases such as air, the vibrational excitation of the molecule is the fastest mode of energy transfer among the electrons and the neutrals. For nitrogen and 1.2 eV electrons, $k_{\mathrm{en}} = 5 \times 10^{-9}\,\mathrm{cm}^3\,\mathrm{s}^{-1}$. From the expression for the heating time, it is obvious that the decisive parameter in this case is the concentration of electrons n_{e}.

From our experimental results, shown in figure 8, we shall estimate the density of electrons n_{e} in the streamer based on the thermal stability condition and we shall compare the obtained value with the results presented in the literature. As the discharge voltage for currents smaller than the one corresponding to point C (for amplitude of acoustic velocity $V_{\mathrm{a}} = 25\,\mathrm{m\,s}^{-1}$) is approximately constant, we can roughly assume that the parameters of the streamers are similar. To the first approximation, we shall also neglect the interaction among the streamers in the case of higher currents. For currents smaller than the current corresponding to point C, the discharge does not transit to a spark; condition (5) must be satisfied for this region of currents. This result can be explained by the fact that the current in the case of higher currents (e.g. point C) is distributed among a bigger number of streamers than it is in the case of a smaller current (point A); therefore, the condition for thermal stability written for one individual streamer is satisfied.

The residence time τ_{res} for a particular frequency of acoustic field can be evaluated as a ratio of the diameter of streamers d_{str} and the amplitude of the acoustic velocity V_{a}. For our experimental conditions, the amplitude of acoustic velocity ranges from 7 to $25\,\mathrm{m\,s}^{-1}$. For evaluation of the gas residence time, we take the time required to travel the distance equal to the diameter of a streamer. The diameter of a streamer d_{str} is certainly a variable quantity, which depends on particular conditions and it also changes during the streamer development. We did not explicitly measure the streamer diameters but we estimated its value from the photographs of the discharge. We obtained values in the range 35–110 μm, which is in good agreement with the values presented in [19–21]. For a rough evaluation, we take as a streamer diameter its average value of $d_{\mathrm{str}} \approx 70\,\mu\mathrm{m}$. Consequently, the gas residence time is constant for a particular value of the acoustic velocity amplitude.

Thus, for the smallest amplitude of acoustic velocity $V_{\mathrm{a}} = 7\,\mathrm{m\,s}^{-1}$, we obtain the gas residence time: $\tau_{\mathrm{res}} \approx 10\,\mu\mathrm{s}$.

For the fulfilment of condition (5), the heating time must be longer than the gas residence time. To estimate the upper limit of the electron density n_{e}, we assume that the heating time is equal to the gas residence time, i.e.

$$\tau_{\mathrm{res}} = \tau_{\mathrm{heat}}. \qquad (6)$$

Taking into account that $\tau_{\mathrm{res}} \approx 10\,\mu\mathrm{s}$, using equation (6), we obtain $n_{\mathrm{e}} \approx 2 \times 10^{13}\,\mathrm{cm}^{-3}$ for the electron density. Therefore, for higher values of electron density the discharge will be more thermally stable. The values of electron density presented in [19, 22] range from 10^8 to $10^{14}\,\mathrm{cm}^{-3}$; therefore, our value fits into this interval.

Similar estimations concerning the electron density can also be performed for the other two values of acoustic velocity of 13 and $25\,\mathrm{m\,s}^{-1}$. It should be, however, pointed out that the presented analysis is very rough and should be considered as a starting point for our in-depth research of the effect of acoustic field on the distribution of streamers in the discharge. A more detailed model will require the knowledge of densities of electrons, densities of neutrals, temperatures, etc, so that e.g. the vibrational–translational relaxation or diffusion could be included in the model.

From figure 8, it is also obvious that if we follow the V–A characteristics of the discharge for one particular amplitude of acoustic velocity, after reaching the maximum current, the V–A characteristics perform a loop. This loop is characterized by the decrease in the discharge voltage accompanied by a decrease in the RMS discharge current and the V–A characteristics approach point B or D. The total current consists of a dc and a pulsed component. The part of V–A characteristics with lower RMS discharge voltage would not appear if mean values of discharge current were used.

Photographs in figures 9 and 11 show the change of visual appearance of the discharge and its change from the filamentary streamer regime (points A and C in figure 8) to the glow regime and filamentary regime (figures 10 and 12, points B and D in figure 8) for various acoustic velocity amplitudes.

Figure 9 shows a discharge in the filamentary streamer regime, which is spread over the entire length of the razor blade. The side effects are also shown, i.e. the spread of the discharge to the sides caused by the acoustic field. In contrast with the situation in figure 10, there is almost no glow in the vicinity of the wire electrode.

In the photograph of the discharge shown in figure 10, a glow can be seen near the anode wire. The presence of this glow is perhaps due to the increased electric field caused by

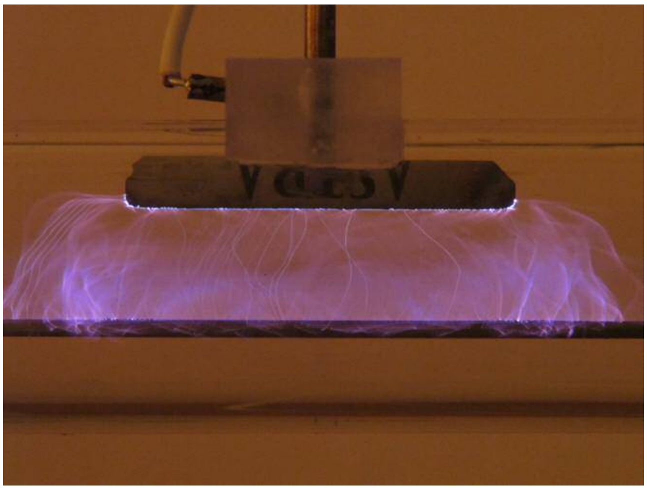

Figure 10. Photograph of the discharge corresponding to point B in figure 8; RMS value of the discharge voltage: 5.0 kV, RMS value of the discharge current: 3.0 mA, amplitude of acoustic velocity: $V_a = 7\,\mathrm{m\,s^{-1}}$.

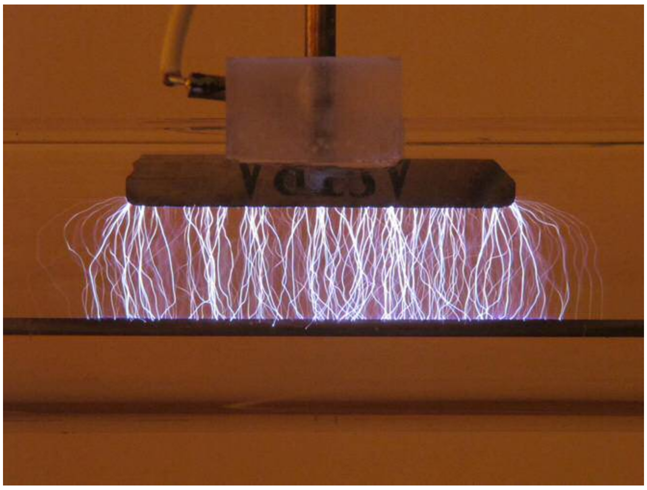

Figure 11. Photograph of the discharge corresponding to point C in figure 8; RMS value of the discharge voltage: 11.0 kV, RMS value of the discharge current: 34.0 mA, amplitude of acoustic velocity: $V_a = 25\,\mathrm{m\,s^{-1}}$.

the negative ion sheath formed in air [23]. As can be seen in figure 12, in the case of higher values of acoustic velocity, we were unable to reach the glow discharge regime and we have only the filamentary streamer discharge regime.

The experimental outcome based on these photographs is that the applied acoustic field affects the shape and positions in which the streamers begin to originate. The streamers occur in the positions where the conditions for their occurrence are fulfilled. The streamers' repetition frequency depends on the parameters of the electrical circuit.

The streamers cause heating of the surrounding air. Owing to the action of the acoustic field, the region of heated air during the time is determined by this repetition frequency displaced into a position depending on the instantaneous value of the acoustic velocity. In this position, the conditions for the occurrence of a new streamer are more favourable, because of the lower density of neutrals in the warmer air compared with the conditions at the original streamer position. Meanwhile, cold air is supplied into the original position of the streamer due to the action of the acoustic field. This mechanism is then repeated. However, it should be noted that the 'direction' of apparent motion of the streamers depends on the coincidence between the time when the streamer originates and the direction of the vector of the acoustic velocity at that time.

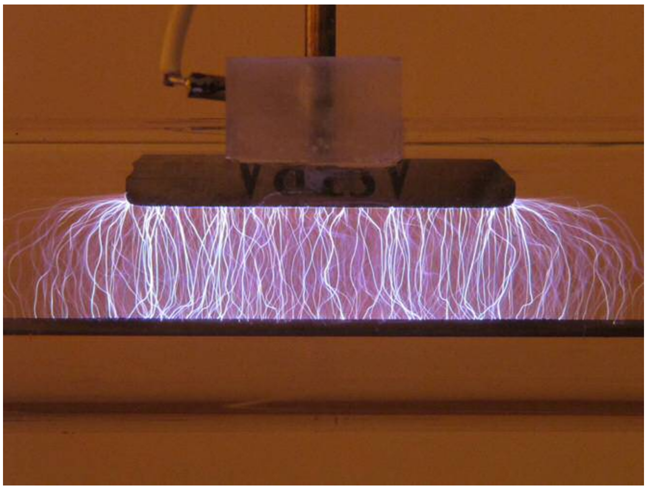

Figure 12. Photograph of the discharge corresponding to point D in figure 8; RMS value of the discharge voltage: 8.4 kV, RMS value of the discharge current: 33.5 mA, amplitude of acoustic velocity: $V_a = 25\,\mathrm{m\,s^{-1}}$.

4. Conclusions

We have developed an experimental setup for the study of the interaction of an acoustic field with a negative corona discharge in different regimes with no acoustic output from the discharge chamber. We investigated the effect of the acoustic field on the electrical parameters of the discharge between the razor blade and wire electrodes and on the change in its visual appearance. Our findings can be summarized as follows:

- We found that the application of the acoustic field on the true corona discharge for a particular current slightly reduces the discharge voltage and extends the region of the diffuse glow discharge to higher currents.
- Application of the acoustic field on the discharge in the filamentary streamer regime and in the following glow discharge substantially extends the range of currents for which the discharge voltage remains more or less constant, i.e. it allows a substantial increase in power delivered to the discharge.
- Application of the acoustic field on the discharge causes the discharge to spread in the discharge chamber and consequently, a highly reactive non-equilibrium plasma is created throughout the entire inter-electrode space.

The obtained results dealing with the effect of acoustic field on a streamer corona discharge could be used for increasing the efficiency of plasma-chemical processes leading to the destruction of toxic pollutants, decomposition of volatile organic compounds or plasma-enhanced combustion. Apart from these uses there are also emerging applications involving the usage of acoustic field for surface modification, surface treatment through enhancement of transport of reactive species generated in the plasma to the treated material in order to improve its wettability, printability or adhesion.

The obtained results dealing with the effect of acoustic field on diffuse glow discharge could also be possibly used for plasma-medical applications, such as sterilization, decontamination purposes or for suppression of microbially induced corrosion.

Acknowledgments

This research has been supported by the Czech Science Foundation grant 'New methods of generation and utilization of finite-amplitude standing acoustic waves' under Contract No P101-12-1925.

References

[1] Chalmers J A 1965 *J. Atmos. Terr. Phys.* **27** 1037
[2] Akishev Y, Goossens O, Callebaut T, Leys C, Napartovich N and Trushkin N 2001 *J. Phys. D: Appl. Phys.* **34** 2875
[3] Pekárek S, Kříha V, Šimek M, Bálek R and Hanitz F 1999 *Plasma Sources Sci. Technol.* **8** 513
[4] Ferreira J L, Monteiro K M, Damasio H J and Kostov K G 1998 *Combust. Sci. Technol.* **140** 1
[5] Park J Y, Kim G H, Kim J D, Koh H S and Lee D C 1998 *Combust. Sci. Technol.* **133** 65
[6] Moon J D, Lee G T and Chung S H 1999 *IEEE Trans. Industry Appl.* **35** 1198
[7] Nakane T 2005 *IEEE Trans. Plasma Sci.* **33** 356
[8] Kusano Y, Singh S V, Norrman K, Drews J, Leipold F, Rozlosnik N, Bardenshtein A and Krebs N 2012 *Surf. Eng.* **28** 453
[9] Pekárek S and Bálek R 2006 *Plasma Sources Sci. Technol.* **15** 52
[10] Komarov S V, Nemeth S and Hirasawa M 2005 *Ultrasonics* **43** 241
[11] Choi K S, Nakamura S and Murata Y 2005 *Japan. J. Appl. Phys.* **44** 3248
[12] Bequin P, Joly V and Herzog P 2013 *J. Phys. D: Appl. Phys.* **46** 175204
[13] Fitaire M and Mantei T D 1972 *Phys. Fluids* **15** 464
[14] Fahy F J 1989 *Sound Intensity* (London: Elsevier Applied Science)
[15] Akishev Y, Grushin M, Kochetov I, Karalnik V, Napartovich A and Trushkin N 2005 *Plasma Sources Sci. Technol.* **14** S18
[16] Blackstock D T 2000 *Fundamentals of Physical Acoustics* (New York: Wiley)
[17] Raizer Y P 1997 *Gas Discharge Physics* (Berlin: Springer)
[18] Staack D, Farouk B, Gutsol A and Fridman A 2005 *Plasma Sources Sci. Technol.* **14** 700
[19] Guo J M and Wu Ch-H 1996 *IEEE Trans Plasma Sci.* **24** 1348
[20] van Veldhuizen E M and Rutgers W R 2001 Corona discharges: fundamentals and diagnostics *Proc. Workshop on Frontiers in Low Temperature Plasma Diagnostics IV (Limburg, The Netherlands)* www.phys.tue.nl/FLTPD/LTPD4.html
[21] Goldman M, Goldman A and Sigmond R S 1985 *Pure Appl. Chem.* **57** 1353
[22] Janda M, Martisovits V and Machala Z 2011 *Plasma Sources Sci. Technol.* **20** 035015
[23] Antao D S, Staack D A, Fridman A and Farouk B 2009 *Plasma Sources Sci. Technol.* **18** 035016

A.6 Variety of acoustic streaming in 2D resonant channels

Červenka, M., Bednařík, M., Variety of acoustic streaming in 2D resonant channels, Wave Motion 66, 21-30, (2016).

Wave Motion 66 (2016) 21–30

Contents lists available at ScienceDirect

Wave Motion

journal homepage: www.elsevier.com/locate/wavemoti

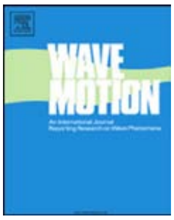

Variety of acoustic streaming in 2D resonant channels

M. Červenka*, M. Bednařík

Czech Technical University in Prague, Faculty of Electrical Engineering, Technická 2, 166 27 Prague 6, Czech Republic

HIGHLIGHTS

- Model equations are derived for study of acoustic streaming using Acoustic Module of COMSOL Multiphysics.
- Excellent agreement between the analytical and numerical results validates the proposed computational approach.
- Complex structures of acoustic streaming were observed in rectangular resonant channels.
- Strong dependence of acoustic streaming on resonant channel shape was observed.

ARTICLE INFO

Article history:
Received 29 September 2015
Received in revised form 27 April 2016
Accepted 4 May 2016
Available online 13 May 2016

Keywords:
Acoustic streaming
Acoustic resonator
Finite element method
COMSOL Multiphysics

ABSTRACT

Acoustic streaming in 2D resonant channels with uniform or non-uniform cross-sections is studied within this work. An inertial force as well as a vibrating boundary are assumed for driving the acoustic field. The method of successive approximations is employed to derive linear equations for calculation of primary acoustic and time-averaged secondary fields including the radiation pressure and the mass transport velocity. The model equations have a standard form which allows their numerical integration using a universal solver; in this case, COMSOL Multiphysics was employed. As this software is based on the finite element method, it is simple and straightforward to perform the calculations with moderate computational costs even for complex geometries, which makes the proposed approach an operative tool for study of acoustic streaming. The numerical results are validated for the case of a rectangular channel by comparison with previously published analytical results; an excellent agreement is found. The numerical results show that the acoustic streaming can be quite complex even in rectangular channels and its structure depends on the manner of driving. Examples of acoustic streaming in wedged and elliptical channels are given to demonstrate a strong dependence of the acoustic streaming structure on the resonator shape.

1. Introduction

Acoustic streaming [1–4] refers to a second-order net mean fluid flow generated by and superimposed on the first-order acoustic field. Based on different mechanisms by which acoustic streaming is generated, it can be sorted [4] into several categories. Boundary-layer-driven streaming, first analysed by Rayleigh [5], appears in a standing wave resonator because of shear viscous forces near the fluid–solid boundary. Eckart streaming (or "quartz wind") is generated as a result of attenuation of high-intensity travelling acoustic waves within the fluid volume. Jet-driven streaming is associated with the periodic suction and ejection of a viscous fluid through a change of cross-section area in a resonator. Finally, there is a travelling-wave (Gedeon) streaming associated with acoustic wave propagating in a waveguide with a looped topology.

---

* Corresponding author.
E-mail addresses: milan.cervenka@fel.cvut.cz, milan.cervenka@seznam.cz (M. Červenka).

http://dx.doi.org/10.1016/j.wavemoti.2016.05.001

Being an inherently nonlinear effect, acoustic streaming cannot be analysed using the apparatus of linear acoustics. If its velocity is considerably smaller than the acoustic particle velocity amplitude, it is called "slow". The effect of inertia on the "slow" streaming motion is neglected by comparison with viscous effects and thus, it can be analysed employing the perturbation theory resulting in linear equations for the second-order field variables including the streaming velocity vector. In the case of "fast" or "nonlinear" streaming, the effect of inertia on the streaming motion cannot be neglected any more and its analysis is usually performed numerically by means of methods of computational fluid dynamics.

Apart from the fact that acoustic streaming is an interesting physical phenomena, it plays an important role in many applications where it can be useful or undesirable. For example, in thermoacoustics [6], streaming is usually an unwanted mechanism of convective heat transfer which reduces the efficiency of high-amplitude thermoacoustic devices; on the other hand, the heat transfer supported by acoustic streaming [7] could find its application in cooling hot objects like electronic components. In acoustofluidics [8], acoustic streaming prevents manipulation of small particles by acoustic radiation force in microfluidic devices; on the other hand, it can be actively utilized in these devices for mixing and pumping fluids.

This work is focused on the numerical analysis of "slow", boundary-layer-driven acoustic streaming in channels (resonators) with non-uniform cross-section. In related previous theoretical works, acoustic streaming in a thermoviscous fluid confined between two arbitrarily separated plates having non-zero mean temperature gradient was studied by Waxler [9]. Bailliet et al. [10] incorporated temperature dependence of viscosity and heat conduction and extended the analysis also for cylindrical geometry. Hamilton et al. [11] presented fully analytical solution for acoustic streaming generated by a standing wave in a rectangular channel of arbitrary width filled with a viscous fluid; in work [12], the authors further generalized the solution to take into account thermal conductivity and temperature-dependence of viscosity of the fluid and extended the analysis for the case of cylindrical tubes. They discussed the structure of inner (boundary layer, Schlichting) and outer (Rayleigh) vortices and the conditions necessary for their development.

In works [9–12] the method of successive approximations was employed limiting the analysis to the case of "slow" streaming.

Employing a perturbation analysis with asymptotic expansions, Menguy and Gilbert [13] calculated "nonlinear" acoustic streaming generated by a standing wave in a cylindrical waveguide demonstrating the distortion of streamlines as a consequence of inertial effects on fluid motion. They have identified a parameter — nonlinear Reynolds number $\mathrm{Re}_{\mathrm{nl}} = (M \times R/\delta_{\mathrm{v}})^2$, where M is the acoustic Mach number, R is the waveguide radius and δ_{v} is the width of the viscous boundary layer, which determines whether the fluid inertia effects on the streaming motion can be neglected ($\mathrm{Re}_{\mathrm{nl}} \ll 1$, streaming can be considered as "slow") or not.

Aktas and Farouk [14], Daru et al. [15] studied acoustic streaming generated by strongly nonlinear acoustic fields in two-dimensional rectangular channels employing numerical integration of compressible Navier–Stokes equations. They observed complex streaming patterns referred to as "irregular" streaming.

Reyt et al. [16] studied numerically (direct numerical integration of Navier–Stokes equations) as well as experimentally "fast" acoustic streaming in a cylindrical duct reporting development of additional outer vortices as a result of inertial effects on streaming motion. Antao and Farouk [17] presented the streaming patterns in a conical resonator.

The methods and tools of computational fluid dynamics are today well-developed, allowing for direct simulation of "fast" acoustic streaming in shaped resonant channels. On the other hand, direct numerical integration of Navier–Stokes equations is computationally very costly, because the need to capture the structure of boundary layers requires a very fine time-step of integration and the transients can be even hundreds or thousands of cycles long. This fact essentially excludes these methods to be used as operative instruments for prediction/control of acoustic streaming in practical applications. The analytical or semi-analytical methods based on the perturbation analysis are limited to "slow" streaming in simple geometries (rectangular, cylindrical), the corresponding formulas are quite complicated and they often require some numerical sub-calculations.

For the case of "slow" streaming, the present work attempts to combine the advantages of these two approaches. The method of successive approximation is used to first calculate the primary acoustic field and subsequently the streaming field. The finite element method is employed for calculation of both the fields so that complex geometries can be easily addressed. Section 2 of the article presents the mathematical model and its implementation in commercial software COMSOL Multiphysics. Section 3 presents the validation of the model and examples of streaming fields in resonant channels with uniform or non-uniform cross-sections, driven by an inertial force or by an oscillating boundary. Finally, Section 4 draws some concluding remarks.

2. Material and methods

2.1. Mathematical model

As the acoustic streaming is generated by nonlinear effects, the Navier–Stokes equations serve as the starting point for its mathematical description. The mass, momentum and energy[1] equation can be written in form

---

[1] Derivation of the energy equation in this particular form can be found e.g. in [18].

$$\frac{\mathrm{d}\rho}{\mathrm{d}t} = -\rho\nabla\cdot\boldsymbol{u}, \tag{1a}$$

$$\rho\frac{\mathrm{d}\boldsymbol{u}}{\mathrm{d}t} = \nabla\cdot\boldsymbol{\sigma} + \boldsymbol{f}, \tag{1b}$$

$$\rho c_{\mathrm{p}}\frac{\mathrm{d}T}{\mathrm{d}t} - \alpha T\frac{\mathrm{d}p}{\mathrm{d}t} = \nabla\cdot(\kappa\nabla T) + \boldsymbol{\tau}:\nabla\boldsymbol{u}, \tag{1c}$$

where ρ is the density, $\boldsymbol{u}$ is the velocity vector, T is the temperature, p is the pressure, $\boldsymbol{f}$ is the body force density, if the resonant channel is driven by an inertial force (by entire-body shaking) it reads $\boldsymbol{f} = -\rho\boldsymbol{a}(t)$, where $\boldsymbol{a}(t)$ is the channel's acceleration. Further, c_{p} is the specific heat capacity at constant pressure, α is the isobaric coefficient of volumetric thermal expansion and κ is the coefficient of thermal conduction. The total stress tensor $\boldsymbol{\sigma}$ is defined as

$$\boldsymbol{\sigma} = -p\boldsymbol{I} + \boldsymbol{\tau} = -p\boldsymbol{I} + \mu\left[\nabla\boldsymbol{u} + (\nabla\boldsymbol{u})^{\mathrm{T}}\right] - \left(\frac{2\mu}{3} - \mu_{\mathrm{B}}\right)(\nabla\cdot\boldsymbol{u})\boldsymbol{I}, \tag{2}$$

where $\boldsymbol{\tau}$ is the viscous stress tensor, μ is the shear viscosity, μ_{B} is the bulk viscosity and $\boldsymbol{I}$ is the identity matrix. In this study, the parameters c_{p}, μ, μ_{B} and κ are assumed to be temperature-independent.

In Eqs. (1), the material derivative is defined as

$$\frac{\mathrm{d}(-)}{\mathrm{d}t} = \frac{\partial(-)}{\partial t} + (\boldsymbol{u}\cdot\nabla)(-).$$

It is assumed that the fluid is an ideal gas for which the state equation has the form $p = \rho RT$, where R is the specific gas constant and thus $\alpha = -(\partial\rho/\partial T)_p/\rho = 1/T$.

Set of Eqs. (1) is solved using the method of successive approximations. It is assumed that the field variables can be expressed as series

$$\begin{aligned} p &= p_0 + \epsilon p_1 + \epsilon^2 p_2 + \cdots, & \boldsymbol{u} &= \epsilon\boldsymbol{u}_1 + \epsilon^2\boldsymbol{u}_2 + \cdots, \\ \rho &= \rho_0 + \epsilon\rho_1 + \epsilon^2\rho_2 + \cdots, & \boldsymbol{a} &= \epsilon\boldsymbol{a}_1, \\ T &= T_0 + \epsilon T_1 + \epsilon^2 T_2 + \cdots, \end{aligned}$$

where $\epsilon \ll 1$ is a small parameter (representing e.g. the acoustic Mach number), p_0, ρ_0 and T_0 are the ambient quantities (without sound) considered as constants in time and space, p_1, ρ_1, T_1 and $\boldsymbol{u}_1$ are the primary acoustic variables supposed to be harmonic with angular frequency ω, which is the frequency of driving. The quantities with indices bigger than one are the nonlinearly generated terms; in this case, the terms with indices bigger than two are omitted.

Within the method of successive approximations, the above series are substituted for the field quantities and the equations for the same order of ϵ are found.

For ϵ^1, we can write

$$\frac{\partial\rho_1}{\partial t} + \rho_0\nabla\cdot\boldsymbol{u}_1 = 0, \tag{3a}$$

$$\rho_0\frac{\partial\boldsymbol{u}_1}{\partial t} - \nabla\cdot\left\{-p_1\boldsymbol{I} + \mu\left[\nabla\boldsymbol{u}_1 + (\nabla\boldsymbol{u}_1)^{\mathrm{T}}\right] - \left(\frac{2\mu}{3} - \mu_{\mathrm{B}}\right)(\nabla\cdot\boldsymbol{u}_1)\boldsymbol{I}\right\} = -\rho_0\boldsymbol{a}_1, \tag{3b}$$

$$\rho_0 c_{\mathrm{p}}\frac{\partial T_1}{\partial t} - \frac{\partial p_1}{\partial t} - \nabla\cdot(\kappa\nabla T_1) = 0, \tag{3c}$$

together with the linearized state equation

$$\frac{p_1}{p_0} = \frac{T_1}{T_0} + \frac{\rho_1}{\rho_0}. \tag{4}$$

Eqs. (3), (4) can be used for calculation of the primary acoustic field.

For ϵ^2 the continuity equation (1a) can be rewritten as

$$\frac{\partial\rho_2}{\partial t} + \nabla\cdot(\rho_0\boldsymbol{u}_2 + \rho_1\boldsymbol{u}_1) = 0. \tag{5}$$

As we are further focused on slowly time-varying processes involving acoustic streaming, Eq. (5) is averaged over one period $\tau = 2\pi/\omega$ resulting in

$$\frac{\partial\bar{\rho}_2}{\partial t_{\mathrm{s}}} + \nabla\cdot(\rho_0\bar{\boldsymbol{u}}_2 + \langle\rho_1\boldsymbol{u}_1\rangle) = 0, \tag{6}$$

where the bar denotes the one-period-averaged quantities, t_{s} is the time related to the large time-scale phenomena [19] such as the acoustic streaming. As the primary field is supposed to be time-harmonic, it holds $\langle fg\rangle = \Re[\tilde{f}\tilde{g}^*]/2$, where $\tilde{f}$, $\tilde{g}$ represent the complex amplitudes of the quantities f, g and the asterisk stands for the complex conjugate.

If we introduce the averaged mass transport velocity, see e.g. [1,11,19]

$$\bar{\boldsymbol{u}}^{\mathrm{M}} = \bar{\boldsymbol{u}} + \langle \rho_1 \boldsymbol{u}_1 \rangle / \rho_0, \tag{7}$$

Eq. (6) can be rewritten as

$$\frac{\partial \bar{\rho}_2}{\partial t_s} + \rho_0 \nabla \cdot \bar{\boldsymbol{u}}^{\mathrm{M}} = 0. \tag{8}$$

Similarly, the momentum equation (1b) for ϵ^2 and the averaged mass transport velocity can be written as

$$\rho_0 \frac{\partial \bar{\boldsymbol{u}}^{\mathrm{M}}}{\partial t_s} - \nabla \cdot \left\{ -\bar{p}_2 \boldsymbol{I} + \mu \left[\nabla \bar{\boldsymbol{u}}^{\mathrm{M}} + (\nabla \bar{\boldsymbol{u}}^{\mathrm{M}})^{\mathrm{T}} \right] - \left(\frac{2\mu}{3} - \mu_{\mathrm{B}} \right) (\nabla \cdot \bar{\boldsymbol{u}}^{\mathrm{M}}) \boldsymbol{I} \right\} = \boldsymbol{F}, \tag{9}$$

where

$$\begin{aligned} \boldsymbol{F} &= -\rho_0 \nabla \cdot \langle \boldsymbol{u}_1 \boldsymbol{u}_1 \rangle \\ &\quad - \frac{1}{\rho_0} \nabla \cdot \left\{ \mu \left[\nabla \langle \rho_1 \boldsymbol{u}_1 \rangle + (\nabla \langle \rho_1 \boldsymbol{u}_1 \rangle)^{\mathrm{T}} \right] - \left(\frac{2\mu}{3} - \mu_{\mathrm{B}} \right) (\nabla \cdot \langle \rho_1 \boldsymbol{u}_1 \rangle) \boldsymbol{I} \right\} - \langle \rho_1 \boldsymbol{a}_1 \rangle. \end{aligned} \tag{10}$$

Finally, the energy equation (1c) for ϵ^2 can be written as

$$\rho_0 c_{\mathrm{p}} \frac{\partial \bar{T}_2}{\partial t_s} - \frac{\partial \bar{p}_2}{\partial t_s} - \nabla \cdot (\kappa \nabla \bar{T}_2) = Q, \tag{11}$$

where

$$Q = -c_{\mathrm{p}} \left\langle \rho_1 \frac{\partial T_1}{\partial t} \right\rangle - \rho_0 c_{\mathrm{p}} \langle \boldsymbol{u}_1 \cdot \nabla T_1 \rangle + \langle \boldsymbol{u}_1 \cdot \nabla p_1 \rangle. \tag{12}$$

The energy-dissipation term from Eq. (1c) was omitted. Eqs. (8), (9) and (11) form together with the state equation

$$\frac{\bar{p}_2}{p_0} = \frac{\bar{T}_2}{T_0} + \frac{\bar{\rho}_2}{\rho_0} + \frac{\langle \rho_1 T_1 \rangle}{\rho_0 T_0} \tag{13}$$

a set of equations for the calculation of the slowly-varying products of nonlinear interactions, where the averaged mass transport velocity $\bar{\boldsymbol{u}}^{\mathrm{M}}$ is of the primary interest here.

In the steady state, when the one-period-averaged quantities do not change with the time t_s, Eqs. (8), (9) and (11) reduce into

$$\nabla \cdot \bar{\boldsymbol{u}}^{\mathrm{M}} = 0, \tag{14a}$$

$$\nabla \bar{p}_2 - \mu \Delta \bar{\boldsymbol{u}}^{\mathrm{M}} = \boldsymbol{F} \tag{14b}$$

$$-\nabla \cdot (\kappa \nabla \bar{T}_2) = Q. \tag{14c}$$

As the viscosity is assumed to be temperature-independent, Eqs. (14a) and (14b) are decoupled from Eq. (14c).

2.2. Numerical solution of the model equations

The model equations were solved numerically using COMSOL Multiphysics, which is a commercial software based on the finite element method. An approach similar to the one presented in work [20] was employed, here, all the calculations were performed using the Acoustics Module, namely, the Aeroacoustics branch. The numerical procedure works as follows.

First, primary field quantities p_1, $\boldsymbol{u}_1$, T_1 and ρ_1 are calculated using the Linearized Navier–Stokes, Frequency Domain (lnsf) study type, which solves Eq. (3) in the frequency domain. The term $-\rho_0 \boldsymbol{a}$ is used as a volume source for the Navier–Stokes equation if the inertial driving is assumed. The resonance frequency is determined using the frequency sweep.

Second, employing again the Linearized Navier–Stokes, Frequency Domain (lnsf) study type, Eqs. (14) are solved for the averaged quantities $\bar{p}_2$, $\bar{\boldsymbol{u}}^{\mathrm{M}}$, $\bar{T}_2$ and $\bar{\rho}_2$; Eqs. (14) have formally the same form as Eqs. (3), only the volume sources differ; they are calculated using formulas (10) and (12) employing the previously calculated primary variables.

Within the Acoustic Module of the COMSOL Multiphysics, only the frequency-domain and the time-domain (transient) studies are implemented for the linearized Navier–Stokes equations. In order to reduce the computational cost, the steady-state secondary field is calculated using the frequency-domain analysis at the frequency of 0 Hz.[2]

The numerical calculations were performed in 2D Cartesian x-y geometry, see Fig. 1, modification for 2D axi-symmetric geometry would be simple and straightforward. Resonant cavities were assumed to be symmetric with respect to the x-axis

---

[2] Actually, frequency of 10^{-16} Hz was used which effectively eliminates the derivatives with respect to time in Eqs. (14).

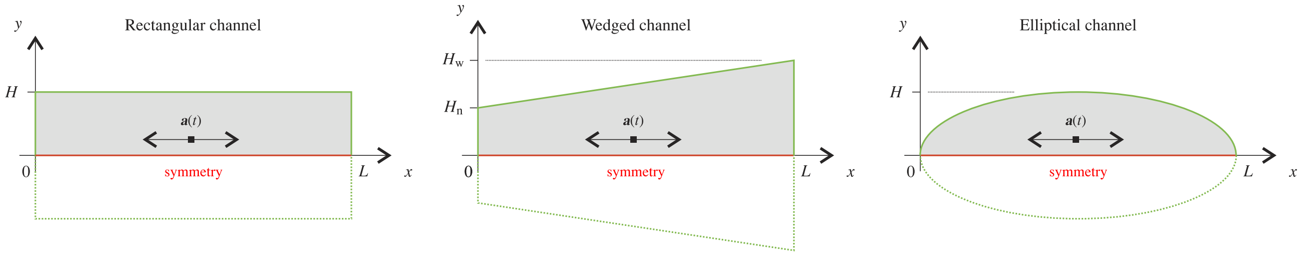

Fig. 1. Geometry of the computational domain — rectangular, wedged and elliptical channel.

with no-slip and isothermal walls; driven with harmonic acceleration with zero y-component in the case of an inertial driving. The isothermal boundary conditions reflect the fact that the solid walls of resonant cavities usually have heat capacity and conduction high enough to enforce constant temperature at the solid–fluid boundaries.

Computational meshes were constructed in order to resolve properly the boundary layers along the walls, mapped (structured) as well as unstructured quadrilateral meshes with refinement along the walls were found to work well; the independence of numerical results on the mesh density was checked. As the volume sources for Eqs. (9), (11) depend on the spatial derivatives of the primary field quantities, the computational mesh must be rather fine.

As the steady averaged mass transport velocity field is divergence-free, see Eq. (14a), it can be represented by a stream function ψ, such that

$$\bar{u}_x^{\mathrm{M}} = \frac{\partial \psi}{\partial y}, \qquad \bar{u}_y^{\mathrm{M}} = -\frac{\partial \psi}{\partial x}.$$

From here, we can write

$$\Delta\psi = \frac{\partial \bar{u}_x^{\mathrm{M}}}{\partial y} - \frac{\partial \bar{u}_y^{\mathrm{M}}}{\partial x}. \tag{15}$$

Eq. (15) is the Poisson's equation for the stream function whose contours represent the streamlines. It can be solved numerically using the COMSOL Multiphysics' Mathematics/Classical PDEs Interface with the homogeneous Dirichlet boundary conditions once the streaming velocity vector components $\bar{u}_x^{\mathrm{M}}$, $\bar{u}_y^{\mathrm{M}}$ have been determined.

3. Results and discussion

Hamilton et al. [11,12] have shown that for given fluid in a rectangular channel, apart from the driving frequency, the acoustic streaming structure depends only on the ratio of the channel half-width H, see Fig. 1, and the viscous penetration depth $\delta_{\mathrm{v}} = \sqrt{2\mu/\rho_0\omega}$. As the resonant channels are usually driven near their first resonance frequencies $\omega_0 \sim \pi c_0/L$, it holds $\delta_{\mathrm{v}} \sim \sqrt{L}$ and for given H/δ_{v} ratio, the resonant channel aspect ratio scales as $L/H \sim \sqrt{L}$. As a result, it is more convenient to perform the numerical experiments for short resonant channels. In this case, the length of the channels, filled with air at temperature $T_0 = 20$ °C and normal atmospheric pressure, was chosen as $L = 1$ cm.

All the numerical results presented below correspond to the "slow" streaming régime and they are valid, see [13], for

$$\mathrm{Re}_{\mathrm{nl}} = \left(\frac{u_{\max}}{c_0} \times \frac{H}{\delta_{\mathrm{v}}}\right)^2 \ll 1,$$

where $u_{\max}$ is the maximum axial acoustic velocity amplitude in the channel.

3.1. *Rectangular channel — an inertial driving*

To validate the proposed computational approach, the numerical results were compared with the analytical ones presented by Hamilton et al. [12] for the case of a rectangular channel driven by an inertial force (the entire-body shaking). These analytical formulas are derived from a simplified mathematical model and they are often employed as a benchmark when algorithms for calculation of acoustic streaming are developed. Slight discrepancies can be thus expected in comparisons with current, more complex model, and that is why a detailed analysis is worthwhile.

Differences between analytical and numerical results can be observed even in the case of the primary acoustic field. Fig. 2 shows the distribution of acoustic pressure and velocity amplitude along the axis of a resonator driven at the $\lambda/2$ resonance (this frequency of $f = 16\,833$ Hz maximizes the amplitude of acoustic velocity at the centre of the resonator) for $H/\delta_{\mathrm{v}} = 20$ and driving acceleration amplitude $a_0 = 1$ m/s^2. It can be observed that the analytical formulas predict the amplitudes higher by ca. 4% compared to the numerical model; the difference decreases with decreasing width of the channel (e.g. for $H/\delta_{\mathrm{v}} = 7$ the analytical model overestimates the amplitudes by ca. 1 %).

This discrepancy stems from the fact that the analytical model [12] does not take into account the thermal losses at the resonator end walls (at $x = 0$ and $x = L$) whereas the current model does. Fig. 3 shows the distribution of acoustic

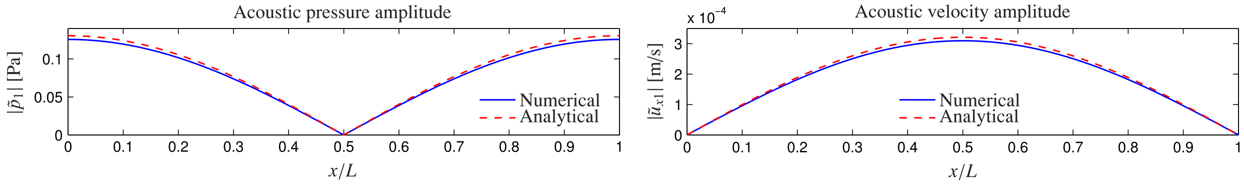

Fig. 2. Acoustic pressure and velocity amplitude distribution along the axis of a rectangular resonator driven by the entire-body shaking at the $\lambda/2$ resonance, $H/\delta_\mathrm{v} = 20$.

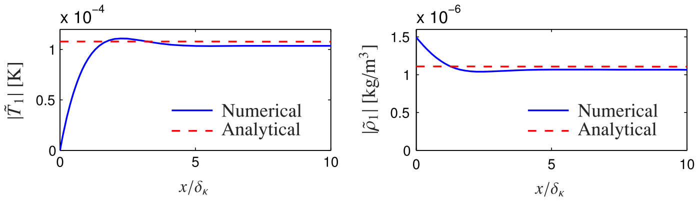

Fig. 3. Acoustic temperature and density amplitude distribution along the axis of a rectangular resonator driven by the entire-body shaking at the $\lambda/2$ resonance, $H/\delta_\mathrm{v} = 20$.

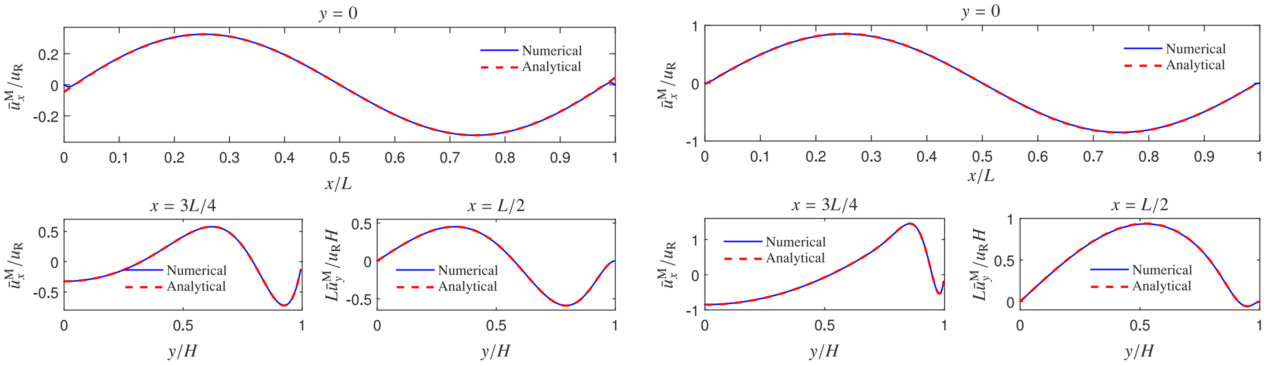

(a) $H/\delta_\mathrm{v} = 7$.

(b) $H/\delta_\mathrm{v} = 20$.

Fig. 4. Averaged mass transport velocity in a rectangular resonator driven by the entire-body shaking at the $\lambda/2$ resonance.

temperature and density along the resonator axis near the left end wall, where the thermal boundary layer with thickness $\delta_\kappa = \sqrt{2\kappa/\rho_0 c_\mathrm{p}\omega}$ connected with the thermal losses can be observed. If the isothermal boundary conditions at the end walls are replaced by adiabatic ones in the numerical model, the differences between the field-quantities amplitudes predicted by numerical and analytical model are negligible. The only exception is the y-component of acoustic velocity near the end walls, as the analytical model does not fulfil the no-slip boundary condition for u_{1y} here in order to comply with a relative simplicity.

Fig. 4 shows the averaged mass transport velocity calculated using the proposed method and analytical formulas for $H/\delta_\mathrm{v} = 7$ and $H/\delta_\mathrm{v} = 20$. The velocities are normalized, following [11,12] using the Rayleigh velocity $u_\mathrm{R} = 3/16 \cdot u_0^2/c_0$, where $u_0 = |\tilde{u}_{1x}(L/2, 0)|$ is the maximum longitudinal velocity in the resonator driven at resonance. It can be observed, that in both the cases, the agreements of the results is perfect. It should be noted, that the physical (non-normalized) values of the velocities would differ because the primary-field amplitudes slightly differ as it was shown above, but, this fact is concealed by the normalization (the corresponding values of u_0 were used in the individual cases). The only appreciable difference between the numerical and analytical results in Fig. 4 can be observed in case of longitudinal component $\bar{u}_x^\mathrm{M}$ near the end walls, where the analytical model, unlike the numerical one, does not fulfil the no-slip boundary condition $\bar{\boldsymbol{u}}^\mathrm{M} = \boldsymbol{0}$ in order to comply with a relative simplicity. The difference is more prominent for lower ratios H/δ_v.

The differences between the numerical and analytical results in the vicinity of the resonator end walls are further shown in Fig. 5(a)–(c), where the streamlines as well as the y-component of averaged mass transport velocity distribution are depicted. Fig. 5(a) shows the case of $H/\delta_\mathrm{v} = 4$, where the left part of the clockwise-rotating inner (Schlichting) vortex is seen together with the region of increased positive velocity $\bar{u}_y^\mathrm{M}$ near the end wall predicted by the numerical model. This increased velocity region is observable also in case of a wider channel, $H/\delta_\mathrm{v} = 7$, see Fig. 5(b), where apart from the inner vortex, the right part of a counter-clockwise-rotating outer (Rayleigh) vortex can be seen.[3] It can be observed that in connection with the increased velocity $\bar{u}_y^\mathrm{M}$ near the end wall, the inner vortex is extended along the wall and the outer vortex to the vicinity of the symmetry axis. Similar inner-vortex distortion near the end wall can be observed in numerical results

---

[3] Hamilton et al. [11] have shown that the outer vortices are present when $H/\delta_\mathrm{v} > 5.7$.

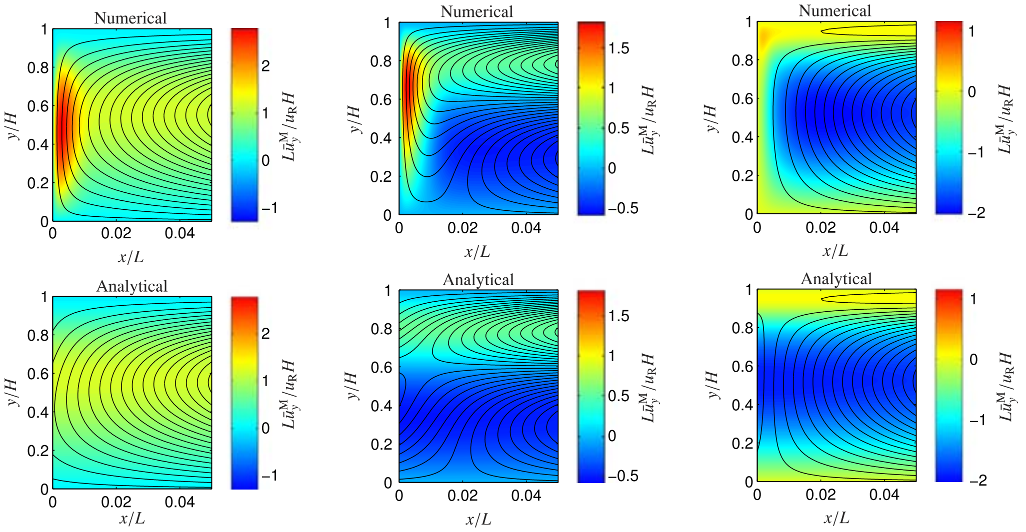

(a) $H/\delta_{\mathrm{v}} = 4, f = 15\,710$ Hz. (b) $H/\delta_{\mathrm{v}} = 7, f = 16\,293$ Hz. (c) $H/\delta_{\mathrm{v}} = 20, f = 16\,833$ Hz.

Fig. 5. Streamlines and $\bar{u}_y^{\mathrm{M}}$ in the vicinity of end wall, driving by the entire-body shaking at $\lambda/2$ resonance.

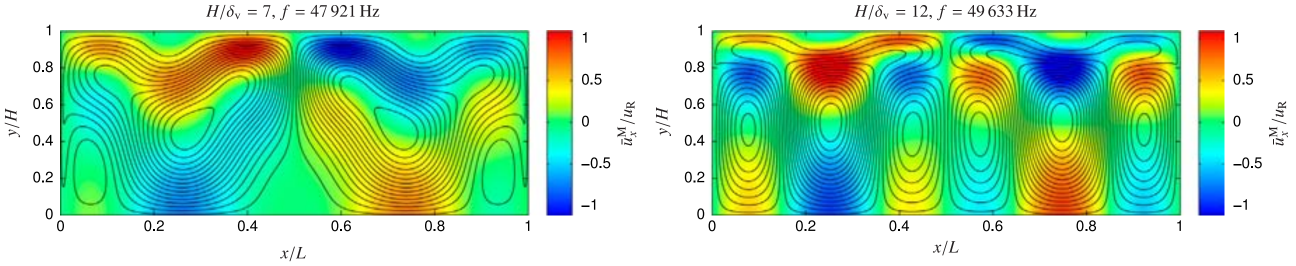

Fig. 6. Streamlines and $\bar{u}_x^{\mathrm{M}}$ in channels with different widths driven by the entire body shaking at $3\lambda/2$ resonance.

by Daru et al. [15]. Fig. 5(c) shows the same situation for $H/\delta_{\mathrm{v}} = 20$, where the outer vortex is dominant and the region of increased velocity $\bar{u}_y^{\mathrm{M}}$ is in the numerical results appreciable only in the vicinity of the inner vortex. It can also be seen in Fig. 5(a)–(c) that the streamlines calculated using the analytical formula crosses the left end wall which is a non-physical effect.

It is well understood, see e.g. [11,12], that the "slow" acoustic streaming structures in resonant channels driven by the entire-body shaking at $\lambda/2$ resonance is composed of $\lambda/4$-long inner and outer vortices (if the channel is wide enough). It should be mentioned that even the structure of the vortices of "slow" streaming can be rather complex, if higher resonant modes are driven, see Fig. 6. For driving at $3\lambda/2$ resonance and $H/\delta_{\mathrm{v}} = 7$ (left panel), some vortices are hardly developed and there are bigger structures appreciable spanning a half the resonator body. If the ratio $H/\delta_{\mathrm{v}} = 12$ (right panel), almost regular structure of the inner and outer vortices appears. These more complex streaming structures are caused by the fact that for lower ratios H/δ_{v}, strong acoustic energy dissipation is present and the primary acoustic field is not entirely spatially periodic, see Fig. 7, but, the acoustic streaming structure preserves the symmetry with respect to axis $x = L/2$.

3.2. Rectangular channel — a boundary driving

Another usual way of exciting acoustic field in a resonator is by means of a vibrating side-wall. In this case, it is assumed that a part of the wall at $x = L$ vibrates harmonically such that its velocity distribution is

$$\boldsymbol{v} = \begin{cases} [v_0 \sin(\omega t), 0] & \text{for } y < \xi H, \\ [0, 0] & \text{for } y \geq \xi H, \end{cases}$$

where v_0 is the vibration velocity amplitude and in the following numerical examples, $\xi = 0.95$.

Fig. 8 shows the comparison of normalized averaged mass transport velocity distribution in a rectangular channel driven by a vibrating wall and by an inertial force at $\lambda/2$ resonance. The left panel 8(a) shows the case of $H/\delta_{\mathrm{v}} = 7, f = 16\,210$ Hz. It can be observed that the streaming velocity amplitude and distribution differ substantially depending on the manner of driving. In the case of boundary driving, the component $\bar{u}_x^{\mathrm{M}}$ does not keep the antisymmetry with respect to $x = L/2$ axis even at the resonance. This behaviour is caused by strong acoustic energy dissipation resulting in broken symmetries of the primary field. The right panel 8(b) shows the case of $H/\delta_{\mathrm{v}} = 20, f = 16\,823$ Hz. It can be seen that with increasing ratio H/δ_{v}, the difference between the results for individual manners of driving decreases. The reason is that for increasing ratio

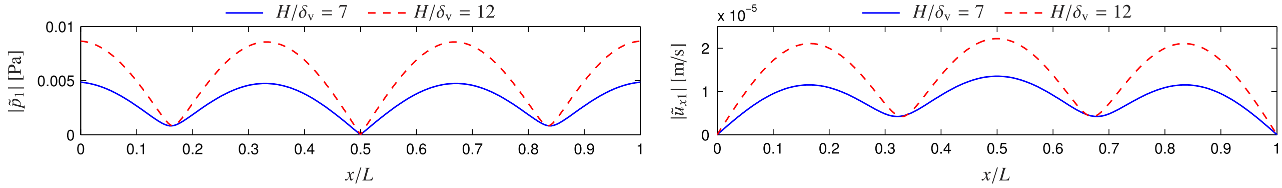

Fig. 7. Acoustic pressure and velocity amplitude distribution along the axis of a rectangular resonator driven by the entire-body shaking at the $3\lambda/2$ resonance, $a_0 = 1$ m/s^2.

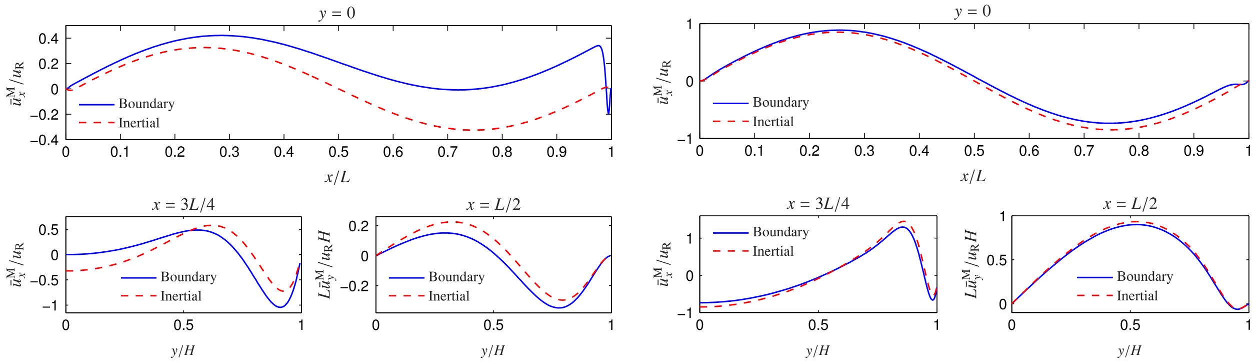

(a) $H/\delta_v = 7$. (b) $H/\delta_v = 20$.

Fig. 8. Averaged mass transport velocity in a rectangular resonator driven by a moving boundary or by an inertial force at the $\lambda/2$ resonance.

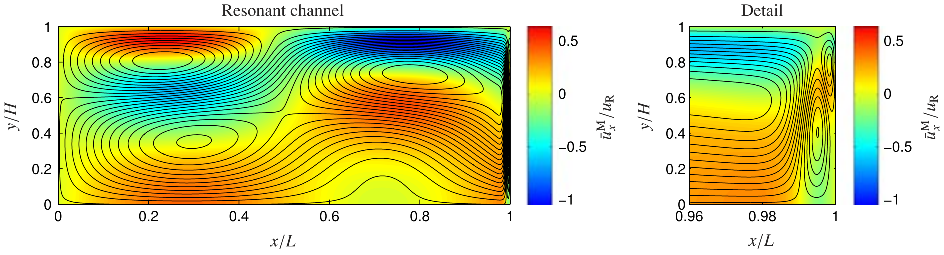

Fig. 9. Streamlines and $\bar{u}_x^M$ in a channel driven by a moving boundary at $\lambda/2$ resonance, $H/\delta_v = 7$.

H/δ_v, the resonator quality factor increases and the asymmetry of the primary as well as the secondary field in the case of the boundary driving is less prominent.

The structure of streamlines for the case $H/\delta_v = 7$ is depicted in Fig. 9. It can be observed that the structure of inner and outer vortices is deformed, some streamlines span the entire resonator body. The detail of streaming near the vibrating wall can be seen in the right part of the figure. The structure of the small vortices depends on the driving velocity distribution (in this case given by the parameter ξ) and the ratio H/δ_v. In any case, the driving velocity distribution influences the streaming structure only in the close proximity of the vibrating wall.

3.3. Wedged channel

As an example of acoustic streaming in a variable-cross-sectioned geometry, the case of a wedged channel driven by an inertial force is presented here. The channel half-width is described using the function

$$y_H = H_n + \frac{H_w - H_n}{L} x,$$

where H_n is the narrow-end half-width and H_w is the wide-end half-width, see Fig. 1.

Fig. 10 shows the x-component of averaged mass transport velocity along the channel axis for $H_n = 0.05$ mm and $H_w/H_n = 1, 1.5, 2, 2.5, \ldots, 5$. In all the cases, the channel was driven at its first resonance frequency, which was determined as the one maximizing acoustic pressure amplitude $|\tilde{p}_1(0, 0)|$. For example, for $H_w/H_n = 1$ (rectangular channel), $f = 14\,805$ Hz ($H_n/\delta_v = 2.8$), for $H_w/H_n = 5$, $f = 17\,618$ Hz. In all the cases, $\bar{u}_x^M$ is normalized by velocities u_R determined with u_0 being the maximum acoustic velocity amplitude along the axis. It can be seen in Fig. 10 that the streaming velocity distribution along the axis changes substantially with increasing H_w/H_n, it even reverses its direction in some regions.

The reason for reversing the streaming direction seen in Fig. 10 can be observed in Fig. 11. If $H_w/H_n = 2$ (the left panel), only two inner vortices are present where the left one rotates clockwise and the right one rotates counter-clockwise which

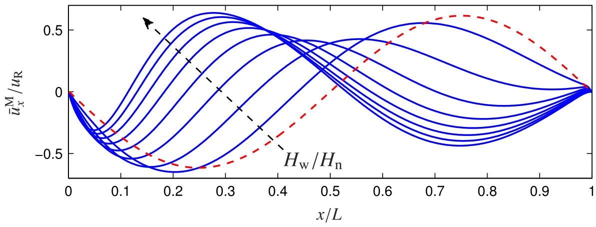

Fig. 10. Normalized $\bar{u}_x^{\mathrm{M}}$ along the axis of a wedged resonator for $H_{\mathrm{w}}/H_{\mathrm{n}} = 1, 1.5, 2, 2.5, \dots, 5$. The case of $H_{\mathrm{w}}/H_{\mathrm{n}} = 1$ is represented by dashed line.

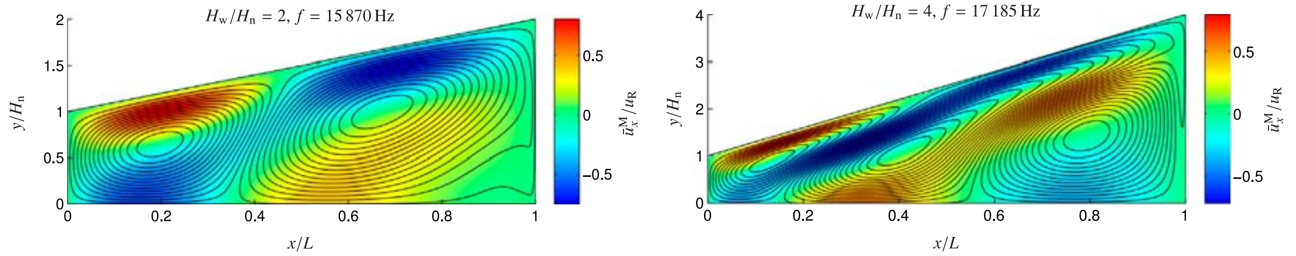

Fig. 11. Streamlines and $\bar{u}_x^{\mathrm{M}}$ in wedged channels driven at the first resonance frequency.

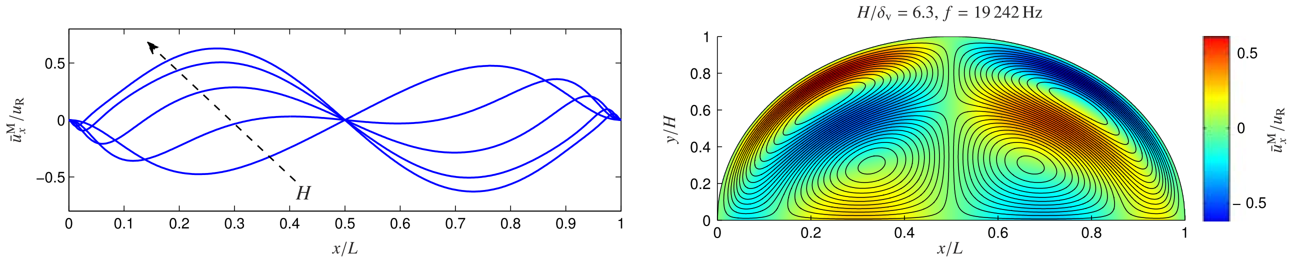

(a) Normalized $\bar{u}_x^{\mathrm{M}}$ along the axis for $H = 0.05, 0.075, 0.1, 0.15, 0.2$ mm.

(b) Streamlines and $\bar{u}_x^{\mathrm{M}}$ for $H = 0.1$ mm.

Fig. 12. Acoustic streaming in an elliptical resonant channel driven at the first resonance frequency.

is why the streaming velocity is negative on the left side and positive on the right side of the channel axis. As the ratio $H_{\mathrm{w}}/H_{\mathrm{n}}$ increases (the case of $H_{\mathrm{w}}/H_{\mathrm{n}} = 4$ is shown in the right panel of Fig. 11), the third (outer) clockwise-rotating vortex begins to develop in the wider part of the resonant channel pushing the first two vortices leftwards, which reverses the streaming velocity direction and makes the streaming structure more complex.

3.4. *Elliptical channel*

An example of acoustic streaming in an elliptical channel driven by an inertial force is presented here. The major semi-axis of the channel is $L/2$, the minor semi-axis is H, see Fig. 1. As before, the resonator is driven by the entire body shaking along its x-axis at its first resonance (maximizing acoustic velocity amplitude at its centre).

Fig. 12(a) shows the x-component of averaged mass transport velocity along the channel axis for $H = 0.05, 0.075, 0.1, 0.15, 0.2$ mm ($H/\delta_{\mathrm{v}} = 3.1, 4.7, 6.3, 9.6, 12.9$). In all the cases, $\bar{u}_x^{\mathrm{M}}$ is normalized by velocities u_{R} determined using the acoustic velocity amplitudes at the channel centre. It can be observed in Fig. 12(a) that for the smallest minor semi-axis, the streaming velocity is negative in the left part of the axis and positive in the right part as there are only two inner vortices present. As the ratio H/δ_{v} increases, two outer vortices begin to appear in the central part of the resonator changing the streaming direction along the axis and pushing the inner vortices out of the bulk of the resonator. For the highest value of H/δ_{v}, the streaming along almost all the axis is dominated by the outer vortices.

The distribution of the x-component of averaged mass transport velocity and the streamlines for the case of $H/\delta_{\mathrm{v}} = 6.3$ can be seen in Fig. 12(b). It can be observed that the outer vortices reside in the central part of the resonant channel and the inner vortices mould them along the entire channel's wall.

4. Conclusions

A set of equations for calculation of the averaged mass transport velocity was derived from the Navier–Stokes equations using the method of successive approximations. As the proposed equations have the standard form of linearized Navier–Stokes equations, they can be numerically integrated using a universal solver, in this case, Acoustic Module of commercially available software COMSOL Multiphysics was employed, which is today a widely used tool in acoustic design. As this software utilizes the finite element method, "slow" acoustic streaming even in complex geometries can be easily studied. If the primary acoustic field is calculated in the frequency domain and the acoustic streaming is studied in the steady state, there is no need for high computational resources, in this case, all the calculations were performed on a contemporary desktop computer. The numerical method was validated using the analytical formulas [12] for the case of a rectangular resonator driven by an inertial force; an excellent agreement was found except for the end-effects, where the proposed model provides more physically accurate results.

It has been shown that the acoustic streaming can be quite complex even in the case of rectangular channels if higher modes are driven; its structure also depends on the manner of driving, especially for lower ratios H/δ_v. The ability of the proposed method to calculate acoustic streaming patterns in complex geometries was demonstrated for the case of a wedged and elliptical resonant channel. It has been shown that the acoustic streaming structure is strongly influenced by the resonator shape which can be employed for designing resonant channels with specific properties.

The proposed computational approach, due to its versatility and simplicity, can find its use as a tool e.g. in designing the lab-on-a-chip acoustophoretic systems or in other areas where the acoustic streaming takes place.

Acknowledgement

This work was supported by GACR Grant No. 15-23079S.

References

[1] W.L. Nyborg, Acoustic streaming, in: W.P. Mason (Ed.), Physical Acoustics, Vo1. lI, Part B, Academic Press, New York, 1965, pp. 265–331.
[2] O.V. Rudenko, S.I. Soluyan, Theoretical Foundations of Nonlinear Acoustics, Consultants Bureau, New York, 1977.
[3] W.L. Nyborg, Acoustic streaming, in: M.F. Hamilton, D.T. Blackstock (Eds.), Nonlinear Acoustics, Academic Press, San Diego, 1998, pp. 207–231.
[4] S. Boluriaan, P.J. Morris, Acoustic streaming: from Rayleigh to today, Int. J. Aeroacoust. 2 (3+4) (2003) 255–292. https://dx.doi.org/10.1260/147547203322986142.
[5] L. Rayleigh, On the circulation of air observed in Kundt's tubes, and on some allied acoustical problems, Philos. Trans. R. Soc. Lond. 175 (1884) 1–21. http://dx.doi.org/10.1098/rstl.1884.0002.
[6] G.W. Swift, Thermoacoustics: A Unifying Perspective for Some Engines and Refrigerators, Acoustical Society of America, Melville, New York, 2002.
[7] G. Mozurkewich, Heat transport by acoustic streaming within a cylindrical resonator, Appl. Acoust. 63 (2002) 713–735. http://dx.doi.org/10.1016/S0003-682X(01)00077-9.
[8] R. Green, M. Ohlin, M. Wiklund, Applications of acoustic streaming, in: T. Laurell, A. Lenshof (Eds.), Microscale Acoustofluidics, The Royal Society of Chemistry, Cambridge, 2015, pp. 312–336.
[9] R. Waxler, Stationary velocity and pressure gradients in a thermoacoustic stack, J. Acoust. Soc. Am. 109 (2001) 2739–2750. http://dx.doi.org/10.1121/1.1370358.
[10] H. Bailliet, V. Gusev, R. Raspet, R.A. Hiller, Acoustic streaming in closed thermoacoustic devices, J. Acoust. Soc. Am. 110 (2001) 1808–1821. http://dx.doi.org/10.1121/1.1394739.
[11] M.F. Hamilton, Y.A. Ilinskii, E.A. Zabolotskaya, Acoustic streaming generated by standing waves in two-dimensional channels of arbitrary width, J. Acoust. Soc. Am. 113 (2003) 153–160. http://dx.doi.org/10.1121/1.1528928.
[12] M.F. Hamilton, Y.A. Ilinskii, E.A. Zabolotskaya, Thermal effects on acoustic streaming in standing waves, J. Acoust. Soc. Am. 114 (2003) 3092–3101. http://dx.doi.org/10.1121/1.1618752.
[13] L. Menguy, J. Gilbert, Non-linear acoustic streaming accompanying a plane stationary wave in a guide, Acust. Acta Acust. 86 (2000) 249–259.
[14] M.K. Aktas, B. Farouk, Numerical simulation of acoustic streaming generated by finite-amplitude resonant oscillations in an enclosure, J. Acoust. Soc. Am. 116 (2004) 2822–2831. http://dx.doi.org/10.1121/1.1795332.
[15] V. Daru, D. Baltean-Carlès, C. Weisman, P. Debesse, G. Gandikota, Two-dimensional numerical simulations of nonlinear acoustic streaming in standing waves, Wave Motion 50 (2013) 955–963. http://dx.doi.org/10.1016/j.wavemoti.2013.03.004.
[16] I. Reyt, V. Daru, H. Bailliet, S. Moreau, J.-C. Valière, D. Baltean-Carlès, C. Weisman, Fast acoustic streaming in standing waves: generation of an additional outer streaming cell, J. Acoust. Soc. Am. 134 (2013) 1791–1801. http://dx.doi.org/10.1121/1.4817888.
[17] D.S. Antao, B. Farouk, High amplitude nonlinear acoustic wave driven flow fields in cylindrical and conical resonators, J. Acoust. Soc. Am. 134 (2013) 917–932. http://dx.doi.org/10.1121/1.4807635.
[18] B. Lautrup, Physics of continuous matter, in: Exotic and Everyday Phenomena in the Macroscopic World, second ed., CRC Pres, Boca Raton, 2011.
[19] A. Boufermel, N. Joly, P. Lotton, M. Amari, V. Gusev, Velocity of mass transport to model acoustic streaming: Numerical application to annular resonators, Acust. Acta Acust. 97 (2011) 219–227. http://dx.doi.org/10.3813/AAA.918401.
[20] Q. Tang, J. Hu, Diversity of acoustic streaming in a rectangular acoustofluidic field, Ultrasonics 58 (2015) 27–34. http://dx.doi.org/10.1016/j.ultras.2014.11.015.

A.7 Effect of inhomogeneous temperature fields on acoustic streaming structures in resonators

Červenka, M., Bednařík, M., Effect of inhomogeneous temperature fields on acoustic streaming structures in resonators, Journal of the Acoustical Society of America 141(6), 4418-4426, (2017).

Effect of inhomogeneous temperature fields on acoustic streaming structures in resonators

Milan Červenka[a] and Michal Bednařík
Faculty of Electrical Engineering, Czech Technical University in Prague, Technická 2, 166 27 Prague 6, Czech Republic

(Received 8 February 2017; revised 17 May 2017; accepted 26 May 2017; published online 14 June 2017)

Acoustic streaming in 2D rectangular resonant channels filled with a fluid with a spatial temperature distribution is studied within this work. An inertial force is assumed for driving the acoustic field; the temperature inhomogeneity is introduced by resonator walls with prescribed temperature distribution. The method of successive approximations is employed to derive linear equations for calculation of primary acoustic and time-averaged secondary fields including the streaming velocity. The model equations have a standard form which allows their numerical integration using a universal solver; in this case, COMSOL Multiphysics was employed. The numerical results show that fluid temperature variations in the direction perpendicular to the resonator axis influence strongly the streaming field if the ratio of the channel width and the viscous boundary layer thickness is big enough; the streaming in the Rayleigh vortices can be supported as well as opposed, which can ultimately lead to the appearance of additional vortices. *© 2017 Acoustical Society of America.*

[http://dx.doi.org/10.1121/1.4985386]

[JDM] Pages: 4418–4426

I. INTRODUCTION

Acoustic streaming[1,2] refers to a second-order net mean fluid flow generated by and superimposed on the first-order acoustic field. There are several different mechanisms by which acoustic streaming is generated;[2] within this work, attention is paid to boundary-layer-driven streaming, first studied by Lord Rayleigh,[3] appearing in a standing wave resonator because of shear viscous forces near the fluid-solid boundary.

If the velocity of acoustic streaming is small enough so that the effect of inertia on the fluid motion can be neglected by comparison with viscous effects, we speak about "slow" streaming. In the case of "fast" or "nonlinear" streaming, the effect of inertia cannot be neglected any more. Whether acoustic streaming is in slow or fast regime can be determined using the nonlinear Reynolds number[4] $\mathrm{Re}_{\mathrm{nl}}$.

Acoustic streaming in resonators has been studied theoretically as well as experimentally. For theoretical study of the slow streaming[5–8] ($\mathrm{Re}_{\mathrm{nl}} \ll 1$), methods of perturbation analysis can be employed, theoretical study of the fast acoustic streaming[9–13] ($\mathrm{Re}_{\mathrm{nl}} \gg 1$) is usually based on methods of computational fluid dynamics. Structure of the slow streaming consists of inner (boundary-layer) and outer (Rayleigh) vortices if the resonant channel is wide enough,[7,8] in the case of the fast streaming, the outer vortices are distorted, additional vortices may appear[10,11] or the streaming structure can be irregular.[9] Experimental methods utilize laser Doppler velocimetry[11,14–16] or particle image velocimetry.[16–19]

Acoustic streaming plays an important role in thermoacoustics, where it usually represents an unwanted mechanism of convective heat transfer which reduces the efficiency of high-amplitude thermoacoustic devices; on the other hand, the heat transfer supported by acoustic streaming[20] could find its application in cooling hot objects like electronic components. In their experimental work, Thompson *et al.*[14] reported a strong sensitivity of acoustic streaming velocity on thermoacoustically induced temperature gradient along the resonator axis. Recently, by comparing experimental data with results of numerical simulations, Reyt *et al.*[11] have shown that the departure of acoustic streaming from slow- to fast-regime (distortion of vortices, the appearance of additional outer vortices) is caused mainly by the effects of inertia on the streaming flow, however, thermal effects are important and may cause the discrepancy between results of numerical simulations and the experimental data. Heat transfer in rectangular channels with differentially heated walls and corresponding streaming structures have also been studied by means of numerical simulations[21–23] as well as experimentally.[24,25]

Even if acoustic streaming in resonators has been extensively studied and its behaviour and properties are relatively well understood, resources regarding its interaction with temperature-inhomogeneous fields are relatively scarce, which was the motivation for us to carry out this study. The work is focused on the properties of slow-streaming structures in fluid-filled rectangular resonant channels (resonators) with spatially variable walls' temperature distribution, which introduces fluid-temperature inhomogeneity.

In Sec. II of this paper, model equations are derived, and a procedure for their numerical integration is proposed. In Sec. III, numerical results are validated against an analytical model, and a strong dependence of acoustic streaming structure on the fluid temperature distribution is demonstrated on three model cases. In Sec. IV, the numerical results are analysed and discussed, and some generalities are outlined; Sec. V concludes the paper.

---

[a] Electronic mail: milan.cervenka@fel.cvut.cz

0001-4966/2017/141(6)/4418/9/$30.00

II. THEORETICAL MODEL

A. Model equations

As the acoustic streaming is a result of nonlinear wave interactions, the Navier-Stokes equations serve as the starting point for its mathematical description. The mass, momentum, and energy equation can be written in form

$$\frac{\mathrm{d}\rho}{\mathrm{d}t} = -\rho \boldsymbol{\nabla} \cdot \boldsymbol{u}, \tag{1a}$$

$$\rho \frac{\mathrm{d}\boldsymbol{u}}{\mathrm{d}t} = \boldsymbol{\nabla} \cdot \boldsymbol{\sigma} + \boldsymbol{f}, \tag{1b}$$

$$\rho c_\mathrm{p} \frac{\mathrm{d}T}{\mathrm{d}t} - \alpha T \frac{\mathrm{d}p}{\mathrm{d}t} = \boldsymbol{\nabla} \cdot (\kappa \boldsymbol{\nabla} T) + \boldsymbol{\tau} : \boldsymbol{\nabla}\boldsymbol{u}, \tag{1c}$$

where ρ is the density, $\boldsymbol{u}$ is the velocity vector, T is the temperature, p is the pressure, $\boldsymbol{f}$ is the body force density, as the resonant channel is driven by an inertial force (by entire-body shaking); it reads $\boldsymbol{f} = -\rho \boldsymbol{a}(t)$, where $\boldsymbol{a}(t)$ is the channel's acceleration. Within this work, effect of gravity on fluid flow is not taken into account. Further, c_p is the specific heat capacity at constant pressure, α is the isobaric coefficient of volumetric thermal expansion and κ is the coefficient of thermal conduction. The total stress tensor $\boldsymbol{\sigma}$ is defined as

$$\begin{aligned} \boldsymbol{\sigma} &= -p\boldsymbol{I} + \boldsymbol{\tau} \\ &= -p\boldsymbol{I} + \mu\left[\boldsymbol{\nabla}\boldsymbol{u} + (\boldsymbol{\nabla}\boldsymbol{u})^\mathrm{T}\right] - \mu\left(\frac{2}{3} - \tilde{V}\right)(\boldsymbol{\nabla}\cdot\boldsymbol{u})\boldsymbol{I}, \end{aligned} \tag{2}$$

where $\boldsymbol{\tau}$ is the viscous stress tensor, μ is the shear viscosity, $\tilde{V} = \mu_\mathrm{B}/\mu$, where μ_B is the bulk viscosity and $\boldsymbol{I}$ is the identity matrix. Generally, the material parameters are temperature-dependent, i.e., $\mu = \mu(T)$, $\kappa = \kappa(T)$, $c_\mathrm{p} = c_\mathrm{p}(T)$.

In Eqs. (1), the material derivative is defined as $\mathrm{d}(-)/\mathrm{d}t = \partial(-)/\partial t + (\boldsymbol{u}\cdot\boldsymbol{\nabla})(-)$. It is assumed that the fluid is an ideal gas for which the state equation has the form $p = \rho R T$, where R is the specific gas constant and thus $\alpha = -(\partial\rho/\partial T)_p/\rho = 1/T$.

Within this work, the set of Eqs. (1) is solved using the method of successive approximations, i.e., it is assumed that the field variables can be expressed as series

$$\begin{aligned} &p = p_0 + \epsilon p_1 + \epsilon^2 p_2 + \cdots, && \boldsymbol{u} = \epsilon\boldsymbol{u}_1 + \epsilon^2\boldsymbol{u}_2 + \cdots, \\ &\rho = \rho_0 + \epsilon\rho_1 + \epsilon^2\rho_2 + \cdots, && \boldsymbol{a} = \epsilon\boldsymbol{a}_1, \\ &T = T_0 + \epsilon T_1 + \epsilon^2 T_2 + \cdots, && \end{aligned}$$

where $\epsilon \ll 1$ is a small dimensionless parameter (corresponding to the acoustic Mach number), p_0, ρ_0, and T_0 are the ambient quantities (without sound) considered as constants in time. It is assumed that $p_0 = \text{const}$, $T_0 = T_0(\boldsymbol{r})$, and $\rho_0 = \rho_0(\boldsymbol{r}) = p_0/RT_0(\boldsymbol{r})$. Further, p_1, ρ_1, T_1 and $\boldsymbol{u}_1$ are the primary acoustic variables supposed to be harmonic with angular frequency ω, which is the frequency of driving. The quantities with indices bigger than one are the nonlinearly generated terms; in this case, the terms with indices bigger than two are neglected.

Within the method of successive approximations, the above series are substituted into Eqs. (1) and the equations for the same order of ϵ are found.

For ϵ^0, we obtain

$$\boldsymbol{\nabla}\cdot(\kappa_0\boldsymbol{\nabla}T_0) = 0, \tag{3}$$

where $\kappa_0 = \kappa(T_0)$.

For ϵ^1, we can write

$$\frac{\partial\rho_1}{\partial t} + \boldsymbol{\nabla}\cdot(\rho_0\boldsymbol{u}_1) = 0, \tag{4a}$$

$$\begin{aligned} \rho_0\frac{\partial\boldsymbol{u}_1}{\partial t} - \boldsymbol{\nabla}\cdot\Bigg\{&-p_1\boldsymbol{I} + \mu_0\left[\boldsymbol{\nabla}\boldsymbol{u}_1 + (\boldsymbol{\nabla}\boldsymbol{u}_1)^\mathrm{T}\right] \\ &- \mu_0\left(\frac{2}{3} - \tilde{V}\right)(\boldsymbol{\nabla}\cdot\boldsymbol{u}_1)\boldsymbol{I}\Bigg\} = -\rho_0\boldsymbol{a}_1, \end{aligned} \tag{4b}$$

$$\rho_0 c_{\mathrm{p}0}\left(\frac{\partial T_1}{\partial t} + \boldsymbol{u}_1\cdot\boldsymbol{\nabla}T_0\right) - \frac{\partial p_1}{\partial t} - \boldsymbol{\nabla}\cdot(\kappa_0\boldsymbol{\nabla}T_1) = 0, \tag{4c}$$

where $c_{\mathrm{p}0} = c_\mathrm{p}(T_0)$, $\mu_0 = \mu(T_0)$, together with the linearised state equation $p_1/p_0 = T_1/T_0 + \rho_1/\rho_0$. Equations (4) can be used for calculation of the primary acoustic field.

For ϵ^2 the continuity equation (1a) can be rewritten as

$$\frac{\partial\rho_2}{\partial t} + \boldsymbol{\nabla}\cdot(\rho_0\boldsymbol{u}_2) = -\boldsymbol{\nabla}\cdot(\rho_1\boldsymbol{u}_1). \tag{5}$$

As we are further focused on slowly time-varying processes involving acoustic streaming, Eq. (5) is averaged over one period $\tau = 2\pi/\omega$ resulting in

$$\frac{\partial\bar{\rho}_2}{\partial t_\mathrm{s}} + \boldsymbol{\nabla}\cdot(\rho_0\bar{\boldsymbol{u}}_2) = M, \tag{6}$$

where the bar denotes the one-period-averaged quantities, t_s is the time related to the large time-scale phenomena.[26] The source term reads

$$M = -\boldsymbol{\nabla}\cdot\langle\rho_1\boldsymbol{u}_1\rangle. \tag{7}$$

Here, $\langle fg\rangle = \Re[\tilde{f}\tilde{g}^*]/2$; the tildes represent the complex amplitudes of the corresponding quantities and the asterisk stands for the complex conjugate.

Similarly, the momentum equation (1b) for ϵ^2 can be written as

$$\begin{aligned} \rho_0\frac{\partial\bar{\boldsymbol{u}}_2}{\partial t_\mathrm{s}} - \boldsymbol{\nabla}\cdot\Bigg\{&-\bar{p}_2\boldsymbol{I} + \mu_0\left[\boldsymbol{\nabla}\bar{\boldsymbol{u}}_2 + (\boldsymbol{\nabla}\bar{\boldsymbol{u}}_2)^\mathrm{T}\right] \\ &-\mu_0\left(\frac{2}{3} - \tilde{V}\right)(\boldsymbol{\nabla}\cdot\bar{\boldsymbol{u}}_2)\boldsymbol{I}\Bigg\} = \boldsymbol{F}, \end{aligned} \tag{8}$$

where

$$\begin{aligned} \boldsymbol{F} = &-\left\langle\rho_1\left(\boldsymbol{a}_1 + \frac{\partial\boldsymbol{u}_1}{\partial t}\right)\right\rangle - \rho_0\langle(\boldsymbol{u}_1\cdot\boldsymbol{\nabla})\boldsymbol{u}_1\rangle \\ &+\boldsymbol{\nabla}\cdot\left\langle\frac{\mu_0 b_\mu}{T_0}T_1\left[\boldsymbol{\nabla}\boldsymbol{u}_1 + (\boldsymbol{\nabla}\boldsymbol{u}_1)^\mathrm{T} - \left(2/3 + \tilde{V}\right)(\boldsymbol{\nabla}\cdot\boldsymbol{u}_1)\boldsymbol{I}\right]\right\rangle. \end{aligned} \tag{9}$$

Here, the following relation was used:

$$\mu(T) \approx \mu(T_0 + \epsilon T_1) \approx \mu_0 + \epsilon \frac{\mu_0 b_\mu}{T_0} T_1,$$

where $b_\mu = T_0 \cdot (\partial\mu/\partial T)_{T_0}/\mu_0$. The last term in the source term (9) accounts for the periodic variation of the viscosity due to the acoustic temperature[6,8] T_1.

The energy equation (1c) for ϵ^2 can be written as

$$\rho_0 c_{p0}\left(\frac{\partial \bar{T}_2}{\partial t_s} + \bar{\boldsymbol{u}}_2 \cdot \boldsymbol{\nabla} T_0\right) - \frac{\partial \bar{p}_2}{\partial t_s} - \boldsymbol{\nabla}\cdot(\kappa_0 \boldsymbol{\nabla}\bar{T}_2) = Q, \tag{10}$$

where

$$Q = -c_{p0}\left\langle \rho_1 \frac{\partial T_1}{\partial t}\right\rangle - \rho_0 c_{p0}\langle \boldsymbol{u}_1 \cdot \boldsymbol{\nabla} T_1\rangle$$
$$-c_{p0}\langle \rho_1 \boldsymbol{u}_1\rangle \cdot \boldsymbol{\nabla} T_0 + \langle \boldsymbol{u}_1 \cdot \boldsymbol{\nabla} p_1\rangle + \boldsymbol{\nabla}\cdot\left\langle \frac{\kappa_0 b_\kappa}{T_0} T_1 \boldsymbol{\nabla} T_1\right\rangle$$
$$+\mu_0\left\langle\left[\boldsymbol{\nabla}\boldsymbol{u}_1 + (\boldsymbol{\nabla}\boldsymbol{u}_1)^{\mathrm{T}} - \left(\frac{2}{3} - \tilde{V}\right)(\boldsymbol{\nabla}\cdot\boldsymbol{u}_1)\boldsymbol{I}\right] : \boldsymbol{\nabla}\boldsymbol{u}_1\right\rangle. \tag{11}$$

Here, the following relation was used:

$$\kappa(T) \approx \kappa(T_0 + \epsilon T_1) \approx \kappa_0 + \epsilon \frac{\kappa_0 b_\kappa}{T_0} T_1,$$

where $b_\kappa = T_0 \cdot (\partial\kappa/\partial T)_{T_0}/\kappa_0$. Acoustic-temperature-induced variation of the heat capacity was not taken into account in Eq. (10) because it is weaker than in the case of the viscosity and thermal conduction coefficients.

In the steady state, the averaged quantities do not depend on time and thus Eqs. (6), (8), and (10) reduce into

$$\boldsymbol{\nabla}\cdot(\rho_0 \bar{\boldsymbol{u}}_2) = M, \tag{12a}$$

$$-\boldsymbol{\nabla}\cdot\left\{-\bar{p}_2 \boldsymbol{I} + \mu_0\left[\boldsymbol{\nabla}\bar{\boldsymbol{u}}_2 + (\boldsymbol{\nabla}\bar{\boldsymbol{u}}_2)^{\mathrm{T}}\right]\right.$$
$$\left. - \mu_0\left(\frac{2}{3} - \tilde{V}\right)(\boldsymbol{\nabla}\cdot\bar{\boldsymbol{u}}_2)\boldsymbol{I}\right\} = \boldsymbol{F}, \tag{12b}$$

$$\rho_0 c_{p0} \bar{\boldsymbol{u}}_2 \cdot \boldsymbol{\nabla} T_0 - \boldsymbol{\nabla}\cdot(\kappa_0 \boldsymbol{\nabla}\bar{T}_2) = Q. \tag{12c}$$

Notice that at this level of approximation, Eqs. (12a) and (12b) are decoupled from Eq. (12c) and Eq. (12c) is not in fact needed for the calculation of the acoustic streaming field. As a result of this, it is necessary to bear in mind that this model does not take into account the convective heat transport due to the acoustic streaming and the consequent temperature re-distribution. The background temperature T_0 for Eqs. (4) and (12) is calculated *a priori* employing Eq. (3) and corresponding boundary conditions.

The structure of acoustic streaming can be easily visualised in the following way. If we introduce the *averaged mass transport density* $\bar{\boldsymbol{m}}^{\mathrm{M}} = \rho_0 \bar{\boldsymbol{u}}_2 + \langle \rho_1 \boldsymbol{u}_1\rangle = \rho_0 \bar{\boldsymbol{u}}^{\mathrm{M}}$, where $\bar{\boldsymbol{u}}^{\mathrm{M}}$ is the averaged mass transport velocity,[7,26] the continuity equation (12a) can be rewritten as

$$\boldsymbol{\nabla}\cdot\bar{\boldsymbol{m}}^{\mathrm{M}} = 0. \tag{13}$$

As the steady averaged mass transport density field is divergence-free, the stream function ψ can be introduced such that in 2D Cartesian coordinates it holds

$$\bar{m}_x^{\mathrm{M}} = \frac{\partial\psi}{\partial y}, \quad \bar{m}_y^{\mathrm{M}} = -\frac{\partial\psi}{\partial x}.$$

From here, we can calculate the stream function as

$$\frac{\partial^2\psi}{\partial x^2} + \frac{\partial^2\psi}{\partial y^2} = \frac{\partial \bar{m}_x^{\mathrm{M}}}{\partial y} - \frac{\partial \bar{m}_y^{\mathrm{M}}}{\partial x}. \tag{14}$$

The contours of the stream function represent the streamlines.

B. Numerical solution of the model equations

All the model equations were solved numerically using finite-element-method software COMSOL Multiphysics. An approach similar to the one presented previously[27–29] was employed here. The numerical procedure is schematically depicted in Fig. 1 and it works as follows.

First, an equilibrium temperature distribution T_0 in the resonant channel is calculated employing Eq. (3) using corresponding boundary conditions for walls' temperature. For this purpose, Heat Transfer in Fluids, Stationary study type is employed.

Second, the primary field quantities p_1, $\boldsymbol{u}_1$, T_1, and ρ_1 are calculated using the Linearised Navier-Stokes, Frequency Domain (lnsf) study type, which solves Eqs. (4) in the frequency domain. The term $-\rho_0 \boldsymbol{a}_1$ is used as a volume source in the momentum equation. The resonance frequency is determined using the frequency sweep.

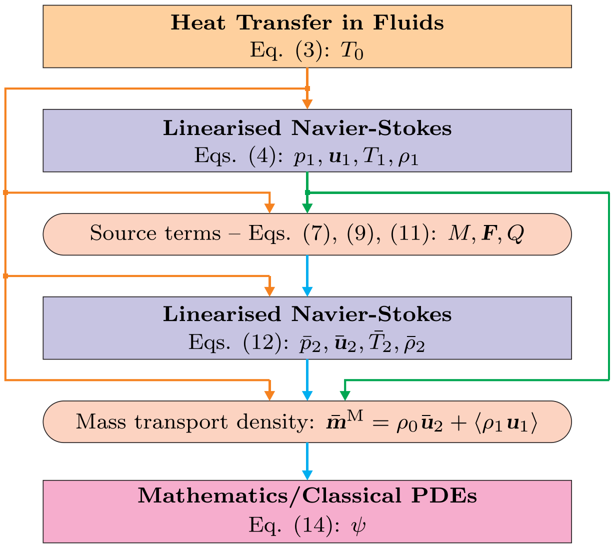

FIG. 1. (Color online) Flowchart of the computational procedure.

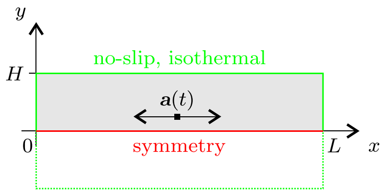

FIG. 2. (Color online) Geometry of the computational domain.

Third, employing again the Linearised Navier-Stokes, Frequency Domain (lnsf) study type, Eqs. (12) are solved for the averaged quantities $\bar{p}_2$, $\bar{\boldsymbol{u}}_2$, $\bar{T}_2$, and $\bar{\rho}_2$; Eqs. (12) have formally the same form as Eqs. (4), only the volume sources differ; they are calculated using formulas (7), (9) and (11) employing the previously calculated primary variables.

Within the Acoustic Module of the COMSOL Multiphysics, only the frequency-domain and the time-domain (transient) studies are implemented for the linearised Navier-Stokes equations. In order to reduce the computational cost, the steady-state secondary field is calculated using the frequency-domain analysis at the frequency of 0 Hz [actually, the frequency of 10^{-16} Hz was used which effectively eliminates the derivatives with respect to time in Eqs. (12)].

Fourth, the Poisson's equation (14) is solved employing Mathematics/Classical PDEs Interface with the homogeneous Dirichlet boundary conditions once the averaged mass transport density has been determined in the previous step.

The numerical calculations were performed in 2D Cartesian x-y geometry (see Fig. 2) modification for 2D axisymmetric geometry would be straightforward. The physical conditions were assumed to be symmetric with respect to the x axis so that the computational domain represented only a half of the resonant cavity. No-slip and isothermal walls of the cavity were assumed; driving with harmonic acceleration with zero y-component was taken into account. The isothermal boundary conditions reflect the fact that the solid walls of resonant cavities usually have heat capacity and conduction high enough to enforce constant temperature at the solid-fluid boundaries.

Computational meshes were constructed in order to properly resolve the boundary layers along the walls, mapped (structured) meshes with refinement along the walls were found to work well; the independence of numerical results on the mesh density was checked. Moreover, numerical results were compared with an analytical model (see Sec. III A).

As the volume sources (7), (9), and (11) depend on the spatial derivatives of the primary field quantities; rather fine computational mesh is required. For example, in the case of a resonant channel with the dimensions of 1.5 cm × 30 cm, the total number of used mesh-points was 240 × 1100, where 20 regularly spaced mesh-points discretized the boundary layer thickness, and 50 mesh-points were used for a smooth transition from the boundary layer to the inner volume, where the mesh-points were regularly spaced again.

III. NUMERICAL RESULTS

Hamilton *et al.*[7,8] have shown that the streaming structure in a rectangular resonant channel driven at its resonance frequency depends on the ratio of the resonator half-width H and the viscous boundary layer thickness $\delta_{\mathrm{v}} = \sqrt{2\mu/\rho_0\omega}$. As at the resonance $\omega \sim \pi c_0/L$, it holds $\delta_{\mathrm{v}} \sim \sqrt{L}$ and thus the resonator aspect ratio scales as $L/H \sim \sqrt{L}$ for given ratio H/δ_{v}. That is why it is more convenient to study *small* resonator cavities, e.g., $L \sim 1$ cm, if various aspects of acoustic streaming are studied (corresponding model equations are solved) numerically.[9–11,13,23] Within this work, we do not limit ourselves to study of *small* resonators. It means that the numerical calculations require higher computational resources, but, as the equations are integrated in the frequency domain, the calculations can be performed on a desktop computer (in all the studied cases, less then 45 GB of RAM were allocated by COMSOL). A typical computational time is ca. 30 s for the calculation of the background temperature, ca. 3 min for the primary field, ca. 3 min for the secondary field, and ca. 30 s for the stream function (Intel Core i7-5820 K processor).

The resonant cavities studied within this work were assumed to have imposed temperature of walls $T_{\mathrm{w}} = T_{\mathrm{w}}(x)$, and to be filled with air at normal atmospheric pressure. The temperature-dependent values of the material parameters μ, κ and c_{p} are implemented in the material database of COMSOL Multiphysics, the ones for air were used here.

All the numerical and analytical results are presented in the conditions of the first resonance which was searched for by a frequency sweep by maximization of the acoustic velocity amplitude in the resonator.

A. Comparison with an analytical model

In order to check that the computational mesh is fine enough to resolve the boundary layer properly and that the numerical results are reliable, they were compared with the predictions of the analytical model by Hamilton *et al.*[8] for the case of a temperature-homogeneous fluid.

In this case, $L = 30$ cm, $H = 1.5$ cm, $T_0 = 20\,°\mathrm{C}$, $f = f_{\mathrm{res}} = 570.5$ Hz, resulting in $H/\delta_{\mathrm{v}} = 164$. Figure 3 shows the averaged mass transport velocity in the resonator as predicted by numerical and theoretical model. The averaged mass transport velocity is normalized using the Rayleigh velocity $u_{\mathrm{R}} = 3/16 \cdot u_0^2/c_0$, where $u_0 = \max[|\tilde{u}_{1x}(x, 0)|]$ is the maximum longitudinal velocity amplitude in the resonator driven at its resonance frequency and c_0 is the speed of sound. It can be seen that the numerical and analytical results

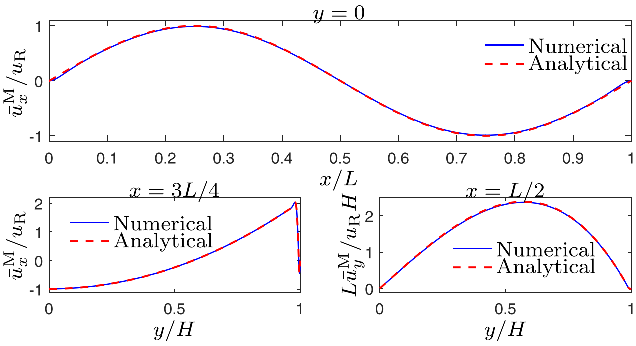

FIG. 3. (Color online) Comparison of numerical and analytical results: averaged mass transport velocity in a resonator, $T_0 = 20\,°\mathrm{C}$, $H/\delta_{\mathrm{v}} = 164$.

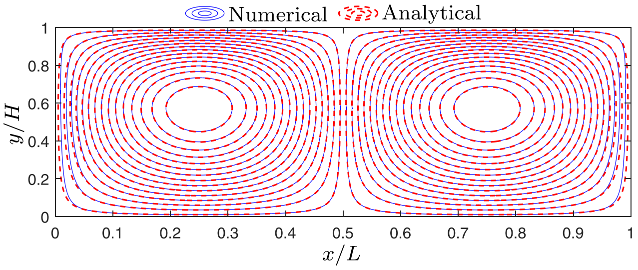

FIG. 4. (Color online) Comparison of numerical and analytical results: streamlines in a resonator, $T_0 = 20\,°\text{C}$, $H/\delta_\text{v} = 164$.

correspond to each other very well. Generally, the analytical model overestimates the amplitudes of the primary-field quantities as it does not take into account thermal losses at the side walls[29] $x = 0$ and $x = L$, this disagreement is concealed in Fig. 3 because of the normalisation.

Figure 4 shows the distribution of streamlines for the same conditions as in the previous case, two Rayleigh vortices rotating in the opposite directions can be observed in the figure. The fluid circulates from the acoustic-velocity nodes (resonator end walls) along the resonator axis toward the acoustic-velocity antinode (resonator centre) and returns in the near wall region to close the loop; the fluid in the left vortex rotates anti-clockwise, the fluid in the right vortex rotates clock-wise. The inner vortices cannot be observed in the figure because of the high value of H/δ_v. Again, the correspondence between the numerical and analytical results is very good except for the close proximity of the side walls $x = 0$ and $x = L$, where the analytical model does not capture the streaming field correctly.[29]

B. Streaming in a fluid with spatially varying temperature

1. Case 1

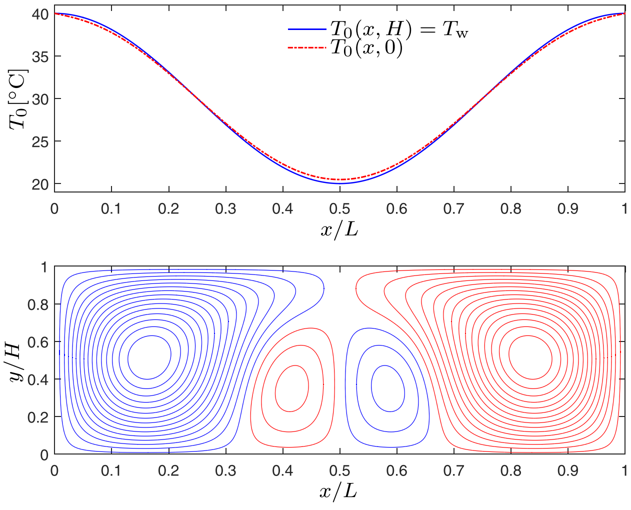

FIG. 5. (Color online) (Top) Distribution of the ambient temperature along the resonator wall and along its axis, T_w given by Eq. (15), $\Delta T = 20\,°\text{C}$, $L = 30\,\text{cm}$, $H = 1.5\,\text{cm}$. (Bottom) Streamlines in the resonator.

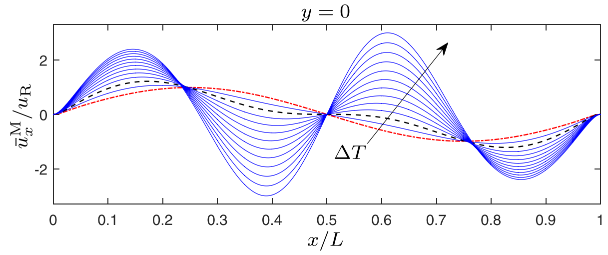

FIG. 6. (Color online) Averaged mass transport velocity along the resonator axis, $L = 30\,\text{cm}$, $H = 1.5\,\text{cm}$, and $\Delta T = 0\,°\text{C}$, $5\,°\text{C}$, $10\,°\text{C}, \ldots, 60\,°\text{C}$; dash-dot (red) line: $\Delta T = 0\,°\text{C}$, dashed (black) line: $\Delta T = 10\,°\text{C}$.

Let us assume the resonator walls with the temperature distribution given as

$$T_\text{w} = \frac{\Delta T}{2}\left[1 + \cos\left(\frac{2\pi x}{L}\right)\right] + T_{\text{w}0}, \tag{15}$$

where $T_{\text{w}0}$ is the minimum temperature of the resonator walls and ΔT is the maximum temperature difference. The formula (15) serves as the boundary condition for Eq. (3) for calculation of the fluid ambient temperature $T_0(\boldsymbol{r})$. In all the following cases, $T_{\text{w}0} = 20\,°\text{C}$ and temperatures ΔT differ.

The wall temperature distribution (15) corresponds to the case of thermoacoustically driven heat transport along the resonator walls from acoustic-velocity antinode toward the acoustic-velocity nodes.[14]

The top part of Fig. 5 shows the distribution of the ambient temperature in a resonator with $L = 30\,\text{cm}$, $H = 1.5\,\text{cm}$, and $\Delta T = 20\,°\text{C}$. The solid line corresponds to the temperature along the wall $T_0(x, H)$, the dash-dot line corresponds to the temperature along the resonator axis $T_0(x, 0)$. The temperatures slightly differ as it follows from the solution of Eq. (3). The bottom part of the figure shows the streaming structure in the resonator. In this and the following figures, the clockwise rotating vortices are denoted by red lines; the anticlockwise rotating ones are denoted by blue lines. It can be observed (in comparison with Fig. 4) that due to the fluid temperature inhomogeneity, there are two additional vortices present in the central part of the resonator. The appearance of the additional vortices is connected with the reversion of the streaming velocity in the central part of the resonator.

Figure 6 shows the averaged mass transport velocity distribution along the x axis in the resonator with $L = 30\,\text{cm}$, $H = 1.5\,\text{cm}$, and $\Delta T = 0\,°\text{C}$, $5\,°\text{C}$, $10\,°\text{C}, \ldots, 60\,°\text{C}$. If $\Delta T \gtrsim 10\,°\text{C}$ (dashed line in Fig. 6), the reversion of the averaged mass transport velocity appears. The figure reveals a strong dependence of acoustic streaming structure on the temperature difference as well as its overall increase with the

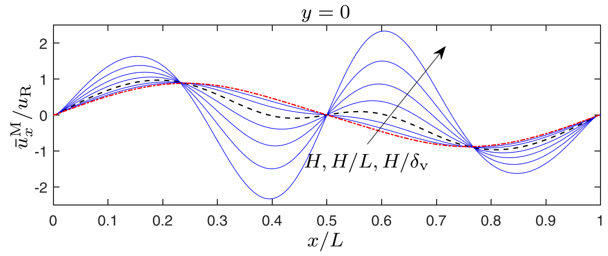

FIG. 7. (Color online) Averaged mass transport velocity along the resonator axis, $L = 30\,\text{cm}$, $H = 5, 6, 7, \ldots, 12\,\text{mm}$ and $\Delta T = 100\,°\text{C}$; dash-dot (red) line: $H = 5\,\text{mm}$, dashed (black) line: $H = 8\,\text{mm}$.

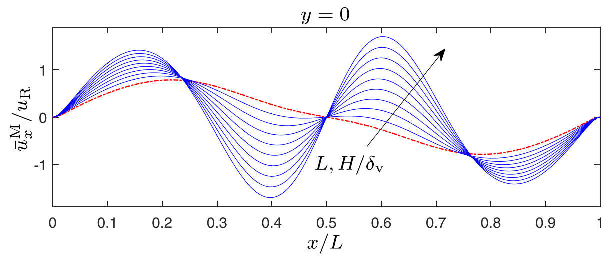

FIG. 8. (Color online) Averaged mass transport velocity along the resonator axis, $L = 1, 2, 3, \ldots, 10$ cm, $H = L/20$ and $\Delta T = 100\,^\circ$C; dash-dot (red) line: $L = 1$ cm.

increased value of ΔT. For bigger values of ΔT, the streaming velocity within additional vortices can exceed the streaming velocity within the Rayleigh vortices.

Figure 7 demonstrates the fact that for the given resonator length and the wall temperature difference ΔT, the appearance of the additional vortices depends on the resonator width. In this case, $L = 30$ cm, $\Delta T = 100\,^\circ$C, and $H = 5, 6, 7, \ldots, 12$ mm. For example, for $H = 5$ mm, the ratio H/δ_{v} varies in the interval 42.8–55.4, for $H = 12$ mm, it varies in the interval 103.0–132.7. It can be observed that the streaming reversion appears in *wider* resonators, in this case, for $H \gtrsim 8$ mm (dashed line).

Figure 8 shows the distribution of the averaged mass transport velocity along the axes of resonators with different lengths $L = 1, 2, 3, \ldots, 10$ cm, but the same aspect ratio $H/L = 1/20$ and $\Delta T = 100\,^\circ$C. For example, for $L = 1$ cm, the ratio H/δ_{v} varies in the interval 23.4 – 30.1, for $L = 10$ cm, it varies in the interval 74.3 – 95.5. It can be observed that the additional vortices do not appear in the resonators with the lengths of 1 cm and 2 cm, and they are more pronounced in bigger resonators with higher ratio H/δ_{v}.

Figure 9 shows the distribution of the averaged mass transport velocity along the axes of resonators with different lengths $L = 5, 10, 15, \ldots, 30$ cm, but the same $\Delta T = 100\,^\circ$C and the same ratio H/δ_{v}, which varies (because of the wall temperature distribution) in the interval ca. 79–101. As the ratio H/δ_{v} is kept constant, the resonator aspect ratio decreases with increasing length. For example, for $L = 5$ cm, $H/L = 1/13.3$, for $L = 30$ cm, $H/L = 1/32.6$. It can be observed that the bigger the resonator aspect ratio H/L, the bigger the streaming velocity within the additional vortices.

It follows from the Figs. 6–9 that for the appearance of the additional vortices in a resonator with given geometry, the wall temperature variation ΔT must be big enough. The additional vortices (if present) are more pronounced in resonators with bigger aspect ratio H/L and the ratio H/δ_{v}.

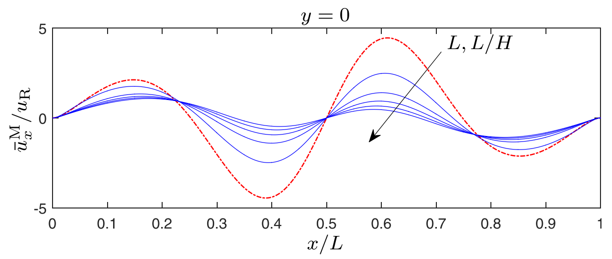

FIG. 9. (Color online) Averaged mass transport velocity along the resonator axis, $L = 5, 10, 15, \ldots, 30$ cm, H/δ_{v} the same for all the resonators, $\Delta T = 100\,^\circ$C; dash-dot (red) line: $L = 5$ cm.

2. Case 2

Let us assume the resonator walls with the temperature distribution given as

$$T_{\mathrm{w}} = \frac{\Delta T}{2}\left[1 - \cos\left(\frac{2\pi x}{L}\right)\right] + T_{\mathrm{w}0}, \tag{16}$$

contrary to the previous case, here, the wall temperature increases toward the resonator centre. The meaning of the individual symbols is the same as before, again, in all the following cases, $T_{\mathrm{w}0} = 20\,^\circ$C and temperatures ΔT differ.

The top part of Fig. 10 shows the distribution of the ambient temperature along the wall and the axis of a resonator with $L = 30$ cm, $H = 1.5$ cm, and $\Delta T = 20\,^\circ$C. Again, temperatures slightly differ as it follows from the solution of Eq. (3). The bottom part of the figure shows the streaming structure in the resonator. It can be observed that due to the fluid temperature inhomogeneity, there are two additional vortices present, which, contrary to the previous case, reside near the end-walls of the resonator cavity.

The appearance of the additional vortices is connected with the reversion of the streaming velocity near the end-walls. Figure 11 shows the averaged mass transport velocity distribution along the x axis in a resonator with $L = 30$ cm, $H = 1.5$ cm, and $\Delta T = 0\,^\circ$C, $5\,^\circ$C, $10\,^\circ$C,…, $60\,^\circ$C. When $\Delta T \gtrsim 15^\circ$C (dashed line in Fig. 11), the reversion of the averaged mass transport velocity appears. Again, a strong dependence of acoustic streaming structure on the temperature difference ΔT can be observed. Numerical results show the similar qualitative behaviour of the additional vortices as a function of the resonator geometry as in the previous case.

3. Case 3

Let us assume the resonator walls with the temperature distribution given as

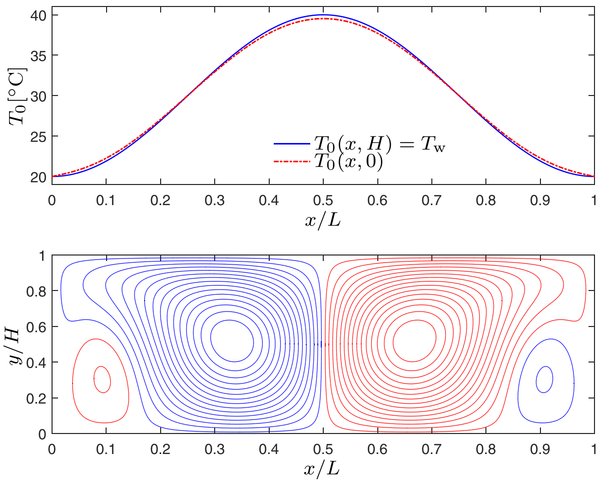

FIG. 10. (Color online) (Top) Distribution of the ambient temperature along the resonator wall and along its axis, T_{w} given by Eq. (16), $\Delta T = 20\,^\circ$C, $L = 30$ cm, $H = 1.5$ cm. (Bottom) Streamlines in the resonator.

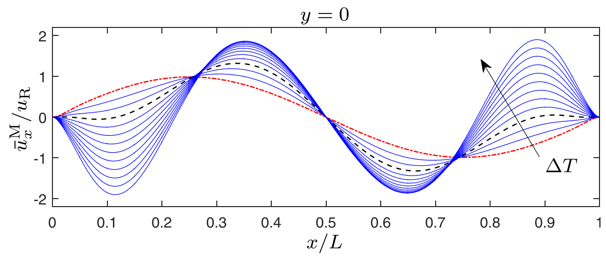

FIG. 11. (Color online) Averaged mass transport velocity along the resonator axis, $L = 30$ cm, $H = 1.5$ cm, and $\Delta T = 0\,^{\circ}$C, $5\,^{\circ}$C, $10\,^{\circ}$C,…, $60\,^{\circ}$C; dash-dot (red) line: $\Delta T = 0\,^{\circ}$C, dashed (black) line: $\Delta T = 15\,^{\circ}$C.

$$T_{\mathrm{w}} = \begin{cases} T_{\mathrm{w0}} & \text{for} \quad x < x_1, \\ T_{\mathrm{w0}} + \Delta T \dfrac{x - x_1}{x_2 - x_1} & \text{for} \quad x_1 \le x < x_2, \\ T_{\mathrm{w0}} + \Delta T & \text{for} \quad x \ge x_2. \end{cases} \tag{17}$$

The temperature distribution (17) is a typical one encountered in thermoacoustics. The meaning of the individual symbols is the same as before, again, in all the following cases, $T_{\mathrm{w0}} = 20\,^{\circ}$C and temperature differences ΔT differ.

The top part of Fig. 12 shows the distribution of ambient temperature along the wall and the axis of a resonator with $L = 30$ cm, $H = 1.5$ cm, and $\Delta T = 20\,^{\circ}$C. The temperatures slightly differ as it follows from the solution of Eq. (3) in the vicinity of $x = x_1$ and $x = x_2$, where the wall-temperature profile changes. The bottom part of the figure shows the streaming structure in the resonator. It can be observed that due to the fluid temperature inhomogeneity, there is one additional vortex present occupying the right-central part of the resonator. It can also be observed that the streamlines are much denser in the right part of the resonator, where the temperature inhomogeneity is present, meaning that the streaming is stronger here.

Figure 13 shows the averaged mass transport velocity distribution along the x axis in a resonator with $L = 30$ cm, $H = 1.5$ cm, and $\Delta T = 0\,^{\circ}$C, $5\,^{\circ}$C, $10\,^{\circ}$C,…, $30\,^{\circ}$C. It can be observed that in the right part of the resonator, the streaming velocity manifests strong dependence on ΔT. Numerical results show the similar qualitative behaviour of the additional vortex as a function of the resonator geometry as in the previous cases.

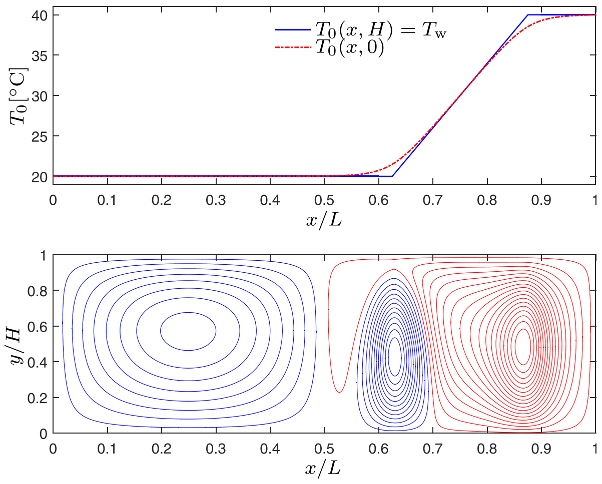

FIG. 12. (Color online) (Top) Distribution of the ambient temperature along the resonator wall and along its axis, T_{w} given by Eq. (17), $\Delta T = 20\,^{\circ}$C, $L = 30$ cm, $H = 1.5$ cm. (Bottom) Streamlines in the resonator.

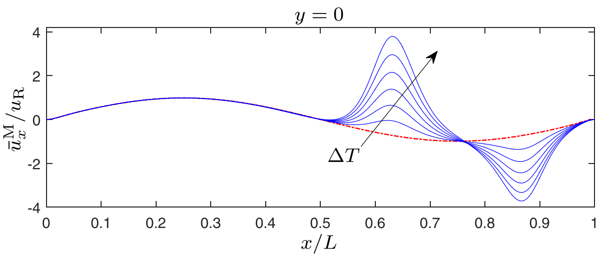

FIG. 13. (Color online) Averaged mass transport velocity along the resonator axis, $L = 30$ cm, $H = 1.5$ cm, and $\Delta T = 0\,^{\circ}$C, $5\,^{\circ}$C, $10\,^{\circ}$C,…, $30\,^{\circ}$C; dash-dot (red) line: $\Delta T = 0\,^{\circ}$C, dashed (black) line.

IV. ANALYSIS OF THE NUMERICAL RESULTS

A. General observations

Numerical results presented in Sec. III B reveal that for the given wall-temperature maximum difference ΔT, the temperature effects on the streaming are more prominent for higher values of H/L and H/δ_{v}.

The Figs. 5, 10, and 12 suggest that the streaming structure is influenced particularly by ambient temperature variation along the y-axis. If $\Delta T_0/\Delta y > 0$, the streaming in the Rayleigh vortices is supported; on the contrary, if $\Delta T_0/\Delta y < 0$, the streaming in the Rayleigh vortices is opposed, which may result in the streaming velocity reversion and appearance of additional vortices.

If we assume that the typical length of the wall-temperature variation is much bigger than the resonator half-width H, we can write[30]

$$T_0(x, y) \approx T_{\mathrm{w}}(x) + \frac{1}{2}\frac{\mathrm{d}^2 T_{\mathrm{w}}}{\mathrm{d}x^2}\left(H^2 - y^2\right), \tag{18}$$

which means that the streaming field is particularly influenced by wall temperature variation at the positions, where $|\mathrm{d}^2 T_{\mathrm{w}}/\mathrm{d}x^2|$ reaches high values, which can be observed in Figs. 5, 10, and 12.

B. Acoustic streaming in a transverse temperature gradient

The fact that the acoustic streaming structure is sensitive to the ambient temperature variation along the y axis can be demonstrated as follows. Let us assume *the fluid ambient temperature distribution* in form

$$T_0(x, y) = T_{\mathrm{w0}} + \Delta T_0 \frac{H - y}{H}, \tag{19}$$

where $T_{\mathrm{w0}} = 20\,^{\circ}$C and temperatures ΔT_0 differ. The relation (19) represents an ambient temperature distribution with a constant slope along the y-axis. For example, the streaming field for resonator dimensions $L = 30$ cm, $H = 1.5$ cm, and $\Delta T_0 = 0.3\,^{\circ}$C can be seen in Fig. 14.

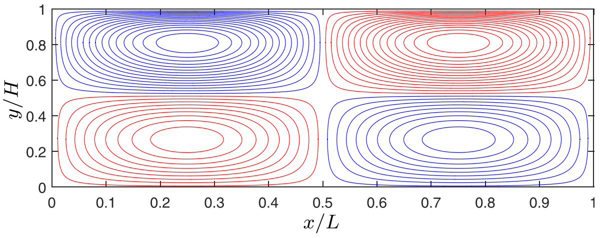

FIG. 14. (Color online) Streamlines in a resonator, T_0 given by Eq. (19), $\Delta T_0 = 0.3\,°\mathrm{C}$, $L = 30\,\mathrm{cm}$, $H = 1.5\,\mathrm{cm}$.

It can be observed that a relatively small temperature inhomogeneity of $\Delta T_0 = 0.3\,°\mathrm{C}$ along the y axis can dramatically change the streaming pattern, here, two additional outer vortices along the resonator axis appear.

Figure 15 shows the distribution of the streaming velocity along the resonator axis $y = 0$ and along the line $x = 3L/4$ for the above case for different values of ΔT_0. If $\Delta T_0 < 0$, it holds $\partial T_0/\partial y > 0$ and the streaming velocity is supported. On the contrary, if $\Delta T_0 > 0$, the streaming velocity begins to reverse in the vicinity of the resonator axis for $\Delta T_0 \gtrsim 0.2°\mathrm{C}$, which is accompanied by the appearance of additional vortices; for $\Delta T_0 = 1.0\,°\mathrm{C}$, these additional vortices occupy most of the resonator volume (the Rayleigh vortices are pushed toward the resonator wall).

C. Summary

The above-presented facts can be summarized as follows. For the given resonator length L and the wall temperature distribution T_w, the streaming is more influenced by the wall temperature distribution for higher aspect ratios H/L, see Fig. 7; first, as with increasing H the temperature difference ΔT_0 along the y axis increases [see Eq. (18)] and second, as the ratio H/δ_v increases as well. If for the given wall temperature distribution the resonator length L is varied and the resonator aspect ratio is kept constant (Fig. 8), the temperature variation along the y axis is the same for all the cases, and the streaming structure dependence on H/δ_v ratio is observed.

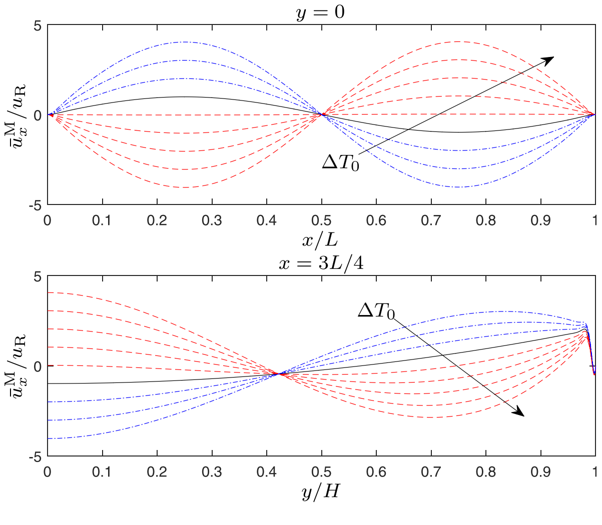

FIG. 15. (Color online) Averaged mass transport velocity along the resonator axis $y = 0$ (top), and along the line $x = 3L/4$ (bottom); $\Delta T_0 = -0.6\,°\mathrm{C}$, $-0.4\,°\mathrm{C}$, $-0.2\,°\mathrm{C}$ [dash-dot (blue) lines], $\Delta T_0 = 0\,°\mathrm{C}$ [solid (black) line], $\Delta T_0 = 0.2\,°\mathrm{C}$, $0.4\,°\mathrm{C}$,…, $1.0\,°\mathrm{C}$ [dashed (red) lines].

V. CONCLUSIONS

A set of equations for calculation of streaming field in a temperature-inhomogeneous fluids was derived from the Navier-Stokes equations using the method of successive approximations. The derived equations have a standard form of the linearised Navier-Stokes equations so that they can be numerically integrated using a universal solver, in this case, Acoustic Module of commercially available COMSOL Multiphysic was employed. As the equations for the primary field are solved in the frequency domain, and the equations for the secondary field are solved for the steady-state, there is no need for extensive computational resources. The influence of fluid-temperature inhomogeneities on the streaming structure was studied in the case of rectangular resonant channels with the spatial distribution of walls' temperature.

It was shown that the fluid temperature inhomogeneity influences the streaming structure significantly if there is a spatial temperature variation in a direction perpendicular to the resonator axis, and if the ratio H/δ_v is big enough. It was shown that depending on the spatial temperature distribution slope, the streaming in the Rayleigh vortices can be supported or opposed. Eventually, additional vortices can appear.

As the corresponding model equations were derived employing the method of successive approximations under the condition of small Mach number, they do capture the effect of the ambient temperature distribution on the streaming structure, but, they do not take into account the streaming as a means of heat transport (advection) influencing the fluid ambient temperature distribution, which is consistent with the assumption of streaming in a slow regime. In strong acoustic fields, dissipation of acoustic energy, as well as thermoacoustic phenomena, lead to complicated fluid temperature distributions which may influence the streaming structure and vice versa.

To sum up, this work indicates that the thermal effects on streaming are strong especially in larger geometries, for which the standard numerical models require an excessive amount of computational effort. In our future work, we would like to address this issue and to propose a theoretical model capable of capturing mutual streaming / thermal field interactions in larger geometries, yet requiring reasonable computational resources.

ACKNOWLEDGMENTS

This work was supported by GACR Grant No. 15-23079S.

[1] W. L. Nyborg, "Acoustic streaming," in *Nonlinear Acoustics*, edited by M. F. Hamilton and D. T. Blackstock (Academic Press, San Diego, CA, 1998), pp. 207–231.

[2] S. Boluriaan and P. J. Morris, "Acoustic streaming: From Rayleigh to today," Int. J. Aeroacoust. **2**, 255–292 (2003).

[3]Lord Rayleigh, "On the circulation of air observed in Kundt's tubes, and on some allied acoustical problems," Philos. Trans. R. Soc. Lond. **175**, 1–21 (1884).

[4]L. Menguy and J. Gilbert, "Non-linear acoustic streaming accompanying a plane stationary wave in a guide," Acust. Acta Acust. **86**, 249–259 (2000).

[5]R. Waxler, "Stationary velocity and pressure gradients in a thermoacoustic stack," J. Acoust. Soc. Am. **109**, 2739–2750 (2001).

[6]H. Bailliet, V. Gusev, R. Raspet, and R. A. Hiller, "Acoustic streaming in closed thermoacoustic devices," J. Acoust. Soc. Am. **110**, 1808–1821 (2001).

[7]M. F. Hamilton, Y. A. Ilinskii, and E. A. Zabolotskaya, "Acoustic streaming generated by standing waves in two-dimensional channels of arbitrary width," J. Acoust. Soc. Am. **113**, 153–160 (2003).

[8]M. F. Hamilton, Y. A. Ilinskii, and E. A. Zabolotskaya, "Thermal effects on acoustic streaming in standing waves," J. Acoust. Soc. Am. **114**, 3092–3101 (2003).

[9]M. K. Aktas and B. Farouk, "Numerical simulation of acoustic streaming generated by finite-amplitude resonant oscillations in an enclosure," J. Acoust. Soc. Am. **116**, 2822–2831 (2004).

[10]V. Daru, D. Baltean-Carlès, C. Weisman, P. Debesse, and G. Gandikota, "Two-dimensional numerical simulations of nonlinear acoustic streaming in standing waves," Wave Motion **50**, 955–963 (2013).

[11]I. Reyt, V. Daru, H. Bailliet, S. Moreau, J.-C. Valière, D. Baltean-Carlès, and C. Weisman, "Fast acoustic streaming in standing waves: Generation of an additional outer streaming cell," J. Acoust. Soc. Am. **134**, 1791–1801 (2013).

[12]D. S. Antao and B. Farouk, "High amplitude nonlinear acoustic wave driven flow fields in cylindrical and conical resonators," J. Acoust. Soc. Am. **134**, 917–932 (2013).

[13]A. A. Gubaidullin and A. V. Yakovenko, "Effects of heat exchange and nonlinearity on acoustic streaming in a vibrating cylindrical cavity," J. Acoust. Soc. Am. **137**, 3281–3287 (2015).

[14]M. W. Thompson, A. A. Atchley, and M. J. Maccarone, "Influences of a temperature gradient and fluid inertia on acoustic streaming in a standing wave," J. Acoust. Soc. Am. **117**, 1839–1849 (2005).

[15]S. Moreau, H. Bailliet, and J.-C. Valière, "Measurements of inner and outer streaming vortices in a standing waveguide using laser Doppler velocimetry," J. Acoust. Soc. Am. **123**, 640–647 (2008).

[16]I. Reyt, H. Bailliet, and J.-C. Valière, "Experimental investigation of acoustic streaming in a cylindrical wave guide up to high streaming Reynolds numbers," J. Acoust. Soc. Am. **135**, 27–37 (2014).

[17]M. Nabavi, K. Siddiqui, and J. Dargahi, "Analysis of regular and irregular acoustic streaming patterns in a rectangular enclosure," Wave Motion **46**, 312–322 (2009).

[18]P. Debesse, D. Baltean-Carlès, F. Lusseyran, and M.-X. François, "Oscillating and streaming flow identification in a thermoacoustic resonator, from undersampled PIV measurements," Meas. Sci. Technol. **25**, 025005 (2014).

[19]E. S. Ellier, W. Kdous, Y. Bailly, L. Girardot, D. Ramel, and P. Nika, "Acoustic streaming measurements in standing wave resonator using particle image velocimetry," Wave Motion **51**, 1288–1297 (2014).

[20]G. Mozurkewich, "Heat transport by acoustic streaming within a cylindrical resonator," Appl. Acoust. **63**, 713–735 (2002).

[21]M. K. Aktas, B. Farouk, and Y. Lin, "Heat transfer enhancement by acoustic streaming in an enclosure," J. Heat Transf. **127**, 1313–1321 (2005).

[22]Y. Lin and B. Farouk, "Heat transfer in a rectangular chamber with differentially heated horizontal walls: Effects of a vibrating sidewall," Int. J. Heat Mass Tran. **51**, 3179–3189 (2008).

[23]M. K. Aktas and T. Ozgumus, "The effects of acoustic streaming on thermal convection in an enclosure with differentially heated horizontal walls," Int. J. Heat Mass Tran. **53**, 5289–5297 (2010).

[24]M. Nabavi, K. Siddiqui, and J. Dargahi, "Effects of transverse temperature gradient on acoustic and streaming velocity fields in a resonant cavity," Appl. Phys. Lett. **93**, 051902 (2008).

[25]M. Nabavi, K. Siddiqui, and J. Dargahi, "Influence of differentially heated horizontal walls on the streaming shape and velocity in a standing wave resonator," Int. Commun. Heat Mass **35**, 1061–1064 (2008).

[26]A. Boufermel, N. Joly, P. Lotton, M. Amari, and V. Gusev, "Velocity of mass transport to model acoustic streaming: Numerical application to annular resonators," Acust. Acta Acust. **97**, 219–227 (2011).

[27]P. B. Muller, R. Barnkob, M. J. H. Jensen, and H. Bruus, "A numerical study of microparticle acoustophoresis driven by acoustic radiation forces and streaming-induced drag forces," Lab Chip **12**, 4617–4627 (2012).

[28]Q. Tang and J. Hu, "Diversity of acoustic streaming in a rectangular acoustofluidic field," Ultrasonics **58**, 27–34 (2015).

[29]M. Červenka and M. Bednařík, "Variety of acoustic streaming in 2D resonant channels," Wave Motion **66**, 21–30 (2016).

[30]N. Sugimoto and K. Tsujimoto, "Amplification of energy flux of nonlinear acoustic waves in a gas-filled tube under an axial temperature gradient," J. Fluid Mech. **456**, 377–409 (2002).

A.8 Numerical study of the influence of the convective heat transport on acoustic streaming in a standing wave

Červenka, M., Bednařík, M., Numerical study of the influence of the convective heat transport on acoustic streaming in a standing wave, Journal of the Acoustical Society of America 143(2), 727-734, (2018).

Numerical study of the influence of the convective heat transport on acoustic streaming in a standing wave

Milan Červenka[a] and Michal Bednařík
Czech Technical University in Prague, Faculty of Electrical Engineering, Technická 2, 166 27 Prague 6, Czech Republic

(Received 31 May 2017; revised 17 January 2018; accepted 21 January 2018; published online 7 February 2018)

Within this work, acoustic streaming in an air-filled cylindrical resonator with walls supporting a temperature gradient is studied by means of numerical simulations. A set of equations based on successive approximations is derived from the Navier-Stokes equations. The equations take into account the acoustic-streaming-driven convective heat transport; as time-averaged secondary-field quantities are directly calculated, the equations are much easier to integrate than the original fluid-dynamics equations. The model equations are implemented and integrated employing commercial software COMSOL Multiphysics. Numerical calculations are conducted for the case of a resonator with a wall-temperature gradient corresponding to the action of a thermoacoustic effect. It is shown that due to the convective heat transport, the streaming profile is considerably distorted even in the case of weak wall-temperature gradients. The numerical results are consistent with available experimental data. © *2018 Acoustical Society of America*. https://doi.org/10.1121/1.5023217

[JDM] Pages: 727–734

I. INTRODUCTION

The acoustic streaming generated by a plane standing wave in an acoustic resonator has been studied extensively in the past both by analytical and experimental methods.

Rayleigh[1] first calculated acoustic streaming in wide two-dimensional channels whose width is much bigger than the viscous boundary layer; the corresponding formulas for wide cylindrical tubes were derived by Schuster and Matz.[2] The thermal effects were first considered by Rott.[3]

Within their theoretical work, Menguy and Gilbert[4] identified a dimensionless parameter characterizing the streaming flow—the nonlinear Reynolds number

$$\mathrm{Re}_{\mathrm{nl}} = \left(\frac{u_0}{c_0}\right)^2 \left(\frac{R}{\delta_{\mathrm{v}}}\right)^2, \qquad (1)$$

where u_0 is the velocity amplitude of the standing wave, c_0 is the speed of sound, R is the resonator radius, and δ_{v} is the viscous boundary layer thickness. If $\mathrm{Re}_{\mathrm{nl}} \ll 1$, the effect of inertia on the streaming flow can be neglected by comparison with viscous effects and we speak about the "slow" streaming; on the contrary, if $\mathrm{Re}_{\mathrm{nl}} \gg 1$, the effect of inertia cannot be neglected anymore and we speak about the "fast" streaming. In the "slow régime," the streaming structure does not depend on the acoustic field amplitude, in the "fast régime," the effect of inertia, according to the theory by Menguy and Gilbert,[4] causes a specific streaming-profile distortion which increases with the increasing value of $\mathrm{Re}_{\mathrm{nl}}$.

Several analytical or semi-analytical models for slow streaming have been proposed[5–8] for resonators of arbitrary width or radius; these models employ the methods of perturbation analysis. Numerical methods of the computational fluid dynamics have been employed for the study of the fast acoustic streaming.[9–11] Within these works, it has been confirmed that if $\mathrm{Re}_{\mathrm{nl}} \gg 1$, the streaming structure is strongly distorted and additional vortices can even appear.

Thompson *et al.*[12] used laser Doppler velocimetry (LDV) for measurement of the acoustic streaming in a cylindrical tube at high values of $\mathrm{Re}_{\mathrm{nl}}$. They found out that for higher values of $\mathrm{Re}_{\mathrm{nl}}$, the streaming profile deviates considerably from the prediction by Rott[3] or Menguy and Gilbert.[4] They have shown in an experimental way that this streaming profile distortion is connected with temperature gradient developed along the resonator walls due to thermoacoustically driven heat flux. At the time, there has not been any theory at hand explaining this behaviour.

Reyt *et al.*[11] compared their measurements of acoustic streaming in a cylindrical resonator using LDV with the numerical data obtained by a direct numerical integration of Navier-Stokes equations. They obtained similar experimental results (distorted streaming profiles) as Thompson *et al.*[12] with a small temperature gradient along the resonator. The numerical calculations were performed at the condition of isothermal resonator walls; qualitative and overall quantitative agreement between the experimental and numerical results has been achieved so that the authors identified the inertial effects as the primary reason for the distortion of the streaming profile for high values of $\mathrm{Re}_{\mathrm{nl}}$.

Červenka and Bednařík[13] have recently shown that (a) the slow-streaming profile is particularly sensitive to the temperature variation in the direction perpendicular to the resonator axis, (b) this variation can be caused by the wall-temperature gradient if the resonator is wide enough, and (c) additional outer streaming cells can appear like in the case of the fast streaming in resonators with isothermal walls.[10,11] The underlying mathematical model does not take into account acoustic streaming as a means of heat transport which means that the results are only valid for small streaming velocities.

---

[a] Electronic mail: milan.cervenka@fel.cvut.cz

In a very recent work, Daru *et al.*[14] argue, based on the results of numerical experiments, that the inertial effects cannot be leading mechanism of streaming structure distortion observed in experiments and direct numerical simulations; they consider the role of the nonlinear interactions between the streaming flow and the acoustic field.

Within this work, we show by means of numerical simulations that even for moderate values of $\mathrm{Re}_{\mathrm{nl}}$, the streaming profile can be considerably distorted from the sinusoidal one predicted by Rayleigh's theory, if there is even weak temperature gradient along the resonator walls. This acoustic-field-amplitude-dependent distortion is not caused by the effect of the fluid inertia, but it is connected with the streaming-driven convective heat transport in a fluid with a mean temperature gradient. The streaming profile distortion described within this work is of the same type as it has been found in experiments.[11,12,15,16]

The results described within this work cannot be obtained using the previous theoretical models dealing with acoustic streaming in temperature-inhomogeneous fluids,[3,5,6,13] as these models do not capture the effect of the acoustic-streaming-driven convective heat transport.

Section II of this paper describes the theoretical model and the numerical procedure; examples of numerical results are presented in Sec. III. A discussion and explanation of the observed effects are given in Sec. IV; Sec. V then concludes the paper.

II. THEORETICAL MODEL

A. Model equations

The study of the acoustic streaming starts with the Navier-Stokes equations, which can be written as[17]

$$\frac{\mathrm{d}\rho}{\mathrm{d}t} = -\rho \nabla \cdot \boldsymbol{u}, \tag{2a}$$

$$\rho \frac{\mathrm{d}\boldsymbol{u}}{\mathrm{d}t} = \nabla \cdot \boldsymbol{\sigma} + \boldsymbol{f}, \tag{2b}$$

$$\rho c_{\mathrm{p}} \frac{\mathrm{d}T}{\mathrm{d}t} - \alpha T \frac{\mathrm{d}p}{\mathrm{d}t} = \nabla \cdot (\kappa \nabla T) + \boldsymbol{\tau} : \nabla \boldsymbol{u}, \tag{2c}$$

where ρ is the fluid density, $\boldsymbol{u}$ is the velocity vector, T is the temperature, p is the pressure, and $\boldsymbol{f}$ is the body force density, as the resonator is assumed to be driven by an inertial force (by entire-body shaking); it reads $\boldsymbol{f} = -\rho \boldsymbol{a}(t)$, where $\boldsymbol{a}(t)$ is the resonator acceleration. Within this work, the effect of the gravity on fluid flow is not taken into account. Further, c_{p} is the specific heat capacity at constant pressure, α is the isobaric coefficient of volumetric thermal expansion, and κ is the coefficient of thermal conduction. The total stress tensor $\boldsymbol{\sigma}$ is defined as

$$\boldsymbol{\sigma} = -p\boldsymbol{I} + \boldsymbol{\tau} = -p\boldsymbol{I} + \mu\left[\nabla \boldsymbol{u} + (\nabla \boldsymbol{u})^{\mathrm{T}}\right] - \mu\left(\frac{2}{3} - \tilde{V}\right)(\nabla \cdot \boldsymbol{u})\boldsymbol{I}, \tag{3}$$

where $\boldsymbol{\tau}$ is the viscous stress tensor, μ is the shear viscosity, $\tilde{V} = \mu_{\mathrm{B}}/\mu$, where μ_{B} is the bulk viscosity and $\boldsymbol{I}$ is the identity matrix. The material parameters are assumed to be temperature-dependent, i.e., $\mu = \mu(T)$, $\kappa = \kappa(T)$, $c_{\mathrm{p}} = c_{\mathrm{p}}(T)$.

In Eq. (2), the material derivative is defined as $\mathrm{d}(-)/\mathrm{d}t = \partial(-)/\partial t + (\boldsymbol{u} \cdot \nabla)(-)$. It is assumed that the fluid is an ideal gas for which the state equation has the form $p = \rho R_{\mathrm{s}} T$, where R_{s} is the specific gas constant and thus $\alpha = -(\partial \rho/\partial T)_p/\rho = 1/T$.

Within this work, Eq. (2) is solved using the method of successive approximations rather than by a direct numerical integration. Similarly, as in Boufermel *et al.*,[18] the field variables are written as

$$\varphi = \varphi_0 + \varphi_{\mathrm{a}} + \varphi_{\mathrm{n}}, \quad \varphi_{\mathrm{n}} \ll \varphi_{\mathrm{a}}, \tag{4}$$

where φ_0 represents the steady state mean value of quantity φ without acoustic perturbation, φ_{a} represents the first-order acoustic perturbation (primary field), harmonic in time with an angular frequency ω, and φ_{n} represents the products of nonlinear interactions including higher harmonics as well as time-independent (or slowly varying) components (secondary field).

If we calculate a one-period time average of relation (4), we get

$$\langle \varphi \rangle = \varphi_{\mathrm{m}}(\boldsymbol{r}, t_{\mathrm{s}}) = \frac{1}{T_{\mathrm{a}}} \int_{t_{\mathrm{s}}}^{t_{\mathrm{s}}+T_{\mathrm{a}}} \varphi(\boldsymbol{r}, t)\, \mathrm{d}t = \varphi_0 + \langle \varphi_{\mathrm{n}} \rangle, \tag{5}$$

where $T_{\mathrm{a}} = 2\pi/\omega$ and t_{s} represents the slow time related to the large-time-scale phenomena.[18]

The equations for the first-order acoustic field quantities can be found by substituting relations (4) and (5) into Eq. (2) and discarding the second-order and higher-order terms except for the time-averaged ones. We get

$$\frac{\partial \rho_{\mathrm{a}}}{\partial t} + \nabla \cdot (\rho_{\mathrm{m}} \boldsymbol{u}_{\mathrm{a}}) = 0, \tag{6a}$$

$$\rho_{\mathrm{m}} \frac{\partial \boldsymbol{u}_{\mathrm{a}}}{\partial t} - \nabla \cdot \left\{ -p_{\mathrm{a}}\boldsymbol{I} + \mu_{\mathrm{m}}\left[\nabla \boldsymbol{u}_{\mathrm{a}} + (\nabla \boldsymbol{u}_{\mathrm{a}})^{\mathrm{T}}\right] - \mu_{\mathrm{m}}\left(\frac{2}{3} - \tilde{V}\right)(\nabla \cdot \boldsymbol{u}_{\mathrm{a}})\boldsymbol{I} \right\} = -\rho_{\mathrm{m}} \boldsymbol{a}, \tag{6b}$$

$$\rho_{\mathrm{m}} c_{\mathrm{pm}} \left(\frac{\partial T_{\mathrm{a}}}{\partial t} + \boldsymbol{u}_{\mathrm{a}} \cdot \nabla T_{\mathrm{m}} \right) - \frac{\partial p_{\mathrm{a}}}{\partial t} - \nabla \cdot (\kappa_{\mathrm{m}} \nabla T_{\mathrm{a}}) = 0, \tag{6c}$$

where $c_{\mathrm{pm}} = c_{\mathrm{p}}(T_{\mathrm{m}})$, $\mu_{\mathrm{m}} = \mu(T_{\mathrm{m}})$, together with the linearised state equation $p_{\mathrm{a}}/p_{\mathrm{m}} = T_{\mathrm{a}}/T_{\mathrm{m}} + \rho_{\mathrm{a}}/\rho_{\mathrm{m}}$. Equation (6) can be used for calculation of the primary acoustic field.

The equations for the time-averaged quantities can be found by the one-period averaging of Eq. (2). Employing $\langle \partial(-)/\partial t \rangle = \partial \langle - \rangle/\partial t_{\mathrm{s}}$ we get[13,18]

$$\frac{\partial \rho_{\mathrm{m}}}{\partial t_{\mathrm{s}}} + \nabla \cdot (\rho_{\mathrm{m}} \boldsymbol{u}_{\mathrm{m}}) = M, \tag{7a}$$

$$\rho_{\mathrm{m}} \frac{\mathrm{d}\boldsymbol{u}_{\mathrm{m}}}{\mathrm{d}t_{\mathrm{s}}} - \nabla \cdot \left\{ -p_{\mathrm{m}}\boldsymbol{I} + \mu_{\mathrm{m}}\left[\nabla \boldsymbol{u}_{\mathrm{m}} + (\nabla \boldsymbol{u}_{\mathrm{m}})^{\mathrm{T}}\right] - \mu_{\mathrm{m}}\left(\frac{2}{3} - \tilde{V}\right)(\nabla \cdot \boldsymbol{u}_{\mathrm{m}})\boldsymbol{I} \right\} = \boldsymbol{F}, \tag{7b}$$

$$\rho_{\mathrm{m}} c_{\mathrm{pm}} \frac{\mathrm{d}T_{\mathrm{m}}}{\mathrm{d}t_{\mathrm{s}}} - \frac{\mathrm{d}p_{\mathrm{m}}}{\mathrm{d}t_{\mathrm{s}}} - \nabla \cdot (\kappa_{\mathrm{m}} \nabla T_{\mathrm{m}}) = Q, \tag{7c}$$

where the source terms $M, \boldsymbol{F}$, and Q read

$$M = -\boldsymbol{\nabla} \cdot \langle \rho_{\mathrm{a}} \boldsymbol{u}_{\mathrm{a}} \rangle, \tag{8a}$$

$$\boldsymbol{F} = -\left\langle \rho_{\mathrm{a}} \left(\boldsymbol{a} + \frac{\partial \boldsymbol{u}_{\mathrm{a}}}{\partial t} \right) \right\rangle - \rho_{\mathrm{m}} \langle (\boldsymbol{u}_{\mathrm{a}} \cdot \boldsymbol{\nabla}) \boldsymbol{u}_{\mathrm{a}} \rangle + \boldsymbol{\nabla} \cdot \left\langle \frac{\mu_{\mathrm{m}} b_{\mu}}{T_{\mathrm{m}}} T_{\mathrm{a}} \times \left[\boldsymbol{\nabla} \boldsymbol{u}_{\mathrm{a}} + (\boldsymbol{\nabla} \boldsymbol{u}_{\mathrm{a}})^{\mathrm{T}} - (2/3 + \tilde{V})(\boldsymbol{\nabla} \cdot \boldsymbol{u}_{\mathrm{a}}) \boldsymbol{I} \right] \right\rangle, \tag{8b}$$

$$Q = -c_{\mathrm{pm}} \left\langle \rho_{\mathrm{a}} \frac{\partial T_{\mathrm{a}}}{\partial t} \right\rangle - \rho_{\mathrm{m}} c_{\mathrm{pm}} \langle \boldsymbol{u}_{\mathrm{a}} \cdot \boldsymbol{\nabla} T_{\mathrm{a}} \rangle - c_{\mathrm{pm}} \langle \rho_{\mathrm{a}} \boldsymbol{u}_{\mathrm{a}} \rangle \cdot \boldsymbol{\nabla} T_{\mathrm{m}} + \langle \boldsymbol{u}_{\mathrm{a}} \cdot \boldsymbol{\nabla} p_{\mathrm{a}} \rangle + \boldsymbol{\nabla} \cdot \left\langle \frac{\kappa_{\mathrm{m}} b_{\kappa}}{T_{\mathrm{m}}} T_{\mathrm{a}} \boldsymbol{\nabla} T_{\mathrm{a}} \right\rangle + \mu_{\mathrm{m}} \left\langle \left[\boldsymbol{\nabla} \boldsymbol{u}_{\mathrm{a}} + (\boldsymbol{\nabla} \boldsymbol{u}_{\mathrm{a}})^{\mathrm{T}} - \left(\frac{2}{3} - \tilde{V} \right) (\boldsymbol{\nabla} \cdot \boldsymbol{u}_{\mathrm{a}}) \boldsymbol{I} \right] : \boldsymbol{\nabla} \boldsymbol{u}_{\mathrm{a}} \right\rangle. \tag{8c}$$

Here, $\langle fg \rangle = \Re[\tilde{f} \tilde{g}^*]/2$; the tildes represent the complex amplitudes of the corresponding quantities and the asterisk stands for the complex conjugate. Further, the following relation was used:

$$\mu(T) \approx \mu(T_{\mathrm{m}} + T_{\mathrm{a}}) \approx \mu_{\mathrm{m}} + \frac{\mu_{\mathrm{m}} b_{\mu}}{T_{\mathrm{m}}} T_{\mathrm{a}},$$

where $b_{\mu} = T_{\mathrm{m}} (\partial \mu / \partial T)_{T_{\mathrm{m}}} / \mu_{\mathrm{m}}$, and

$$\kappa(T) \approx \kappa(T_{\mathrm{m}} + T_{\mathrm{a}}) \approx \kappa_{\mathrm{m}} + \frac{\kappa_{\mathrm{m}} b_{\kappa}}{T_{\mathrm{m}}} T_{\mathrm{a}},$$

where $b_{\kappa} = T_{\mathrm{m}} (\partial \kappa / \partial T)_{T_{\mathrm{m}}} / \kappa_{\mathrm{m}}$. Acoustic-temperature-induced variation of the heat capacity was not taken into account in Eq. (7c) because it is weaker than the variation of the viscosity or thermal conduction coefficients.

The source terms [Eq. (8)] emerge in Eq. (7) as a consequence of employing the method of successive approximations; they comprise nonlinear combinations of the first-order acoustic field quantities. Namely, M is the mass source, $\boldsymbol{F}$ represents the excitation force (Reynolds stress, the force caused by the dependence of viscosity on acoustic temperature), and Q represents a heat source.

In the steady state, the averaged quantities do not depend on the slow time and thus Eqs. (7a), (7b), and (7c) reduce into

$$\boldsymbol{\nabla} \cdot (\rho_{\mathrm{m}} \boldsymbol{u}_{\mathrm{m}}) = M, \tag{9a}$$

$$\rho_{\mathrm{m}} \boldsymbol{u}_{\mathrm{m}} \cdot \boldsymbol{\nabla} \boldsymbol{u}_{\mathrm{m}} - \boldsymbol{\nabla} \cdot \left\{ -p_{\mathrm{m}} \boldsymbol{I} + \mu_{\mathrm{m}} \left[\boldsymbol{\nabla} \boldsymbol{u}_{\mathrm{m}} + (\boldsymbol{\nabla} \boldsymbol{u}_{\mathrm{m}})^{\mathrm{T}} \right] - \mu_{\mathrm{m}} \left(\frac{2}{3} - \tilde{V} \right) (\boldsymbol{\nabla} \cdot \boldsymbol{u}_{\mathrm{m}}) \boldsymbol{I} \right\} = \boldsymbol{F}, \tag{9b}$$

$$\rho_{\mathrm{m}} c_{\mathrm{pm}} \boldsymbol{u}_{\mathrm{m}} \cdot \boldsymbol{\nabla} T_{\mathrm{m}} - \boldsymbol{u}_{\mathrm{m}} \cdot \boldsymbol{\nabla} p_{\mathrm{m}} - \boldsymbol{\nabla} \cdot (\kappa_{\mathrm{m}} \boldsymbol{\nabla} T_{\mathrm{m}}) = Q. \tag{9c}$$

Within this model, we do not take into account the fast time-varying products of the nonlinear interactions (higher harmonics), which can cause the distortion of the time-harmonic primary acoustic field. This seems not to have any significant impact on the results, as a considerable streaming-profile distortion has been observed within the experiments[11,12,15] for high values of $\mathrm{Re}_{\mathrm{nl}}$ and time-harmonic acoustic field.

The structure of the acoustic streaming can be easily visualised in the following way. If we introduce the *averaged mass transport density* $\boldsymbol{M}_{\mathrm{m}} = \rho_{\mathrm{m}} \boldsymbol{u}_{\mathrm{m}} + \langle \rho_{\mathrm{a}} \boldsymbol{u}_{\mathrm{a}} \rangle = \rho_{\mathrm{m}} \boldsymbol{U}_{\mathrm{m}}$, where $\boldsymbol{U}_{\mathrm{m}}$ is the averaged mass transport velocity,[7,18] the continuity Eq. (9a) can be rewritten as

$$\boldsymbol{\nabla} \cdot \boldsymbol{M}_{\mathrm{m}} = 0. \tag{10}$$

As the steady averaged mass transport density field is divergence-free, the stream function ψ can be introduced such that in axi-symmetric cylindrical coordinates, it holds

$$M_{\mathrm{m}z} = \frac{1}{r} \frac{\partial \psi}{\partial r}, \quad M_{\mathrm{m}r} = -\frac{1}{r} \frac{\partial \psi}{\partial z}.$$

From here, we can calculate the stream function as

$$\frac{\partial^2 \psi}{\partial r^2} + \frac{\partial^2 \psi}{\partial z^2} = \frac{\partial}{\partial r} (r M_{\mathrm{m}z}) - \frac{\partial}{\partial z} (r M_{\mathrm{m}r}). \tag{11}$$

The contours of the stream function represent the streamlines.

B. Numerical solution of the model equations

Equations (6) and (7) represent one set of equations which must be solved simultaneously to capture properly the effect of acoustic-streaming-driven convective heat transport on the streaming structures. The source terms [Eq. (8)] for Eq. (7) are calculated using the first-order quantities obtained by solving Eq. (6), the mean values T_{m}, ρ_{m}, and p_{m} in Eq. (6) are calculated using Eq. (7).

The model equations were solved numerically using finite-element-method software COMSOL Multiphysics; axi-symmetric geometry was used, see Fig. 1. Equation (6) is implemented in the Acoustic Module's Linearised Navier-Stokes Interface; the equations were solved in the frequency domain with no-slip and isothermal ($T_{\mathrm{a}} = 0$) boundary conditions at the resonator walls. The term $-\rho_{\mathrm{m}} \boldsymbol{a}$ was used as a volume source in the momentum Eq. (6b); the driving acceleration is assumed to have non-zero only the z-component and to vary sinusoidally in time with an angular frequency ω. Equation (7) is implemented in CFD Module's Non-Isothermal Laminar Flow Interface; the equations were solved using the stationary as well as the time-dependent solver. The boundary conditions at the resonator walls were implemented as no-slip and isothermal ones with prescribed wall temperature ($T_{\mathrm{m}} = T_{\mathrm{w}}$).

The resonance frequency was determined by a frequency sweep for a small driving acceleration for which the convective heat transport by the streaming could be neglected.

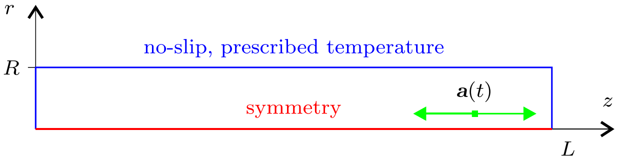

FIG. 1. (Color online) Geometry of the problem.

The Poisson's Eq. (11) was solved employing Mathematics/Classical PDEs Interface with the homogeneous Dirichlet boundary conditions.

The computational mesh was constructed in order to properly resolve the boundary layer along the walls; mapped (structured) mesh with refinement along the walls was found to work well; the independence of numerical results on the mesh density was checked.

For the numerical results presented below, the total number of used mesh-points was $N_r \times N_z = 100 \times 200$, where 15 regularly-spaced mesh-points discretized three-times the viscous boundary layer thickness, and mesh-points with linearly increasing separation-distances were used in the inner volume.

III. NUMERICAL RESULTS

A. Parameters of the numerical simulations

Within the numerical simulations, the acoustic streaming was calculated in a resonator represented by a cylindrical tube with rigid end-caps, length $L = 30$ cm, radius $R = 1.5$ cm, filled with air at normal atmospheric pressure. The temperature-dependent values of the material parameters μ, κ, and c_p are implemented in the material database of COMSOL Multiphysics, the ones for air were used here. For ambient temperature $T_0 = 20\,^\circ\mathrm{C}$, the resonance frequency was calculated to be $f_\mathrm{res} = 569.2$ Hz and the ratio of the resonator radius to the viscous boundary layer thickness $R/\delta_\mathrm{v} = 163.4$.

The resonant cavity is assumed to have imposed temperature of walls

$$T_\mathrm{w} = \frac{\Delta T_\mathrm{w}}{2}\left[1 + \cos\left(\frac{2\pi z}{L}\right)\right] + T_{\mathrm{w}0}, \qquad (12)$$

where $T_{\mathrm{w}0}$ is the minimum temperature of the resonator walls and ΔT_w is the maximum wall-temperature difference. Formula (12) serves as the boundary condition for Eq. (7c) for calculation of the fluid mean temperature T_m. In all the following cases, $T_{\mathrm{w}0} = 20\,^\circ\mathrm{C}$ and temperatures ΔT_w differ.

Formula (12) models[12] the steady-state wall temperature distribution due to the thermoacoustic heat transport. In the standing wave, there exists a time-averaged heat flux between the walls and the inner fluid which transports the heat from the acoustic-velocity antinodes toward the acoustic-velocity nodes.[19,20] This flux, which is proportional to the square of the acoustic velocity amplitude,[19] is balanced by the heat conduction within the walls and the heat flux to the outer environment; the resulting wall-temperature gradient thus depends on particular external factors, and that is why it is *prescribed* by Eq. (12) here.

All the numerical results are presented in the conditions of the first resonance which was searched for by a frequency sweep by maximization of the acoustic velocity amplitude in the resonator.

B. The case of $\Delta T_\mathrm{w} = 8\,^\circ\mathrm{C}$

Within this subsection, we analyse the case of a relatively large wall-temperature difference of $\Delta T_\mathrm{w} = 8\,^\circ\mathrm{C}$ (this wall-temperature difference was reported to be thermoacoustically induced in experiment[15]).

Figure 2 shows the distribution of steady-state averaged mass transport velocity along the resonator axis for individual values of Re_nl both normalized to the Rayleigh velocity $U_\mathrm{R} = (3/8)u_0^2/c_0$ (top panel) and non-normalized (bottom panel), where u_0 is the maximum axial acoustic velocity amplitude on the resonator axis, and c_0 is the speed of sound. Within this work, we do not exclusively understand Re_nl as a measure of flow-inertia effect on the streaming field; we employ it as an established parameter related to the streaming velocity (according to the Rayleigh's theory, streaming velocity should be proportional to Re_nl).

In the case of $\mathrm{Re}_\mathrm{nl} = 0.001$, the streaming velocity has such a small value that the convective heat transport is negligible. The normalized streaming velocity along the axis reaches the maximum value of $U_{\mathrm{m}z}/U_\mathrm{R} = 1.009$; the distribution slightly differs from the sinusoidal one,[2] which is also in line with the observations made earlier.[13] If the streaming velocity increases, its distribution quickly gets distorted, and the value of the normalized streaming velocity in maxima decreases; the maxima are shifted toward the acoustic velocity nodes (resonator end-walls). For example, for $\mathrm{Re}_\mathrm{nl} = 0.2$, the maximum value of $U_{\mathrm{m}z}/U_\mathrm{R} = 0.771$. With further increasing Re_nl, the normalised streaming velocity between the velocity nodes and antinodes further decreases; it reaches zero value for $\mathrm{Re}_\mathrm{nl} \approx 2.4$ and its direction reverses for higher values of Re_nl. Considering the non-normalised streaming velocity, the situation looks somewhat more complex; while its value increases with Re_nl monotonically near the acoustic velocity nodes and antinode, between them, it first increases, then reaches maximum, decreases and then changes its sign. It can be seen in both versions of the figure that the incremental change of the streaming velocity is bigger for lower values of Re_nl than for higher ones.

Figure 3 shows the distribution of the z-component of the steady-state averaged mass transport velocity along the r-axis for $z = L/4 = 7.5$ cm, both normalized to the Rayleigh

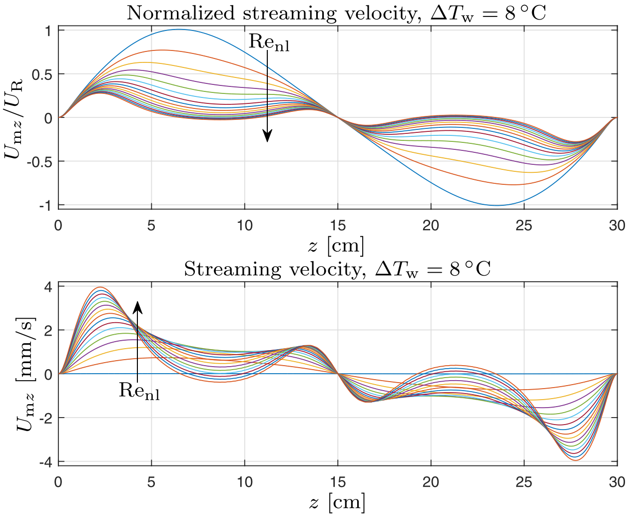

FIG. 2. (Color online) Normalized (top panel) and non-normalized (bottom panel) averaged mass transport velocity along the resonator axis, $\Delta T_\mathrm{w} = 8\,^\circ\mathrm{C}$, $\mathrm{Re}_\mathrm{nl} = 0.001, 0.2, 0.4, \ldots, 2.8, 3.0$; steady state.

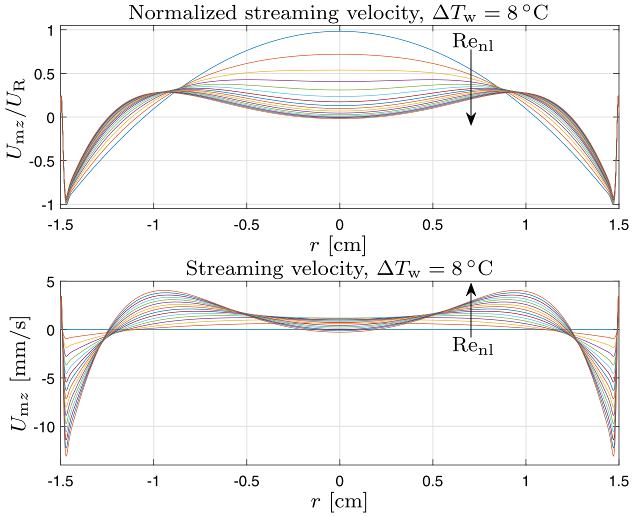

FIG. 3. (Color online) Normalized (top panel) and non-normalized (bottom panel) averaged mass transport velocity along the line $z = L/4$, $\Delta T_\mathrm{w} = 8\,^\circ\mathrm{C}$, $\mathrm{Re}_\mathrm{nl} = 0.001, 0.2, 0.4, \ldots, 2.8, 3.0$; steady state.

velocity (top panel) and non-normalized (bottom panel). Again, it can be observed that for higher values of Re_nl, it deviates considerably from the "parabolic" distribution.[2,3] It is interesting to notice that despite the streaming structure is sensitive to the value of Re_nl in the inner parts of the resonator, it is more or less unaffected near the walls (the normalized velocity does not depend on Re_nl, non-normalized velocity increases proportionally to Re_nl).

Figure 4 shows the streamlines for the case of $\mathrm{Re}_\mathrm{nl} = 0.001$ and $\mathrm{Re}_\mathrm{nl} = 3.0$. If the streaming velocity is small (top panel), two outer vortices can be observed as expected.[8] The inner vortices are not appreciable because of the high value of the ratio R/δ_v. For higher streaming velocity (bottom panel) the streamlines are distorted, and two weak additional outer vortices appear near the resonator axis, which is the cause of the reversion of the streaming velocity at the resonator axis seen in Figs. 2 and 3.

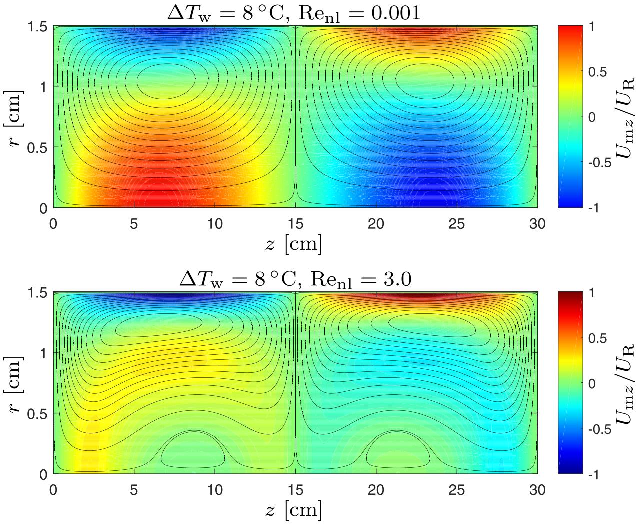

FIG. 4. (Color online) Averaged mass transport velocity and streamlines for $\Delta T_\mathrm{w} = 8\,^\circ\mathrm{C}$ and different values of Re_nl; steady state.

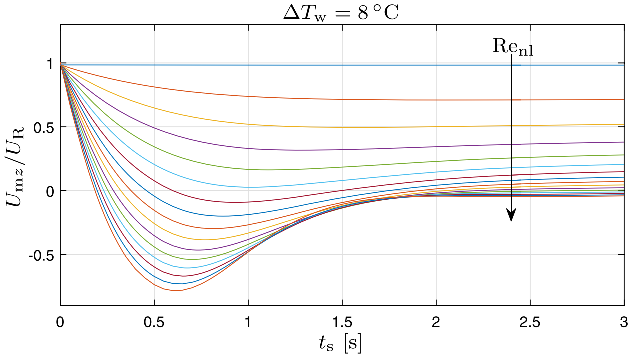

FIG. 5. (Color online) Time evolution of the averaged mass transport velocity at $z = L/4$ on the resonator axis; $\Delta T_\mathrm{w} = 8\,^\circ\mathrm{C}$, and $\mathrm{Re}_\mathrm{nl} = 0.001, 0.2, 0.4, \ldots, 2.8, 3.0$.

In order to get some conception of the time scale of the processes connected with the convective heat transport by the acoustic-streaming, Fig. 5 shows the time evolution of the averaged mass transport velocity at $z = L/4$ on the resonator axis for individual values of Re_nl. As an initial condition, the steady-state solution of Eqs. (6)+(9) was used, where the convective term $\boldsymbol{u}_\mathrm{m} \cdot \nabla T_\mathrm{m}$ was omitted in the energy Eq. (9c). It can be seen that for small values of Re_nl, the streaming velocity monotonically decreases toward the steady-state value; for the higher values, there is an overshoot with possible temporary direction reversion. After the initial faster development, the streaming velocity slowly reaches the steady-state in less than ca. 20 s.

Figure 6 shows the distribution of the steady-state mean temperature T_m along the resonator axis for various values of Re_nl. It can be observed that with increasing Re_nl, mean temperature in the central part of the resonator (especially in the regions where the temperature gradient reaches the highest values) increases as the streaming convects heat along the axis from the acoustic velocity nodes toward the acoustic velocity antinode. An effect of saturation can be observed in the figure—despite that there is appreciable temperature difference between the cases of $\mathrm{Re}_\mathrm{nl} = 0.001$ and $\mathrm{Re}_\mathrm{nl} = 1$, it is only negligible for the cases of $\mathrm{Re}_\mathrm{nl} = 2$ and $\mathrm{Re}_\mathrm{nl} = 3$. This behaviour can be attributed to the decrease and reversion of the streaming velocity seen in Figs. 2 and 3.

C. Different values of ΔT_w

Similar behaviour as the one described in Sec. III B can be observed in the case of different wall temperature differences ΔT_w.

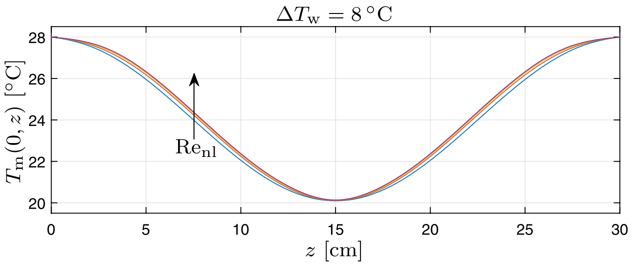

FIG. 6. (Color online) Mean temperature along the resonator axis $\Delta T_\mathrm{w} = 8\,^\circ\mathrm{C}$, and $\mathrm{Re}_\mathrm{nl} = 0.001, 1.0, 2.0, 3.0$; steady state.

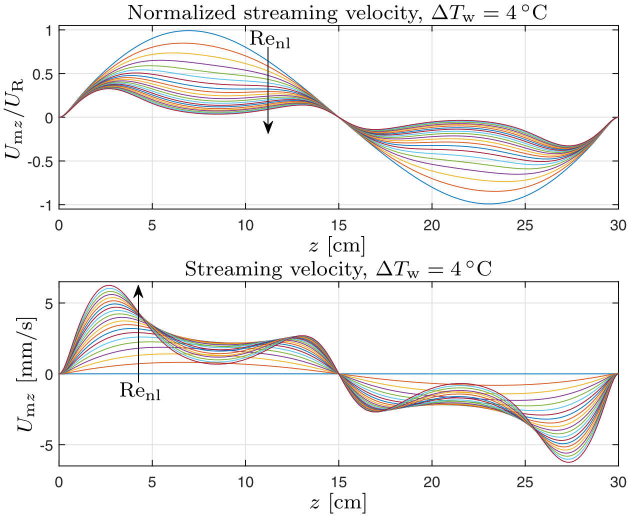

FIG. 7. (Color online) Normalized (top panel) and non-normalized (bottom panel) averaged mass transport velocity along the resonator axis, $\Delta T_\mathrm{w} = 4\,^\circ\mathrm{C}$, $\mathrm{Re}_\mathrm{nl} = 0.001, 0.2, 0.4, \ldots, 3.8, 4.0$; steady state.

For example, Fig. 7 shows the steady-state distribution of the averaged mass transport velocity along the resonator axis for $\Delta T_\mathrm{w} = 4\,^\circ\mathrm{C}$ and different values of Re$_\mathrm{nl}$. The streaming velocity shows the same kind of distortion as in the previous case (see Fig. 2); higher values of Re$_\mathrm{nl}$ are needed though to cause it. It is unclear whether the further increase of Re$_\mathrm{nl}$ would cause the streaming velocity reversion as we were not able to reach the algorithm convergence for these conditions.

Figure 8 shows the distribution of the steady-state normalized averaged mass transport velocity along the resonator axis for $\mathrm{Re}_\mathrm{nl} = 1$ and different values of the wall temperature difference $\Delta T_\mathrm{w} = 0\,^\circ\mathrm{C}$, $0.5\,^\circ\mathrm{C}$, $1\,^\circ\mathrm{C}$, $2\,^\circ\mathrm{C}$, $4\,^\circ\mathrm{C}$, $8\,^\circ\mathrm{C}$, and $16\,^\circ\mathrm{C}$. The figure reveals that the deviation from the sinusoidal distribution of the streaming velocity behaves similarly as in the case of constant wall-temperature difference and increasing value of Re$_\mathrm{nl}$—see Figs. 2 and 7. It can be observed that for the high wall-temperature differences, the streaming velocity pattern is considerably distorted even for small values of Re$_\mathrm{nl}$.

The sensitivity of the acoustic streaming velocity on the wall-temperature difference is depicted in Fig. 9 where $U_\mathrm{mz}/U_\mathrm{R}$ at $z = L/4 = 7.5\,\mathrm{cm}$ on the resonator axis is plotted as a function of Re$_\mathrm{nl}$ for individual values of ΔT_w. For $\Delta T_\mathrm{w} = 0\,^\circ\mathrm{C}$, the streaming velocity decreases with increasing Re$_\mathrm{nl}$ only weakly due to the effect of streaming fluid inertia, as it has been shown by Menguy and Gilbert.[4] The higher the maximum wall-temperature difference ΔT_w, the stronger the dependence on Re$_\mathrm{nl}$. It is interesting that the dependence is quite appreciable even for small values of ΔT_w, for example, for $\mathrm{Re}_\mathrm{nl} = 4$ and $\Delta T_\mathrm{w} = 0.5\,^\circ\mathrm{C}$, the value of $U_\mathrm{mz}/U_\mathrm{R}$ reaches only 70% of the value for $\Delta T_\mathrm{w} = 0\,^\circ\mathrm{C}$.

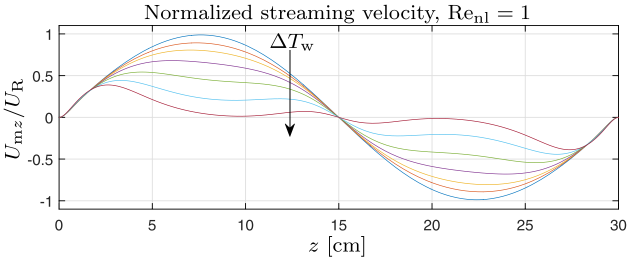

FIG. 8. (Color online) Normalized averaged mass transport velocity along the resonator axis for $\mathrm{Re}_\mathrm{nl} = 1$ and $\Delta T_\mathrm{w} = 0\,^\circ\mathrm{C}$, $0.5\,^\circ\mathrm{C}$, $1\,^\circ\mathrm{C}$, $2\,^\circ\mathrm{C}$, $4\,^\circ\mathrm{C}$, $8\,^\circ\mathrm{C}$, and $16\,^\circ\mathrm{C}$; steady state.

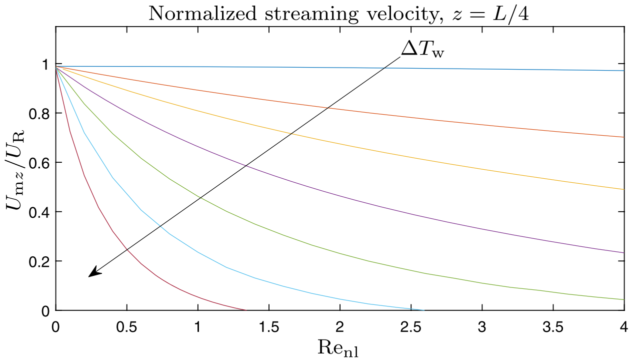

FIG. 9. (Color online) Normalized averaged mass transport velocity at $z = L/4 = 7.5\,\mathrm{cm}$ on the resonator axis for $\Delta T_\mathrm{w} = 0\,^\circ\mathrm{C}$, $0.5\,^\circ\mathrm{C}$, $1\,^\circ\mathrm{C}$, $2\,^\circ\mathrm{C}$, $4\,^\circ\mathrm{C}$, $8\,^\circ\mathrm{C}$, and $16\,^\circ\mathrm{C}$ and various values of Re$_\mathrm{nl}$; steady state.

IV. DISCUSSION

It has been shown recently[13] that the acoustic streaming structure is particularly influenced by the mean temperature gradient in the direction perpendicular to the resonator axis. If $\Delta_r T_\mathrm{m}(z) = T_\mathrm{m}(0, z) - T_\mathrm{m}(R, z) < 0$, acoustic streaming near the resonator axis is locally supported, if $\Delta_r T_\mathrm{m}(z) > 0$, it is locally opposed which may even result in the development of additional outer vortices.[13] If the streaming velocity is small enough for the convective heat transport to be effective, it can be approximately written[21] [for the wall temperature distribution Eq. (12)] that

$$\Delta_r T_\mathrm{m}(z) \approx -\frac{\pi^2 R^2 \Delta T_\mathrm{w}}{2L^2}\cos\left(\frac{2\pi z}{L}\right).$$

This explains a small departure from the sinusoidal streaming velocity distribution seen in Figs. 2 and 7 (the cases of $\mathrm{Re}_\mathrm{nl} = 0.001$).

If the resonator driving is increased, Re$_\mathrm{nl}$ increases; acoustic streaming becomes a more effective means of the heat transport which results in the re-distribution of the mean fluid temperature. Acoustic streaming convects the heat along the resonator axis from the warmer areas near the end-walls toward the resonator centre, see Fig. 10, which explains the temperature increase as seen in Fig. 6.

However, this heat transport also increases the value of $\Delta_r T_\mathrm{m}(z)$ in the resonator central part, see an example in Fig. 11, leading to the opposition to the acoustic streaming and reducing its effectiveness in convecting the heat. This effect manifests itself by decreasing incremental temperature change with increasing Re$_\mathrm{nl}$. This feedback behaviour explains the distortion of the streaming structure in temperature-inhomogeneous fluids and its dependence on Re$_\mathrm{nl}$ through the convective term $\boldsymbol{u}_\mathrm{m} \cdot \nabla T_\mathrm{m}$ in the energy equation.

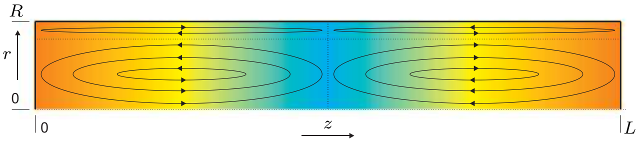

FIG. 10. (Color online) Heat transport in a resonator due to acoustic streaming.

The departure of the streaming velocity distribution from the sinusoidal one presented in Figs. 2, 7, and 8 is of the same type as has been found experimentally by Thompson *et al.*[12] (Figs. 5, 6, 7, and 8 there), Reyt *et al.*[11] (Figs. 6, 7, and 8 there), and Reyt *et al.*[15] (Figs. 5, 6, and 10 there). In the above-mentioned experiments, the reason for the departure is two-fold: (a) because of the thermoacoustically induced temperature distribution along the resonator walls, and (b) because of the inertial effects of the streaming flow. In the experiments, these two effects come hand in hand as the streaming velocity, as well as the heat flux between the resonator wall and the inner fluid, are proportional to the square of the acoustic velocity. All the numerical results presented here were obtained for $\mathrm{Re}_{\mathrm{nl}} \le 4$, which means that the inertial effects on the streaming fluid flow are small[4] and the streaming field distortion is caused purely by the fluid temperature inhomogeneity. The situation captured in Fig. 8 is also in compliance with experimental results by Thompson *et al.*[12] who also observed that for given $\mathrm{Re}_{\mathrm{nl}}$, the streaming distortion depends on the temperature variation along the resonator walls.

The feedback mechanism described above may explain the behaviour observed in experiments;[11,12,15] in strong acoustic fields (for $\mathrm{Re}_{\mathrm{nl}} \gg 1$), the streaming velocity between acoustic velocity nodes and antinode has a much smaller value than predicted by Rayleigh's theory. In a strong acoustic field, thermoacoustic heat flux builds up a temperature gradient along the resonator walls. The acoustic-streaming-driven convective heat transport increases the temperature difference in the direction perpendicular to the resonator axis, which causes the suppression of acoustic streaming, its ability to convect the heat, and to further increase the temperature difference.

V. CONCLUSIONS

A set of equations for calculation of the acoustic streaming in resonators with walls supporting a temperature gradient has been derived from the Navier-Stokes equations. The model equations are based on successive approximations; they take into account the acoustic-streaming-driven convective heat transport; as time-averaged secondary-field quantities are directly calculated, there is no need for an excessive amount of the computational effort for their integration. The proposed computational procedure has been implemented in COMSOL Multiphysics.

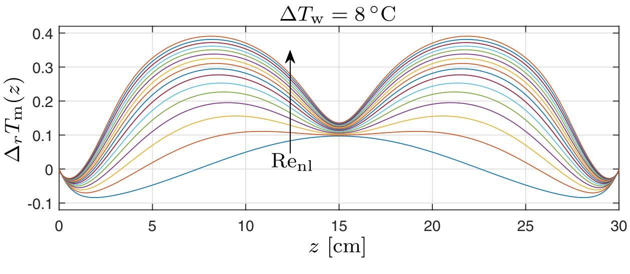

FIG. 11. (Color online) Distribution of temperature difference $\Delta_r T_{\mathrm{m}}(z)$ along the resonator for $\Delta T_{\mathrm{w}} = 8\,^\circ\mathrm{C}$ and $\mathrm{Re}_{\mathrm{nl}} = 0.001, 0.2, 0.4, \ldots, 2.9, 3.0$.

A parametric study has been conducted for the case of an air-filled cylindrical resonator with walls with a temperature distribution corresponding to the one caused by the thermoacoustic effect.

It has been shown that even in the case of relatively weak wall-temperature gradients, the acoustic-streaming-driven convective heat transport is responsible for a considerable distortion of streaming profile; this effect is much stronger than the effect of the fluid inertia on the streaming flow. The streaming profiles observed within this work are consistent with the available experimental data.

Based on the results obtained within this work, we arrive at the conclusion that for a good quantitative agreement between experimental and theoretical data, the thermal effects must be comprised within the model describing acoustic streaming, and even slight wall-temperature gradients cannot be ignored anymore.

ACKNOWLEDGMENTS

This work was supported by GACR Grant No. 15-23079S and by The Ministry of Education, Youth, and Sports from the Large Infrastructures for Research, Experimental Development, and Innovations project "IT4Innovations National Supercomputing Center—LM2015070."

[1] Lord Rayleigh, "On the circulation of air observed in Kundt's tubes, and on some allied acoustical problems," Philos. Trans. R. Soc. London **175**, 1–21 (1884).

[2] K. Schuster and W. Matz, "Über stationare Strömungen im Kundtschen Rohr" ("On stationary streaming in a Kundt's tube"), Akust. Z. **5**, 349–352 (1940).

[3] N. Rott, "The influence of heat conduction on acoustic streaming," Z. Angew. Math. Phys. **25**, 417–421 (1974).

[4] L. Menguy and J. Gilbert, "Non-linear acoustic streaming accompanying a plane stationary wave in a guide," Acta Acust. Acust. **86**, 249–259 (2000).

[5] R. Waxler, "Stationary velocity and pressure gradients in a thermoacoustic stack," J. Acoust. Soc. Am. **109**, 2739–2750 (2001).

[6] H. Bailliet, V. Gusev, R. Raspet, and R. A. Hiller, "Acoustic streaming in closed thermoacoustic devices," J. Acoust. Soc. Am. **110**, 1808–1821 (2001).

[7] M. F. Hamilton, Y. A. Ilinskii, and E. A. Zabolotskaya, "Acoustic streaming generated by standing waves in two-dimensional channels of arbitrary width," J. Acoust. Soc. Am. **113**, 153–160 (2003).

[8] M. F. Hamilton, Y. A. Ilinskii, and E. A. Zabolotskaya, "Thermal effects on acoustic streaming in standing waves," J. Acoust. Soc. Am. **114**, 3092–3101 (2003).

[9] M. K. Aktas and B. Farouk, "Numerical simulation of acoustic streaming generated by finite-amplitude resonant oscillations in an enclosure," J. Acoust. Soc. Am. **116**, 2822–2831 (2004).

[10] V. Daru, D. Baltean-Carlès, C. Weisman, P. Debesse, and G. Gandikota, "Two-dimensional numerical simulations of nonlinear acoustic streaming in standing waves," Wave Motion **50**, 955–963 (2013).

[11] I. Reyt, V. Daru, H. Bailliet, S. Moreau, J.-C. Valière, D. Baltean-Carlès, and C. Weisman, "Fast acoustic streaming in standing waves: Generation of an additional outer streaming cell," J. Acoust. Soc. Am. **134**, 1791–1801 (2013).

[12] M. W. Thompson, A. A. Atchley, and M. J. Maccarone, "Influences of a temperature gradient and fluid inertia on acoustic streaming in a standing wave," J. Acoust. Soc. Am. **117**, 1839–1849 (2005).

[13] M. Červenka and M. Bednařík, “Effect of inhomogeneous temperature fields on acoustic streaming structures in resonators,” J. Acoust. Soc. Am. **141**(6), 4418–4426 (2017).

[14] V. Daru, C. Weisman, D. Baltean-Carlès, I. Reyt, and H. Bailliet, “Inertial effects on acoustic Rayleigh streaming flow: Transient and established regimes,” Wave Motion **74**, 1–17 (2017).

[15] I. Reyt, H. Bailliet, and J.-C. Valière, “Experimental investigation of acoustic streaming in a cylindrical wave guide up to high streaming Reynolds numbers,” J. Acoust. Soc. Am. **135**, 27–37 (2014).

[16] V. Daru, I. Reyt, H. Bailliet, C. Weisman, and D. Baltean-Carlès, “Acoustic and streaming velocity components in a resonant waveguide at high acoustic levels,” J. Acoust. Soc. Am. **141**, 563–574 (2017).

[17] B. Lautrup, *Physics of Continuous Matter*, *Second Edition*: *Exotic* and *Everyday Phenomena in the Macroscopic World* (CRC Press, Boca Raton, FL, 2011).

[18] A. Boufermel, N. Joly, P. Lotton, M. Amari, and V. Gusev, “Velocity of mass transport to model acoustic streaming: Numerical application to annular resonators,” Acta Acust. Acust. **97**, 219–227 (2011).

[19] P. Merkli and H. Thomann, “Thermoacoustic effects in a resonance tube,” J. Fluid Mech. **70**, 161–177 (1975).

[20] G. W. Swift, “Thermoacoustic engines,” J. Acoust. Soc. Am. **84**(1), 1145–1180 (1988).

[21] N. Sugimoto and K. Tsujimoto, “Amplification of energy flux of nonlinear acoustic waves in a gas-filled tube under an axial temperature gradient,” J. Fluid Mech. **456**, 377–409 (2002).

A.9 Non-paraxial model for a parametric acoustic array

Červenka, M., Bednařík, M., Non-paraxial model for a parametric acoustic array, Journal of the Acoustical Society of America 134(2), 933-938, (2013).

Non-paraxial model for a parametric acoustic array

Milan Cervenka[a] and Michal Bednarik
Czech Technical University in Prague, Faculty of Electrical Engineering, Technicka 2, 166 27 Prague 6, Czech Republic

(Received 27 February 2012; revised 10 May 2013; accepted 24 June 2013)

This study is concerned with parametric radiation from an arbitrary axisymmetric planar source with a special focus on low-frequency difference-frequency fields. As a model equation accounting for nonlinearity, diffraction, and dissipation, the Westervelt equation is used. The difference-frequency-field patterns are calculated in the quasi-linear approximation by the method of successive approximations. A multi-layer integral for calculation of the acoustic field is reduced to a three-dimensional one by employing an approximate analytical description of the primary field with the use of a multi-Gaussian beam expansion. This integral is subsequently reduced in the paraxial approximation to a one-dimensional form which has previously been published in literature and which represents a means for fast calculations of secondary acoustic fields. The three-dimensional integral is calculated numerically and the numerical results predict nonzero amplitude of the low-frequency field in the vicinity of the source which is an effect that cannot be correctly encompassed in the paraxial approximation. © *2013 Acoustical Society of America*.

[http://dx.doi.org/10.1121/1.4813223]

PACS number(s): 43.25.Lj [ROC] Pages: 933–938

I. INTRODUCTION

Many contemporary acoustic applications make use of the fact that relatively directional low-frequency sound can be radiated from small sources by means of a parametric array.[1,2] This technique is based on radiation of two high-frequency sound beams (primary field) of similar frequencies $\omega_a \sim \omega_b$ in the same direction, where at least one of them must have a finite amplitude. As these waves propagate in medium, nonlinear interactions give rise to the generation of a secondary field consisting of higher harmonics, sum- and difference-frequencies, etc., by forming a phased array of virtual sources that resonantly pump acoustic energy into these components. It is obvious that a small percentage change of one of the primary frequencies results in a large percentage change in the difference-frequency, which means that wideband radiation (in difference-frequency) can be accomplished using a narrowband transducer.

Parametric radiation provides a means for generation of a substantially more directional and side-lobes-free sound beam at lower frequencies than is possible by direct small-signal radiation by a source of the same size. However, the former method is less efficient than the latter one.

Many papers have been dedicated to this topic. Far-field properties of the difference-frequency waves were studied in the pioneering work of Westervelt[1] based on the assumption that the nonlinear interactions are limited to the near-field of the primary waves which were modeled as collimated plane waves. Muir and Willette[3] calculated the sum- and difference-frequency field under the condition that the nonlinear interactions take place in the far-field of the primary waves, which were modeled analytically using the formula for the far-field of a uniformly vibrating piston. Garrett *et al*.[4] proposed a model for the parametric radiation from an arbitrary axisymmetric source in the quasilinear and parabolic approximation based on a numerical calculation of a triple integral. Kamakura *et al*.[5] studied the propagation of high-amplitude waves generated by a piston vibrating at two similar frequencies by numerical integration of the KZK equation using the algorithm proposed by Aanonsen *et al*.,[6] as well as experimentally. In Refs. 7 and 8, the authors utilized the method of multi-Gaussian beam (MGB) expansion of the sound field[9] for fast calculation of the secondary fields radiated by an arbitrary axisymmetric source in the quasilinear and paraxial approximation. The method was further extended for rectangular-aperture sources.[10,11]

The common characteristic of most of the above-mentioned papers and many others is the difference-frequency field calculated in the paraxial approximation. Even if this approach is applicable in the case of higher difference-frequencies as is undisputedly confirmed by many experiments, it is a question of whether the paraxial approximation provides correct results even in the case of lower difference-frequencies. This question is the subject of this paper. An analytic formula based on the three-fold integral is derived from the Westervelt equation; an appropriate algorithm is proposed for its numerical calculation. Certain numerical results are presented in order to demonstrate the differences between the low-frequency field patterns calculated using a fast algorithm based on the paraxial approximation and the proposed model which is not based on the paraxial approximation.

II. THEORY

A. Westervelt equation

The Westervelt wave equation[1,12] reads

---

[a] Author to whom correspondence should be addressed. Electronic mail: milan.cervenka@fel.cvut.cz

$$\Delta p' - \frac{1}{c_0^2}\frac{\partial^2 p'}{\partial t^2} + \frac{\delta}{c_0^4}\frac{\partial^3 p'}{\partial t^3} = -\frac{\beta}{\rho_0 c_0^4}\frac{\partial^2 p'^2}{\partial t^2}. \tag{1}$$

Here p' is the acoustic pressure, c_0 is small-signal sound speed, ρ_0 is ambient density of fluid, $\beta = (\gamma + 1)/2$ is the coefficient of nonlinearity, where γ is the adiabatic exponent and

$$\delta = [\zeta + 4\eta/3 + \varkappa(1/c_V - 1/c_p)]/\rho_0$$

is the diffusivity of sound corresponding to thermoviscous attenuation, ζ and η stand for the bulk and shear viscosities, $\varkappa$ is the coefficient of heat conduction, and c_V and c_p are the specific heats at constant volume and pressure, respectively.

The method of successive approximations is used for integration of Eq. (1); its quasilinear solution is assumed to have the form

$$p' = p'_1 + p'_2,$$

where p'_1 is the linear solution (the first approximation) of Eq. (1) representing the primary field and p'_2 is a small correction to p'_1 (the second approximation, $|p'_2| \ll |p'_1|$) due to the nonlinear interaction representing the secondary field (second harmonics, sum- and difference-frequency waves, etc.).

As the acoustic field is assumed to be periodic in time, individual frequency components can be written in the form

$$\begin{aligned} p'_j(\boldsymbol{r}, t) &= p'_{0j}(\boldsymbol{r})\cos[\omega_j t - \phi_j(\boldsymbol{r})] \\ &= \frac{1}{2}\left[q_j(\boldsymbol{r})\mathrm{e}^{-\mathrm{i}\omega_j t} + q_j^*(\boldsymbol{r})\mathrm{e}^{\mathrm{i}\omega_j t}\right], \end{aligned} \tag{2}$$

where $\mathrm{i} = \sqrt{-1}$, $q_j(\boldsymbol{r}) = p'_{0j}(\boldsymbol{r})\mathrm{e}^{\mathrm{i}\phi_j(\boldsymbol{r})}$ is the complex amplitude of acoustic pressure and the asterisk denotes the complex conjugate (c.c.).

B. Primary field

For the two primary waves with angular frequencies ω_a and ω_b, where $\omega_\mathrm{a} > \omega_\mathrm{b}$, substitution of relation (2) into the linearized Eq. (1) yields

$$\Delta q_j + k_j'^2 q_j = 0, \tag{3}$$

where $j = \mathrm{a}, \mathrm{b}$ and $k'_j = \sqrt{k_j^2 + i\omega_j^3\delta/c_0^4} \approx k_j + \mathrm{i}\alpha_j, k_j = \omega_j/c_0$ is the wavenumber and $\alpha_j = \omega_j^2\delta/2c_0^3$ is the thermoviscous attenuation coefficient at the frequency ω_j. In audio- and low ultrasonic-frequency region, relaxation processes are responsible for most of the sound absorption, which is in air dependent on temperature, atmospheric pressure, and water vapor content. The sound attenuation coefficient α_j for the given frequency ω_j can be generalized[13,14] to account for these effects.

Supposing that the vibrating piston radiating the primary wave is placed in a baffle at the plane $z = 0$ and the z-component of its vibration velocity reads $v_{zj}(x, y, t) = [w_j(x, y)\mathrm{e}^{-\mathrm{i}\omega_j t} + \mathrm{c.c.}]/2$, then the solution of Eq. (3) can be constructed with Green's functions[15] in the form of the Rayleigh surface integral

$$q_j(\boldsymbol{r}) = -\frac{\mathrm{i}\omega_j\rho_0}{2\pi}\int_{-\infty}^{\infty}\int_{-\infty}^{\infty} w_j(x'', y'')\frac{\mathrm{e}^{\mathrm{i}k'_j R_0}}{R_0}\mathrm{d}x''\mathrm{d}y'', \tag{4}$$

where $R_0 = |\boldsymbol{R}_0| = \sqrt{(x - x'')^2 + (y - y'')^2 + z^2}$ is the distance between a source element $\mathrm{d}S'' = \mathrm{d}x''\mathrm{d}y''$ and the point, at which the acoustic field is calculated, see Fig. 1.

C. Difference-frequency secondary field

For the secondary difference-frequency wave with the angular frequency $\omega_\mathrm{d} = \omega_\mathrm{a} - \omega_\mathrm{b}$, Eq. (1) reduces to

$$\Delta q_\mathrm{d} + k_d'^2 q_\mathrm{d} = \frac{\beta\omega_\mathrm{d}^2}{\rho_0 c_0^4} q_\mathrm{a} q_\mathrm{b}^*. \tag{5}$$

As it is assumed that $(\partial q_\mathrm{d}/\partial z)_{z=0} = 0$ (the plane $z = 0$ is assumed to be rigid and it does not vibrate at the angular frequency ω_d), the solution of Eq. (5) can be constructed with Green's functions[15] in the form of the volume integral

$$\begin{aligned} q_\mathrm{d}(\boldsymbol{r}) = &-\frac{\beta\omega_\mathrm{d}^2}{4\pi\rho_0 c_0^4}\int_{z'=0}^{\infty}\int_{y'=-\infty}^{\infty}\int_{x'=-\infty}^{\infty} q_\mathrm{a}(\boldsymbol{r}')q_\mathrm{b}^*(\boldsymbol{r}') \\ &\times\left(\frac{\mathrm{e}^{\mathrm{i}k'_\mathrm{d}R+}}{R^+} + \frac{\mathrm{e}^{\mathrm{i}k'_\mathrm{d}R-}}{R^-}\right)\mathrm{d}x'\mathrm{d}y'\mathrm{d}z', \end{aligned} \tag{6}$$

where

$$R^- = |\boldsymbol{R}^-| = \sqrt{(x - x')^2 + (y - y')^2 + (z - z')^2},$$

$$R^+ = |\boldsymbol{R}^+| = \sqrt{(x - x')^2 + (y - y')^2 + (z + z')^2}$$

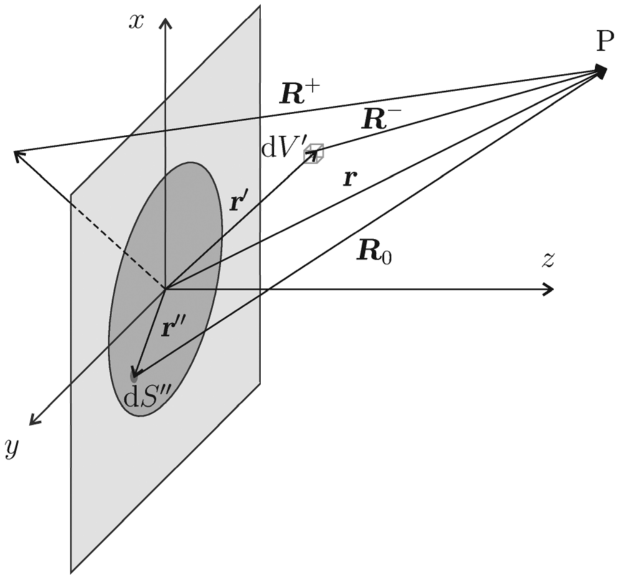

FIG. 1. Geometrical arrangement; P is the point, where acoustic field is determined.

(see Fig. 1). The Green's function used in this integral includes contribution of the element $\mathrm{d}V'$ of the virtual source formed by the primary field (the term containing R^-) as well as the contribution of its image representing the wave reflected from the plane $z = 0$ (the term containing R^+).

Equation (6) for calculation of $q_\mathrm{d}(\boldsymbol{r})$ together with Eq. (4) represents the fifth-fold integral that is almost impossible to be calculated numerically. For this reason, an approximate analytic solution of integral (4) is used under the condition of the high-frequency primary field.

D. High-frequency approximation of the primary field

If the piston radiates at such frequencies that the condition $k_j a \gg 1$ is fulfilled, where a is the piston characteristic radius, the beam is reasonably directional; it is localized in the vicinity of the z axis and the waveforms are quasi-planar, the Green's function in Eq. (4) can be simplified into the paraxial (Fresnel) approximation[16] as

$$\frac{\mathrm{e}^{\mathrm{i}k'_j R_0}}{R_0} \approx \frac{1}{z}\exp\left\{\mathrm{i}k'_j[z + [(x - x'')^2 + (y - y'')^2]/2z]\right\}. \tag{7}$$

If, subsequently, the distribution of the piston velocity is assumed to have an axial symmetry, it can be expanded into the series of the Gaussian functions[9]

$$w_j(x, y) \approx W_j \sum_{n=1}^{N} A_n \mathrm{e}^{-B_n(x^2+y^2)/a^2},$$

where W_j represents amplitude and the complex coefficients A_n, B_n are calculated for an appropriate distribution by a numerical multidimensional optimization method.[9,17–19] Then, the integrals in Eq. (4) can be calculated analytically resulting in the formula

$$q_j(\boldsymbol{r}) = \rho_0 a^2 \omega_j W_j \mathrm{e}^{\mathrm{i}k'_j z} \sum_{n=1}^{N} \frac{A_n \exp\left[-\frac{k'_j B_n (x^2+y^2)}{k'_j a^2 + 2\mathrm{i}B_n z}\right]}{k'_j a^2 + 2\mathrm{i}B_n z}. \tag{8}$$

Substitution of this formula into Eq. (6) results in the three-fold integral for calculation of the difference-frequency wave

$$\begin{aligned} q_\mathrm{d}(\boldsymbol{r}) = &-\frac{\beta\rho_0 a^4 \omega_\mathrm{d}^2 \omega_\mathrm{a} \omega_\mathrm{b} W_\mathrm{a} W_\mathrm{b}^*}{4\pi c_0^4 k'_\mathrm{a} k'^*_\mathrm{b}} \\ &\times \int_{z'=0}^{\infty} \mathrm{e}^{\mathrm{i}(k'_\mathrm{a} - k'^*_\mathrm{b})z'} \sum_{n=1}^{N}\sum_{m=1}^{N} \frac{A_n A_m^* F_\mathrm{a} F_\mathrm{b}^*}{B_n B_m^*} \\ &\times \int_{r'=0}^{\infty} r' \mathrm{e}^{-(F_\mathrm{a} + F_\mathrm{b}^*)r'^2} \\ &\times \int_{\varphi'=0}^{2\pi} \left(\frac{\mathrm{e}^{\mathrm{i}k'_\mathrm{d}R^+}}{R^+} + \frac{\mathrm{e}^{\mathrm{i}k'_\mathrm{d}R^-}}{R^-}\right) \mathrm{d}\varphi' \mathrm{d}r' \mathrm{d}z', \end{aligned} \tag{9}$$

where

$$F_\mathrm{a} = \frac{k'_\mathrm{a} B_n}{k'_\mathrm{a} a^2 + 2\mathrm{i}B_n z'}, \qquad F_\mathrm{b} = \frac{k'_\mathrm{b} B_m}{k'_\mathrm{b} a^2 + 2\mathrm{i}B_m z'}.$$

For the field at the symmetry axis, integral (9) reduces into the two-fold one

$$\begin{aligned} q_\mathrm{d}(0, 0, z) = &-\frac{\beta\rho_0 a^4 \omega_\mathrm{d}^2 \omega_\mathrm{a} \omega_\mathrm{b} W_\mathrm{a} W_\mathrm{b}^*}{2 c_0^4 k'_\mathrm{a} k'^*_\mathrm{b}} \\ &\times \int_{z'=0}^{\infty} \mathrm{e}^{\mathrm{i}(k'_\mathrm{a} - k'^*_\mathrm{b})z'} \sum_{n=1}^{N}\sum_{m=1}^{N} \frac{A_n A_m^* F_\mathrm{a} F_\mathrm{b}^*}{B_n B_m^*} \\ &\times \int_{r'=0}^{\infty} r' \mathrm{e}^{-(F_\mathrm{a} + F_\mathrm{b}^*)r'^2} \left(\frac{\mathrm{e}^{\mathrm{i}k'_\mathrm{d}R^+}}{R^+} + \frac{\mathrm{e}^{\mathrm{i}k'_\mathrm{d}R^-}}{R^-}\right) \mathrm{d}r' \mathrm{d}z'. \end{aligned} \tag{10}$$

Integrals (9) and (10) are calculated numerically.

E. Paraxial approximation of the secondary field

Using the paraxial approximation, integral (9) can be reduced to the form equivalent to the results presented formerly in the work.[8] The reduction consists of neglecting the term with R^+ in the Green's function (assuming that no secondary wave reflects from the source plane) and approximating the remaining term using a formula similar to Eq. (7). The integrals with respect to the coordinates x', y' can be then calculated analytically yielding

$$q_\mathrm{d}(\boldsymbol{r}) = -\frac{\mathrm{i}\beta\rho_0 a^4 \omega_\mathrm{d}^2 \omega_\mathrm{a} \omega_\mathrm{b} W_\mathrm{a} W_\mathrm{b}^*}{2 c_0^4 k'{}_\mathrm{a} k'^*_\mathrm{b} k'_\mathrm{d}} \int_0^z \mathrm{e}^{\mathrm{i}(k'_\mathrm{a} - k'^*_\mathrm{b})z'} \sum_{n=1}^{N}\sum_{m=1}^{N} \frac{A_n A_m^* F_\mathrm{a} F_\mathrm{b}^* \exp\{\mathrm{i}k'_\mathrm{d}|z - z'| - (F_\mathrm{a} + F_\mathrm{b}^*)(x^2 + y^2)/[1 + \mathrm{i}(F_\mathrm{a} + F_\mathrm{b}^*)F_\mathrm{g}]\}}{B_n B_m^*[1 + \mathrm{i}(F_\mathrm{a} + F_\mathrm{b}^*)F_\mathrm{g}]} dz', \tag{11}$$

where $F_\mathrm{g} = 2|z - z'|/k'_\mathrm{d}$. The higher limit of integration is limited to z because in this approximation, it is assumed that only the nonlinear interactions between the source (piston) plane and the appropriate point contribute significantly to the sound field. This assumption is consistent with the paraxial approximation describing only one-way (forward) propagating secondary waves. The integral in Eq. (11) is calculated numerically.

III. NUMERICAL ALGORITHM

High-accuracy evaluation of multidimensional integrals is not easy because among other reasons it makes great demands on computational performance. For this reason, it is necessary to utilize highly-efficient numerical algorithms.

In the case of integrals (9) and (10), the infinite computational domain was reduced to a reasonable size limited by a certain $r_{\max}$ and $z_{\max}$. The repeated one-dimensional integration method[20] was used. Within this approach, the respective procedure calculating the inner integral is repeatedly invoked as required by the procedure calculating the outer integral.

In the case of the above-mentioned integrals, it is necessary to utilize algorithms allowing pre-defined accuracy of calculations (it was observed that with a fixed number of discrete points at which the integrated functions are evaluated, the accuracy of results decreases with the increasing difference-frequency value, because the integrated function becomes more oscillatory). Here, the Romberg method utilizing open formulas[20] was used for calculation of the individual one-dimensional integrals.

The numerical algorithms are implemented with use of the Numerical Recipes C++ library,[20] a substantial reduction of the computational time was achieved by parallelization of the algorithms using the OpenMP library and running on a multi-processor computer.

Coefficients of the MGB decomposition of the piston velocity distribution were calculated using a heuristic optimization method.[19]

IV. RESULTS

Within the numerical calculations, it was assumed that the source velocity distribution possesses the form

$$v_z(r,t) = \mathrm{e}^{-(r/a)^{16}}[v_{0\mathrm{a}}\cos(2\pi f_\mathrm{a} t) + v_{0\mathrm{b}}\cos(2\pi f_\mathrm{b} t)], \qquad (12)$$

which means that the two-frequency vibration is almost spatially uniform within the circle of radius a; here $a = 0.2\,\mathrm{m}$. The corresponding coefficients of the MGB decomposition are listed in Table I. In all the presented cases $f_\mathrm{a} = 50\,\mathrm{kHz}$ and $f_\mathrm{b} = f_\mathrm{a} - f_\mathrm{d}$, where f_d is required difference-frequency. The acoustic field is assumed to be radiated into the air with the temperature of 24 °C, atmospheric pressure 101 325 Pa, and 40% relative humidity. A model accounting for molecular relaxation processes[13] was used for calculation of the sound absorption coefficients α_j.

TABLE I. Complex coefficients of decomposition of the spatial part of function (12) into the series of Gaussian functions.

n	A_n	B_n
1	1.952546 – 7.094992i	5.627804 – 10.20442i
2	−9.479406 + 5.913680i	5.036574 + 4.307618i
3	7.678386 + 0.949987i	4.017862 + 0.175230i
4	5.963587 – 5.346673i	4.396490 + 5.519961i
5	−7.478762 – 0.945619i	4.348546 – 3.827380i
6	−3.949745 + 1.589160i	4.008304 – 10.03536i
7	−0.224418 + 0.091363i	1.951061 + 9.945993i
8	6.537564 + 4.840994i	7.537466 – 7.511751i

As in this case $k_\mathrm{a} a = 192 \gg 1$, the primary wave is well-directional and the paraxial approximation for calculation of the primary field is applicable.

Figure 2 shows the distribution of acoustic pressure amplitude at the frequency f_a along the axis of symmetry calculated in the linear approximation using Eq. (8) (paraxial approximation) and using the Rayleigh integral (4). It can be observed that except for the close vicinity of the source, the results are almost identical so that the paraxial approximation of the formulas for calculation of the primary field does not decrease the accuracy of the algorithm in a substantial way.

The distribution of normalized acoustic pressure amplitude at difference frequency f_d along the piston axis calculated in the non-paraxial approximation using Eq. (10) and in the paraxial approximation using Eq. (11) is shown in Fig. 3. For individual frequencies f_d, the normalized acoustic pressure amplitude is defined as the ratio of the acoustic pressure amplitude and the maximum acoustic pressure amplitude calculated in the paraxial approximation.

For all the difference frequencies f_d, the paraxial equation (11) predicts a zero difference-frequency field at the piston and a steep increase of its amplitude with increasing distance from the piston, which becomes steeper as the difference frequency lowers. By contrast, the non-paraxial Eq. (10) predicts a non-zero amplitude of the acoustic field for very low difference-frequencies. This situation is caused by the fact that for low f_d, the product $k_\mathrm{d} L$, where L is the effective length of the phased virtual source, attains a small value which means that the source is not highly directional. It radiates partly in the direction opposite the primary waves and this backwards-traveling wave reflects from the source plane.

For higher values of the difference-frequencies (in this case for $f_\mathrm{d} = 2000\,\mathrm{Hz}$), both the equations provide almost the same results. This is caused by a higher value of $k_\mathrm{d} L$ resulting in a higher directivity of the virtual source and negligible backward radiation The differences between the results for all the frequencies f_d decreases with the distance from the piston.

Figure 4 shows a comparison of the directivity of the difference-frequency wave in the far-field (at the distance of $200a$ from the piston) calculated using the non-paraxial model (9) and in the paraxial approximation using the

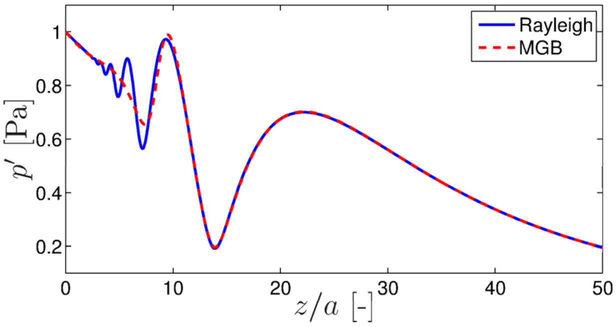

FIG. 2. (Color online) Distribution of the primary wave acoustic pressure amplitude along the piston axis calculated using Eq. (8) and the Rayleigh integral (4), $f_\mathrm{a} = 50\,\mathrm{kHz}$, $v_{0\mathrm{a}} = 2.43 \times 10^{-3}\mathrm{m}\cdot\mathrm{s}^{-1}$.

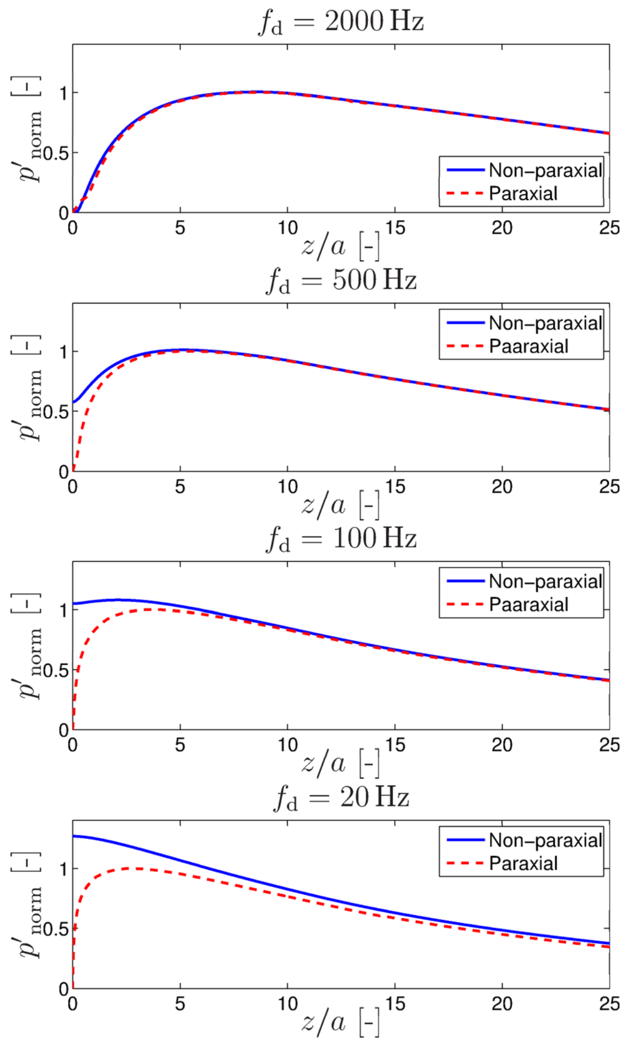

FIG. 3. (Color online) Distribution of normalized acoustic pressure amplitude of the difference-frequency wave along the piston axis for different values of f_d. In the non-paraxial approximation, integral (10) was used, in the paraxial approximation, integral (11) was used.

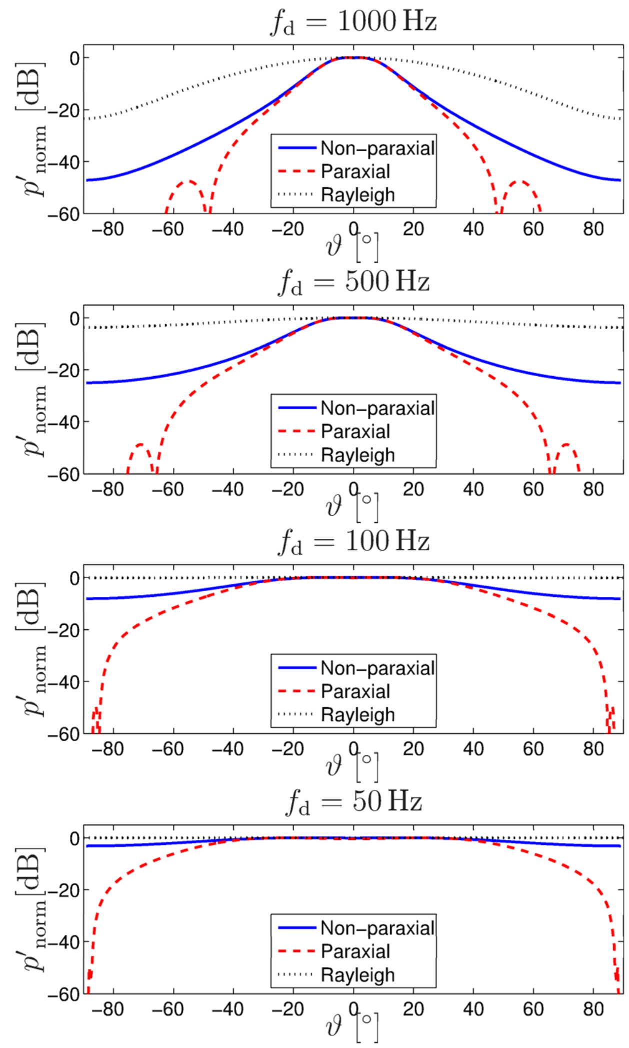

FIG. 4. (Color online) Comparison of the difference-frequency wave directivity calculated in the paraxial and non-paraxial approximation. For illustration, directivity of the wave radiated directly at the frequency f_d is shown (calculated using the Rayleigh integral). ϑ is the polar angle (with respect to the symmetry axis).

integral (11). The case of the direct radiation of a small-amplitude wave with frequency f_d, calculated using the Rayleigh integral (4) is also included. All the courses are normalized to have 0 dB at the axis of symmetry (in all the presented cases, the difference-frequency acoustic field predicted by the paraxial and non-paraxial models are the same at the axis of symmetry, $\vartheta = 0°$).

It can be observed that even for very low frequencies, up to the angle ca. 30°, both the approximations (paraxial and non-paraxial) provide the same results. For bigger angles, the paraxial approximation predicts a lower amplitude of the acoustic field than the approximation that is non-paraxial. It can be observed that directivity of the difference-frequency wave (calculated using the non-paraxial approximation) decreases with its frequency. For instance, at the angle of $\vartheta = 45°$ with respect to the axis, the acoustic pressure amplitude decreases by 28.8 dB at 1000 Hz, by 17.4 dB at 500 Hz, by 3.9 dB at 100 Hz, and only by 0.9 dB at 50 Hz. At this frequency, the acoustic field is almost omnidirectional.

V. CONCLUSION

A formula based on a three-fold integral was proposed for calculation of the difference-frequency wave caused by nonlinear interactions of the two-frequency primary wave generated by a baffled axisymmetric piston. As the formula is not based on the paraxial approximation of the secondary field, it can be used for calculation of near-field as well as wide-angle far-field patterns. On the other hand, the numerical calculation of multi-fold integrals requires a relatively large amount of the computational work compared with the fast algorithms based on the paraxial approximation and one-fold integration. Nevertheless, the proposed formula allows a direct comparison of the numerical results with the ones obtained in the paraxial approximation under otherwise the same conditions and thus it allows delimitation of the applicability of the paraxial model.

The numerical results clearly demonstrate that in the case of the low-frequency secondary field, its amplitude is nonzero at the vicinity of the source, which is caused by low directivity of the virtual source and which is a result that cannot be predicted by any model based on the one-way (forward) propagation of acoustic waves.

ACKNOWLEDGMENTS

This work was supported by GACR Grant No. P101/12/1925. The numerical calculations were performed on a SGI Altix XE 340 computer at the Computing and Information Centre of CTU.

[1] P. J. Westervelt, "Parametric acoustic array," J. Acoust. Soc. Am. **35**, 535–537 (1963).

[2] M. F. Hamilton, "Sound beams," in *Nonlinear Acoustics*, edited by M. F. Hamilton and D. T. Blackstock (Academic Press, San Diego, CA, 1998), Chap. 8, pp. 246–250.

[3] T. G. Muir and J. G. Willette, "Parametric acoustic transmitting arrays," J. Acoust. Soc. Am. **52**, 1481–1486 (1972).

[4] G. S. Garrett, J. Naze Tjøta, and S. Tjøta, "Near-field of a large acoustic transducer, Part II: Parametric radiation," J. Acoust. Soc. Am. **74**, 1013–1020 (1983).

[5] T. Kamakura, N. Hamada, K. Aoki, and Y. Kumamoto, "Nonlinearly generated spectral components in the near-field of a directive sound source," J. Acoust. Soc. Am. **85**, 2331–2337 (1989).

[6] S. I. Aanonsen, T. Barkve, J. Naze Tjøta, and S. Tjøta, "Distortion and harmonic generation in the near-field of a finite amplitude sound beam," J. Acoust. Soc. Am. **75**, 749–768 (1984).

[7] D. Ding, Y. Shui, J. Lin, and D. Zhang, "A simple calculation approach for the second harmonic sound field generated by an arbitrary axial-symmetric source," J. Acoust. Soc. Am. **100**, 727–733 (1996).

[8] D. Ding, "A simplified algorithm for the second-order sound fields," J. Acoust. Soc. Am. **108**, 2759–2764 (2000).

[9] J. J. Wen and M. A. Breazeale, "A diffraction beam field expressed as the superposition of Gaussian beams," J. Acoust. Soc. Am. **83**, 1752–1756 (1988).

[10] K. Sha, J. Yang, and W. S. Gan, "A complex virtual source approach for calculating the diffraction beam field generated by a rectangular planar source," IEEE Trans. Ultrason. Ferroelectr. Freq. Control. **50**, 890–897 (2003).

[11] J. Yang, K. Sha, W. S. Gan, and J. Tian, "Nonlinear wave propagation for a parametric loudspeaker," IEICE Trans. Fundamentals **E87-A**, 2395–2400 (2004).

[12] M. F. Hamilton and C. L. Morfey, "Model equations," in *Nonlinear Acoustics*, edited by M. F. Hamilton and D. T. Blackstock (Academic Press, San Diego, CA, 1998), Chap. 3, pp. 54–56.

[13] H. E. Bass, L. C. Sutherland, A. J. Zuckerwar, D. T. Blackstock, and D. M. Hester, "Atmospheric absorption of sound: Further developments," J. Acoust. Soc. Am. **97**, 680–683 (1995).

[14] H. E. Bass, L. C. Sutherland, A. J. Zuckerwar, D. T. Blackstock, and D. M. Hester, "Erratum: Atmospheric absorption of sound: Further developments [J. Acoust. Soc. Am. **97**, 680–683 (1995)]," J. Acoust. Soc. Am. **99**, 1259 (1996).

[15] P. M. Morse and K. Uno Ingard, *Theoretical Acoustics* (McGraw-Hill, New York, 1968), Chap. 7.

[16] J. W. Goodman, *Introduction to Fourier Optics* (McGraw-Hill, New York, 1996), Chap. 4, pp. 66–73.

[17] H.-J. Kim, L. W. Schmerr, and A. Sedov, "Generation of the basis sets for multi-Gaussian ultrasonic beam models: An overview," J. Acoust. Soc. Am. **119**, 1971–1978 (2006).

[18] D. Ding and Y. Zhang, "Notes on the Gaussian beam expansion," J. Acoust. Soc. Am. **116**, 1401–1405 (2004).

[19] M. Cervenka, M. Bednarik and P. Konicek, "Numerical simulation of parametric field patterns of ultrasonic transducer arrays," on the CD-ROM: *2009 EEE International Ultrasonics Symposium Proceedings*, September 20–23, 2009, Roma (available also at http://ieeexplore.ieee.org/, DOI: 10.1109/ULTSYM. 2009.5441905; last viewed May 23, 2013).

[20] W. H. Press, S. A. Teukolsky, W. T. Vetterling, and B. P. Flannery, *Numerical Recipes 3rd Edition: The Art of Scientific Computing* (Cambridge University Press, Cambridge, 2007), Chap. 4.

A.10 On the structure of multi-Gaussian beam expansion coefficients

Červenka, M., Bednařík, M., On the structure of multi-Gaussian beam expansion coefficients, Acta Acustica United with Acustica 101(1), 15-23, (2015).

ACTA ACUSTICA UNITED WITH ACUSTICA
Vol. 101 (2015) 15 – 23

DOI 10.3813/AAA.918800

On the Structure of Multi-Gaussian Beam Expansion Coefficients

M. Červenka, M. Bednařík
Czech Technical University in Prague, Faculty of Electrical Engineering, Technická 2, 166 27 Prague 6,
Czech Republic. milan.cervenka@fel.cvut.cz

Summary

This work deals with the structure and properties of multi-Gaussian beam expansion coefficients. An alternative formulation of an objective function is proposed for heuristic calculation of the coefficients together with a procedure for reducing the dimensionality of the corresponding optimization problem to a quarter of its original size. The proposed objective function enables us to avoid numerical integration within the process of its evaluation in some practically important cases, which greatly speeds up the calculations. An evolutionary algorithm is employed for global minimization of the objective function resulting in determination of the multi-Gaussian beam expansion coefficients enabling us high-accuracy analytical calculation of acoustic (ultrasonic) fields radiated by planar sources. The calculated expansion coefficients are provided for the case of an axisymmetric uniform piston, a simply supported or clamped disc and a thin membrane. A simple relation delimiting validity of the approximation is found.

PACS no. 43.20.Rz

1. Introduction

Calculation of an acoustic field radiated by a baffled planar source is a classic in acoustics, for which the well-known Rayleigh integral, see e.g. [1], is most often employed. As its general exact analytical solution is not known, many numerical and approximate analytical methods have been developed for this purpose.

A simple analytical approach based on the description of the acoustic field as a superposition of Gaussian beams was proposed by Wen and Breazeale [2]. The key point of this method is in the least-squares approximation of the axisymmetric-source velocity distribution by a series of complex Gaussian functions, provided that $(ka)^2 \gg 1$, where k is the wavenumber and a is a characteristic radius of the source. The complex coefficients of the series, due to non-orthogonality of Gaussian functions, are determined in the most straightforward way by means of optimization methods, which is the key element of this approach. As this method provides accurate results in the farfield, transient region, as well as the nearfield and due to its intrinsic simplicity, it has been further developed by many authors.

Wen and Breazeale [3] modified the optimization algorithm by including knowledge of the on-axis field to increase accuracy of the method in the nearfield. Ding *et al.* [4] extended the method for acoustic fields radiated by rectangular or elliptical sources. Sha *et al.* [5] proposed a method of calculation of acoustic fields generated by rectangular sources, where the Gaussian-functions coefficients are calculated by optimization in the k-space domain. In their summarizing paper, Kim *et al.* [6] showed the relationship between the Gaussian-functions coefficients calculated in spatial domain [2, 3] or k-space domain [5]. Ding and Xu [7] further generalized the method for arbitrary planar sources and showed the relationship between the coefficients for spatial and k-space domain.

As the numerical optimization for calculation of the expansion coefficients is considered a numerically demanding task, there have been a few attempts addressing this issue. Ding and Zhang [8] proposed to pre-define some coefficients in a simple way and utilize linear dependence to calculate the others; Liu and Yang [9] employed a similar approach for calculation of the starting point for numerical optimization, whereby they were able to obtain large sets of expansion coefficients. Schmerr *et al.* [10] proposed a procedure based on Prony's method in k-space domain allowing computationally efficient calculation of the expansion coefficients, fully avoiding the numerical optimization process.

Other authors [11, 12] provided some extensions concerning calculation of acoustic field radiated by a certain class of sources utilizing the expansion coefficients for a uniform piston.

The method of multi-Gaussian expansion was further extended by Zhao and Gang [13] who proposed a non-paraxial approximation model; some other works [14, 15, 16] have dealt with calculation of nonlinearly generated secondary fields.

Received 18 July 2014,
accepted 13 October 2014.

Even if the method of multi-Gaussian beam expansion is mature and wide-used, relatively little has been said about the structure and properties of the expansion coefficients which is the main focus of this work. In spite of the fact that the k-space Prony's method [10] is probably the most effective way to calculate the expansion coefficients, it utilizes some free parameters and its results are sub-optimal as the method does not minimize the squared error of the approximation [17, 18]. That is why the original approach by Wen and Breazeale [2] is adopted and extended here. An alternative objective function is proposed for the optimization procedure enabling its fast evaluation without necessity of numerical integration in some important cases. Utilizing linearity of the approximation functions with respect to some parameters, dimension of the optimization problem is significantly reduced so that a more accurate approximation can be reached. A heuristic optimization algorithm is utilized in order to maximize the probability of finding the global minimum of the objective function. Finally, based on the numerical results, the structure and properties of the expansion coefficients are discussed.

2. Theory

2.1. Mathematical model

Rayleigh integral, see e.g. [1], for calculation of an acoustic field radiated by a planar source placed in an infinite baffle reads

$$\hat{p}'(\boldsymbol{r}) = \frac{\mathrm{j}k\rho_0 c_0}{2\pi} \int_{S_0} \hat{v}_\mathrm{n}(x', y') \frac{\mathrm{e}^{-\mathrm{j}kl}}{l} \,\mathrm{d}x'\mathrm{d}y', \tag{1}$$

where $\hat{p}'(\boldsymbol{r})$ is the acoustic pressure phasor at point $\boldsymbol{r} = (x, y, z)$, $\hat{v}_\mathrm{n}(x, y)$ is the phasor of normal component of the radiator's vibration velocity, $k = 2\pi/\lambda$ is the wavenumber, λ is the wavelength, ρ_0 is the ambient fluid density, c_0 is the small-signal speed of sound, $l = \sqrt{(x - x')^2 + (y - y')^2 + z^2}$ and S_0 is an active area of the source. It is assumed that the baffle with the radiator are situated in plane $z = 0$ and the sound is radiated into the half-space $z > 0$. Time-dependent quantities are calculated from their phasor counterparts as $q(\boldsymbol{r}, t) = \Re\left[\hat{q}(\boldsymbol{r})\exp(\mathrm{j}\omega t)\right]$, ω being the angular frequency and $\mathrm{j} = \sqrt{-1}$.

In the Fresnel approximation, see e.g. [19],

$$l \approx z + \frac{(x - x')^2}{2z} + \frac{(y - y')^2}{2z}$$

is substituted into argument of the exponential (phase term) in (1) whereas $l \approx z$ in the denominator (amplitude term) resulting in

$$\hat{p}'(\boldsymbol{r}) = \frac{\mathrm{j}k\rho_0 c_0 \mathrm{e}^{-\mathrm{j}kz}}{2\pi z} \int_{S_0} \hat{v}_\mathrm{n}(x', y') \cdot \exp\left\{-\mathrm{j}k\left[\frac{(x - x')^2}{2z} + \frac{(y - y')^2}{2z}\right]\right\} \mathrm{d}x'\mathrm{d}y'. \tag{2}$$

If the source distribution has an axial symmetry $\hat{v}_\mathrm{n}(x, y) = \hat{v}_\mathrm{n}(r = \sqrt{x^2 + y^2})$ so has the acoustic field and the two-fold Fresnel field integral can be reduced to one-fold one

$$\hat{p}'(r, z) = \frac{\mathrm{j}k\rho_0 c_0 \mathrm{e}^{-\mathrm{j}k(z + r^2/2z)}}{z} \cdot \int_0^\infty r' \hat{v}_\mathrm{n}(r') \mathrm{J}_0(krr'/z) \mathrm{e}^{-\mathrm{j}kr'^2/2z} \mathrm{d}r', \tag{3}$$

where $\mathrm{J}_0(\cdot)$ is the first-kind zeroth-order Bessel function. The source distribution $\hat{v}_\mathrm{n}(r) = 0$ outside the radiator.

As exact analytical solutions of integral (1) and its approximation (2), (3) are known for only a few special cases, Wen and Breazeale [2] proposed to approximate the source distribution as

$$\hat{v}_\mathrm{n}(r = a\xi) = v_{0\mathrm{n}} f(a\xi) \approx v_{0\mathrm{n}} g(a\xi), \tag{4}$$
$$\text{where} \quad g(\xi) = \sum_{i=1}^{N} A_i \mathrm{e}^{-B_i \xi^2},$$

where a is an effective source radius and A_i, B_i are complex coefficients. Substituting relation (4) into (3) enables the integral to be evaluated analytically resulting in

$$\hat{p}'(r, z) = \mathrm{j}ka^2 \rho_0 c_0 v_{0\mathrm{n}} \mathrm{e}^{-\mathrm{j}kz} \cdot \sum_{i=1}^{N} \frac{A_i}{2B_i z + \mathrm{j}ka^2} \exp\left(-\frac{\mathrm{j}kB_i r^2}{2B_i z + \mathrm{j}ka^2}\right), \tag{5}$$

which is a superposition of Gaussian beams. Introducing the dimensionless axial distance $\zeta = z/z_0$, where $z_0 = a^2/\lambda$ is the Fresnel distance, equation (5) can be simplified into form

$$\frac{\hat{p}'(\xi, \zeta)}{\rho_0 c_0 v_{0\mathrm{n}}} = \mathrm{j}\pi \mathrm{e}^{-\mathrm{j}kz_0\zeta} \cdot \sum_{i=1}^{N} \frac{A_i}{B_i \zeta + \mathrm{j}\pi} \exp\left(-\frac{\mathrm{j}\pi B_i \xi^2}{B_i \zeta + \mathrm{j}\pi}\right). \tag{6}$$

2.2. Objective function

Analytical formula (6) can be used for calculation of the radiated field in the Fresnel approximation, if corresponding coefficients A_i, B_i are known. As the Gaussian functions are non-orthogonal it is most straightforward to use a heuristic method for calculation of these coefficients. Unlike Wen and Breazeale [2] and others, we propose to search for them by minimization of the function

$$Q'(A_1, B_1, \ldots, A_N, B_N) = \int_0^\infty \left| f(\xi) - \sum_{i=1}^{N} A_i \mathrm{e}^{-B_i \xi^2} \right|^2 \xi \,\mathrm{d}\xi. \tag{7}$$

The differential $\xi\mathrm{d}\xi$ stems from the fact that the integration takes place in the polar coordinates (Wen and Breazeale [2] and others omitted the multiplicative weighting factor ξ in the differential). Apart from the geometrical meaning of the coefficient ξ, its presence in formula (7) greatly simplifies evaluation of the function in some important cases

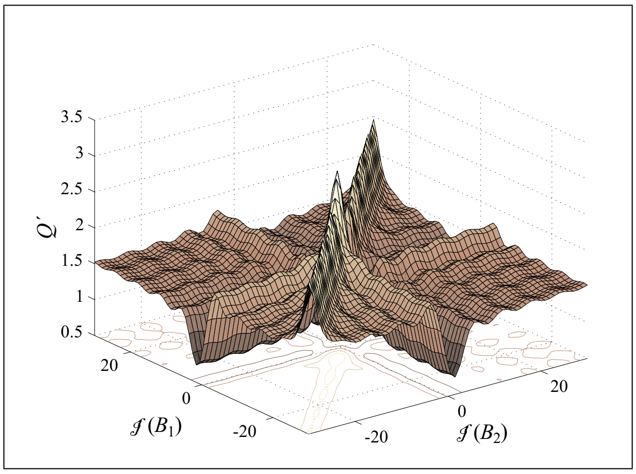

Figure 1. Objective function Q' for $f(\xi) = \mathrm{circ}(\xi)$, $N = 2$, $A_1 = A_2 = 1 + \mathrm{j}$, $\Re(B_1) = \Re(B_2) = 1$.

as it is described below. Relation (7) requires $\Re(B_i) > 0$ in order to assure its convergence.

Searching for the coefficients A_i, B_i represents an optimization problem of minimization of a function of $4N$ real variables. The main goal is to find for a given function $f(\xi)$ a set of coefficients A_i, B_i, minimizing the objective function with N as small as possible, i.e., it is highly desirable to find the global minimum for a given N.

Due to an oscillatory character of function (4), the objective function Q' is multimodal, i.e., there are many local minima, where deterministic search algorithms are prone to get stuck. An elementary example can be seen in Figure 1.

In order to increase the probability of finding the global minimum, it is necessary to 1) reduce the problem dimension as much as possible because the time complexity of a multidimensional search increases exponentially with the problem dimension, 2) to reduce the evaluation time of the objective function Q', and most importantly 3) to employ an algorithm which is able to avoid these numerous local minima.

These needs can be accomplished as follows. First, we can utilize the fact that the function $f(\xi)$ is usually real, so that the approximation function $g(\xi)$ should be real as well. It means that we can impose

$$\begin{aligned} g(\xi) &= \sum_{i=1}^{N/2} \left(A_i \mathrm{e}^{-B_i \xi^2} + A_i^* \mathrm{e}^{-B_i^* \xi^2} \right) \qquad (8) \\ &= 2 \sum_{i=1}^{N/2} \mathrm{e}^{-b_{i\mathrm{re}}\xi^2} [a_{i\mathrm{re}} \cos(b_{i\mathrm{im}}\xi^2) + a_{i\mathrm{im}} \sin(b_{i\mathrm{im}}\xi^2)], \end{aligned}$$

where the asterisk denotes the complex conjugate and $C_i = c_{i\mathrm{re}} + \mathrm{j}c_{i\mathrm{im}}$. Here, N is supposed to be even. The objective function (7) can thus be rewritten as

$$\begin{aligned} Q' = \int_0^\infty \Bigg\{ f(\xi) - 2 \sum_{i=1}^{N/2} \mathrm{e}^{-b_{i\mathrm{re}}\xi^2} [a_{i\mathrm{re}} \cos(b_{i\mathrm{im}}\xi^2) \qquad (9) \\ + a_{i\mathrm{im}} \sin(b_{i\mathrm{im}}\xi^2)] \Bigg\}^2 \xi \, \mathrm{d}\xi, \end{aligned}$$

which means that the minimization problem reduces to a $2N$-dimensional one. It holds $a_{i\mathrm{re}}, a_{i\mathrm{im}} \in \mathbb{R}$, $b_{i\mathrm{re}} > 0$ and $b_{i\mathrm{im}} \geq 0$.

The dimension of the problem can be further reduced by utilizing the fact that relation (8) is linear with respect to coefficients $a_{i\mathrm{re}}, a_{i\mathrm{im}}$. At a minimum of function (9) it holds

$$\left.\frac{\partial Q'}{\partial a_{k\mathrm{re}}}\right|_{\mathrm{minimum}} = 0, \qquad \left.\frac{\partial Q'}{\partial a_{k\mathrm{im}}}\right|_{\mathrm{minimum}} = 0.$$

Evaluating the derivatives, we can write a set of linear equations

$$\sum_{i=1}^{N/2} a_{i\mathrm{re}} \mathcal{I}_{ik}^{\mathrm{cc}} + \sum_{i=1}^{N/2} a_{i\mathrm{im}} \mathcal{I}_{ik}^{\mathrm{sc}} = \mathcal{I}_k^{\mathrm{fc}}, \qquad (10a)$$

$$\sum_{i=1}^{N/2} a_{i\mathrm{re}} \mathcal{I}_{ik}^{\mathrm{cs}} + \sum_{i=1}^{N/2} a_{i\mathrm{im}} \mathcal{I}_{ik}^{\mathrm{ss}} = \mathcal{I}_k^{\mathrm{fs}}, \qquad (10b)$$

where

$$\begin{aligned} \mathcal{I}_{ik}^{\mathrm{cc}} &= \int_0^\infty \mathrm{e}^{-(b_{i\mathrm{re}}+b_{k\mathrm{re}})\xi^2} \\ &\quad \cdot \cos(b_{i\mathrm{im}}\xi^2) \cos(b_{k\mathrm{im}}\xi^2) \xi \mathrm{d}\xi, \qquad (11a) \\ \mathcal{I}_{ik}^{\mathrm{sc}} &= \int_0^\infty \mathrm{e}^{-(b_{i\mathrm{re}}+b_{k\mathrm{re}})\xi^2} \\ &\quad \cdot \sin(b_{i\mathrm{im}}\xi^2) \cos(b_{k\mathrm{im}}\xi^2) \xi \mathrm{d}\xi, \qquad (11b) \\ \mathcal{I}_{ik}^{\mathrm{ss}} &= \int_0^\infty \mathrm{e}^{-(b_{i\mathrm{re}}+b_{k\mathrm{re}})\xi^2} \\ &\quad \cdot \sin(b_{i\mathrm{im}}\xi^2) \sin(b_{k\mathrm{im}}\xi^2) \xi \mathrm{d}\xi, \qquad (11c) \\ \mathcal{I}_k^{\mathrm{fc}} &= \frac{1}{2} \int_0^\infty \mathrm{e}^{-b_{k\mathrm{re}}\xi^2} f(\xi) \cos(b_{k\mathrm{im}}\xi^2) \xi \mathrm{d}\xi, \qquad (11d) \\ \mathcal{I}_k^{\mathrm{fs}} &= \frac{1}{2} \int_0^\infty \mathrm{e}^{-b_{k\mathrm{re}}\xi^2} f(\xi) \sin(b_{k\mathrm{im}}\xi^2) \xi \mathrm{d}\xi, \qquad (11e) \end{aligned}$$

where $\mathcal{I}_{ik}^{\mathrm{cs}} = \mathcal{I}_{ki}^{\mathrm{sc}}$. Integrals (11a) – (11c) are elementary

$$\begin{aligned} \mathcal{I}_{ik}^{\mathrm{cc}} &= \frac{1}{4} \left[\frac{b_{i\mathrm{re}} + b_{k\mathrm{re}}}{(b_{i\mathrm{re}} + b_{k\mathrm{re}})^2 + (b_{i\mathrm{im}} - b_{k\mathrm{im}})^2} \right. \\ &\quad \left. + \frac{b_{i\mathrm{re}} + b_{k\mathrm{re}}}{(b_{i\mathrm{re}} + b_{k\mathrm{re}})^2 + (b_{i\mathrm{im}} + b_{k\mathrm{im}})^2} \right], \qquad (12) \\ \mathcal{I}_{ik}^{\mathrm{sc}} &= \frac{1}{4} \left[\frac{b_{i\mathrm{im}} - b_{k\mathrm{im}}}{(b_{i\mathrm{re}} + b_{k\mathrm{re}})^2 + (b_{i\mathrm{im}} - b_{k\mathrm{im}})^2} \right. \\ &\quad \left. + \frac{b_{i\mathrm{im}} + b_{k\mathrm{im}}}{(b_{i\mathrm{re}} + b_{k\mathrm{re}})^2 + (b_{i\mathrm{im}} + b_{k\mathrm{im}})^2} \right], \qquad (13) \\ \mathcal{I}_{ik}^{\mathrm{ss}} &= \frac{1}{4} \left[\frac{b_{i\mathrm{re}} + b_{k\mathrm{re}}}{(b_{i\mathrm{re}} + b_{k\mathrm{re}})^2 + (b_{i\mathrm{im}} - b_{k\mathrm{im}})^2} \right. \\ &\quad \left. - \frac{b_{i\mathrm{re}} + b_{k\mathrm{re}}}{(b_{i\mathrm{re}} + b_{k\mathrm{re}})^2 + (b_{i\mathrm{im}} + b_{k\mathrm{im}})^2} \right], \qquad (14) \end{aligned}$$

integrals (11d), (11e) depend on the form of function $f(\xi)$. For example, for a uniform piston, it holds

$$f(\xi) = \mathrm{circ}(\xi) = \begin{cases} 1, & \text{for } \xi \leq 1, \\ 0, & \text{for } \xi > 1, \end{cases} \qquad (15)$$

which results in

$$\mathcal{I}_k^{\mathrm{fc}} = \frac{b_{k\mathrm{re}}\left[1-\mathrm{e}^{-b_{k\mathrm{re}}}\cos(b_{k\mathrm{im}})\right]}{4(b_{k\mathrm{re}}^2+b_{k\mathrm{im}}^2)} + \frac{b_{k\mathrm{im}}\mathrm{e}^{-b_{k\mathrm{re}}}\sin(b_{k\mathrm{im}})}{4(b_{k\mathrm{re}}^2+b_{k\mathrm{im}}^2)}, \tag{16a}$$

$$\mathcal{I}_k^{\mathrm{fs}} = \frac{b_{k\mathrm{im}}\left[1-\mathrm{e}^{-b_{k\mathrm{re}}}\cos(b_{k\mathrm{im}})\right]}{4(b_{k\mathrm{re}}^2+b_{k\mathrm{im}}^2)} - \frac{b_{k\mathrm{re}}\mathrm{e}^{-b_{k\mathrm{re}}}\sin(b_{k\mathrm{im}})}{4(b_{k\mathrm{re}}^2+b_{k\mathrm{im}}^2)}. \tag{16b}$$

Similar relations can be easily obtained for a simply supported disc [20]

$$f(\xi) = \left(1-\xi^2\right)\mathrm{circ}(\xi), \tag{17}$$

a clamped disc [20]

$$f(\xi) = \left(1-\xi^2\right)^2\mathrm{circ}(\xi), \tag{18}$$

or for a general function

$$f(\xi) = \left(\sum_{m=0}^{M}\alpha_m\xi^{2m}\right)\mathrm{circ}(\xi).$$

Equations (10) form a set of N linear equations for N unknown coefficients $a_{k\mathrm{re}}, a_{k\mathrm{im}}$. The coefficients $a_{k\mathrm{re}}, a_{k\mathrm{im}}$ can thus be calculated using the coefficients $b_{k\mathrm{re}}, b_{k\mathrm{im}}$, minimization of function (9) then represents only an N-dimensional optimization problem. Moreover, the objective function (9) can be rewritten using the already-calculated quantities as

$$\begin{aligned} Q' = {} & \mathcal{I}^{\mathrm{ff}} - 8\sum_{k=1}^{N/2}\left(a_{k\mathrm{re}}\mathcal{I}_k^{\mathrm{fc}} + a_{k\mathrm{im}}\mathcal{I}_k^{\mathrm{fs}}\right) \\ & + 4\sum_{k=1}^{N/2}\sum_{l=1}^{N/2}\left(a_{k\mathrm{re}}a_{l\mathrm{re}}\mathcal{I}_{kl}^{\mathrm{cc}}\right. \\ & \left. + a_{k\mathrm{im}}a_{l\mathrm{im}}\mathcal{I}_{kl}^{\mathrm{ss}} + 2a_{k\mathrm{im}}a_{l\mathrm{re}}\mathcal{I}_{kl}^{\mathrm{sc}}\right), \end{aligned} \tag{19}$$

where

$$\mathcal{I}^{\mathrm{ff}} = \int_0^\infty f^2(\xi)\xi\,\mathrm{d}\xi \tag{20}$$

is a constant for given function $f(\xi)$.

To sum up, the above-mentioned approach enables us to reduce the dimensionality of the (exponentially complex) optimization problem to a quarter of its original size and in some practically important cases, to avoid the lengthy numerical calculation of (improper) integrals. In the cases where analytical solutions of integrals (11d), (11e) are not known, they must be calculated numerically, but we can still greatly benefit from the advantage of the reduction of the problem dimension.

2.3. Optimization algorithm

Due to the multimodal character of the objective function, see Figure 1, deterministic algorithms are unsuitable for searching the global minimum as they are generally prone to get stuck in a local minimum, see e.g. [21]. Even if we repeatedly generated random start-points for a deterministic search (Multidimensional downhill simplex method [21] was used), the results were much worse than when we employed an evolutionary approach. In fact, utilization of a deterministic algorithm would not allow to study precision of the approximation as a function of number of the expansion terms, especially for large N.

The method of choice here was a self-adaptation variant (μ, λ)-ES of Evolution Strategies [22], which in short works as follows.

First, *population* of λ *individuals* is generated, each of whom has a *genome* represented by vector

$$\mathbf{g}^{(n)} = \left[b_{1\mathrm{re}}^{(n)},\ldots,b_{N/2\mathrm{re}}^{(n)},b_{1\mathrm{im}}^{(n)},\ldots,b_{N/2\mathrm{im}}^{(n)}\right],$$

$n = 1,\ldots,\lambda$, values of which are generated randomly with uniform distribution from interval

$$b_{k\mathrm{re}}^{(n)} \in \left\langle 0, B_{\mathrm{re\,max}}\right\rangle, \quad b_{k\mathrm{im}}^{(n)} \in \left\langle 0, B_{\mathrm{im\,max}}\right\rangle.$$

Then, coefficients $a_{k\mathrm{re}}^{(n)}, a_{k\mathrm{im}}^{(n)}$ are calculated using equations (10) and the individuals are assessed using equation (19). The μ ones with lowest value of Q' become *parents* who generate new population of λ *offspring* by *recombinations* and *mutations* [22]. The parents are eliminated (they *die*) and the process of evolution repeats for pre-defined number of *generations*; the evolution was repeated many times in order to be able to assess the dispersion of the results.

The algorithm is very easy to implement and it is robust against numerical instabilities [system matrix (10) close to singular], as the corresponding individuals are simply penalized. Set of linear equations (10) is solved using *LU* decomposition [21].

For example, for a uniform piston [equation (15)], population of $\lambda = 105$ individuals, one evolution for 20 000 generations lasts 3 s of running time for $N = 10$, 8 s for $N = 20$, 16 s for $N = 30$ and 31 s for $N = 40$ on Intel Core i7-2600, 3.4 GHz.

3. Numerical results

In this section, numerical results are presented which were obtained using the above-described algorithm.

Figure 2 shows the dependence of minimum value of the objective function Q' on the number of terms N of the Gaussian-series expansion for a uniform piston [equation (15)], simply supported [equation (17)] and clamped [equation (18)] disc. In all these cases, integrals (11d), (11e) are calculated analytically.

It can be observed that in the case of the uniform piston, value of Q'_{min} decreases with N very slowly, $Q'_{\mathrm{min}} \sim 1/N^{1.14}$, as the function (15) is discontinuous. A more significant decrease can be observed in the case of the simply

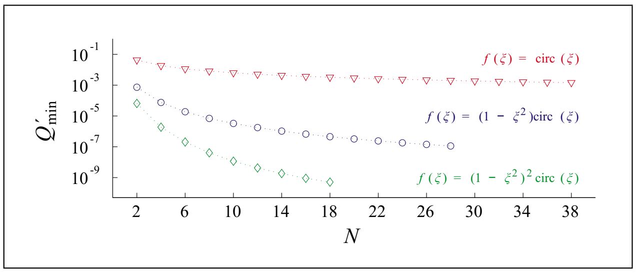

Figure 2. Calculated minima of the objective function Q' for different approximated functions $f(\xi)$ and different number N of terms of Gaussian-series expansion.

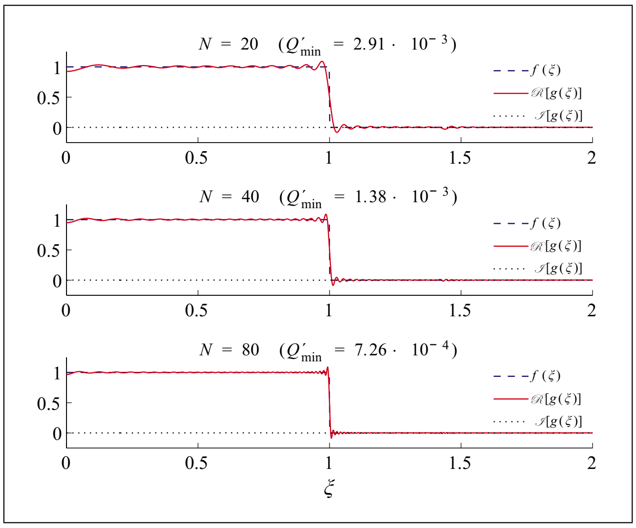

Figure 3. Approximation of function $f(\xi) = \mathrm{circ}(\xi)$ with series of Gaussian functions for various number N of terms.

supported disc, $Q'_{\min} \sim 1/N^{3.35}$, as the function (17) is continuous but not smooth, the smallest values for given N are obtained for a clamped disc, $Q'_{\min} \sim 1/N^{5.41}$, as the function (18) is both continuous and smooth.

Comparison of approximated function $f(\xi)$ with approximate functions $g(\xi)$ for a uniform piston is shown in Figure 3 for $N = 20, 40$ and 80. It can be observed that for $N = 80$, the step at $\xi = 1$ is well approximated, but the Gibbs oscillations are present as it is known from the theory of Fourier series. In all the cases, imaginary part of the approximate function is exactly zero by definition.

Normalized acoustic pressure amplitude along the axis of a uniform piston is depicted in Figure 4; the distribution obtained by numerical solution of Fresnel field integral (3) is compared with the approximate analytical one [equation (6)] for $N = 20$ and 40. It can be seen that the higher N, the closer to the source the approximate solution corresponds to the structure of the nearfield. For $N = 20$, the numerical and approximate solutions correspond to each other for ca. $\zeta > 0.06$, for $N = 40$ then for ca. $\zeta > 0.03$.

Gaussian-series expansion coefficients for $N = 20$ and 40 are given[1] in Tables I and II; they are listed in ascending order along the imaginary part of coefficient $\boldsymbol{B}_i$. It can be observed that the values $\Im(\boldsymbol{B}_i)$ increase more-or-less equidistantly with the value of index i; the values $\Im(\boldsymbol{B}_i)$ for corresponding i but different N are similar. This behaviour was observed in all the studied cases, for different distributions $f(\xi)$ and different N, which corresponds to the findings by Liu and Yang [9]. Real parts of $\boldsymbol{B}_i$ decrease monotonically with increasing value of index i; their values for corresponding i but different N differ. This is summarized graphically in Figure 5.

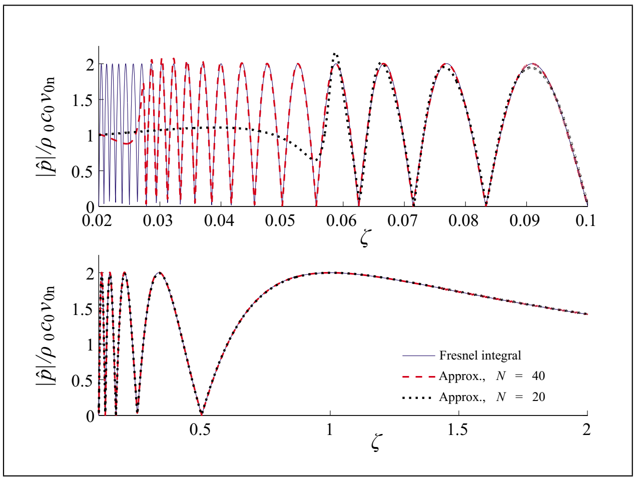

Figure 4. Normalized acoustic pressure along the axis of uniform piston; comparison of numerical solution of Fresnel field integral (3) and the approximate solution (6) with coefficients from Tables I and II.

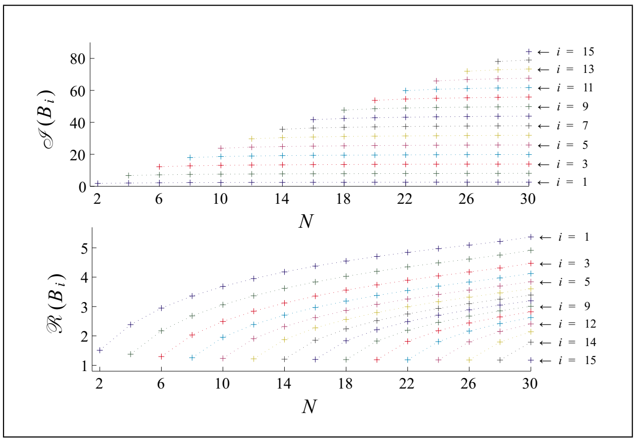

Figure 5. Imaginary and real parts of coefficients $\boldsymbol{B}_i$ for a uniform piston and various number N of Gaussian-series expansion terms.

On the other hand, values of real and imaginary parts of coefficients A_i do not manifest any appreciable structure (but $|A_i|$ generally decreases with increasing i) and they differ by many orders (more than a million times in the case of a uniform piston and $N = 40$, see Tab. II). That is also why it is extremely useful to calculate them [equations (10)] and not to search for them by minimizing the function Q'.

The fact that the number N of terms in approximation influences its precision in the nearfield follows from

---

[1] Actually, only one half (for $i = 1, \ldots, N/2$) of the coefficients is provided as the second half consists of their complex conjugates, see equation (8).

Table I. Coefficients for Gaussian-series expansion for $f(\xi) = \mathrm{circ}(\xi)$ and $N = 20$; $Q'_{\min} = 2.91 \cdot 10^{-3}$.

i	A_i	B_i
1	−8.6553 +14.6250j	4.7052 +2.5238j
2	5.2591 +4.1360j	4.1982 +7.9418j
3	2.7368 −0.2637j	3.7368 +13.7056j
4	1.1244 −0.8024j	3.3771 +19.5740j
5	0.3782 −0.6929j	3.0749 +25.4628j
6	0.0279 −0.4835j	2.7977 +31.3366j
7	−0.1225 −0.2802j	2.5202 +37.1679j
8	−0.1547 −0.1109j	2.2135 +42.9194j
9	−0.1083 +0.0051j	1.8244 +48.5171j
10	−0.0235 +0.0370j	1.1892 +53.7313j

Table II. Coefficients for Gaussian-series expansion for $f(\xi) = \mathrm{circ}(\xi)$ and $N = 40$; $Q'_{\min} = 1.38 \cdot 10^{-3}$.

i	A_i	B_i
1	−919.0626+1787.6665j	10.1017 +3.2824j
2	971.9608 −890.4911j	9.3680 +5.2055j
3	−22.4075 −86.0819j	7.0585 +11.5776j
4	−12.5680 −22.0331j	6.1791 +17.8905j
5	−7.1328 −7.4678j	5.5605 +24.0453j
6	−3.8204 −2.7572j	4.9771 +30.2200j
7	−2.1162 −1.2535j	4.5059 +36.4759j
8	−1.3087 −0.6602j	4.1460 +42.7313j
9	−0.8873 −0.3665j	3.8631 +48.9656j
10	−0.6406 −0.1970j	3.6267 +55.1749j
11	−0.4835 −0.0883j	3.4292 +61.3549j
12	−0.3706 −0.0121j	3.2479 +67.4988j
13	−0.2823 +0.0406j	3.0791 +73.6147j
14	−0.2080 +0.0761j	2.9117 +79.6956j
15	−0.1426 +0.0971j	2.7450 +85.7333j
16	−0.0837 +0.1033j	2.5623 +91.7274j
17	−0.0319 +0.0954j	2.3628 +97.6493j
18	0.0096 +0.0714j	2.1149+103.4645j
19	0.0311 +0.0338j	1.7743+109.1111j
20	0.0200 −0.0020j	1.1690+114.3444j

the structure of the coefficients and equation (6). The higher i, the higher value of $\Im(B_i)$; each i-th term in equation (6) has its counterpart with coefficients A_i^*, B_i^*. This counterpart-term reaches its maximum value at $\zeta_0 = \pi/\Im(B_i)$, which means that with N terms, we can expect a good approximation for

$$\zeta > \frac{\pi}{\Im(B_{N/2})} \approx \frac{1}{N}, \tag{21}$$

which is in good agreement with all the results presented in this paper.

It should be emphasized here that the results presented in Figure 4 and further in the text are compared with numerical solutions of Fresnel field integral (3), which only approximates Rayleigh integral (1) for large values of ka. It is shown in the Appendix by way of example of a uniform piston that Fresnel integral provides accurate results for $\zeta > \zeta_f$, where ζ_f decreases with increasing value of ka.

Table III. Coefficients for Gaussian-series expansion for $f(\xi) = (1-\xi^2)\mathrm{circ}(\xi)$ and $N = 20$; $Q'_{\min} = 3.25 \cdot 10^{-7}$.

i	A_i	B_i
1	−3.77477 +16.91879j	7.1732 +2.3510j
2	5.35464 −3.01026j	6.5632 +7.2932j
3	−0.57540 −1.29063j	5.7106 +12.7261j
4	−0.34236 −0.11426j	4.9401 +18.5372j
5	−0.12015 +0.02345j	4.3779 +24.5100j
6	−0.04058 +0.03290j	3.9719 +30.4059j
7	−0.00691 +0.02137j	3.4778 +36.1402j
8	0.00184 +0.00835j	2.7792 +41.9362j
9	0.00206 +0.00249j	2.0998 +47.7882j
10	0.00098 +0.00016j	1.3011 +53.2824j

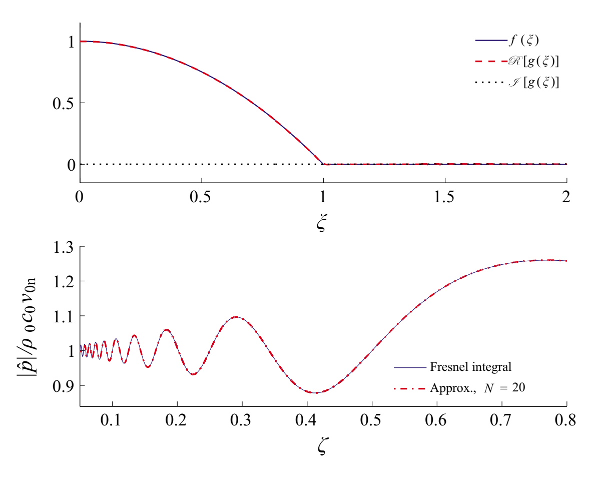

Figure 6. Top:comparison of function (17) – a simply supported disc – with Gaussian-series approximation for $N = 20$ (Table III). Bottom: normalized acoustic pressure along the axis of a simply supported disc; comparison of numerical solution of Fresnel field integral (3) and the approximate solution (6).

Equating ζ_0 and ζ_f can be then used for estimation of N (for given ka) in order that multi-Gaussian beam expansion was consistent with the accuracy of Fresnel approximation.

Below in the text, Gaussian-series expansion coefficients are provided for some practically important cases together with a comparison of numerically and analytically calculated acoustic fields.

Table III gives the expansion coefficients for a simply supported disc described by equation (17) and $N = 20$. It can be seen in Figure 6 that the numerical and approximate solutions correspond to each other for ca. $\zeta > 0.06$.

Table IV gives the expansion coefficients for a clamped disc described by equation (18) and $N = 16$. It can be seen in Figure 7 that the numerical and approximate solutions correspond to each other for ca. $\zeta > 0.08$.

Table V gives the expansion coefficients for the first symmetric mode of a thin circular membrane which can be described as

$$f(\xi) = \mathrm{J}_0(\alpha\xi)\,\mathrm{circ}(\xi), \tag{22}$$

Table IV. Coefficients for Gaussian-series expansion for $f(\xi) = (1-\xi^2)^2\mathrm{circ}(\xi)$ and $N = 16$; $Q'_{\min} = 9.29 \cdot 10^{-10}$.

i	A_i	B_i
1	0.42318+ 12.57547j	8.80684+ 2.18977j
2	0.67681− 4.45349j	8.14912+ 6.74378j
3	−0.66361+ 0.39995j	7.05756+ 11.74892j
4	0.04467+ 0.09666j	5.85251+ 17.22696j
5	0.01564+ 0.00402j	4.69467+ 23.02244j
6	0.00277− 0.00085j	3.61568+ 29.00378j
7	0.00046− 0.00039j	2.60674+ 35.03026j
8	0.00004− 0.00011j	1.50967+ 40.78563j

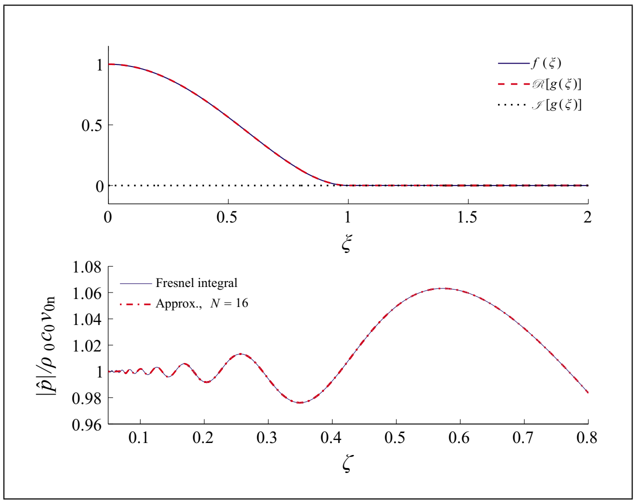

Figure 7. Top: comparison of function (18) – a clamped disc – with Gaussian-series approximation for $N = 16$ (Table IV). Bottom: normalized acoustic pressure along the axis of a clamped disc; comparison of numerical solution of Fresnel field integral (3) and the approximate solution (6).

Table V. Coefficients for Gaussian-series expansion for $f(\xi) = \mathrm{J}_0(\alpha\xi)\mathrm{circ}(\xi)$ where α is the first root of $\mathrm{J}_0(\xi)$ and $N = 16$; $Q'_{\min} = 2.68 \cdot 10^{-7}$.

i	A_i	B_i
1	−1.12651 +16.23151j	7.6719 +2.0600j
2	2.56649 −4.38086j	6.7151 +6.6436j
3	−0.77689 −0.33961j	5.5254 +11.9874j
4	−0.14468 +0.07612j	4.5183 +17.7681j
5	−0.02082 +0.03624j	3.6929 +23.6839j
6	−0.00082 +0.01266j	2.9414 +29.6186j
7	0.00162 +0.00381j	2.2159 +35.4900j
8	0.00099 +0.00051j	1.3476 +41.0253j

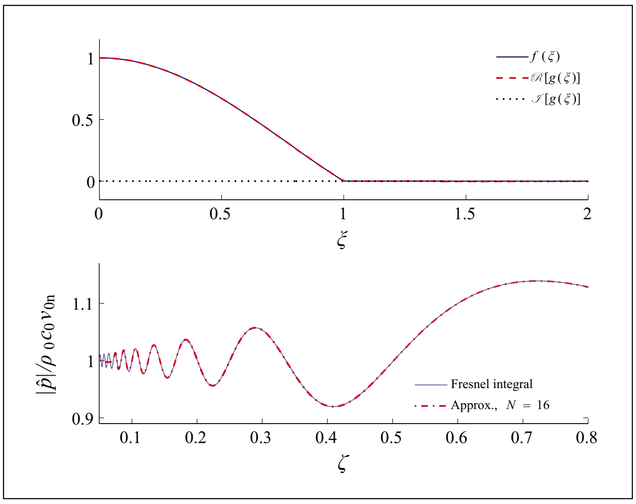

Figure 8. Top: comparison of function (22) – a thin circular membrane – with Gaussian-series approximation for $N = 16$ (Table V). Bottom: normalized acoustic pressure along the axis of a thin circular membrane; comparison of numerical solution of Fresnel field integral (3) and the approximate solution (6).

where $\alpha = 2.4048\ldots$ is the first root of $\mathrm{J}_0(\xi)$. It can be seen in Figure 8 that for $N = 16$ the numerical and approximate solutions correspond to each other for ca. $\zeta > 0.08$. In this case, integrals (11d), (11e) were calculated numerically using the Romberg method [21].

4. Conclusion

We present an alternative form of the objective function for Gaussian-series expansion based on least-squares approximation enabling its analytical evaluation in some practically important cases. Furthermore, a procedure is proposed for significantly reducing the dimension of the search space, which simplifies the search for optimum parameters minimizing the objective function globally.

Gaussian-series expansion coefficients are provided for model cases of a uniform piston, simply supported or clamped disc and a thin circular membrane demonstrating the capability of the proposed method to approximate transducers' velocity distribution with high accuracy.

Structure and properties of the coefficients are analysed; simple relationship between their number and the distance from where the expansion approximates the numerical results well is found.

It is necessary to consider that the analytical formulae (5) or (6) approximate numerical solution of Fresnel field integral (3) and not the Rayleigh integral (1). This means that increasing the number of terms in multi-Gaussian beam expansion increases the approximation accuracy in nearfield only if the value of ka is high enough for Fresnel approximation to describe the appropriate region of nearfield accurately.

Acknowledgement

This work was supported by GACR grant P101/12/1925. Some numerical calculations were performed at Computing and Information Centre of CTU.

A. Applicability of the Fresnel approximation

Within this section it is shown by way of an example that results obtained using Fresnel integral (2) or (3) approx-

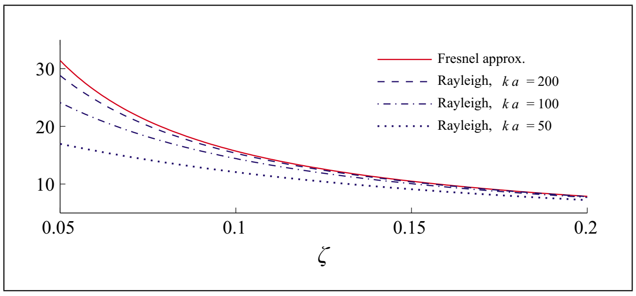

Figure 9. Argument of equation (26) (Fresnel approximation) and equation (24) (Rayleigh integral) for various values of ka.

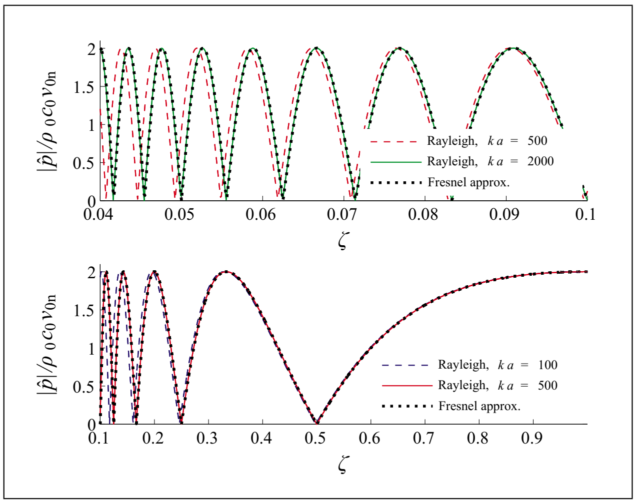

Figure 10. Normalized acoustic pressure amplitude along the axis of uniform piston; comparison of Fresnel approximation (26) and exact solution (24) for various values of ka.

imate results calculated using Rayleigh integral (1) for $\zeta > \zeta_\mathrm{f}$, where the value of ζ_f depends on the value of ka.

It is well-known, see e.g. [1], that acoustic pressure amplitude along the axis of a uniform circular piston of radius a can be calculated using Rayleigh integral (1) in closed form as

$$\frac{|\hat{p}'(0,0,z)|}{\rho_0 c_0 v_{0\mathrm{n}}} = 2\left|\sin\left[\frac{k}{2}\left(\sqrt{z^2+a^2}-z\right)\right]\right|, \tag{23}$$

where $v_{0\mathrm{n}}$ is the piston velocity amplitude. If we introduce the dimensionless distance $\zeta = z/z_0$, where z_0 is the Fresnel distance, we can rewrite equation (23) as

$$\frac{|\hat{p}'(0,0,\zeta)|}{\rho_0 c_0 v_{0\mathrm{n}}} = 2\left|\sin\left[\frac{(ka)^2}{4\pi}\left(\sqrt{\zeta^2+\frac{4\pi^2}{(ka)^2}}-\zeta\right)\right]\right|, \tag{24}$$

which means that the only physical parameter characterizing the structure of the acoustic field is the product ka.

Similar relation can be derived in Fresnel approximation as follows. Substituting $r = 0$ into equation (3) results in

$$\begin{aligned}\hat{p}'(0,0,z) &= \frac{\mathrm{j}k\rho_0 c_0 v_{0\mathrm{n}}\mathrm{e}^{-\mathrm{j}kz}}{z}\int_0^a r'\mathrm{e}^{-\mathrm{j}kr'^2/2z}\mathrm{d}r' \\ &= 2\mathrm{j}\rho_0 c_0 v_{0\mathrm{n}}\mathrm{e}^{-\mathrm{j}k(z+a^2/4z)}\sin\left(\frac{ka^2}{4z}\right).\end{aligned} \tag{25}$$

Thus, introducing the dimensionless distance ζ, we can write

$$\frac{|\hat{p}'(0,0,\zeta)|}{\rho_0 c_0 v_{0\mathrm{n}}} = 2\left|\sin\left(\frac{\pi}{2\zeta}\right)\right|. \tag{26}$$

Relations (24) and (26) differ only in arguments of the sine function. Their comparison is given in Figure 9. It can be seen that the higher value of ka, the better is the Fresnel approximation for given ζ.

Moreover, it holds true that

$$\lim_{ka\to\infty}\frac{(ka)^2}{4\pi}\left(\sqrt{\zeta^2+\frac{4\pi^2}{(ka)^2}}-\zeta\right) = \frac{\pi}{2\zeta}. \tag{27}$$

The value ζ_f beyond which arguments of equation (24) and (26) differ less than certain Δ can be found as

$$\frac{\pi}{2\zeta_\mathrm{f}} - \frac{(ka)^2}{4\pi}\left(\sqrt{\zeta_\mathrm{f}^2+\frac{4\pi^2}{(ka)^2}}-\zeta_\mathrm{f}\right) = \Delta, \tag{28}$$

which can be recast into cubic equation

$$2(ka)^2\Delta\zeta_\mathrm{f}^3 - 4\pi\Delta^2\zeta_\mathrm{f}^2 + 4\pi^2\Delta\zeta_\mathrm{f} - \pi^3 = 0, \tag{29}$$

the real root of which is of the interest. It approximately holds true for large values of ka and small Δ that

$$\zeta_\mathrm{f} \approx \frac{\pi}{\sqrt[3]{2(ka)^2\Delta}}. \tag{30}$$

Comparison of normalized acoustic pressure along the axis of uniform piston calculated using Fresnel approximation (26) and exact solution (24) for various values of ka can be seen in Figure 10.

References

[1] D. T. Blackstock: Fundamentals of physical acoustics. Wiley-Interscience, New York, 2000.

[2] J. J. Wen, M. A. Breazeale: A diffraction beam field expressed as the superposition of Gaussian beams. J. Acoust. Soc. Am. **83** (1988) 1752–1756.

[3] J. J. Wen, M. A. Breazeale: Computer optimization of the Gaussian beam description of an ultrasonic field. – In: Computational Acoustics; Scattering, Gaussian Beams, and Aeroacoustics, Vol. 2. D. Lee, A. Cakmak, R. Vichnevetsky (eds.). Elsevier Science, North Holland, 1990, 181–196.

[4] D. S. Ding, Y. Zhang, J. Q. Liu: Some extensions of the Gaussian beam expansion: Radiation fields of the rectangular and the elliptical transducer. J. Acoust. Soc. Am. **113** (2003) 3043–3048.

[5] K. Sha, J. Yang, W. S. Gan: A complex virtual source approach for calculating the diffraction beam field generated

by a rectangular planar source. IEEE Trans. Ultrason. Ferroelectr. Freq. Control. **50** (2003) 890–897.

[6] H. J. Kim, L. W. Schmerr, A. Sedov: Generation of the basis sets for multi-Gaussian ultrasonic beam models – an overview. J. Acoust. Soc. Am. **119** (2006) 1971–1978.

[7] D. Ding, J. Xu: The Gaussian beam expansion applied to Fresnel field integrals. IEEE Trans. Ultrason. Ferroelectr. Freq. Control. **53** (2006) 246–250.

[8] D. S. Ding, Y. Zhang: Notes on the Gaussian beam expansion. J. Acoust. Soc. Am. **116** (2004) 1401–1405.

[9] W. Liu, J. Yang: A simple and accurate method for calculating the Gaussian beam expansion coefficients. Chinese Phys. Lett. **27** (2010).

[10] L. W. Schmerr, A. L. Lopez-Sanchez, A. Sedov: K-space Prony's method for generating the basis functions of multigaussian beam models. Ultrasonics **50** (2010) 600–605.

[11] D. S. Ding, X. J. Tong, P. Z. He: Supplementary notes on the Gaussian beam expansion. J. Acoust. Soc. Am. **118** (2005) 608–611.

[12] Y. R. Dai, D. S. Ding: Further notes on the Gaussian beam expansion. Chinese Phys. Lett. **29** (2012).

[13] X. Y. Zhao, T. Gang: Nonparaxial multi-Gaussian beam models and measurement models for phased array transducers. Ultrasonics **49** (2009) 126–130.

[14] D. Ding, Y. Shui, J. Lin, D. Zhang: A simple calculation approach for the second harmonic sound field generated by an arbitrary axial-symmetric source. J. Acoust. Soc. Am. **100** (1996) 727–733.

[15] D. Ding: A simplified algorithm for the second-order sound fields. J. Acoust. Soc. Am. **108** (2000) 2759–2764.

[16] M. Červenka, M. Bednařík: Non-paraxial model for a parametric acoustic array. J. Acoust. Soc. Am. **134** (2013) 933–939.

[17] M. D. Prange, R. G. Shenoy: A fast Gaussian beam description of ultrasonic fields based on prony's method. Ultrasonics **34** (1996) 117–119.

[18] S. M. Kay, S. L. Marple: Spectrum analysis - A modern perspective. Proceedings of the IEEE **69** (1981) 1380–1419.

[19] J. W. Goodman: Introduction to Fourier optics. McGraw-Hill, New York, 1996.

[20] D. L. Dekker, R. L. Piziali, E. Dong: Effect of boundary-conditions on ultrasonic-beam characteristics of circular disks. J. Acoust. Soc. Am. **56** (1974) 87–93.

[21] W. H. Press, S. A. Teukolsky, W. T. Vetterling, B. P. Flannery: Numerical recipes 3rd edition: The art of scientific computing. Cambridge University Press, Cambridge, 2007.

[22] A. E. Eiben, J. E. Smith: Introduction to evolutionary computing. Springer, Berlin, 2010.

A.11 Aversatile computational approach for the numerical modelling of parametric acoustic array

Červenka, M., Bednařík, M., A versatile computational approach for the numerical modelling of parametric acoustic array, Journal of the Acoustical Society of America 146(4), 2163-2169, (2019).

A versatile computational approach for the numerical modelling of parametric acoustic array

Milan Červenka[a] and Michal Bednařík
Czech Technical University in Prague, Faculty of Electrical Engineering, Technická 2, 166 27 Prague 6, Czech Republic

(Received 17 May 2019; revised 31 July 2019; accepted 3 September 2019; published online 3 October 2019)

This work presents a versatile computational approach for the numerical modelling of a parametrically generated low-frequency sound. The proposed method is based on the quasi-linear approximation, and it does not employ the paraxial approximation. The primary acoustic field is calculated by the Rayleigh integral or the boundary element method; the secondary difference-frequency field is calculated by the finite element method. As governing wave equations, a general second-order wave equation for acoustic pressure, the Westervelt equation, and Kuznetsov equation are tested, and the corresponding numerical results are compared. The proposed approach allows studying the near-field, far-field, as well as the off-axis field of the difference-frequency wave parametrically radiated from complex emitters. As numerical examples, parametric radiation from a baffled piston and a piston combined with a horn are examined. © *2019 Acoustical Society of America.*
https://doi.org/10.1121/1.5126863

[NAG] Pages: 2163–2169

I. INTRODUCTION

The concept of parametric acoustic array (PAA) was introduced in 1963 by Westervelt.[1] This technique allows to generate low-frequency highly directional side-lobes-free sound beams from sources (radiators) with relatively small aperture. The principle is as follows; see, e.g., Refs. 1–3. Two collimated ultrasonic beams of similar frequencies are radiated in the same direction, where at least one of them has a finite amplitude. As these (primary) waves propagate in the medium, nonlinear effects give rise to the generation of a secondary field, one component of which is the (low-frequency) difference-frequency one, by forming a phased array of virtual sources that resonantly pump acoustic energy into this component. The directivity of this low-frequency wave is much higher than if it were radiated directly by the primary-field radiator.

Since its discovery the PAA has found its application in sonar, parametric loudspeakers, etc.; see, e.g., Refs. 4–9.

The process of the generation of a difference-frequency wave in a field of highly directional finite-amplitude primary waves is a rather complex one, and its mathematical description requires some degree of approximation and simplification. This problem has been addressed by many authors in different ways; some examples are given below.

In his pioneering work, Westervelt[1] described the far-field properties of the difference-frequency waves based on the assumption that the nonlinear interactions are limited only to the near-field of the primary waves, which were modelled as collimated plane waves. Muir and Willette[10] calculated the sum- and difference-frequency field under the assumption that the nonlinear interactions take place only in the far-field of the primary waves, which were modelled analytically using the formula for the far-field of a uniformly vibrating piston. Garrett *et al.*[11] proposed a model for the parametric radiation from an axisymmetric source in the quasilinear and parabolic approximation based on the numerical calculation of a triple integral. Kamakura *et al.*[12] studied the propagation of high-amplitude waves generated by a piston vibrating at two similar frequencies by numerical integration of parabolic KZK equation. In Refs. 13–15, the method of multi-Gaussian beam expansion has been employed for the fast calculation of difference-frequency fields in the quasi-linear approximation, where in Refs. 13 and 14 the parabolic approximation has been employed for the calculation of the difference-frequency field. Nomura *et al.*[16] simulated the parametric sound generation by means of direct numerical integration of Navier-Stokes equations in the time domain. This approach, in principle, allows to study more complex configurations; however, the numerical integration in the time domain over a large spatial domain (if the far-field behaviour is studied) results in a long computational time and a big amount of stored data, which need to be post-processed in order to obtain the spectral content of the sound field.

The aim of this work is to propose a versatile and computationally efficient approach to calculate the parametrically generated sound field from an arbitrary primary-wave source, not only a baffled planar piston. The only approximation adopted here is the quasi-linear one, which means that the acoustic field is assumed to be only weakly nonlinear.

The paper is organised as follows. In Sec. II, the second-order wave equations of nonlinear acoustics suitable for the calculation of the parametric radiation are reviewed, and the mutual relationships between them are mentioned. In Sec. III, the method of the successive approximations is employed to convert the model equations into a form suitable for the solution in the frequency domain. Section IV describes the numerical method used for the solution of the model equations. In Sec. V, predictions of the individual model equations are

---

[a] Electronic mail: milan.cervenka@fel.cvut.cz

compared in the case of a baffled planar piston radiator, and an example of a horned piston is given to demonstrate the versatility of the proposed approach. Section VI then draws some conclusions.

II. NONLINEAR WAVE EQUATIONS

The second-order nonlinear wave equation describing the wave propagation in a homogeneous and quiescent fluid reads[2,17]

$$\begin{aligned}\nabla^2 p' - \frac{1}{c_0^2}\frac{\partial^2 p'}{\partial t^2} + \frac{\delta}{c_0^2}\nabla^2\frac{\partial p'}{\partial t} \\ = -\frac{\beta}{\rho_0 c_0^4}\frac{\partial^2 p'^2}{\partial t^2} - \nabla^2\mathcal{L} - \frac{1}{c_0^2}\frac{\partial^2\mathcal{L}}{\partial t^2},\end{aligned} \tag{1}$$

where p' is the acoustic pressure, t is the time, c_0 is the small-signal adiabatic sound speed, ρ_0 is the ambient fluid density, β is the parameter of nonlinearity of the fluid for an ideal gas $\beta = (\gamma + 1)/2$, where γ is the adiabatic exponent, $\delta = [4\mu/3 + \mu_B + \kappa(1/c_V - 1/c_p)]/\rho_0$ is the diffusivity of sound, where μ, μ_B are the coefficients of shear and bulk viscosity, respectively, κ is the coefficient of thermal conduction, and c_p,c_V are the specific heats at constant pressure and volume, respectively. The symbol $\mathcal{L}$ stands for the Lagrangian density, which reads

$$\mathcal{L} = \rho_0\frac{v^2}{2} - \frac{p'^2}{2\rho_0 c_0^2}, \tag{2}$$

where $v^2 = \boldsymbol{v}\cdot\boldsymbol{v}$ is the square of the acoustic particle velocity vector. Equation (1) is an approximate wave equation valid to the second order in acoustic Mach number $\varepsilon = v_0/c_0$, where v_0 is the maximum acoustic particle velocity. Equation (1) accounts for mutual interactions of nonlinear and thermoviscous dissipative processes modifying the wave propagation in three-dimensional space.

In the second approximation, $\mathcal{L} = 0$ in the case of progressive plane waves. Then, the general model equation Eq. (1) reduces into the well-known Westervelt equation,[1,2,17] which reads

$$\nabla^2 p' - \frac{1}{c_0^2}\frac{\partial^2 p'}{\partial t^2} + \frac{\delta}{c_0^2}\nabla^2\frac{\partial p'}{\partial t} = -\frac{\beta}{\rho_0 c_0^4}\frac{\partial^2 p'^2}{\partial t^2}. \tag{3}$$

As it is discussed in Refs. 2 and 17, the Westervelt equation describes correctly (in the second-order approximation) plane progressive waves; however, even with the omission of the Lagrangian density, the cumulative nonlinear effects are still captured correctly even in the case of non-plane wave propagation, the Lagrangian density is associated only with local (non-cumulative) nonlinear effects. Due to its relative simplicity [compared to Eq. (1)], the Westervelt equation is widely used in the modelling of PAA.

If we introduce the velocity potential φ such that $\boldsymbol{v} = \nabla\varphi$ and employ the second-order relationship between the acoustic pressure and the velocity potential; see, e.g., Ref. 18,

$$p' = -\rho_0\frac{\partial\varphi}{\partial t} - \frac{\rho_0}{2}(\nabla\varphi)^2 + \frac{\rho_0}{2c_0^2}\left(\frac{\partial\varphi}{\partial t}\right)^2, \tag{4}$$

in the second approximation, wave equation Eq. (1) can be recast[17] into

$$\begin{aligned}\nabla^2\varphi - \frac{1}{c_0^2}\frac{\partial^2\varphi}{\partial t^2} + \frac{\delta}{c_0^2}\nabla^2\frac{\partial\varphi}{\partial t} \\ = \frac{1}{c_0^2}\frac{\partial}{\partial t}\left[(\nabla\varphi)^2 + \frac{\beta - 1}{c_0^2}\left(\frac{\partial\varphi}{\partial t}\right)^2\right],\end{aligned} \tag{5}$$

which is the well-known Kuznetsov equation.[19] Equations (1) and (5) are derived under the same degree of approximation, and they are equivalent.

III. SUCCESSIVE APPROXIMATIONS

Within this work, acoustic fields are assumed to be only weakly nonlinear, which allows to employ the method of the successive approximations[2] for solving the governing equations (1), (3), or (5). The quasi-linear solutions of the governing equations are assumed to have the form

$$\psi(\boldsymbol{r}, t) = \psi_1(\boldsymbol{r}, t) + \psi_2(\boldsymbol{r}, t), \tag{6}$$

where ψ represents the given acoustic variable (acoustic pressure, velocity potential), ψ_1 is the linear solution (approximation) of Eqs. (1), (3), or (5), representing the primary field, and ψ_2 is a small correction to ψ_1, representing the secondary field due to the nonlinear interactions. Obviously, $|\psi_2| \ll |\psi_1|$.

The primary acoustic field is assumed to be composed of two time-harmonic fields at similar frequencies f_c (carrier) and f_s (side-band), where $f_c > f_s$. Within this work, the difference-frequency component f_d of the secondary field is of interest, where $f_d = f_c - f_s$. Being time-harmonic, all the components of the acoustic variables are further represented by their complex amplitudes $\psi_j(\boldsymbol{r}, t) = \Re[\tilde{\psi}_j(\boldsymbol{r})\mathrm{e}^{\mathrm{i}\omega_j t}]$, where $j = c, s, d$, and $\mathrm{i} = \sqrt{-1}$.

For the primary-field components, the linearised equations (1), (3), or (5) reduce to the homogeneous Helmholtz equation

$$\nabla^2\tilde{\psi}_j + k_j^2\tilde{\psi}_j = 0, \tag{7}$$

where $j = c, s$, and

$$k_j^2 = \frac{\omega_j^2/c_0^2}{1 + \mathrm{i}\omega_j\delta/c_0^2} \Rightarrow k_j \approx \frac{\omega_j}{c_0} - \mathrm{i}\frac{\omega_j^2\delta}{2c_0^3} \tag{8}$$

is the complex wavenumber, the imaginary part of which describes the thermoviscous attenuation. In audio- and low-ultrasonic-frequency regions, relaxation processes are responsible for most of the sound absorption, which in air is dependent on temperature, atmospheric pressure, and water vapor content. The sound attenuation coefficient for the given frequency ω_j can be generalized[20,21] to account for these effects.

For the difference-frequency secondary field, Eqs. (1) and (3) reduce to the inhomogeneous Helmholtz equation

$$\nabla^2\tilde{p}_d + k_d^2\tilde{p}_d = \tilde{q}_{pd}, \tag{9}$$

where the source term

$$\tilde{q}_{pd} = \frac{\beta\omega_d^2}{\rho_0 c_0^4}\tilde{p}_c\tilde{p}_s^* - (\nabla^2 - k_d^2)\tilde{\mathcal{L}}_d, \tag{10}$$

where

$$\tilde{\mathcal{L}}_d = \frac{\rho_0}{2}\tilde{\boldsymbol{v}}_c\cdot\tilde{\boldsymbol{v}}_s^* - \frac{\tilde{p}_c\tilde{p}_s^*}{2\rho_0 c_0^2} \tag{11}$$

for Eq. (1). The asterisk stands for the complex conjugate, and $\tilde{\mathcal{L}}_d = 0$ for the Westervelt equation [Eq. (3)].

For the difference-frequency secondary field, Eq. (5) reduces to

$$\nabla^2\tilde{\varphi}_d + k_d^2\tilde{\varphi}_d = \tilde{q}_{\varphi d}, \tag{12}$$

where

$$\tilde{q}_{\varphi d} = \frac{\mathrm{i}\omega_d}{c_0^2}\left[\tilde{\boldsymbol{v}}_c\cdot\tilde{\boldsymbol{v}}_s^* + (\beta-1)\frac{\omega_c\omega_s}{c_0^2}\tilde{\varphi}_c\tilde{\varphi}_s^*\right]. \tag{13}$$

Using the difference-frequency, and primary-field velocity potentials, the difference-frequency acoustic pressure can be calculated, employing Eq. (4), as

$$\tilde{p}_d = -\mathrm{i}\omega_d\rho_0\tilde{\varphi}_d - \frac{\rho_0}{2}\tilde{\boldsymbol{v}}_c\cdot\tilde{\boldsymbol{v}}_s^* + \frac{\rho_0\omega_c\omega_s}{2c_0^2}\tilde{\varphi}_c\tilde{\varphi}_s^*. \tag{14}$$

IV. NUMERICAL METHOD

As it has been shown above, employing the method of the successive approximations for the time-harmonic fields, the governing nonlinear wave equations (1), (3), or (5) reduce to the homogeneous Helmholtz equation (7) for the primary field, and into the inhomogeneous Helmholtz equations (9) and (12) for the difference-frequency secondary field. The source terms [Eqs. (10) and (13)] for the secondary-field equations are calculated from the primary-field quantities.

The original idea was to calculate the primary-field, as well as the secondary-field quantities employing the finite element method (FEM). However, as the general rule of thumb states that there are at least six elements per wavelength needed for the discretization, calculation of the high-frequency primary field in a large computational domain (external radiation problem) resulted in an extreme amount of the computer-memory needed. Moreover, in the case of Eq. (1), where there are second spatial derivatives of the primary-field quantities needed for the calculation of the source terms [Eqs. (10) and (11)], the computational mesh must be way more fine.

In order to circumvent these obstacles, the following two approaches have been tested for the calculation of the high-frequency primary field quantities: (a) for the case of the radiation from a baffled piston, the Rayleigh integral was evaluated numerically; (b) the boundary element method (BEM) was employed. In both the cases, the low-frequency secondary field was calculated employing FEM in COMSOL Multiphysics (Acoustic Module, Pressure Acoustics Interface, frequency-domain, COMSOL AB, Stockholm, Sweden).

A. Rayleigh integral

Geometrical arrangement of the piston baffled in an infinite rigid plane is shown in Fig. 1.

The complex amplitude of the acoustic pressure of the primary field at point *P*, for the calculation of the source terms [Eqs. (10) and (13)], can be calculated employing the Rayleigh integral (see, e.g., Ref. 22) as

$$\tilde{p}_j(\boldsymbol{r}) = \frac{\mathrm{i}k_j\rho_0 c_0}{2\pi}\int_{-\infty}^{\infty}\int_{-\infty}^{\infty}\tilde{u}_j(x',y')\frac{\mathrm{e}^{-\mathrm{i}k_jR}}{R}\,\mathrm{d}x'\,\mathrm{d}y', \qquad j = c, s, \tag{15}$$

where $\tilde{u}_j(x,y)$ is the complex amplitude of the piston vibration velocity (at the given frequency)—considered to be zero outside the piston, and

$$R = \sqrt{(x-x')^2 + (y-y')^2 + z^2}.$$

The complex amplitude of the velocity potential is then calculated using the formula $\tilde{\varphi}_j = \mathrm{i}\tilde{p}_j/k_j\rho_0 c_0$, and from here, the x- and z-components of the acoustic particle velocity vector

$$\tilde{v}_{jx}(\boldsymbol{r}) = \frac{\partial\tilde{\varphi}_j}{\partial x} = \frac{1}{2\pi}\int_{-\infty}^{\infty}\int_{-\infty}^{\infty}\tilde{u}_j(x',y')(x-x') \times (1+\mathrm{i}k_jR)\frac{\mathrm{e}^{-\mathrm{i}k_jR}}{R^3}\,\mathrm{d}x'\,\mathrm{d}y', \tag{16a}$$

$$\tilde{v}_{jz}(\boldsymbol{r}) = \frac{\partial\tilde{\varphi}_j}{\partial z} = \frac{z}{2\pi}\int_{-\infty}^{\infty}\int_{-\infty}^{\infty}\tilde{u}_j(x',y')(1+\mathrm{i}k_jR) \times \frac{\mathrm{e}^{-\mathrm{i}k_jR}}{R^3}\,\mathrm{d}x'\,\mathrm{d}y'. \tag{16b}$$

The x-component of the acoustic particle velocity vector in Eq. (16a) represents a component perpendicular to the z

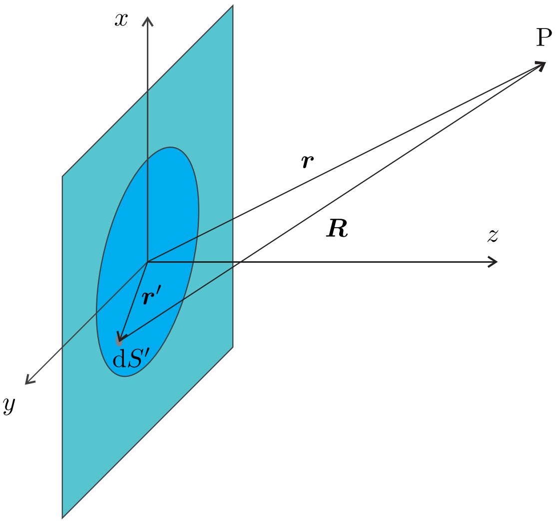

FIG. 1. (Color online) Geometrical arrangement; *P* is the point where the acoustic field is determined.

axis; the y-component, or the r-component (cylindrical coordinates) would be calculated analogously. The Laplacian operator in Eq. (10) was approximated using the second-order finite differences. The surface integrals [Eqs. (15) and (16)] were implemented as MATLAB (MathWorks, Natick, MA) functions (employing the MATLAB function integral2); these functions were called from COMSOL Multiphysics as MATLAB functions—which is a feature provided by package LiveLink for MATLAB for COMSOL Multiphysics. As the infinite baffle is supposed to be rigid, its vibration velocity is zero and the surface integrals [Eqs. (15) and (16)] are in fact evaluated only over the piston surface.

B. BEM

Within the BEM, the boundary conditions are used to fit the boundary values on the surfaces. Subsequently, the acoustic field quantities in the fluid domain are calculated using the boundary values during the post-processing. This technique is usually more efficient (than, e.g., FEM) in the cases where the surface/volume ratio of the computational domain is small, which is the case of the problem studied within this work (external radiation problem). Compared to the Rayleigh integral (see Sec. IV A), radiation from more complex sources can be studied.

Within this work, the high-frequency primary-field acoustic quantities and the source terms [Eqs. (10) and (13)] were calculated using Pressure Acoustics, Boundary Elements Interface of Acoustics Module of COMSOL Multiphysics, exported as text files, and imported to the Acoustic Module, Pressure Acoustics Interface of COMSOL Multiphysics to calculate the secondary field by FEM.

V. NUMERICAL RESULTS

Within all the examples shown in this section, acoustic field is calculated in air at normal conditions, and classical thermoviscous attenuation is taken into account. Namely, $c_0 = 343.2\ \mathrm{m\ s^{-1}}$, $\rho_0 = 1.204\ \mathrm{kg\ m^{-3}}$, $\gamma = 1.4$, and $\delta = 3.764 \times 10^{-5}\ \mathrm{m^2\ s^{-1}}$.

In all the following cases, the carrier frequency $f_c = 40$ kHz. The primary-field source (radiator) is assumed to have an axial symmetry so that the acoustic field is calculated in (r,z) axisymmetric cylindrical coordinates.

A. Baffled piston

Here, radiation from a baffled circular piston (see Fig. 1) of radius $a = 2$ cm is examined. The complex amplitude of its vibration velocity at frequencies f_c, f_s is assumed to have the form

$$\begin{aligned} \tilde{u}_j(r) &= u_0 \quad (\text{uniform distribution}),\\ \tilde{u}_j(r) &= u_0(1 - r^2/a^2) \quad (\text{parabolic distribution}),\\ \tilde{u}_j(r) &= u_0(1 - r^2/a^2)^2 \quad (\text{quartic distribution}), \end{aligned} \qquad (17)$$

(see Fig. 2) where $j = c, s,\ r = \sqrt{x^2 + y^2} \le a$ and, for simplicity, $u_0 = 1\ \mathrm{m\ s^{-1}}$. In all the numerical results presented in this subsection, the primary acoustic field is calculated employing the Rayleigh integral (see Sec. IV A), however, BEM provides the same results.

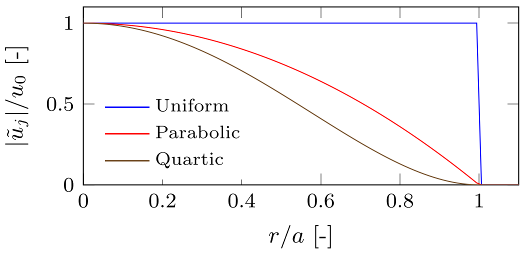

FIG. 2. (Color online) Spatial distributions of the piston velocity amplitude.

Figure 3 shows the distribution of the amplitude of the acoustic pressure of the difference-frequency wave ($f_d = 1$ kHz) along the z axis in the near-field of the carrier wave (for $f_c = 40$ kHz, the Rayleigh distance $R_r = \Re[k_c]a^2/2 = 14.6$ cm). The velocity-distribution of the piston is the parabolic one; see Eq. (17).

The difference-frequency field is calculated employing Eq. (1) (red line in Fig. 3), the Westervelt equation [Eq. (3), blue line in Fig. 3], and the Kuznetsov equation [Eq. (5), green line in Fig. 3]. As Eq. (1) and the Kuznetsov equation are derived under the same approximation, the numerical results correspond to each other very well. As in the Westervelt equation, the Lagrangian density [Eq. (2)] is assumed to be zero, which is not fulfilled in the near-field of the primary wave, and the prediction by the Westervelt equation differs from Eq. (1) and the Kuznetsov equation. However, in the far-field, beyond the Rayleigh distance, the predictions of all the three equations match each other as is expected.

As the numerical evaluation of the source term [Eq. (10)] for Eq. (1) is much more expensive than the source term [Eq. (13)] for the Kuznetsov equation, and as it is necessary to calculate the second-order spatial derivatives of the primary-field quantities, the Kuznetsov equation [Eq. (5)] is employed for the calculation of the near-field further on.

Figure 4 shows the acoustic pressure amplitude of the difference-frequency wave along the z axis for $f_d = 1$ kHz and individual piston velocity distributions [see Eq. (17)]. The solid lines correspond to the predictions by the Kuznetsov equation, and the dashed lines are related to the Westervelt equation. It can be observed that the structure of the near-field (resolved by the Kuznetsov equation) depends on the piston velocity distribution and, again, the predictions of both the equations correspond to each other in the far-field.

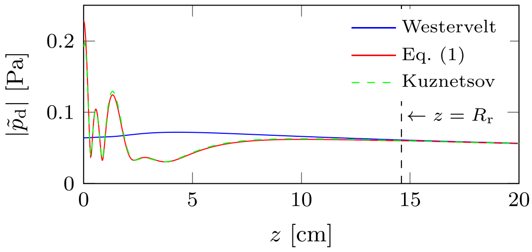

FIG. 3. (Color online) Comparison of the numerical results: difference-frequency wave, $f_d = 1$ kHz, piston with parabolic velocity distribution; the vertical dashed line marks the Rayleigh distance.

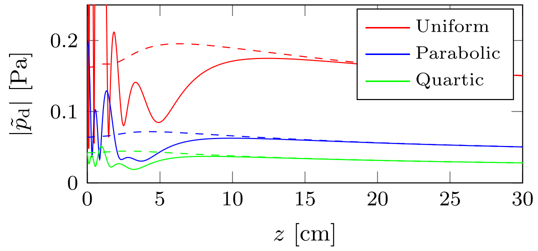

FIG. 4. (Color online) Difference-frequency wave along the z axis for $f_d = 1$ kHz, and individual piston velocity distributions. Predictions are shown by the Kuznetsov equation (solid lines) and Westervelt equation (dashed lines).

The difference in the amplitudes (at a given point in the far-field) for the individual piston velocity distributions are caused by the fact that the amount of radiated acoustic energy for the individual cases differs.

Figure 5 shows the normalized acoustic pressure amplitude of the difference-frequency wave along the $z$axis for the parabolic piston velocity distribution and individual frequencies f_d. The waveforms for the individual frequencies are normalized by the factor $(f_d/1\text{ kHz})^2$ for better legibility of the details. The solid lines correspond to the predictions by the Kuznetsov equation, and the dashed lines are associated with the Westervelt equation. It can be seen that the near-field structure resolved by the Kuznetsov equation depends on the difference-wave frequency and is more prominent for lower frequencies f_d. In all the cases in the far-field, the predictions by both the equations match.

Figure 6 shows the directivity function $D(\vartheta) = |\tilde{p}(r_0,\vartheta)/\tilde{p}(r_0,0)|$ calculated at the distance $r_0 = 2$ m from the centre of the piston with the parabolic velocity distribution. It can be observed that the low-frequency difference-frequency field (solid lines) has a similar directivity as the high-frequency carrier wave (dashed line), and the directivity of the difference-frequency wave increases with its frequency. Radiation from this piston directly at the frequencies shown in Fig. 6 (500 Hz–5 kHz) would be essentially omnidirectional.

Figure 7 shows the directivity function calculated at the distance $r_0 = 2$ m from the centre of the piston with various velocity distributions [Eq. (17)] for the difference-frequency wave at $f_d = 1$ kHz. It can be observed that the uniform velocity distribution provides the highest directivity, which is associated with the fact that, in this case, the entire piston surface vibrates with the same velocity, compared to the case of the parabolic or quartic distributions, where the vibration velocity decreases toward the piston edge.

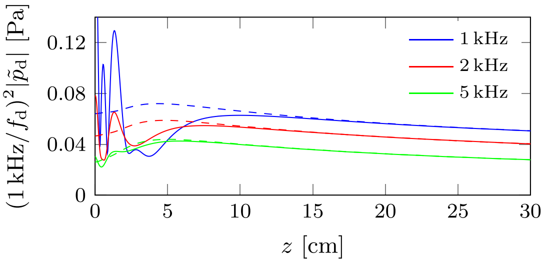

FIG. 5. (Color online) Normalized difference-frequency wave along the z axis for the parabolic piston velocity distribution and individual difference frequencies. Predictions are shown by the Kuznetsov equation (solid lines) and Westervelt equation (dashed lines).

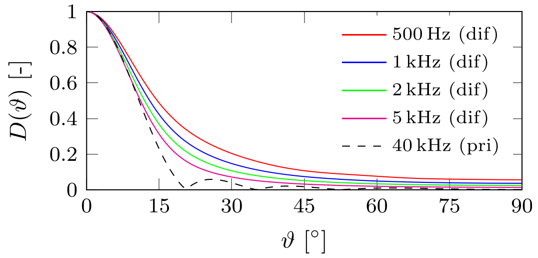

FIG. 6. (Color online) Directivity function of the piston with the parabolic velocity distribution calculated at the distance $r_0 = 2$ m from the piston centre; dashed line, the primary wave (40 kHz); solid lines, individual difference frequencies.

B. Horned piston

Within this subsection, the capabilities of the proposed computational approach are demonstrated on an example of a piston equipped with a simple horn. It has been demonstrated in the experimental work[23] that if a parametric radiator is equipped with a horn, its directivity and efficiency strongly increases; later, a simple model[24] is proposed.

In this work, the horn is supposed to have a hyperbolic-cosine shape, described as

$$r(z) = a\cosh(\alpha z), \quad \text{where } \alpha = \frac{1}{l}\,\text{arccosh}\left(\frac{b}{a}\right), \tag{18}$$

(see also Fig. 8) where a is the small horn radius (throat, the same as the piston radius), b is the larger horn radius (mouth), and l is the horn length.

In all the numerical results presented in this subsection, $a = 2$ cm, $b = 4$ cm, and $f_c = 40$ kHz; the primary acoustic field is calculated employing BEM (see Sec. IV B).

Figure 9 shows the distribution of the normalized acoustic pressure amplitude of the carrier wave along the z axis for uniform piston velocity distribution and individual lengths l of the horn. It can be observed that the structure of the near-field is very much dependent on the horn length; however, the far-field is not affected by the presence of the horn significantly. The far-field directivity is similar for all the cases, and with the increasing horn length, the on-axis pressure slightly increases. For example, at the distance of

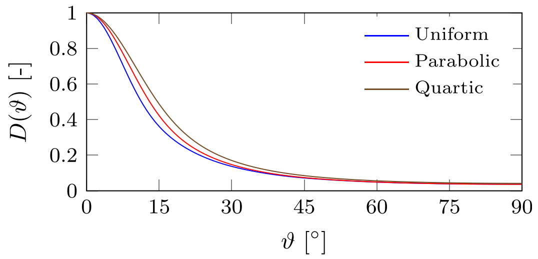

FIG. 7. (Color online) Directivity function of a piston with various velocity distributions calculated at the distance $r_0 = 2$ m from the piston centre, $f_d = 1$ kHz.

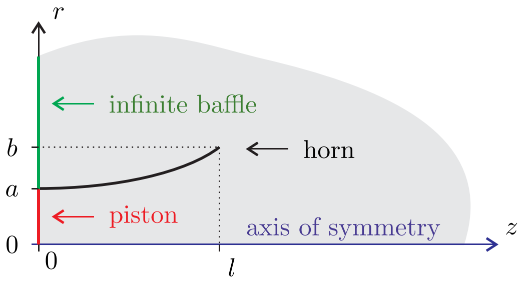

FIG. 8. (Color online) Computational domain for a piston equipped with a horn.

$r_0 = 2$ m from the piston, the on-axis pressure amplitude with the horn with $l = 8$ cm is by about 11% higher than without the horn. The primary wave radiation efficiency is not influenced by the presence of the horn significantly because in this case $\Re[k_c]a = 14.6 \gg 1$, which means that the piston radiation impedance is close to the characteristic one (the presence of the horn does not influence it significantly), and the beam emitted by the piston alone is rather directional—the first null-radiation angle for the carrier wave is $\theta_1 = 15^\circ 10'$.

Figure 10 shows the acoustic pressure amplitude of the difference-frequency wave at $f_d = 1$ kHz along the z axis for the same conditions as before. The solid lines represent the predictions by the Kuznetsov equation, and the dashed lines are related to the Westervelt equation. It can be observed that with the increasing horn length, the acoustic pressure in the vicinity of the piston rapidly increases, and this region of the increased pressure is more-or-less limited to the dimensions of the horn. Farther away from the horn (in the far-field), the acoustic pressure amplitude is not very much dependent on the horn length. In contrast to the predictions by the Westervelt equation, the Kuznetsov equation predicts small ripples in the near-field, probably caused by the existence of a partial standing wave in the horn.

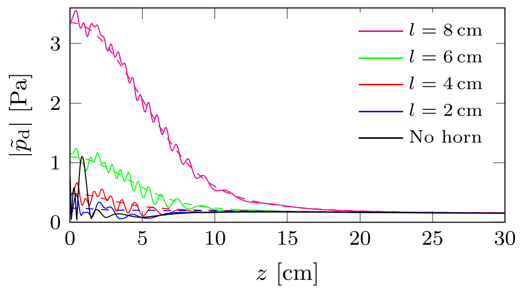

FIG. 10. (Color online) Acoustic pressure amplitude of the difference-frequency wave at $f_d = 1$ kHz along the z axis for the uniform piston velocity distribution and individual horn lengths; solid lines, prediction by the Kuznetsov equation; dashed lines, prediction by the Westervelt equation.

The influence of the presence of a horn on the difference-frequency wave in the far-field is demonstrated in Fig. 11. All the parameters are the same as before, and the acoustic field is calculated at the distance $r_0 = 2$ m from the piston centre. It can be seen that with the increasing horn length (from $l = 0$ cm to $l = 6$ cm), the on-axis pressure increases with the horn length. For example, for the horn with length $l = 6$ cm, the on-axis pressure is 11.3% higher than without the horn. But, with the horn length increased to $l = 8$ cm, the on-axis pressure decreases, and its amplitude is similar to the case of $l = 4$ cm. Also, the presence of a "side-lobe" can be observed in this case.

Figure 12 shows the directivity pattern of the difference-frequency wave for the same parameters as shown in Fig. 11 but for the piston with parabolic velocity distribution. Contrary to the previous case with increasing horn length l, the on-axis pressure amplitude decreases. As before, the presence of a side-lobe can be observed in the case of $l = 8$ cm.

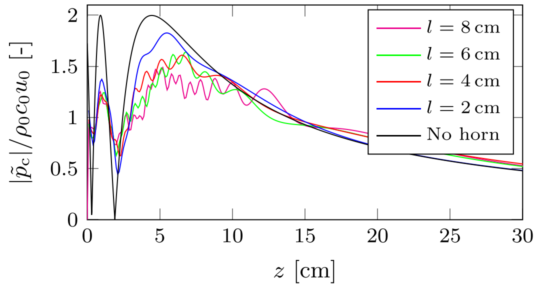

FIG. 9. (Color online) Normalized acoustic pressure amplitude of the carrier wave at $f_c = 40$ kHz along the z axis for the uniform piston velocity distribution and individual horn lengths.

VI. CONCLUSIONS

Within this work, a versatile computational approach for the numerical modelling of parametric generation of a low-frequency sound has been described. The proposed method is based on the quasi-linear approximation and it does not employ the paraxial approximation. The primary acoustic field is calculated by BEM or employing the Rayleigh integral in the case of a baffled piston; the secondary difference-frequency field is calculated by FEM. Three nonlinear wave equations derived in the second approximation have been compared: a general equation for the acoustic pressure, the Westervelt equation, and the Kuznetsov equation for the velocity potential. It has been demonstrated that as the Lagrangian density is neglected in the Westervelt equation, it does not correctly capture the near-field complexity of the secondary difference-frequency field. All the equations provide the same results in the far-field. If the information about the near-field structure of the difference-frequency wave is needed, the Kuznetsov equation for the velocity potential is the most suitable model equation as its nonlinear terms do not contain the second-order spatial

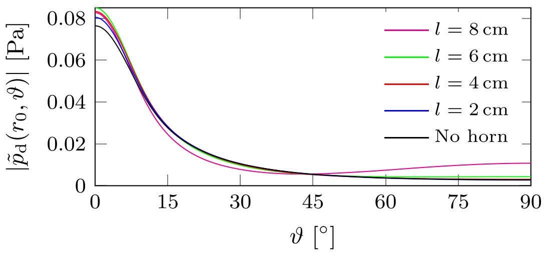

FIG. 11. (Color online) Directivity pattern of the difference-frequency wave at $f_d = 1$ kHz for various horn lengths l, calculated at the distance $r_0 = 2$ m from the piston centre; piston with uniform velocity distribution.

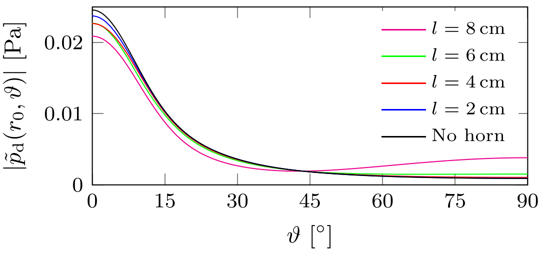

FIG. 12. (Color online) Directivity pattern of the difference-frequency wave at $f_d = 1$ kHz for various horn lengths l, calculated at the distance $r_0 = 2$ m from the piston centre; piston with parabolic velocity distribution.

derivatives whose numerical evaluation is expensive and prone to the numerical discretization errors. Two numerical examples have been given. First, the near-field, as well as the far-field, of a difference-frequency wave parametrically radiated from a baffled circular piston with different velocity distributions have been examined. Second, the radiation pattern of a parametric emitter combined with a horn has been studied. The numerical results show that in the studied cases, the directivity of the difference-frequency wave can be increased as well as decreased by the presence of the horn, depending on its geometry and the piston velocity distribution. These findings are in accord with the results reported in the experimental work,[23] where, unfortunately, the geometrical details have not been given. Contrary to the experimental work[23] a prominent directivity improvement, thanks to the horn, has not been observed, which means that this effect may be rather delicate, and it requires further study.

ACKNOWLEDGMENTS

This work was supported by Grant Agency of the Czech Republic (GACR) Grant No. GA18-24954S.

[1] P. J. Westervelt, “Parametric acoustic array,” J. Acoust. Soc. Am. **35**, 535–537 (1963).

[2] M. F. Hamilton, “Sound beams,” in *Nonlinear Acoustics*, edited by M. F. Hamilton and D. T. Blackstock (Academic, San Diego, 1998), pp. 233–261.

[3] W.-S. Gan, J. Yang, and T. Kamakura, “A review of parametric acoustic array in air,” Appl. Acoust. **73**, 1211–1219 (2012).

[4] M. Yoneyama, J. Fujimoto, Y. Kawamo, and S. Sasabe, “The audio spotlight: An application of nonlinear interaction of sound waves to a new type of loudspeaker design,” J. Acoust. Soc. Am. **73**, 1532–1536 (1983).

[5] F. J. Pompei, “The use of airborne ultrasonics for generating audible sound beams,” J. Audio Eng. Soc. **47**, 726–731 (1999).

[6] U. Sayin, P. Artís, and O. Guascha, “Realization of an omnidirectional source of sound using parametric loudspeakers,” J. Acoust. Soc. Am. **134**, 1899–1907 (2013).

[7] N. Tanaka and M. Tanaka, “Active noise control using a steerable parametric array loudspeaker,” J. Acoust. Soc. Am. **127**, 3526–3537 (2010).

[8] K. Tanaka, Ch. Shi, and Y. Kajikawa, “Binaural active noise control using parametric array loudspeakers,” Appl. Acoust. **116**, 170–176 (2017).

[9] M. Arnela, O. Guasch, P. Sánchez-Martín, J. Camps, R. M. Alsina-Pages, and C. Martínez-Suquía, “Construction of an omnidirectional parametric loudspeaker consisting in a spherical distribution of ultrasound transducers,” Sensors **18**, 4317-1–4317-17 (2018).

[10] T. G. Muir and J. G. Willette, “Parametric acoustic transmitting arrays,” J. Acoust. Soc. Am. **52**, 1481–1486 (1972).

[11] G. S. Garrett, J. N. Tjøta, and S. Tjøta, “Nearfield of a large acoustic transducer, Part II: Parametric radiation,” J. Acoust. Soc. Am. **74**, 1013–1020 (1983).

[12] T. Kamakura, N. Hamada, K. Aoki, and Y. Kumamoto, “Nonlinearly generated spectral components in the nearfield of a directive sound source,” J. Acoust. Soc. Am. **85**, 2331–2337 (1989).

[13] D. Ding, “A simplified algorithm for the second-order sound fields,” J. Acoust. Soc. Am. **108**, 2759–2764 (2000).

[14] J. Yang, K. Sha, W. S. Gan, and J. Tian, “Nonlinear wave propagation for a parametric loudspeaker,” EICE Trans. Fundam. **E87A**, 2395–2400 (2004).

[15] M. Červenka and M. Bednařík, “Non-paraxial model for a parametric acoustic array,” J. Acoust. Soc. Am. **134**, 933–938 (2013).

[16] H. Nomura, C. M. Hedberg, and T. Kamakura, “Numerical simulation of parametric sound generation and its application to length-limited sound beam,” Appl. Acoust. **73**, 1231–1238 (2012).

[17] S. I. Aanonsen, T. Barkve, J. N. Tjøtta, and S. Tjøtta, “Distortion and harmonic generation in the nearfield of a finite amplitude sound beam,” J. Acoust. Soc. Am. **75**, 749–768 (1984).

[18] M. Bednařík and M. Červenka, “Equations for description of nonlinear standing waves in constant-cross-sectioned resonators,” J. Acoust. Soc. Am. **135**, EL134–EL139 (2014).

[19] V. P. Kuznetsov, “Equation of nonlinear acoustics,” Sov. Phys. Acoust. **16**, 467–468 (1970).

[20] H. E. Bass, L. C. Sutherland, A. J. Zuckerwar, D. T. Blackstock, and D. M. Hester, “Atmospheric absorption of sound: Further developments,” J. Acoust. Soc. Am. **97**, 680–683 (1995).

[21] H. E. Bass, L. C. Sutherland, A. J. Zuckerwar, D. T. Blackstock, and D. M. Hester, “Erratum: Atmospheric absorption of sound: Further developments [J. Acoust. Soc. Am. **97**, 680–683 (1995)],” J. Acoust. Soc. Am. **99**, 1259–1259 (1996).

[22] D. T. Blackstock, *Fundamentals of Physical Acoustics* (Wiley-Interscience, New York, 2000), Chap. 13.

[23] U. Sayin and O. Guasch, “Directivity control and efficiency of parametric loudspeakers with horns,” J. Acoust. Soc. Am. **134**, EL153–EL157 (2013).

[24] L. H. Tong, S. K. Lai, J. W. Yan, and C. Li, “Highly directional acoustic waves generated by a horned parametric acoustic array loudspeaker,” J. Vib. Acoust. **141**, 011012-1 (2019).